Halometallate Ionic Liquids and Deep Eutectic Solvents

Rebecca Rowe

Department of Chemistry, Imperial College London

Submitted in part fulfilment of the requirements

for the award of Doctor of Philosophy

in Chemistry, Imperial College London

2019

Contents

List of Figures

11

13

List of Tables

Glossary

AO atomic orbital.

DES deep eutectic solvent.

DFT density functional theory.

EXAFS extended X-ray absorption fine structure.

HF Hartree-Fock.

HMDES halometallate deep eutectic solvent.

HMIL halometallate ionic liquid.

HOMO highest occupied molecular orbital.

IL ionic liquid.

LETC ligand exchange thermochromism.

LMCT ligand to metal charge transfer.

MO molecular orbital.

TD-DFT time dependent density functional theory.

Declaration of Originality

The work reported in this thesis (unless otherwise noted and referenced) was undertaken by myself, Rebecca Rowe, at the Department of Chemistry, Imperial College London between 2014 and 2019.

Copyright Declaration

Abstract

Ionic liquids and deep eutectic solvents have engendered wide and increasing research interest in recent years due to their interesting and tunable physical, chemical and solvation properties. The addition of metal halide salts to ionic liquids and deep eutectic solvents results in HMILs (halometallate ionic liquids) and HMDESs (halometallate deep eutectic solvents). A detailed understanding of these systems is vital to develop a relationship between chemical structure and properties which would enhance the useful application of HMILs and HMDESs.

In this work bismuth based HMILs and nickel based HMDESs were studied via DFT calculations. The aims of studying both systems were: to understand the speciation in solution, and the driving forces determining speciation; to analyse the intermolecular interactions present; and to investigate the electronic structure of the systems.

In the bismuth HMIL system the anionic speciation was elucidated; Cl^-, $[BiCl_4]^-$, $[BiCl_5]^{2-}$, $[Bi_2Cl_7]^-$, $[Bi_2Cl_8]^{2-}$, and $[Bi_2Cl_9]^{3-}$ anions can be accessed by varying the mole fraction of BiX_3 added to the ionic liquid (X = Cl, Br, I). An associative halide exchange mechanism was found, with a low barrier to reaction indicating that rapid exchange of halide atoms is likely to occur in solution. Experimental valence band XPS was reproduced, indicating that the theoretical method describes the electronic structure of HMILs well.

In the nickel HMDES system speciation was found to be influenced by both enthalpic and entropic factors. Highly charged complexes were enthalpically favoured over neutral species due to stronger intermolecular interactions, including doubly ionic hydrogen bonds. The previously reported thermochemical equilibrium between octahedral (low temperature) and tetrahedral (high temperature) species was rationalised via thermochemical analysis; the octahedral species is enthalpically favoured and the tetrahedral species entropically favoured. As temperature is a factor in the entropic part of Gibbs free energy the tetrahedral species becomes favoured at elevated temperatures.

Acknowledgments

Chapter 1

Introduction

ILs (ionic liquids) and the related class of DESs (deep eutectic solvents) have been of substantial and increasing interest to researchers over the past two decades, due to both their useful and tunable properties, and the potential for greener alternatives to conventional solvents. [1–4]

Metal halide salts may be added to both ILs and DESs, forming halometallate solvents, usually containing metal halide anions, Fig. 1.1. Areas of application of halometallate solvent systems include electrochemistry, catalysis, and separation/extraction. [5]
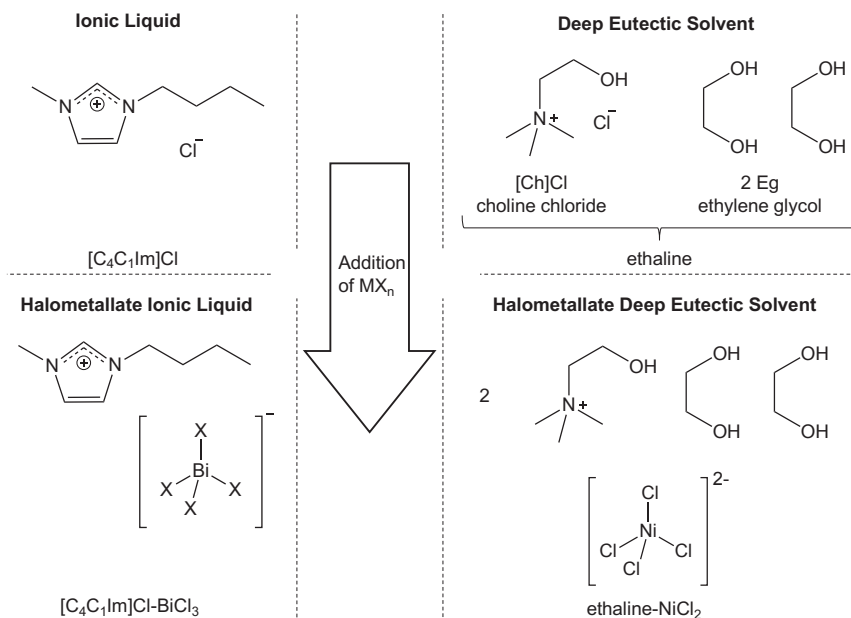
Figure 1.1: Representative IL (ionic liquid) and DES (deep eutectic solvent) systems. When metal halide salts are dissolved the corresponding halometallate systems are generated: HMILs (halometallate ionic liquids), and HMDESs (halometallate deep eutectic solvents).

The focus of this thesis is the computational investigation of a HMIL (halometallate ionic liquid): $[C_4C_1Im]X-BiX_3$ (X = Cl, Br, I), and a HMDES (halometallate deep eutectic solvent): ethaline$-NiCl_2$, Fig. 1.1.

The remainder of this thesis is structured into 5 chapters. This introduction begins by giving an overview of ionic liquids in general, then discussing halometallate ionic liquids in particular. Deep eutectic solvents are then introduced. Metal-ligand interactions for main group metals (especially bismuth) and d-block metals (especially nickel) are then reviewed, with the d-block section including an overview of ligand exchange thermochromism (LETC).

THESIS OUTLINE

- Define HMILs and HMDESs
- Will study BiX in HMILs, and NiX in HMDESs
- Outline of thesis

1. INTRODUCTION - BACKGROUND

- ILs and HMILs
- DESs and HMDESs
- Main group halometallates
- D-block metal complexes

2. THEORY

- DFT
- TDDFT
- SMD solvation model
- AIM analysis
- Thermochemistry

ORIGINAL CONTRIBUTIONS

3. Bi HMIL

- Anion structure
- Anion-cation interactions
- Speciation
- Experimental UV-vis
- TDDFT

4. Ni HMDES

- Nickel vs other metals
- Nickel coordination
- Intermolcular interactions
- Effect of solvation
- Electronic structure

5. CONCLUSIONS

Figure 1.2: Graphical outline of the structure of this thesis and the key points in each chapter.

Chapter 2 provides the theoretical background for the computational methods utilised in this research.

Chapter 3 presents the computational investigation into $[C_4C_1Im]X-BiX_3$ (X = Cl, Br, I). The key contributions made are: the prediction of anionic speciation at various compositions; the analysis of anion and ion cluster structures; the analysis of anion-cation interactions; the finding that the SMD solvation model accurately reproduces the ionic liquid environment; the prediction of an associative mechanism of halide exchange between anions; and the rationalisation of experimental UV-vis spectra via TD-DFT.

Chapter 4 presents the computational investigation into ethaline$-NiCl_2$. The key contributions are: the rationalisation of the different complexation reported for M = Ni compared to other 3d metals; the prediction of the relative stability of a series of nickel containing complexes; and the analysis of intermolecular interactions between nickel complexes and other species in solution.

The findings are summarised in Chapter 5.

1.1 Ionic liquids

ILs are substances made up entirely of anions and cations (Fig. 1.3) which melt at "low" temperatures, where low is usually defined as <100°C. The ions in ILs are larger than the ions in common, high melting salts, such as table salt (NaCl). Larger ions pack into

Cations

$[C_4C_1Im]^+$ $[N_{4,1,1,1}]^+$

$[C_4HIm]^+$ $[Ch]^+$

Anions

$[BF_4]^-$ $[Tf_2N]^-$

Cl^- SCN^-
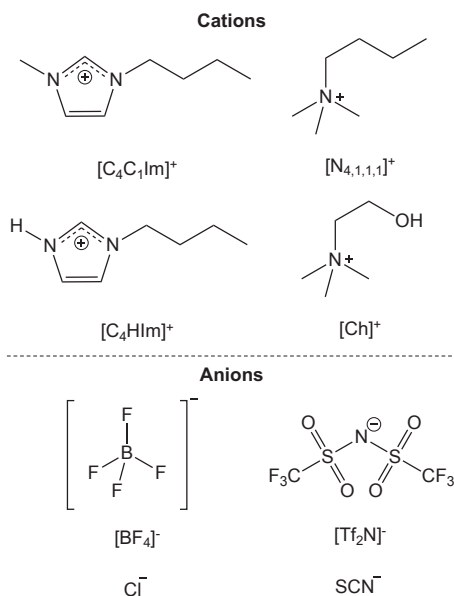
Figure 1.3: Chemical structures and conventional names of some common IL cations and anions.

space less efficiently than smaller ions, and have lower charge densities, causing weaker intermolecular interactions and contributing to the lower melting points present in ILs. Entropy also contributes to the low melting points of ILs; the large, flexible ions are conformationally undiscerning, both as individual ions, and in relation to the other ions in solution. The high degree of conformational flexibility leads to a large increase in entropy in the liquid phase, decreasing the melting point of the IL.

Applications

Applications of ILs in academia and industry are numerous and varied, Table 1.1. The popularity of ILs is partially due to a number of useful properties common to most ILs: negligible vapour pressure, high thermal stability, catalytic activity, ionic conductivity, low flammability, and strong solvation activity.[3] However the most interesting feature of ILs is their tunability. If 1000 possible anions and cations exist (a broad array of ion types are available, including different R groups and functional groups) then there are 10^6 potential simple ion combinations which could form ILs, and 10^{12} possible binary mixtures of ILs. Understanding of the relationship between ion structure and emergent properties is therefore key for the further development of IL applications. Predictive models would open the door to "designer solvents" where a desired set of properties is provided by a bespoke IL.[14]

Classes of IL

ILs have been categorised into classes, based on a variety of features, in an *ad hoc* manner as the field has evolved. For example, classifications of ILs based on melting point temperature, ion type, and chemical features are all popular in the literature, Fig. 1.4.

The most common classes are based on melting point, these include 'room temperature ILs' and 'low temperature ILs' which are ILs with melting points below 20

Area of application	Specific example
Synthesis and catalysis[2,3,6]	Biphasic acid scavenging (BASIL)
Electrochemical and energy[7,8]	Electrolytes in supercapacitors
Analytical chemistry[9]	Optical sensors
Medical and biological[10]	Drug delivery
Gas processing[11]	CO_2 capture
Metal processing[12]	Nuclear fuel extraction from waste
Biomass processing[13]	Dissolution of cellulose

Table 1.1: Areas where ILs are applied and associated examples of application. Relevant review articles are cited for each area.
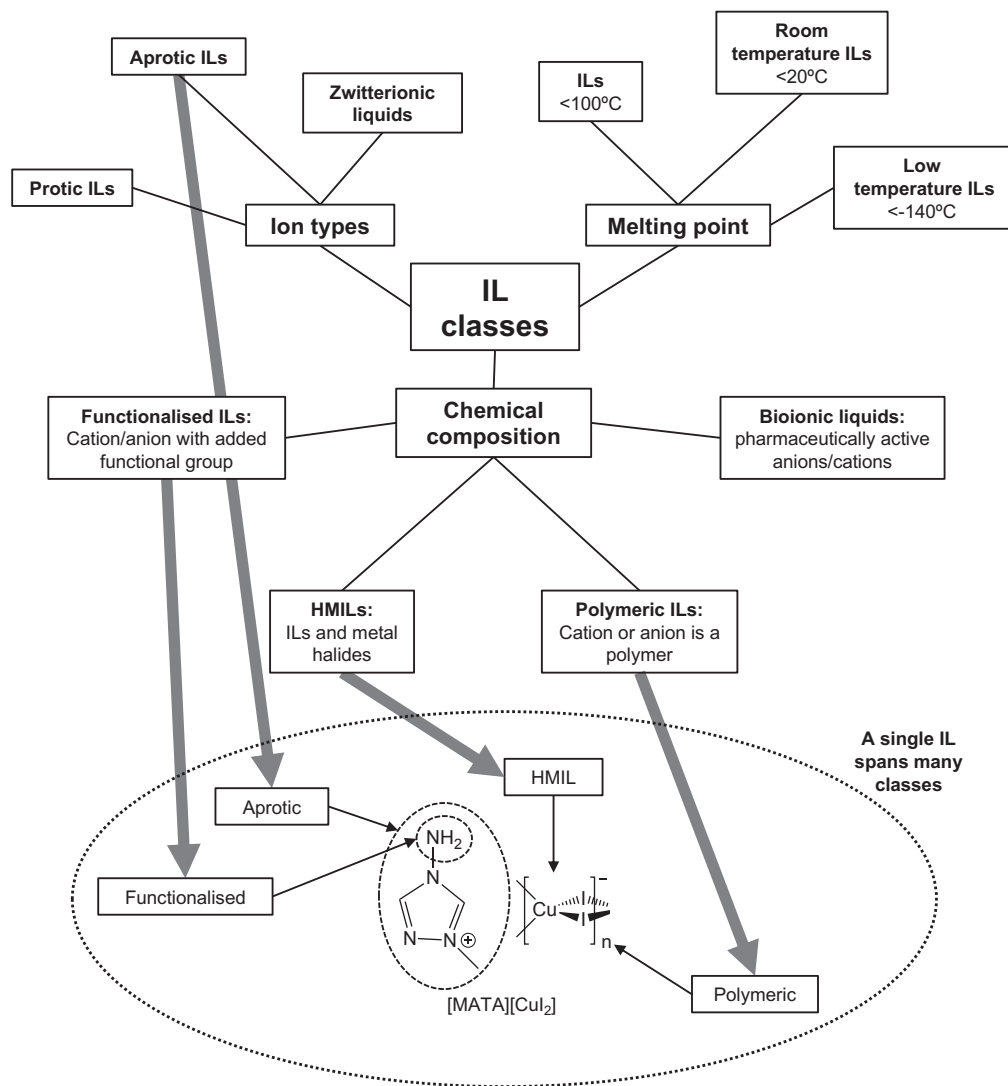
Figure 1.4: Mind map representing relationships between classes of ILs.

and -100°C respectively. In the latter category the IL $[C_2C_1Im][EtOSO_3]$ melts at -100°C and has been proposed as the liquid medium for a lunar-based liquid mirror telescope.[15] As well as the ILs low melting point, its high viscosity and low vapour pressure also make it a suitable candidate for a liquid mirror telescope in a vacuum environment.

Ion type in Fig. 1.4 refers to charge distribution in the IL. For example zwitterionic liquids have positive and negative charges on the same molecule. Protic ILs are formed from the reaction of a Brønsted acid (proton donor) and a Brønsted base (proton acceptor) to form charged species: $B + AH \longrightarrow HB^+ + A^-$.[16] Protic ILs have different charge distributions to aprotic ILs because incomplete proton transfer, or aggregation of the species (instead of separation into clear anions and cations) is commonplace.

The chemical composition of the ions within the IL defines many classes. Functionalised IL have functional groups incorporated within the ions.[17] Polymeric ILs have polymeric anions or cations.[18] Bioionic liquids have pharmaceutically active anions or cations.[10]

A single IL may fall into many classes; the IL [MATA][CuI$_2$] is an example of an aprotic, polymeric, functionalised HMIL, Fig. 1.4. The cation [MATA]$^+$ is functionalised with an amine group, and the halometallate anion is a polymeric chain of [CuI$_2$]$^-$ units.

1.1.1 Structure and interactions

Understanding the interplay between molecular structure (atoms in ions and their arrangement), local interactions (between one ion and its neighbours) and nanostructure (the general organisation of ions at the nanoscale) is one of the primary aims of research in the ILs field. This is a complex task, requiring detailed research on specific interactions, as well as rigorous models of the underlying physical forces. Understanding nanostructure in liquids as a whole has presented a greater challenge to researchers than substances in the solid or gas phases. For this reason liquids have been called the "Cinderella of modern physics".[19] In the following section ion-ion interactions are introduced, then the nanostructural features commonly produced by these interactions are summarised.

Ion-ion interactions

Specific types of ion-ion intermolecular interactions in ILs arise from more general physical origins, Fig. 1.5. This section will outline the underlying physical forces, and then discuss each type of specific intermolecular interaction relevant to ILs. Imidazolium based ILs will be used to exemplify these concepts; see the lower left portion of Fig. 1.5 for the conventional atom numbering and directional schemes used when discussing imidazolium cations.

Coulombic forces are the electrostatic attractive forces between positive and negative charged species, and the electrostatic repulsive forces between positive and positive or negative and negative charged species. Coulombic forces are strong (for example ionic bonding in high melting salts such as NaCl) and have a distance dependence of $\sim \frac{1}{r^2}$.

Covalent bonding is the attractive interaction arising from the sharing of electrons between species; MOs (molecular orbitals) with contributions from both species are

formed. Covalent bonding mostly occurs within molecules but can be a significant component of intermolecular interactions such as H-bonding.

Van der Waals forces are those between molecular dipoles. There are two types of molecular dipole. Permanent dipoles are found in polar molecules which have atoms of differing electronegativity anisotropically located in the molecule. Induced dipoles occur in polarisible non-polar molecules, when the electron cloud is shifted by a nearby charged or polar species. Induced dipoles also arise in substances made up entirely of non-polar neutral species when the random nature of electron distribution instantaneously forms a dipole in one species, which may then induce dipoles in other species, creating a chain of induced dipoles.

Van der Waals forces may be split into three types: permanent dipole - permanent dipole (known as Keesom forces), permanent dipole - induced dipole (known as Debye forces) and induced dipole - induced dipole (known as London forces). London forces are also known as dispersion, and the term dispersion has often been used to describe any dipole - dipole forces between molecules. The leading term of Van der Waals forces has a distance dependence of $\sim \frac{1}{r^6}$.

From an understanding of the basic underpinning interactions; coulomb, covalent,
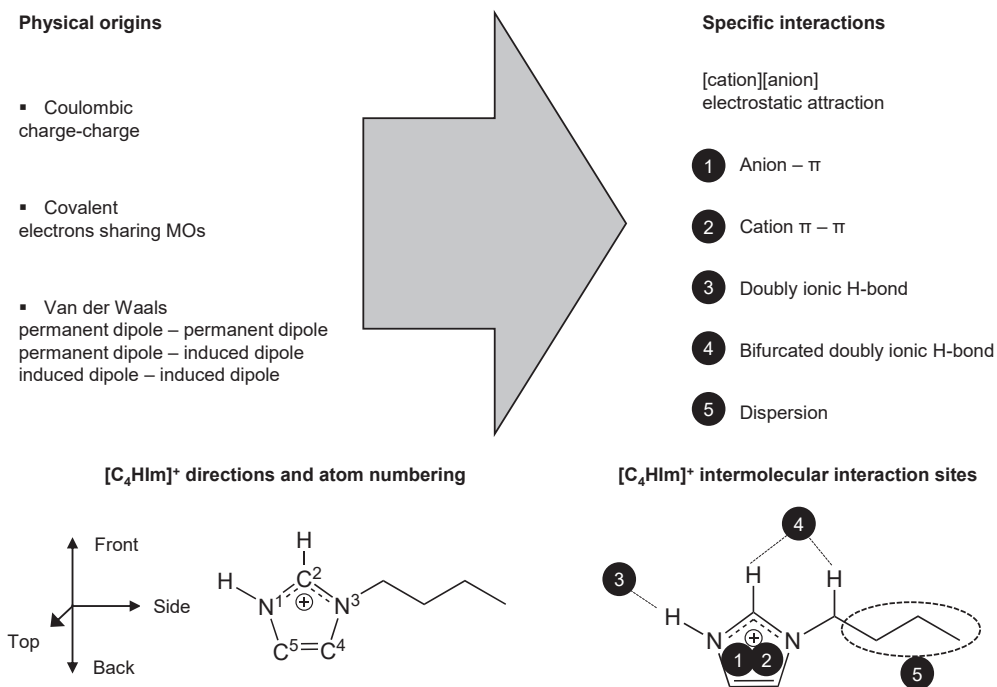
Figure 1.5: The physical origins of specific intermolecular interactions in ILs. The sites around a protic imidazolium cation $[C_4HIm]^+$ where these interactions occur. The directions used to describe regions of imidazolium cations are shown to the bottom left, with the conventional atom numbering.

and dispersion, the different types of intermolecular interactions between ions in ILs can now be discussed. The largest contributions to ion-ion forces come from the electrostatic attraction between anions and cations, and electrostatic repulsion between like ions. For simple ILs described by the formula [cation]$^+$[anion]$^-$ there is a wide range of strength and directionality of electrostatic interactions between different ILs. This is due to variations in ion size and charge distribution across ions. These variations have a large impact on the properties and structure of ILs.

Though Coulombic forces are the strongest effect by an order of magnitude, the weaker forces are important to understand and can have large effects on the macroscopic properties. An example of the effect of dispersion on physical properties is the melting points of [C$_n$C$_1$Im][anion] ILs. For n<5 increasing n disrupts the Coulombic matrix and the melting point is decreased, however for n>5 increasing n results in stronger dispersion interactions between alkyl chains and the melting point increases. A further intricacy is that introducing a *cis* double bond in long alkyl chains disrupts the dispersive forces and the melting point is again reduced.[20]

Two [C$_2$C$_1$Im]Cl conformers (optimised at the B3LYP-GD3BJ/aug-cc-pVDZ level, in the gas phase) demonstrate H-bonding and anion-π interactions in ILs, Fig. 1.6. The MOs of [C$_2$C$_1$Im]$^+$ are shown in the centre of Fig. 1.6, split into blue σ-type MOs and pink π-type MOs. The σ-type MOs interact with Cl$^-$ in the front conformer, and the π-type in the top conformer (conformer names refer to the position of the Cl$^-$ anion). The front conformer is the lowest energy structure, and the top conformer has a ΔG value of +5 kJ mol^{-1}.

In the front conformer the Cl$^-$ anion sits in the plane of the ring, near to the C^2 H atom, Fig. 1.6. The Cl 3p AO (atomic orbital) interacts with a low energy [C$_2$C$_1$Im]$^+$ σ MO, forming a bonding-antibonding pair of [C$_2$C$_1$Im]Cl MOs. The MO picture demonstrates the covalent (electron sharing) component of the H-bond, but the ionic contribution is likely to be larger as the H-bond is a 'doubly ionic' H-bond.[21] This type of H-bond forms between a H-bond donor with a positive charge (here [C$_2$C$_1$Im]$^+$) and a H-bond acceptor with a negative charge (Cl$^-$).

In the top conformer the Cl$^-$ is out of the plane of the ring, above the C^2-H bond, Fig. 1.6. The Cl 3p AO interacts with the [C$_2$C$_1$Im]$^+$ π type HOMO (highest occupied molecular orbital) forming bonding and antibonding [C$_2$C$_1$Im]Cl MOs. The covalent component of the anion-π interaction arises from this MO interaction. Electrostatic components are likely to contribute significantly.[22] The C^2–H moiety at the front of the
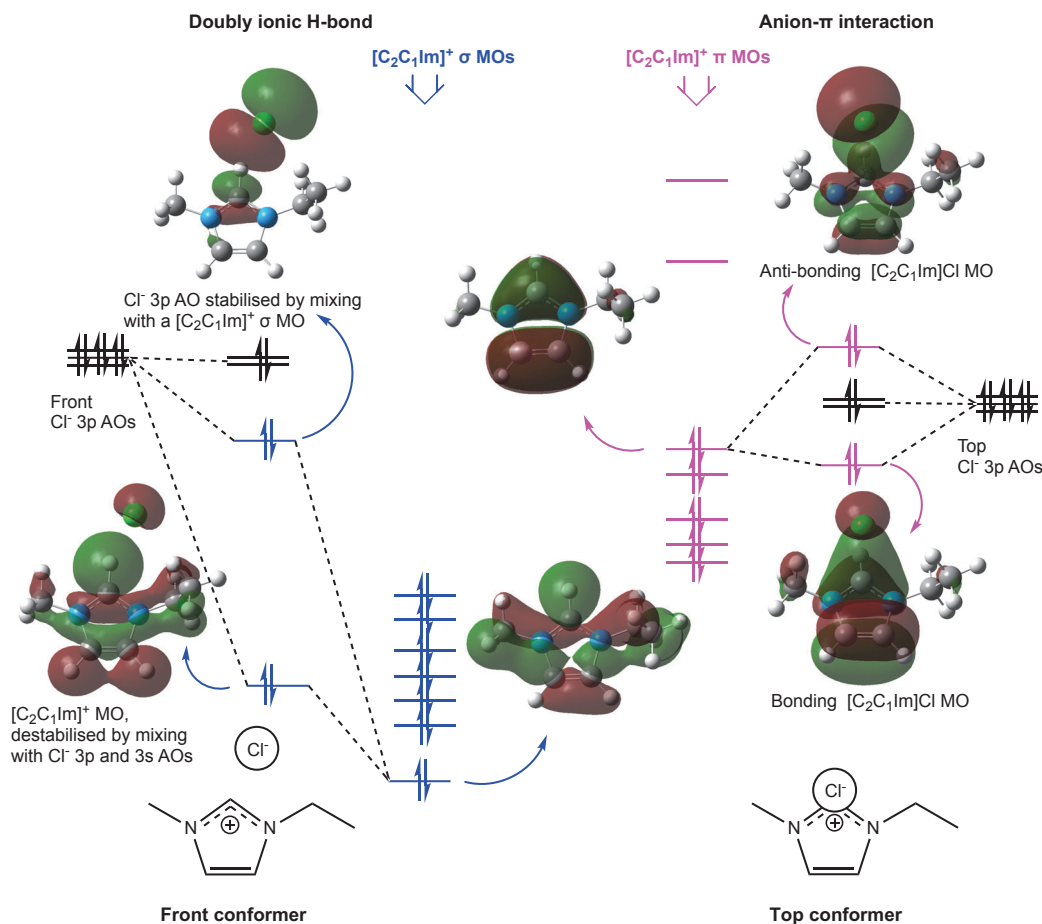
Figure 1.6: Doubly ionic H-bonding is present in the front conformer of $[C_2C_1Im]^+$ and anion-π interaction in the top conformer. The MOs of $[C_2C_1Im]^+$ are shown in the centre of the figure, split into blue σ-type MOs and pink π-type MOs. Structures optimised at the B3LYP-GD3BJ/aug-cc-pVDZ level.

ring is δ^+ due to the withdrawing effect of the two nitrogen atoms to either side.[23] Polarisation of the ring electron cloud may increase this effect leading to electrostatic interaction between the Cl^- ion and the imidazolium ring.[22]

Ion pairing

Cation-anion ion pairing has been a subject of much debate in the ILs field.[26] Ion-pairing is defined as a large proportion of ions being involved in persistent intermolecular interactions with one particular ion of the opposite charge, and that these interactions are stronger than those with the other surrounding species. Substantial ion pairing in pure ILs is not borne out in the modern literature.[26] However, when ILs are dissolved in molecular solvents, persistent ion pairing may be observed.[27] Although ion pairs are not generally indicated, the ions in ILs do have preferred relative distances and orientations between different species.

Probability of Cl⁻ is ≥ 150% of that in a random distribution

Top   Side
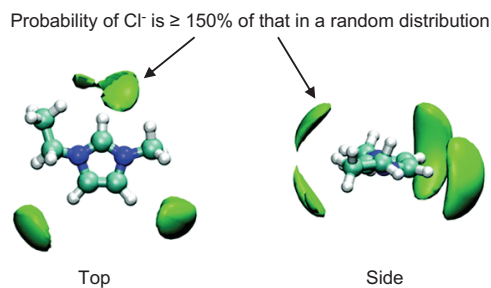
Figure 1.7: Spatial distribution function of Cl⁻ around $[C_2C_1Im]^+$ in a molecular dynamics simulation.[24] At the green isosurfaces the probability of finding Cl⁻ is 50% or more higher than the probability of finding a Cl⁻ in a randomly populated box of the same density. Adapted with permission from the PCCP Owner Societies.[25]

For example, spatial distribution functions of the relative positions of Cl⁻ around each $[C_2C_1Im]^+$ were plotted from molecular dynamics simulations of $[C_2C_1Im]Cl$, Fig. 1.7.[28] H-bonding sites are disproportionally occupied by Cl⁻ ions.

Polar and non-polar domains

"The evidence that IL ions self-assemble into amphiphilic nanostructures is now overwhelming."[26] At larger length scales than from one molecule to another there is persistent, directed structure in ILs: a split into polar and non-polar regions occurs.

In imidazolium ILs the polar regions contain the imidazolium rings and the anions, and the non-polar regions contain the alkyl chains, Fig. 1.8.[29] The relative volumes of the polar and non-polar portions of the ions influence the nanostructure of
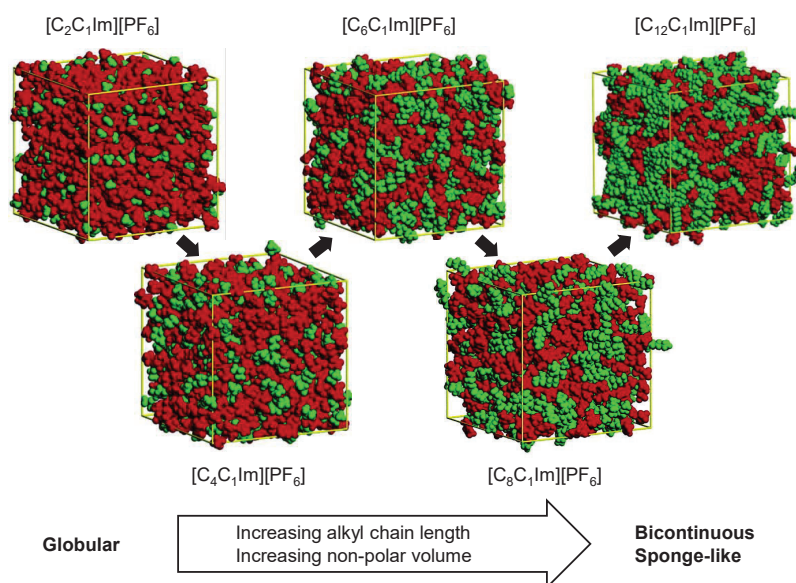
Figure 1.8: Polar (imidazolium rings and anions) regions (red) and non-polar (alkyl chains) regions (green) in molecular dynamics simulated boxes of the IL $[C_nC_1Im][PF_6]$. Adapted with permission, copyright 2019 American Chemical Society.[26,29]

30

the IL. When the non-polar volume is relatively low non-polar domains form within the continuous polar domain. The non-polar domains are globular and disconnected at low non-polar volumes. As the non-polar volume increases the globules interconnect and a bicontinuous, sponge-like structure develops. In fluorous ILs (ILs containing fluoridated alkyl groups) a third domain forms; the fluorous domain.[26] In ILs with alkyl chains and fluoridated groups the three domains are tricontinuous.

Amphiphilic self-assembly is ubiquitous in bulk ILs as well as in solid IL crystals and at interfaces.[26] In contrast molecular solvents have a much more homogeneous nano-structure; they generally contain only one component so separate domains are not formed. Molecular solvents are thought of as having a single polarity, which dictates which molecules may be dissolved according to the maxim: "like dissolves like". ILs with multiple domains dissolve a broader range of molecules; charged or polar solutes join the polar regions, and non-polar solutes are absorbed into the non-polar zones.[26]

1.1.2 Halometallate ionic liquids

HMILs are a key subcategory of ILs, defined by the presence of metal halide anions. The unique chemistry of HMILs has led to the potential for diverse applications in electrochemistry, biomass processing, catalysis, and gas storage.[5] HMILs are formed from the reaction of an organic halide salt, for example $[C_4C_1Im]Cl$, with a metal halide, such as $AlCl_3$. The reactive dissolution of $AlCl_3$ in equal parts $[C_4C_1Im]Cl$ forms the HMIL $[C_4C_1Im][AlCl_4]$. The HMIL system is $[C_4C_1Im]Cl-AlCl_3$,[5] denoted as *[cation][anion]-metal halide* to encompass liquids containing varying mole fractions of metal halide, and varying anionic speciation.

The ability to vary the choice of metal, mole fraction, halide atom and cation is indicative of a huge scope for tunability in HMIL systems. In 2014 a comprehensive review found that 22 different metal centres had been incorporated into HMILs,[5] and since then Bi(III) has been added to the group.[30] From group 13: Al(III), Ga(III), and In(III); from group 14: Sn(II), and Pb(II); from group 15: Bi(III); from the *d*-block: Ti(IV), Zr(IV), Hf(IV), Nb(V), Mn(II), Fe(II), Fe(III), Co(II), Ni(II), Pd(II), Pt(II), Cu(I), Cu(II), Au(III), Zn(II), Cd(II), and Hg(II).

"Anionic speciation" refers to the set of anionic species present in a HMIL. The anionic speciation of a HMIL is primarily determined by the mole fraction of metal halide and the choice of metal.[5] For example if a 1:1 mixture of $[C_4C_1Im]Cl$ and $AlCl_3$ is prepared, the mole fraction of $AlCl_3$ is $\chi_{AlCl_3} = 0.5$. The anionic speciation in this HMIL

is described by a point in the following equilibrium:

$\chi_{AlCl_3} = 0.5$:

$$[C_4C_1Im]Cl + AlCl_3 \rightleftharpoons [C_4C_1Im][AlCl_4]$$
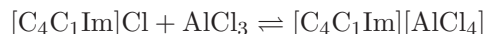
The position of this equilibrium is far to the right; there is negligible $AlCl_3$ or Cl^- present. The only anionic species observed is $[AlCl_4]^-$.[5,31] However, if a 2:1 mixture of $[C_4C_1Im]Cl$ and $AlCl_3$ is prepared the equilibrium is changed:

$\chi_{AlCl_3} = 0.33$:

$$2[C_4C_1Im]Cl + AlCl_3 \rightleftharpoons [C_4C_1Im]Cl + [C_4C_1Im][AlCl_4]$$

The anionic species now present are $[AlCl_4]^-$ and Cl^-.[5,31] $[AlCl_5]^{2-}$ is conceivable but does not form, probably due to the instability of the dianion $[AlCl_5]^{2-}$. In this case there is an excess of Cl^- anions. If an excess of $AlCl_3$ is added to the IL the equilibrium is changed again:

$\chi_{AlCl_3} = 0.67$:

$$[C_4C_1Im]Cl + 2AlCl_3 \rightleftharpoons [C_4C_1Im][AlCl_4] + AlCl_3 \rightleftharpoons [C_4C_1Im][Al_2Cl_7]$$

At this mole fraction of metal halide the anion observed is $[Al_2Cl_7]^-$.[5,31] Replacing Al(III) with In(III) changes the positions of the equilibria: At $\chi_{InCl_3} = 0.33$ the anionic species is $[InCl_5]^{2-}$, and at $\chi_{InCl_3} > 0.5$ the only observed anion is $[InCl_4]^-$, and a solid precipitate of $InCl_3$ is formed.[32,33]

Computational studies

Insight into the structure, bonding, and properties of ILs have been provided by theoretical investigations.[38] A wide variety of computational methods have been applied to a similarly wide variety of ILs, including comparatively very few HMIL systems.

$[BF_4]^-$ is a common IL anion with 4 halide atoms attached to a central atom, analogous to the $[MX_4]^-$ anions often present in HMILs. Anions with multiple δ^- atoms may simultaneously engage in multiple H-bonding interactions with the imidazolium ring, in contrast to the anion Cl^- which forms single H-bonds (although these may be bifurcated), Fig. 1.6. $[BF_4]^-$ has been studied in combination with $[C_2C_1Im]^+$ at the DFT (density functional theory) level (B3LYP/6-311++G(d,p)).[39] The lowest energy $[C_2C_1Im][BF_4]$ conformer is shown in Fig. 1.9.a. The F atoms in $[BF_4]^-$ H-bond preferentially to the C^2 H atom. The determined structures show a tendency for the
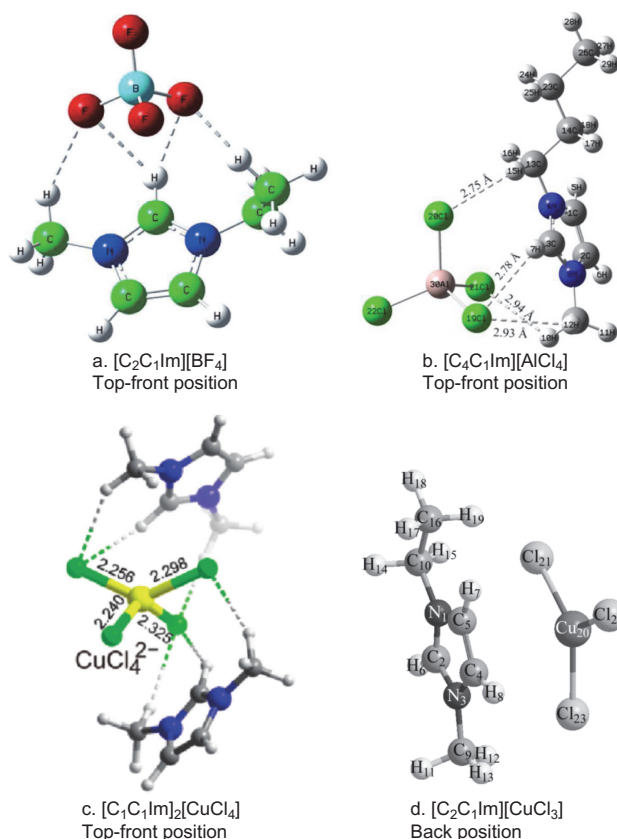
Figure 1.9: Selected optimised structures of HMIL ion clusters. a. [C$_2$C$_1$Im][BF$_4$], reproduced with permission from Wiley.[34] b. [C$_4$C$_1$Im][AlCl$_4$], reproduced with permission, copyright 2019 American Chemical Society.[35] c. [C$_1$C$_1$Im]$_2$[CuCl$_4$], reproduced with permission, copyright 2019 American Chemical Society.[36] d.[C$_2$C$_1$Im][CuCl$_3$]$^-$, reproduced with permission from Elsevier.[37]

anion to orientate with multiple F atoms pointing towards the cation. Each F atom H-bonds to two protons. The anion is positioned at the front of the cation to enable multiple interactions with both the C^2 proton and the alkyl protons.[39]

There have been several theoretical studies in the HMIL area. 12 out of 18 works (of which the author is aware) include Al(III)Cl systems.[31,35,40–49] Chlorides of the following metals have also been investigated: Au(III),[50] Fe(II),[51] Fe(III),[48,51] Cu(II),[36,52] Cu(I),[49,52] Cr(II),[36] Cr(III),[48] Zn(II),[46,48,49] and Hg(II).[46] Halides other than chloride have been included in three computational studies: Fe(III)Br;[53] [AlCl$_3$I]$^-$ and [ZnCl$_3$Br]$^{2-}$;[46] and Cu(I)I.[54] 8 works contain quantum chemical analysis (most via DFT) of HMIL ion pairs. The following metal centres were included: Al(III),[35,46–49] Fe(III),[48] Cu(II),[36] Cu(I),[37,49,54] Cr(II),[36] Cr(III),[48] Zn(II),[46,48,49] and Hg(II).[46] Figure 1.9 b-d. shows several example ion pair structures.

Pidko *et al.* studied Cr(II) and Cu(II) systems including variously charged monometallic and dimetallic anions (PBE0/6-31+G(d)).[36] Each anion was coupled with

the correct number of $[C_1C_1Im]^+$ cations to give a neutrally charged cluster. In every case each cation favoured an orientation such that the anion was above/below the front portion of the cation. One example is $[C_1C_1Im]_2[CuCl_4]$, shown in Fig. 1.9.c. This front-top conformer was determined for almost every ion pair structure reported in the literature.

Lu *et al.* investigated three Cu(I) ion pairs, $[C_2C_1Im][CuCl_2]$, $[C_2C_1Im][Cu_2Cl_3]$ and $[C_2C_1Im][CuCl_3]^-$ via Hartree-Fock (HF/6-31+G(d,p)(C, N, Cl, H atoms)Hay-Wadt ECPs(Cu atoms)).[37] In the first two cases the anions were found to sit in the front-top position, where H-bonds were possible to both the C^2 and the methyl protons. However the $[CuCl_3]^{2-}$ anion was determined to lie in the plane of the ring with two Cl atoms H-bonding with the C_4 and C_5 protons.[37] The structure is shown in Fig. 1.9.d. This example represents an interesting departure from the results for the other systems.

Wang *et al.* combined DFT with experimental work to study Cu(I) iodide HMILs (ωB97XD/def2-SVP with Stuttgart-Dresden relativistic ECPs on Cu and I atoms).[54] Crystallographic studies of $[C_2C_1Im]_4[Cu_4I_8]$, $[C_2C_1Im]_6[Cu_8I_{14}]$, and $[C_2C_1Im]_2[Cu_5I_7]$ showed H-bonding between the halometallate anions and the imidazolium cations. Cation stacking was also observed; in the solid state separate anion and cation channels form. In $[C_2C_1Im]_2[Cu_5I_7]$ the anionic species is polymeric in the solid phase. The Cu(I)I ILs were investigated as promoters for green propulsion fuels used in combustion engines. A theoretical mechanism was calculated for $2\,H_2O_2 +$ $[C_2C_1Im]_2[CuI_3] \longrightarrow O_2 + H_2O + [C_2C_1Im]_2[CuI_3]$, representing the ignition reaction. Throughout the mechanism the calculated structures have the Cu-containing species sandwiched between the two cations, in a top position relative to both. Anion-π interactions are indicated by this structure.

Li *et al.* examined the good performance of the $[C_4C_1Im]Cl-AlCl_3$ system in extractive desulfurisation via a detailed theoretical analysis (M06-2X/6-31++G(d,p)).[35] Energetic analysis of the anionic speciation reproduced the experimental findings that $[AlCl_4]^-$ is the main anion at $\chi_{AlCl_3} = 0.5$, and that $[Al_2Cl_7]^-$ forms at higher mole fractions. Using interaction energy and structural analysis the performance in extractive desulfurisation was correlated to stronger IL - sulfur containing compound interactions. The sulfur containing compound was found to interact with the HMIL anion via hydrogen bonding, and the cation via π - π interactions.[35]

Wang *et al.* investigated the effect of using different cations in aluminium deposition from [cation][Al_2Cl_7], in a combined experimental and theoretical approach

(B3LYP/6-31++G(d,p)).[47] Out of four cations the $[C_4C_1Im]^+$ species gave good quality aluminium surfaces at the lowest temperature. This result was rationalised theoretically by $[C_4C_1Im]^+$ having the lowest association energy with $[Al_2Cl_7]^-$, and the lowest viscosity, due to the low association energy and the relatively small size of $[C_4C_1Im]^+$.

Several authors have related quantum chemical parameters to experimentally determined measures of acidity and basicity of HMILs.[46,48,49] This process has allowed deeper understanding of how chemical structure influences the chemical properties and behaviours of ILs. Lewis acidity is the ability of a species to accept electrons, and Lewis basicity the ability to donate electrons. HMILs have enhanced Lewis acidity compared to other ILs, leading to better performance as Lewis acid catalysts.[55]

Wu *et al.* utilised electrostatic potential surfaces to quantify and rationalise the increase in Lewis acidity from $[C_4C_1Im]Cl$ to $[C_4C_1Im]Cl-AlCl_3$ to $[C_4C_1Im]I-AlCl_3$, Fig. 1.10.[46] The most-positive surface electrostatic potential, $V_{s,max}$, is used as a quantum chemical measure of acidity; high values mean higher acidity. In $[C_4C_1Im]Cl$ the Cl^- ion is located at the front of the cation, forming H-bonds with the $C^{2-}H$ and an alkyl H atom. The imidazolium ring is polarised due the Cl^- ion pulling electron density towards itself, at the front of the ring. The back of the ring is acidic with a positive electrostatic potential surface. When $AlCl_3$ is added and coordinates to Cl^- to form
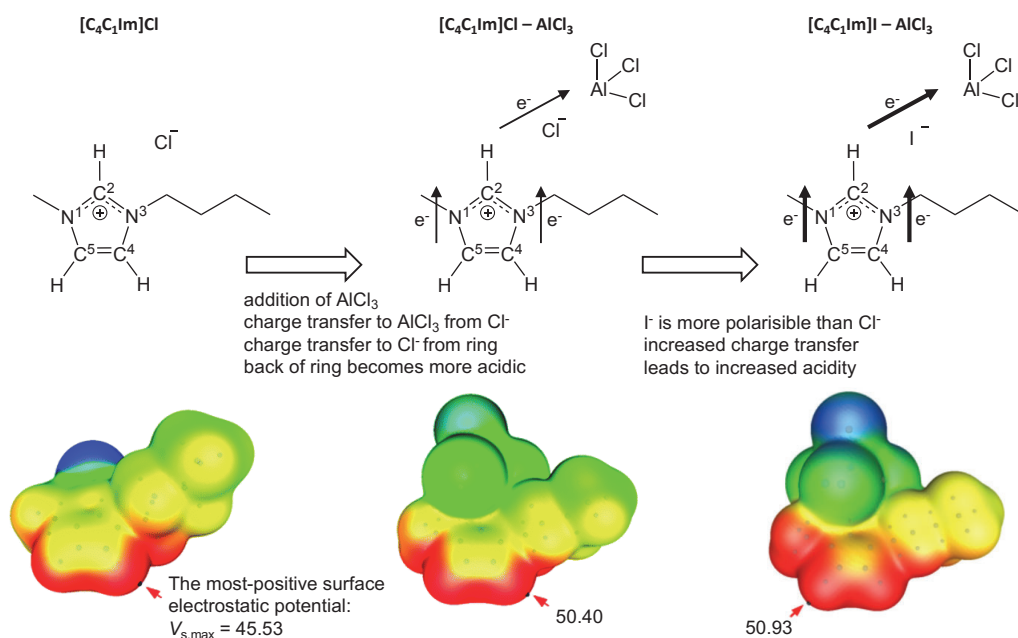
Figure 1.10: The addition of $AlCl_3$ to $[C_4C_1Im]Cl$ increases acidity. Switching $[C_4C_1Im]Cl-AlCl_3$ for $[C_4C_1Im]I-AlCl_3$ further increases acidity due to enhanced charge transfer away from the imidazolium ring.[46] Adapted with permission from the PCCP Owner Societies.[46] Coloured surfaces show electrostatic potential at the 0.001 a.u. contour of the electron density. Red arrows show the position of the most positive value $V_{s,max}$, in kcal mol^{-1}. The colour mapping is blue < -30 < green < -4 < yellow < 20 < red, in kcal mol^{-1}.

$[AlCl_4]^-$ electron density is transferred away from the Cl atom, and in turn from the ring, causing an increase in the electrostatic potential (and therefore acidity) at the back of the ring. In $[C_4C_1Im]I-AlCl_3$ the process of electron transfer is enhanced due to I^- being more polarisible than Cl^-.

From theoretical studies on HMILs in the current literature it is concluded that a range of anion-cation interactions influence the structure, physical properties and chemical behaviours of HMILs. Metal type, halide type, choice of cation, and mole fraction of metal halide all contribute in a complex manner to produce the observed behaviors. There is a lack of theoretical research into metals other than aluminium, and also into how anionic speciation is influenced by molecular and electronic structure. For HMILs understanding of these factors is important for electrochemical and catalytic applications.

1.2   Deep eutectic solvents

Eutectic mixtures are mixtures of 2 (or more) components, whose melting point at any composition is lowered compared to the expected melting point of an ideal mixture, Fig. 1.11.a. The composition at which the lowest melting point is achieved is the eutectic point. There are 4 phases of a simple binary eutectic mixture. At temperatures below the eutectic point a solid mixture of both components exists. Above the eutectic point the phase depends both on temperature and on the composition of the mixture; a liquid mixture of both components, or a liquid mixture of both components plus solid component A or component B will form, Fig. 1.11.a. Eutectic mixtures may have more than one eutectic point; the binary $Mg(NO_3)_2-H_2O$ system has three eutectic points.[56]
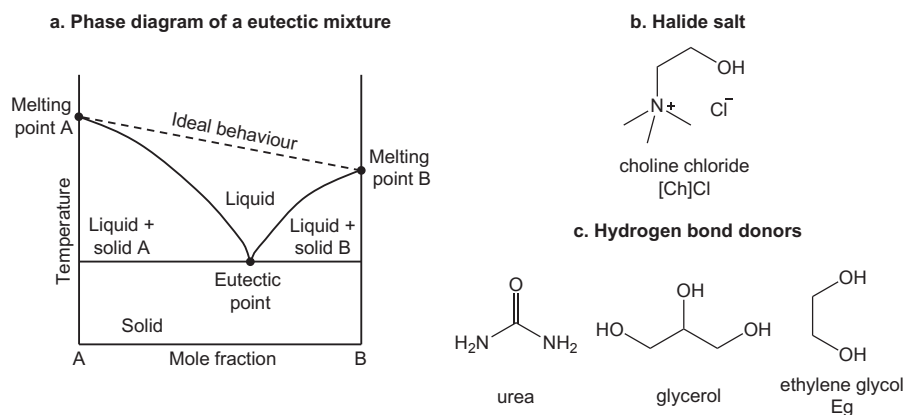
Figure 1.11: a. Sketch of the phase diagram for a binary eutectic mixture. b. The archetypal halide salt used in DESs, choline chloride. c. Common DES hydrogen bond donors urea, glycerol, ethylene glycol.

The comprehensive review by Smith *et al.* delineated DESs into four types, depending on their constituent molecules, Table 1.2.[57] For the purposes of this thesis the term DES will be used to refer only to type-III DESs; mixtures of salts consisting of organic cations and halide anions, and neutral molecules acting as hydrogen bond donors, Fig. 1.11.b,c. Type-I DESs are referred to in this work as HMILs. DESs (Smith type-III) with metal halides added will be referred to as HMDESs.

DESs are eutectic mixtures of a salt and a hydrogen bond donor, with physical properties which are often similar to ionic liquids - low vapour pressure, thermal stability and high ionic conductivity. Chemical properties that differ from ILs lead to different applications for DESs, compared to ILs. Over the past two decades research interest has increased in this category with investigations into applications in metal processing,[57] organic reaction media and catalysts,[58] nanomaterials,[59] gas separation,[60] and various types of extraction processing.[61] In general DESs are simpler and cheaper to synthesise than ILs (especially imidazolium varieties), less reactive with water, less toxic, and more often biodegradable.[57]

DESs may be tuned or functionalised in a similar manner to ILs, by selection of different types of hydrogen bond donor or adding functional groups to the organic cation - usually a quaternary ammonium moiety. Figure 1.11.a. is the phase diagram for a binary eutectic mixture. The melting point expected for an ideally behaving mixture is indicated by the dashed line. In eutectic mixtures the H-bonding between the salt and the hydrogen bond donor results in a deviation from ideality - the melting point is much lower than in an ideal mixture, and lower than for the pure constituents. The eutectic point is at the composition with the lowest melting point - the eutectic composition. For the common DESs with choline chloride as the salt and urea, ethylene glycol or glycerol as the hydrogen bond donor the eutectic composition is 1 salt : 2 hydrogen bond donor.

DESs with choline chloride salt components are often termed "choline based DESs." Choline is produced on the megaton scale for animal feed and is therefore cheap

Smith *et al.* type	Formula	Composition	Name in this work
I	$[\text{cation}]\text{X} + \text{MX}_x$	$[\text{cation}][\text{MX}_y]$	HMIL
II	$[\text{cation}]\text{X} + \text{MX}_x \cdot z\text{H}_2\text{O}$	$[\text{cation}][\text{MX}_y] + z\text{H}_2\text{O}$	n/a
III	$[\text{cation}]\text{X} + \text{R}-\text{Z}$	$[\text{cation}]\text{X} + \text{R}-\text{Z}$	DES
IV	$\text{R}-\text{Z} + \text{MX}_x$	$[\text{MX}_w \cdot \text{R}-\text{Z}][\text{MX}_y]$	n/a
n/a	$[\text{cation}]\text{X} + \text{R}-\text{Z} + \text{MX}_x$	$[\text{cation}][\text{MX}_y] + \text{R}-\text{Z}$	HMDES

Table 1.2: The classes of DES as defined by Smith *et al.*[57] The formula column shows the compounds mixed together and the composition column refers to the species formed in solution. M = metal, X = Cl, Br, I, R = alkyl group, Z = hydrogen bond donor, e.g. $-\text{OH}$, $-\text{COOH}$, $-\text{CONH}_2$.

and readily available. Choline based DESs are the most widely studied DES systems by a wide margin.

1.2.1 Structure and interactions

Several types of intermolecular interactions are present between the cationic, anionic, and neutral species in a DES, as is the case in ILs, Section 1.1.1. In initial reports on choline chloride DESs the hydrogen bond donor - chloride hydrogen bonding was assumed to be the primary interaction present and to be responsible for the melting point depression in these systems.[62,63] The 1 salt : 2 hydrogen bond donor ratio at the eutectic point could be naively interpreted to signify the complexation of Cl^- by exactly 2 hydrogen bond donor molecules. It had been posited that the negative charge would then be delocalised across the complex formed, and the intermolecular forces between complexes reduced, leading to the decreased melting point.[64] This will be referred to as "charge spreading", Fig. 1.12. However several subsequent computational studies have not supported this hypothesis. Deeper consideration of the other interactions and species present gave rise to a broad agreement that DESs contain a cooperative H-bond network, where competition between cation-anion, anion-HBD and cation-HBD disrupts the long range order found in the individual components and results in "charge separation" (Fig. 1.12) leading to the decrease in melting point.[65–71]

García *et al.* used DFT (B3LYP/6-31+G(d,p)) to study clusters of 30 choline based DESs.[66] Minimally sized clusters, consisting of the minimum number of molecules required to represent the stoichiometry of the DES, were optimised. The AIM (atoms in molecules) protocol was used to analyse the topology of the electron density calculated.[73] In AIM theory several types of critical point exist: atomic critical points, bond critical points (between two atoms), ring critical points (within a loop formed by several bonds) and cage critical points (within a cage formed by several adjoining rings). Each cluster was found to contain a network of hydrogen bonds between all the moieties in the cluster. The cage critical point (or sum of cage critical points for clusters with more than one) characterises the entire network. The authors cited the previous AIM analysis of ring systems by Palusiak *et al.*, who found that lower electron density at ring critical points correlated with increased electronic delocalisation across the ring.[74] Lower electron density at the cage critical point in the DES cluster was therefore interpreted as an indication of a more delocalised H-bonding network.

The melting point of the DESs was positively correlated with the electron density
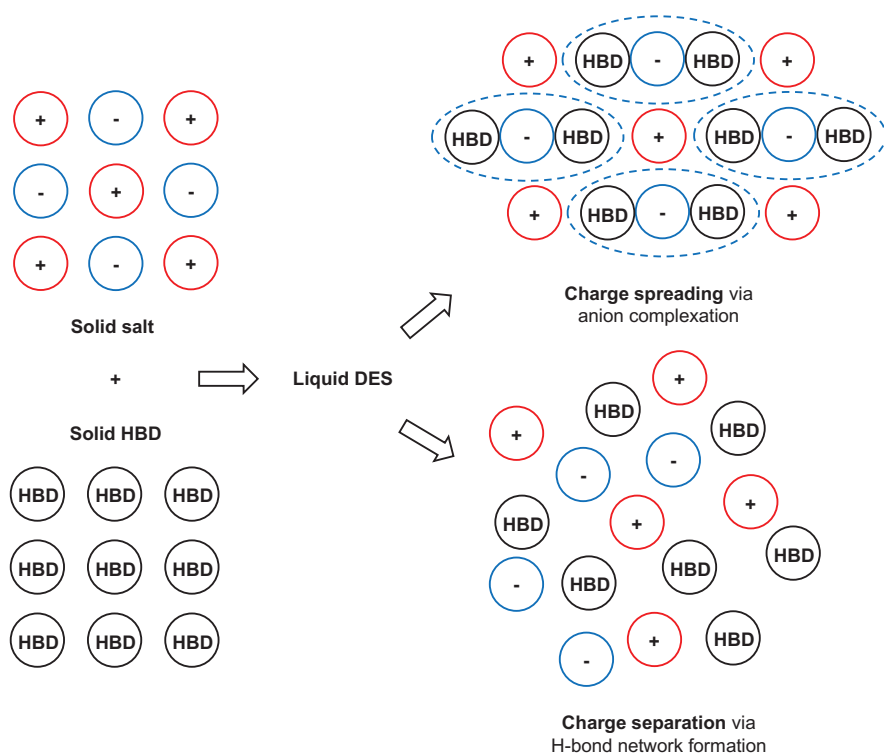
Figure 1.12: Charge spreading from the anion to the HBD molecules via complexation of the anion (through H-bonds) has been posited as a mechanism by which the melting point of the eutectic mixture is reduced.[72] Subsequently charge separation via formation of a H-bonding network between the cations, anions, and HBD molecules which results in loss of long range order and reduction of the sum of anion-cation interactions has been supported by theoretical investigations.[59,65,68]

at the cage critical point, with an R^2 value of 0.81. García *et al.* concluded that more delocalised H-bonding networks would increase charge transfer between species and therefore lower the melting point of the DES. This is the charge spreading model, Fig. 1.12. However one could also conclude that a more delocalised H-bond network means more disruption to the structure of the choline salt is present and therefore melting points are lowered - the charge separation model.

Ashworth *et al.* also used DFT calculations (B3LYP-D2/6-311++G(d,p)) and AIM analysis, to investigate the network of H-bonds in many small clusters (consisting of: Ch-Cl, Cl-urea, Ch-urea, and urea-urea) relevant to the ChCl-urea DES.[68] The calculated association energy was highest for the Ch-Cl cluster. An "alphabet soup" of different H bonding interactions, all moderate to weak in strength, was found: OH⋯O=C, NH⋯O=C, OH⋯Cl, NH⋯Cl, OH⋯NH, CH⋯Cl, CH⋯O=C, NH⋯OH and NH⋯NH. These H-bonds may be classified as neutral (between two neutral species), singly ionic (between one neutral and one charged species) or doubly ionic (between a cation and an anion).[21] The study did not support the formation of $[Cl(urea)_2]^-$, instead finding competitive interactions between the urea molecules and the Cl^- and Ch^+

39

species - both $[Cl(urea)]^-$ and $[Ch(urea)]^+$ were found to be energetically favoured. The extent of charge delocalisation between molecules in these clusters was low. The authors concluded that the melting point depression was better explained by the urea molecules inducing charge separation, than by charge spreading into urea molecules. The strongest H-bond located was between the O-H group on the choline cation and the =O on the urea molecule.

The importance of the choline O-H to urea =O H-bond was echoed in the joint theoretical and experimental study by Zhu *et al.* who also used DFT (B3LYP-D3/6-311++G(2d,p)) to calculate small clusters of DESs and carried out experimental IR/Raman spectroscopy on the same systems.[69] The calculated vibrational frequencies correlated well with the experimental values: the correlation coefficients were over 0.999 in all cases. Significant redshifts arising from the choline-urea H-bond were noted.

Wagle *et al.* studied three DESs : ethaline (2Eg : [Ch]Cl), reline (2 urea : [Ch]Cl), maloline (malonic acid ($HO_2C-CH_2-CO_2H$) : [Ch]Cl) via DFT (M06-2X/6-31++G(d,p)).[70] Calculations on minimally sized clusters found a strong correlation ($R^2 = 0.9977$) between the sum of the bond orders of the Ch^+-Cl^- interactions and the melting point of the DESs. (The authors do not include a description or reference for the method of calculation of bond orders.) Lower Ch^+-Cl^- bond order gave lower melting points. The CHELPG charges in clusters of the pure components were compared with the charges in the DES clusters and the smallest amount of charge spreading was found in the choline chloride - urea DES, which has the lowest melting point of the DESs studied. In fact the Cl^- anion was more negatively charged in the DES cluster than in neat choline chloride, indicating that charge spreading from the anion to the HBD is not reducing the anion charge.

Molecular dynamics has also been utilised to investigate these systems.[65,67,71] Sun *et al.* investigated several systems from pure choline chloride to pure urea, including mixtures of 25, 50, 67.5 and 70% urea. The lifetimes of H-bonds between choline and chloride, urea and chloride and choline and urea were minimised at the eutectic composition of 67.5% urea. The authors conclude that this is due to an optimal balance between HBD-anion and anion-cation interactions at the 67.5% urea composition maximising the long range disorder. In pure choline chloride there is long range order with alternating anions and cations around a given central cation. When urea is added it is accommodated in the coordination sphere around the cation, long range order and

cation-anion interactions are therefore reduced, which may lead to the reduction in melting point.

1.2.2   Halometallate deep eutectic solvents

The phrase HMDES (halometallate deep eutectic solvent) is used to indicate systems of type-III DESs to which have been added metal halide salts. HMILs as described in Section 1.1.2 have also been referred to in the literature as type-I DESs, Table 1.2.[57] The salient difference between HMDESs and HMILs or type-I DESs is that HMDESs contain neutral molecules (hydrogen bond donors) whereas HMILs contain only cations and anions, Fig. 1.1. Compared to HMILs there are few reports of HMDESs systems. Several authors investigated the addition of $NiCl_2$ to ethaline,[75–77] and reline.[78] Only one study included other transition metal halides.[79] Of interest to these authors were the electrodeposition and thermochromic properties of the Ni(II) HMDES. No theoretical investigations have been published. The literature on Ni(II) and the other transition metal HMDES systems will be reviewed in Section 1.4.9.

1.3   Main group metal halides

In order to investigate halometallate ionic liquids and deep eutectic solvents a good understanding of the bonding within the metal complexes is required. This section provides a general background of main group metal-halide interactions, with a focused section on bismuth halide complexes.

All but one of the (stable) main group metals in groups 13 onwards have been successfully incorporated into HMILs, however HMILs based on the group 1 and 2 metals have not been reported, Fig. 1.13.[5] Across the range of main group based HMILs a wide variation in maximum soluble mole fraction of metal halide salt and in anionic speciation is observed. It is unclear whether maximum soluble mole fraction is limited by temperature (the melting point of the eutectic mixture increases above the temperature used in the synthesis) or absolute solubility (no temperature exists where a single liquid forms at high mole fractions). The limiting factor of solubility may also be system-dependent. The metal chosen has a large impact on the properties of HMILs, mediated via the metal-halide interaction. This section discusses the interactions between main group metals and halides.

The electronegativity a metal impacts its interaction with halides; the less electronegative a metal is the more ionic its interactions with halides are. For example

41

Figure 1.13: Condensed periodic table, showing only the stable main group metals, and their Pauling electronegativity values. Metals which have been incorporated into a HMIL are underlined, and those which have Pauling electronegativity values of > 1.5 are highlighted in grey.

Na and Bi interact differently with Cl. Bi has an electronegativity value significantly closer to Cl (gap of 1.14) than Na does (gap of 2.23), Fig. 1.13. A simple computational analysis of the diatomics M–Cl was completed, via DFT (B3LYP/LanL2DZ, geometry optimisation, frequency analysis, NPA analysis), Fig. 1.14. Natural population analysis (NPA) yielded charge transfer values of 0.83 for Na–Cl and 0.46 for Bi–Cl. As expected the NPA values show a strongly ionic interaction in Na–Cl, and a partially ionic, partially covalent interaction in Bi–Cl. The difference in the interactions may also be observed in the molecular orbitals (MOs) calculated for each diatomic, Fig. 1.14. In Fig. 1.14 a. the Na 3s orbital is higher in energy than the Cl 3p AOs (due to the large electronegativity difference). No interaction between the Na orbitals and the Cl 3s AO is observed. The Cl $3p_z$ (along bond) AO interacts weakly with the Na 3s orbital; the occupied bonding MO is predominantly Cl $3p_z$ based with a small amount of polarisation towards the Na atom visible, whereas the unoccupied anti-bonding MO is primarily Na 3s, with a small Cl contribution. It is clear from these MOs that the valence electron from the Na atom becomes localised on the Cl atom when the diatomic is formed - a strongly ionic interaction. In contrast in Fig. 1.14 b. the Bi 6s and 6p orbitals are only slightly higher in energy than the Cl 3s and 3p AOs respectively. The 3s and $3p_z$ orbitals form bonding interactions where there are strong contributions from

both atoms to both bonding and anti-bonding MOs. Polarisation of electron density towards the Cl atom is in evidence: bonding MOs have larger Cl contributions and anti-bonding MOs have larger Bi contributions. Overall the Bi–Cl interaction has a much larger covalent component than Na–Cl.

The nature of metal halide salts MXn is related to the electronegativity of the metal. The group 1 and 2 (low electronegativity) metal halide salts are high melting crystals, with an ionic lattice structure. Molten group 1 and 2 halide salts are conductive. These salts have low solubilities in ionic liquids, for example only 0.065 weight % of NaCl will dissolve in [C_4C_1Im]Cl at 75°C.[80] The lack of solubility in ionic liquids may be attributed to the strong, ionic, interactions between metal and halide, which mean crystal formation is energetically favoured over dissolution.

The group 13 onwards metal halide salts more often have covalent molecular structures, and tend to be non-conductive in molten form. All except Tl have been added to ionic liquids to form HMILs, made up of organic cations and molecular metal halide anions. High-melting compounds of molecular organic cations and metal halide complexes are known. The metal halide anions may be molecular or polymeric. For
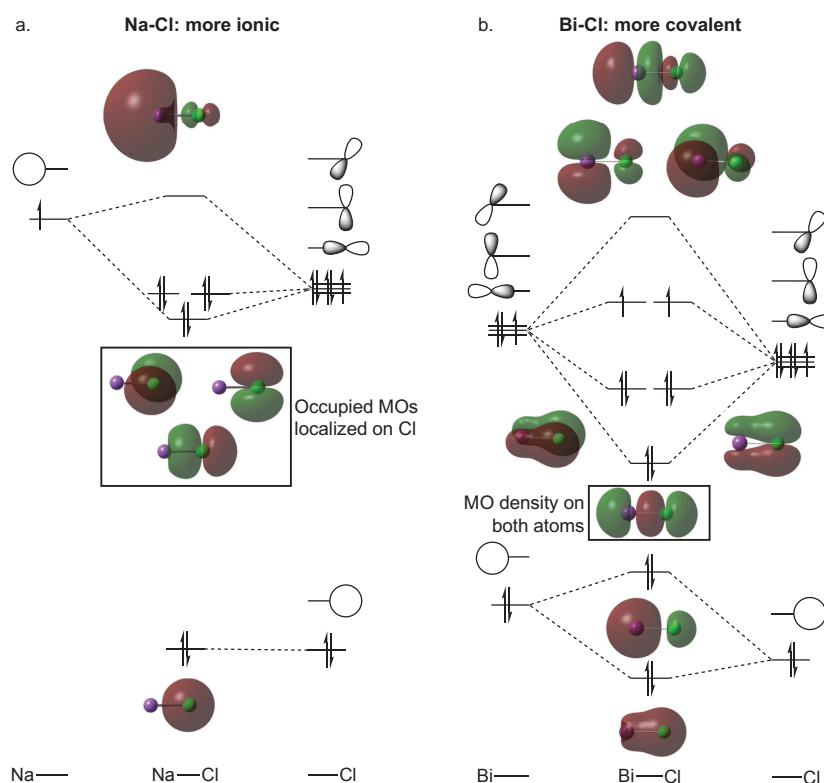
Figure 1.14: MO diagrams (not to scale) constructed for Na−Cl and Bi−Cl. MO visualisations are from DFT calculations (B3LYP/LanL2DX).

example the most common perovskites used in solar cells have the formula $[CH_3NH_3][PbX_3]$.[81]

1.3.1 Bismuth(III) halide complexes

Recent interest in polyhalide bismuthates, both discrete and polymeric, has been inspired by the useful physical properties of materials containing these complexes including photochromism, thermochromism, semiconductivity, and luminescence.[82] Adonin *et al.* published a comprehensive review of polyhalide bismuthates in 2016,[82] and previously Fisher *et al.* reviewed group 5 complexes with halides in general.[83] This section is a brief summary of the known structures of bismuth complexes with halides, with selected additional details on other group 5 elements where relevant. For the this section X refers to Cl, Br, and I.

Mononuclear species

BiX_3 is the neutral halide salt of bismuth. For all X the predominant bonding type has been described as covalent, however there are significant differences between the structures of $BiCl_3$, $BiBr_3$ and BiI_3. $BiCl_3$ forms distinct trigonal pyramidal units, with 3 short bonds between Bi and Cl, and 5 longer Bi$-$Cl interactions.[83] The bonding picture can be described as covalent molecular units linked by intermolecular interactions. BiI_3 is different - the Bi centres are octahedrally coordinated, and interact with 6 equidistant I atoms, the bonding has been described as delocalised covalent. $BiBr_3$ has two forms, one more similar to $BiCl_3$ with distinct molecules and intermolecular interactions, and one more similar to BiI_3 with all bond lengths equivalent.[83]

$[BiX_4]^-$ and $[BiX_5]^{2-}$ are not reported in the literature, however analogous complexes of other group 15 metals, $[PCl_4]^-$ and $[SbCl_5]^{2-}$, are known.[83] $[PCl_4]^-$ has a sawhorse structure and $[SbCl_5]^{2-}$ is square pyramidal, consistent with VSEPR (Valence Shell Electron Repulsion) theory predictions. Both structures have vacancies in the coordination shell of the central atom (sawhorse = trigonal bipyramidal with an equatorial vacancy, square pyramidal = octahedral with a vacancy) which VSEPR theory assigns to localised lone pairs in the vacant positions - often termed stereochemically active lone pairs. Monomeric $[BiX_6]^{3-}$ is reported, with octahedral geometry.[83]

a. Square pyramidal Bi

edge-sharing

$[Bi_2X_8]^{2-}$

$[Bi_2I_8]^{2-}$, crystal structure (Liu *et al.*)

b. Octahedral Bi

i. face-sharing   ii. edge-sharing   iii. vertex-sharing   iv. polymeric vertex-sharing (zig-zag type)

$[Bi_2X_9]^{3-}$ $[Bi_2X_{10}]^{4-}$ $[Bi_2X_{11}]^{5-}$

$[(BiCl_5)_n]^{2n-}$, crystal structure (Zhan *et al.*)
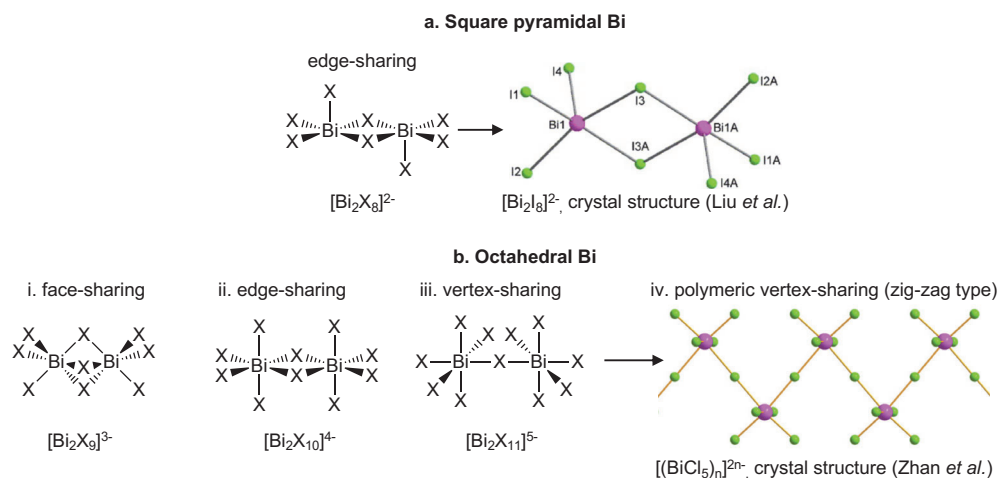
Figure 1.15: a. The structure of the binuclear polyhalide bismuthate $[Bi_2X_8]^{2-}$, and the crystal structure of $[Bi_2I_8]^{2-}$ reproduced with permission from Elsevier.[84] The Bi atom is coordinated by halides at square pyramidal sites. b. Octahedrally coordinated structures. i. Face-sharing molecular $[Bi_2X_9]^{3-}$. ii. Edge-sharing molecular $[Bi_2X_{10}]^{4-}$. iii. Vertex-sharing molecular $[Bi_2X_{11}]^{5-}$. iv. Vertex sharing polymeric $[(BiCl_n)]^{2n-}$ crystal structure, reproduced with permission from Elsevier.[85]

Binuclear species:

$[Bi_2X_8]^{2-}$, $[Bi_2X_9]^{3-}$, $[Bi_2X_{10}]^{4-}$ and $[Bi_2X_{11}]^{5-}$ are all reported, structures are edge-sharing square pyramidal, face-sharing octahedral, edge-sharing octahedral and vertex-sharing octahedral respectively, Fig. 1.15.[82] Bond lengths increase with halide size, and bridging bonds are longer than terminal bonds.

Polynuclear species

$[Bi_xX_y]^z$ $(z = 3x - y)$ are reported for $1 \leq x \leq 8$. Those with a nuclearity higher than two have similar motifs to the binuclear structures in Fig. 1.15; the Bi atoms are octahedrally coordinated by halide atoms, and share either faces, edges or vertices (3, 2, or 1 bridging halides) with adjacent octahedra.[82]

Polymeric species

Several types of $[\{Bi_xX_y\}_n]^{nz}$ polymeric structures made up of various repeating units have been reported.[82] The salient features are octahedral Bi coordination and face/edge/vertex sharing of neighbouring octahedra, as noted in the polynuclear discrete structures. All reported species are contained in crystalline salts, which are solid at room temperature.

1.3.2 Bismuth(III) halide complexes in ionic liquids

Cousens *et al.* synthesised a wide range of Bi(III) HMILs, applying variations in mole fraction and in halide choice, including mixed halide systems, Fig. 1.16.[30] The Bi(III) HMILs are the densest ILs reported; $[C_1C_4Im][BiBr_3Cl][BiBr_3]_{0.5}$ has a density of 2.65 g cm^{-3}. Density correlates with molecular weight of the incorporated halides. A mixed species $[C_4C_1Im]_2[Tf_2N][BiBr_3Cl]$ was also synthesised; the addition of $[C_4C_1Im][Tf_2N]$ to $[C_4C_1Im][BiBr_3Cl]$ reduced the viscosity of the liquid from 648 Pa s to 1.37 Pa s.

The identity of the anionic species in solution is unclear. Mass spectrometry was applied, however a large portion of anions may break down into constituent parts en route to the detector thus providing a misleading view of the speciation in the bulk liquid.[30,86] The liquids were also probed with X-ray Photoelectron Spectroscopy (XPS), but this method is not able to distinguish between atoms in similar but not identical environments. For example a Cl atom in $[BiCl_4]^-$ would give the same signal as one in $[Bi_2Cl_7]^-$. XPS is sensitive enough to distinguish free halide ions from ions within a complex. Free halide ions were not observed for any of the mole fractions measured.

Antinomy, the metalloid element above Bismuth in the periodic table, has also been incorporated into an IL.[87] Combination of $SbCl_3$ with two equivalents of
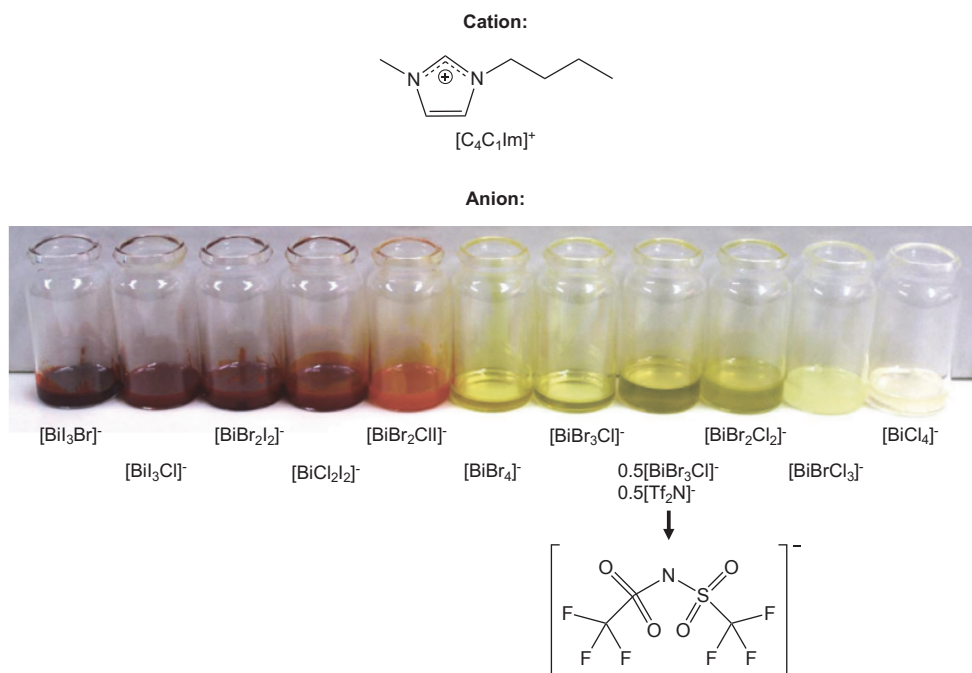
Figure 1.16: Cousens *et al.* synthesised bismuth(III) halide HMILs via addition of various BiX_3 to $[C_4C_1Im]X$. The anions listed show the stoichiometry of the anionic species but are not necessarily the species present in solution. One HMIL was mixed with $[C_1C_4Im][Tf_2N]$. Adapted with permission from Cousens *et al.*[30]

[C$_4$C$_1$Im]Cl produced an IL with a melting point of 76°. The Sb(III) based IL exhibited photoluminescence, emitting yellow and white light with a quantum yield of 86%. Crystallography of the solid IL at room temperature revealed discrete [SbCl$_5$]$^{2-}$ anions. H-bonding and anion-π interactions between the anions and cations occur both within and between layers producing a 3D supramolecular network.

1.4   d-block metal complexes

Chapter 4 concerns the complexation of the 3d metals Fe(II)-Zn(II) in a HMDES. This section provides a background understanding of the currently accepted models used to describe metal-ligand interactions in d-block complexes; how the electronic structure interacts with the geometrical structure of complexes; and how electronic transitions arise in these complexes. An overview of specific complexes relevant to the HMDES system follows.

First the simple crystal field theory model will be introduced, and used to rationalise Jahn-Teller effects and the existence of high-spin and low-spin complexes. Then an MO theory approach will provide more detail on metal-ligand bonding and the arising electronic structure of d-block complexes. Tanabe-Sugano diagrams and selection rules used to understand UV-vis absorbance spectroscopy are then outlined. Lastly, experimental and theoretical studies of complexes relevant to the HMDES system ethaline$-$NiCl$_2$ are summarised.

1.4.1   Crystal field theory

In crystal field theory the metal-ligand interactions are considered to be completely electrostatic, with no covalent bonding present. The ligands are treated as negative point charges whose presence creates an electric field which affects the energy of the metal d-orbitals, depending on their relative geometry. On the extreme left of Figure 1.17 the metal is in a vacuum environment and all the d AOs are degenerate. In a spherical environment the d AOs remain degenerate but their energy is increased relative to the vacuum environment, due to electrostatic repulsion between the negative field and the electrons occupying the d orbitals. In an octahedral ligand environment the orbitals which have density maxima directed towards the ligands are increased in energy (d$_{z^2}$, d$_{x^2-y^2}$) and the 3 AOs directed between the ligands (d$_{xy}$, d$_{xz}$, d$_{yz}$) are relatively reduced in energy. The energy gap created between the two sets of orbitals is known as Δ_{oct}, the size of which is dictated by the position of the ligands on the spectrochemical series.
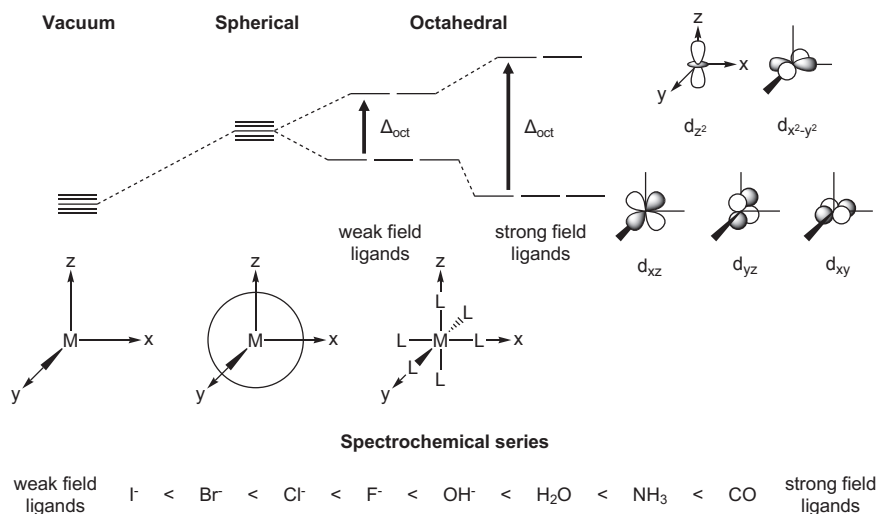
Figure 1.17: Crystal field theory - splitting of d atomic orbitals in an octahedral ligand environment. On moving from a vacuum to an octahedral ligand coordination the 2 d orbitals with maxima along the axis oriented towards the ligands increase in energy. The 3 orbitals with nodes along the ligand axes and maxima between the ligands also increase in energy, but to a lesser extent. The magnitude of this effect depends on the position of the ligand in the spectrochemical series.

Strong field ligands result in large Δ_{oct} and weak field ligands induce small Δ_{oct} values.

The magnitude of Δ_{oct} affects the order in which the d AOs are filled, Fig. 1.18. This is because Δ_{oct} is of a comparable size to the energy cost of pairing electrons in an orbital. To minimise the energy of a given electron configuration both electron pairing and occupation of the higher e_g AOs must be minimised. For d^1-d^3 and d^8-d^{10}
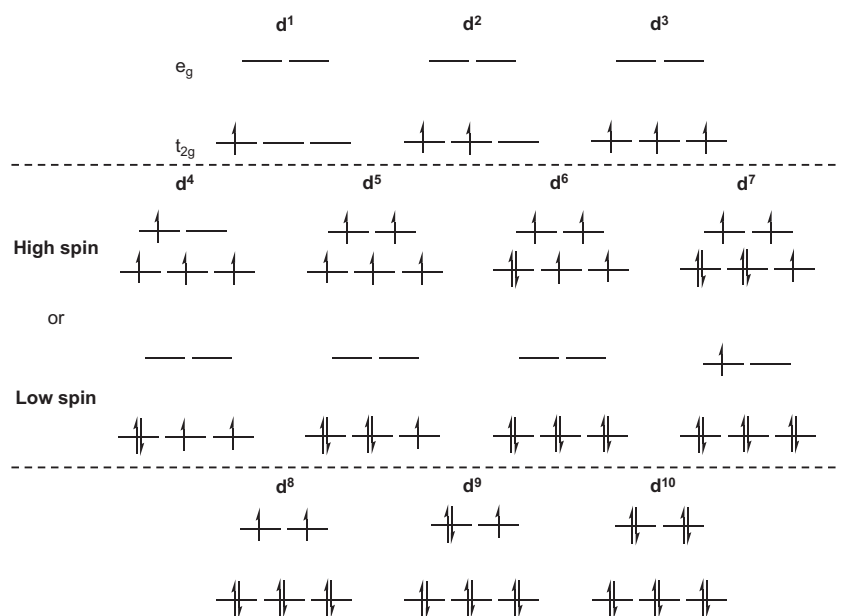
Figure 1.18: Electronic configurations of the d atomic orbitals of an octahedrally coordinated metal. d^4-d^7 metals may form high or low spin complexes, depending on the relative magnitude of Δ_{oct} and the electron pairing energies.

complexes this is simple as a single configuration minimises both electron pairing and e_g occupation. However for d^4 complexes either electron pairing (low spin, 2 unpaired) or e_g occupation (high spin, 4 unpaired) must occur. The relative size of these factors determines which spin state arises. For complexes with strong field ligands and therefore large Δ_{oct} values electron pairing is energetically favoured over promotion of electrons to the e_g level, giving low spin complexes. For complexes with weak field ligands (small Δ_{oct}) promotion to the e_g level is preferred, and high spin complexes result.

The crystal field theory principles may also be applied to ligand coordinations other than octahedral. The splitting energies for tetrahedral complexes are typically smaller than Δ_{oct} as the ligands do not approach the d AOs as directly, Fig. 1.19. For this reason there are very few known examples of low spin tetrahedral complexes - the energy cost of pairing electrons is usually larger than the cost of occupying the higher energy levels. The square planar splitting pattern is a result of the removal of the z-axis ligands from an octahedral complex; the AOs with density along the z-axis are stabilised, while the AOs directed along the x and y axes towards the remaining ligands are destabilised, especially the $d_{x^2-y^2}$ orbital.

1.4.2 Jahn-Teller distortion

The Jahn-Teller theorem states that any (non-linear) molecule with a spatially degenerate electronic ground state will undergo a geometrical distortion, removing that degeneracy, because the distortion lowers the overall energy of the species. The key points of Jahn-Teller distortion in d-block complexes can be rationalised by application of the simple crystal field theory already introduced.

In octahedral complexes elongation of the axial $M-L$ bonds reduces the point
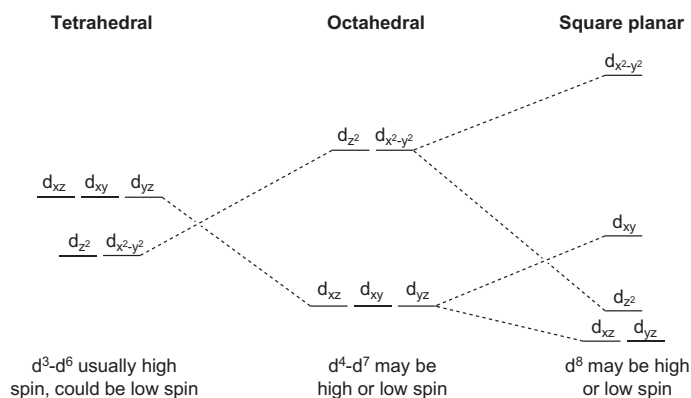
Figure 1.19: Crystal field theory predicted splitting patterns for octahedral, tetrahedral and square planar complexes. Levels vary depending on exact interactions present, especially for square planar complexes.
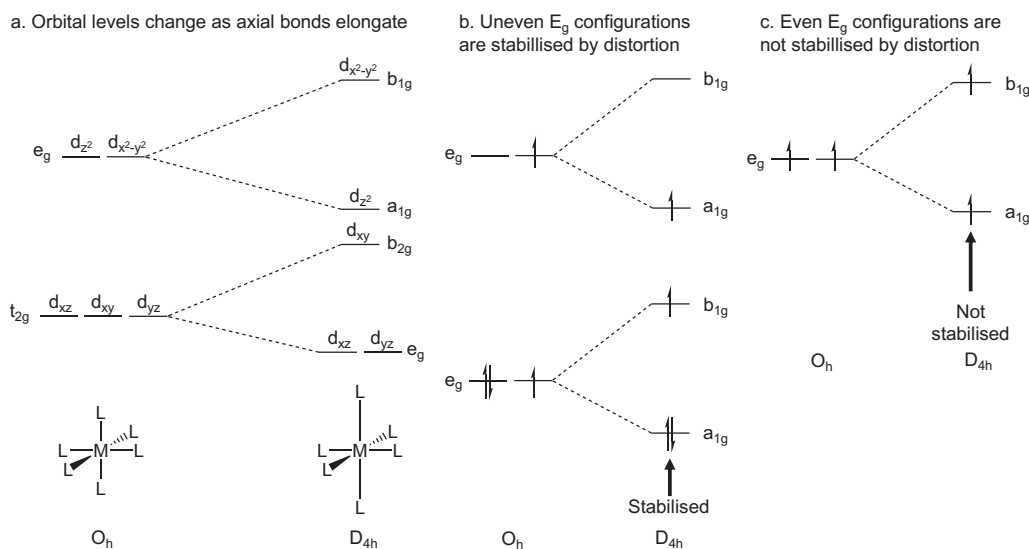
Figure 1.20: Jahn-Teller distortion in octahedral complexes. a. As the axial bonds elongate the relative energy levels of the d orbitals change. b. If the E_g level is unevenly occupied then Jahn-Teller distortion is energetically favoured. c. Complexes with an evenly occupied E_g level are not stabilised by Jahn-Teller distortion.

group from O_h to D_{4h} and splits the t_{2g} and e_g energy levels, Fig. 1.20.a. To a first approximation the splitting of the bottom t_{2g} level may be neglected, as it has been experimentally determined that only the splitting of the top e_g level has significant effects. Distortion and splitting of the e_g level is only favoured for electron configurations with uneven occupation of the e_g level, Fig. 1.20.b. For evenly occupied e_g levels the stabilisation of the d_{z^2} orbital is outweighed by the destabilisation of the $d_{x^2-y^2}$ orbital and distortion does not lower the energy of the complex, Fig. 1.20.c. Returning to the Jahn-Teller theorem, note that evenly occupied degenerate energy levels are not *degenerate states* as there is only one energetically equivalent way to arrange the electrons; for $(e_g)^2$ the only ground state configuration is $(d_{z^2})^1(d_{x^2-y^2})^1$, this is not a degenerate state. For $(e_g)^3$ however two possible electronic arrangements are possible $((d_{z^2})^2(d_{x^2-y^2})^1, (d_{z^2})^1(d_{x^1-y^2})^2)$; this state is degenerate and undergoes Jahn-Teller distortion.

The same principles may be applied to four coordinate complexes, which may be tetrahedral, square planar, sawhorse or distortions of or between these shapes, Fig. 1.21.a. Complexes with evenly filled t_2 levels are not stabilised by Jahn-Teller distortion, complexes with one d-orbital less occupied than the others in the t_2 level are stabilised by distortion towards a square planar structure, and complexes with one d-orbital more occupied than the others in the t_2 level are stabilised by distortion towards a sawhorse structure, Fig. 1.21.b.

The crystal field theory model is a simplification and works best when applied to
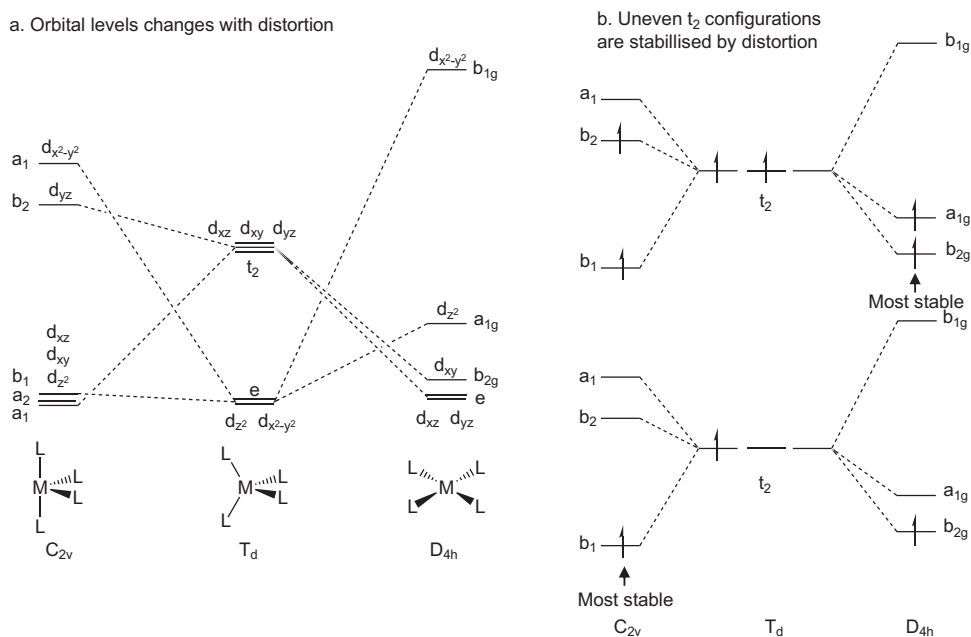
Figure 1.21: Jahn-Teller distortion in tetrahedral complexes. a. Crystal field theory derived energy levels for sawhorse, tetrahedral and square planar complexes. Dashed lines are between matching d-orbitals. b. If the t_2 level is unevenly occupied then Jahn-Teller distortion is energetically favoured. The bottom 2 orbitals are omitted as no change in their occupation is expected upon geometry distortion. Dashed lines indicate where the electrons occupying the t_2 level in tetrahedral complexes move to in sawhorse and square planar complexes.

homoleptic complexes with σ-donor or π-acceptor type ligands. Systematic comparison of the model's predictions with crystal structures of such 4 coordinate complexes have been carried out by Cirera *et al.*, who found broad agreement between the two, especially for simple homoleptic complexes with monodentate ligands.[88,89] For example the majority of Ni(II) and Co(I) (both d^8) complexes were found to be square planar for low spin cases, and tetrahedral with distortion towards sawhorse in high spin cases.

1.4.3 MO theory

Looking at the molecular orbitals of idealised complexes reveals the specific interactions between metals and ligands, giving a more detailed understanding of how the energy levels from crystal field theory are modified by including orbital effects. An idealised representation of the valence MO diagram of an octahedral 3d-block complex with 6 σ-type ligands is shown in Fig. 1.22. The metal fragment orbitals on the left hand side are the 3d (t_{2g} and e_g), 4s (a_{1g}) and 4p (t_{1u}) AOs. The ligand fragment MOs are on the right hand side (in grey) are shown as simple s-type AOs on each ligand interacting to form a_{1g}, t_{1u}, and e_g MOs. All the ligand MOs interact with metal AOs of the equivalent symmetry to form bonding and antibonding pairs.

Assuming the ligands are more electronegative than the metal, the bonding MOs
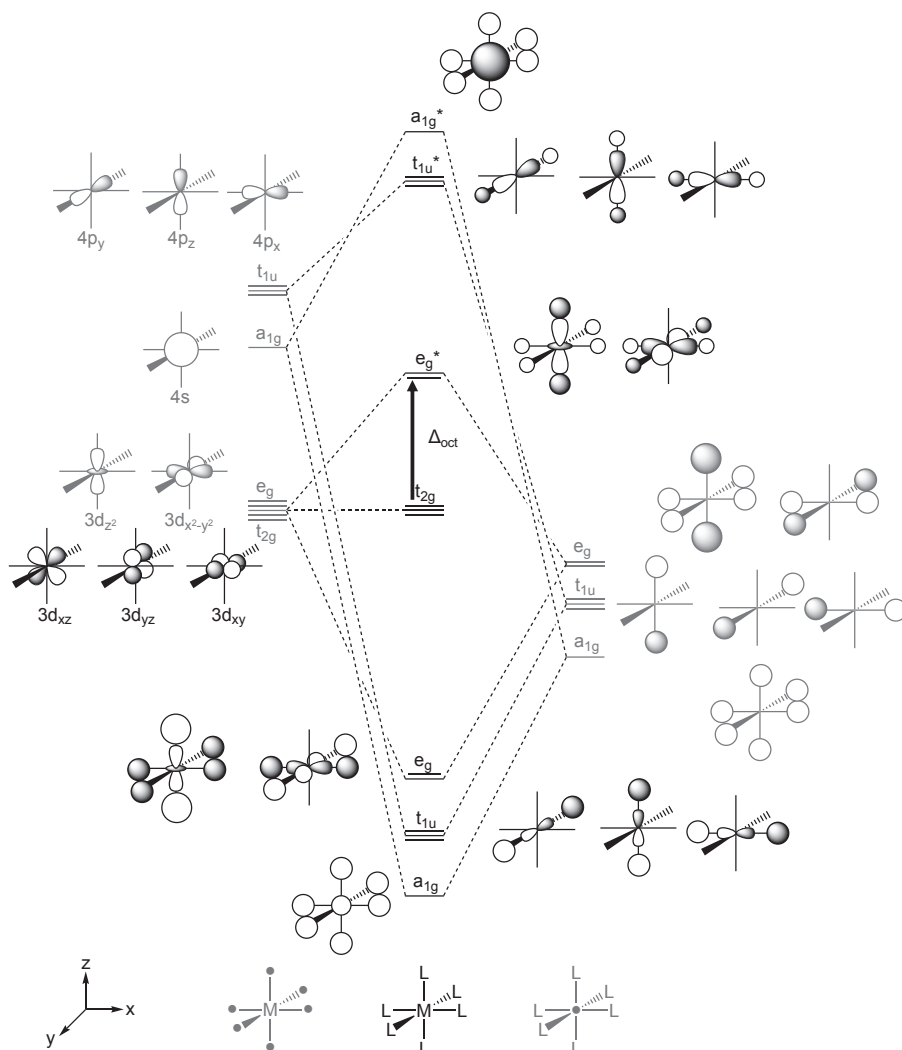
Figure 1.22: MO diagram for an octahedral 3d-block complex with 6 σ-type ligands. Fragment MOs (grey) from the metal and the ligands combine to generate the complex MOs (black). Electrons are not shown for clarity; for 1 electron σ-ligands the bottom 3 MO levels (a_{1g}, t_{1u}, e_g) are filled by ligand electrons, and there are a total of d^n electrons in the t_{2g} and e_g* levels.

are close in energy to the ligand fragment MOs and are ligand-based. The relative energies of the first 3 MOs are explained by the number of nodal points and planes present in each MO. The lowest energy MO is the a_{1g} level, formed of metal 4s and ligand fully bonding contributions, there are no nodes in the MO. t_{1u} is the next MO, with the metal 4p AOs, there is one node on each MO, at the metal. The e_g MO has contributions from the metal 3d MOs (d_{z^2} and $d_{x^2-y^2}$). Each MO has two nodal planes through space. The next MO is the t_{2g} level, containing the metal 3d AOs d_{xy}, d_{xz}, and d_{yz} which do not have the correct symmetry to interact with any of the ligand fragment MOs, and are therefore non-bonding. The next 3 MOs are the antibonding counterparts to the first 3 bonding levels. They are closer in energy to the metal AOs than the ligand

fragment orbitals and have large metal contributions. The ordering is the reverse of the bonding MOs, with the lowest energy antibonding MO being the and e_g level, followed by the t_{1u} MOs and then the a_{1g} level.

The electrons are omitted for clarity in Fig. 1.23, but the 3 ligand-based bonding MOs are fully occupied for 1-electron σ ligands, and there are a total of d^n electrons in the t_{2g} and e_g* levels, as predicted by crystal field theory. The MO diagram shows how the ligands may affect the energy levels and Δ_{oct} of a complex. If the ligand orbitals are closer in energy to the metal AOs, or if they have more spatial overlap then the splitting of the bonding and antibonding MOs is greater, increasing Δ_{oct}. This is an idealised description; in real systems the MO energies and composition of AOs vary depending on many factors.

When ligands also interact with metals through additional π interactions Δ_{oct} is also affected, Fig. 1.23. Ligand-metal π interactions occur through t_{2g} ligand fragment orbitals interacting with the t_{2g} 3d AOs (d_{xy}, d_{xz}, and d_{yz}), which are non-bonding in
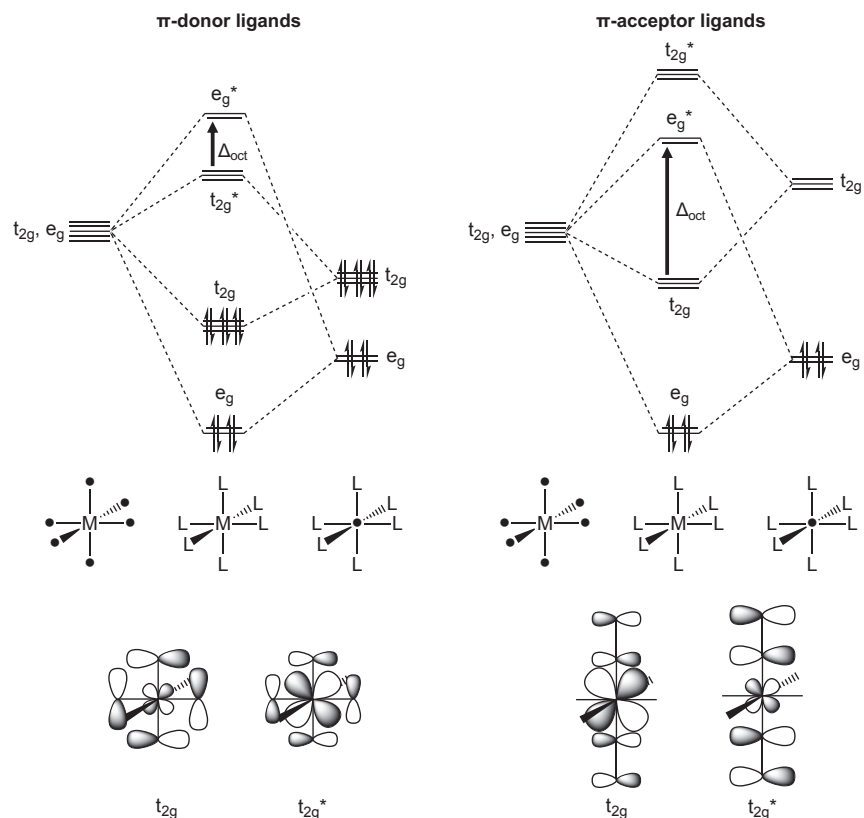
Figure 1.23: Simplified MO diagrams for octahedral complexes with both σ and π metal-ligand interactions. Only the metal d-orbitals and the ligand orbitals which interact with the d-orbitals are included, and only the ligand electrons are shown. In complexes with π-donor ligands (e.g. Cl⁻) Δ_{oct} is reduced, and with π-acceptor ligands (e.g. CO) Δ_{oct} is increased. Below both diagrams there are sketches of the t_{2g} and t_{2g}* MOs, each is triply degenerate with one identical MO in each Cartesian plane.

the pure σ diagram. This interaction can decrease or increase Δ_{oct}, depending on whether the ligands are π-donors or π-acceptors respectively.

A typical π-donor ligand is Cl^-, which participates in both σ and π interactions through its filled 3p AOs. An octahedral arrangement of 6 Cl^- ions produces 18 ((6×3)) 3p based fragment AOs, of which Fig. 1.23 only shows the t_{2g} and the e_g levels which interact with the metal d AOs of the same symmetry. Cl^- is termed a π-donor as the t_{2g} fragment orbital is occupied and lower in energy than the metal AOs. The t_{2g} interaction results in the non-bonding MO from the σ only complex splitting into a fully occupied, ligand-based bonding MO and a higher energy metal-based antibonding MO ($t_{2g}*$) occupied by metal electrons depending on d^n. Effectively this results in an increase in the t_{2g} level (compared to the σ only complex), giving a reduced Δ_{oct}.

A typical π-acceptor ligand is CO, which participates in π interactions via vacant, high lying, t_{2g} fragment orbitals, composed of $\pi*$ antibonding MOs from each ligand. Similarly to the π-donor case the metal t_{2g} AOs are split into two levels - bonding and antibonding. However due to the higher lying π-acceptor ligand orbitals the antibonding $t_{2g}*$ level is shifted to above the e_g level, increasing Δ_{oct}. These MO diagrams rationalise the relative positions of Cl^- and CO ligands in the spectrochemical series - Cl^- is a weak field ligand resulting in smaller Δ_{oct} values and CO is a strong field ligand resulting in larger Δ_{oct} values.

In four coordinate complexes π-donor ligands favour tetrahedral structures over square planar, due to increased ligand-ligand repulsion, caused by through space overlap of formally occupied pAOs. Tetrahedral conformations allow larger ligand-ligand distances for a given ligand-metal bond distance. The ligand orbitals also overlap less in tetrahedral conformations as in square planar conformation each ligand has two antibonding interactions with co-planar neighboring ligands, but in tetrahedral complexes each ligand is only co-planar with one other ligand.[89]

Cirera et $al.$ identified that for homoleptic d^3-d^7 tetrahedral d-block complexes three factors determine whether a high or low spin state is preferred.[89] High spin states are preferred for metals in an oxidation state of +3 or lower, metals in period 3, and complexes with π-donor ligands. The authors conducted a comprehensive survey of the crystallographic literature and found that when two or three of the determining factors apply to a complex it is high spin. If one or zero applied the complex was low spin.

Cirera et $al.$ invoked MO theory to explain why π-donor ligands increase the propensity of tetrahedral complexes to be high spin. On moving from a complex with
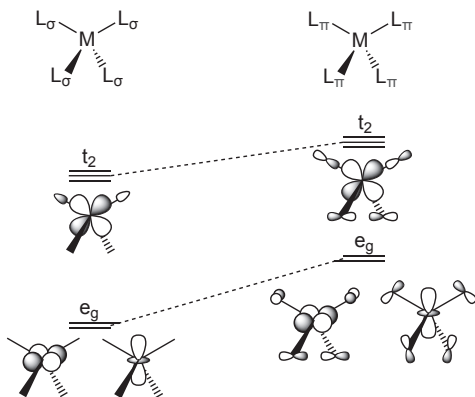
Figure 1.24: The contraction in the e_g to t_2 energy gap when π-donor ligands are introduced is due to more additional antibonding interactions in the e_g than the t_2 level. This contraction increases the propensity of π-donor tetrahedral complexes to be high-spin. The MOs sketched here represent the interactions in calculated (B3LYP/TZV) $TiCl_4$ MOs presented by Cirera *et al.*[89]

σ-donor ligands only to a complex including π-donor ligands the e_g level is more destabilised than the t_2 level by the π interactions, reducing the energy gap between the levels, Fig. 1.24. The e_g level is non-bonding in σ-donor complexes but has 4 antibonding interactions in π-donor complexes, whereas the t_2 level only has an additional 2 antibonding π interactions.

1.4.4 UV-vis spectroscopy

UV-Vis spectra of both systems studied in this work (bismuth halide based HMILs and nickel chloride based HMDESs), have been reported. Insight into the electronic properties of the metal containing species is provided.

The bands in UV-vis absorption spectroscopy arise from light photons of a specific energy promoting a chemical species from one electronic state to another, via interaction with the molecular dipole moment, μ. The absorbance (A) of a band is the logarithm of the ratio of the intensity of the incident light (I_0) to the intensity of the transmitted light (I), Section 1.4.4.

$$\log_{10} \frac{I_0}{I} = A = \varepsilon lc \tag{1.1}$$

Absorbance is proportional to the path length through the sample (l /cm) and concentration of the sample (c /M). ε ($/M^{-1}cm^{-1}$) is the molar absorptivity coefficient. In UV-vis spectroscopy of d-block metal complexes the value of ε is substantially determined by whether the transition concerned is "allowed" or "forbidden" under

several selection rules, Table 1.3. This section will first summarise the use of the term symbol formalism to describe the electronic states of d-block metal complexes, and then describe the selection rules governing the transitions between such states observed via spectroscopy.

The state of a single electron is defined by its quantum numbers. The state of an atom is defined by analogous quantum numbers, which depend upon the state of the electrons occupying any unfilled sub-shells, Table 1.4. Electrons in inner, filled, sub-shells do not contribute to the state of the atom as they cancel out each other's momenta and spin. Equivalent quantum numbers for molecules also exist, but the UV-vis spectra of d-block complexes is typically discussed in terms of an atom in a ligand field, using the atomic quantum numbers.

For an atom of a given electronic configuration there are many ways electrons may be arranged. Each arrangement is called a microstate. The number of microstates is D_t (total degeneracy) and (considering only unfilled sub-shells) may be calculated as follows:

$$D_t = \frac{N!}{N_e! N_h!}$$

where $N!$ is the number of spin-orbitals in the unfilled sub-shell (twice the number of atomic orbitals), N_e is the number of electrons occupying the unfilled sub-shell, and N_h is the number of holes in the unfilled sub-shell. $N_e + N_h = N$.

Microstates of the same orbital and spin angular momenta are grouped into terms, Fig. 1.25.a. shows this for a free d^2 ion, following the Russell-Saunders scheme of sequential coupling, with the first coupling engendering the largest split in energy and the last the smallest. Beginning with 2 non-interacting electrons, all configurations will have the same energy. Then s-s coupling is considered and the states are split into two groups; the lower energy triplet group has spins aligned and the higher energy singlet group has spins opposed. l-l coupling splits each group into terms; the lowest energy term has the highest $L = \sum m_l$. Higher L corresponds to less repulsion between

Transition type	Laporte allowed?	Parity allowed	Spin allowed	ε
d-d (O_h)	✗	✗	✗	0.1
d-d (T_d)	✗	n/a	✗	1
d-d (O_h)	✗	✗	✓	10
d-d (T_d)	✗	n/a	✓	100
Charge transfer	✓	✓	✓	1000+

Table 1.3: Types of transition in UV-vis absorbance spectra and corresponding rough ε /M^{-1}cm^{-1} values.

1 e⁻ quantum number	Range	Atomic quantum number	Range for 2e⁻ system
Principal, n (energy level)	1 to ∞		
Orbital angular momentum, l (orbital type)	n to 0	Total orbital angular momentum, L	$(l_1 + l_2)$ to $(l_1 + l_2)$ $(l_1 \geq l_2)$
Magnetic, m_l (sub-orbital)	l to $-l$	Total magnetic, M_l	$(l_1 + l_2)$ to $(-l_1 - l_2)$
Spin magnetic, m_s (spin direction)	$\frac{1}{2}, -\frac{1}{2}$	Total spin magnetic, M_s	$1, 0, -1$
Inherent spin, s (spin magnitude)	$\frac{1}{2}$	Total inherent spin, S	$1, 0$
		Multiplicity, M	$2S + 1$
		Total angular momenta, J	$(L + S)$ to $(L - S)$

Table 1.4: Single electron quantum numbers and the corresponding atomic quantum numbers.

electrons as they occupy sub-orbitals with less overlap. L values take the same representative letters as l; $L = 0$ is S, $L = 1$ is P, etc. The final splitting is within terms and due to spin-orbit coupling; L and S may combine in different ways and each has a distinct energy. This splitting is small for 3d metals and will be neglected subsequently.

Term symbols (Fig. 1.25.b.) are made up of the corresponding letter for L, with M as a superscript on the left hand side. J may be specified as a subscript on the right hand side of L. The degeneracy of a term is the product of the multiplicity (spin degeneracy, $2S + 1$) and the orbital degeneracy ($2L + 1$). The sum of the degeneracy of the terms is equal to D_t.

When an octahedral ligand field is applied to a free-ion the terms are split into ligand field states, Fig. 1.26. In stronger octahedral fields the energies of the e_g and t_{2g} levels are split further apart, and the ligand field states converge into groups corresponding to electron configuration between the two levels. For a d^2 ion the lowest energy ligand field states are those with the configuration $(t_{2g})^2$. States with the configuration $(t_{2g})^1(e_g)^1$ are intermediate in energy and $(e_g)^2$ states are high in energy. Figure 1.26 is qualitative visualisation of ligand field splitting of terms. Tanabe-Sugano diagrams show quantitatively the change in relative energy between terms, from a free ion to a strong ligand field.[90]
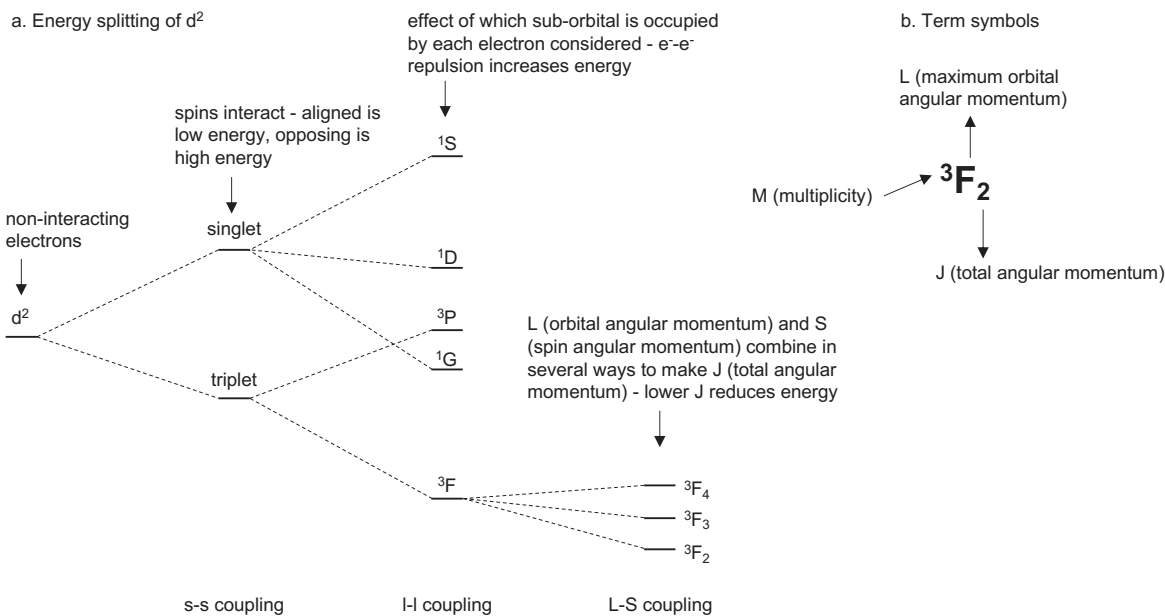
Figure 1.25: a. The splitting of a d^2 configuration into terms. $L\text{-}S$ coupling is only shown for the ^{3}F term. b. Term symbol components.
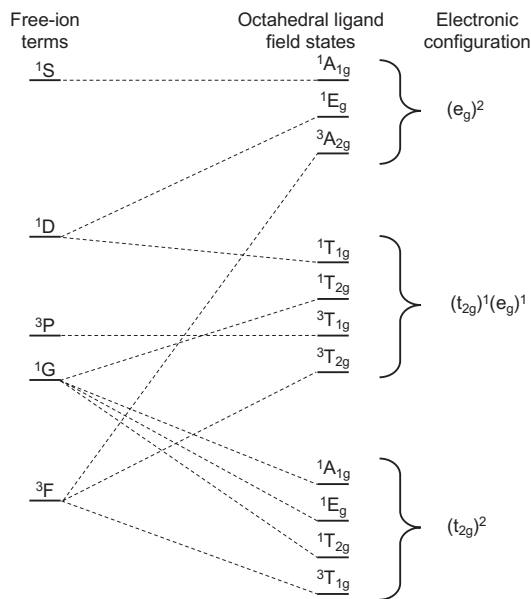
Figure 1.26: The splitting of d^2 free ion terms in an octahedral ligand field.

1.4.5 Selection rules

Assigning term symbols to atomic states in a ligand field allows the use of symmetry to determine whether transitions are allowed under several selection rules. For a symmetry-allowed transition:

$$\int \Psi_i \mu \Psi_f d\tau \neq 0$$

58

where Ψ_i is the initial wavefunction (before the electronic transition), Ψ_f is the final wavefunction (after the transition), μ is the vector quantity dipole moment, and $d\tau$ indicates integration over all variables in the wavefunction.

For $\int \Psi_i \mu \Psi_f d\tau$ to be non-zero its symmetry must span the totally symmetric representation. If any component of the binary product of the symmetries of Ψ_i and Ψ_f matches the symmetry of any component of μ then the totally symmetric representation will be produced and the transition is allowed. The spin, Laporte, and parity selection rules all arise because they are necessary conditions for non-zero $\int \Psi_i \mu \Psi_f d\tau$.

The spin selection rule states that for a spin-allowed transition there is no change in overall spin, ie:

$$\Delta S = 0$$

The parity selection rule states that an allowed transition must have a change in parity. $u \longrightarrow u$ and $g \longrightarrow g$ transitions are parity-forbidden. The parity selection rule only applies to molecules with a centre of inversion; octahedral complexes are subject to the parity rule but tetrahedral complexes are not.

The Laporte selection rule states that a change in orbital angular momentum is required for a Laporte-allowed transition:

$$\Delta l \pm 1$$

Relaxation due to coupling

The Laporte selection rule forbids all d-d transitions in d-block complexes. The parity rule also forbids d-d transitions in octahedral complexes (but not tetrahedral complexes). However forbidden d-d transitions are observed experimentally, due to relaxation of the selection rules via coupling effects which make $\int \Psi_i \mu \Psi_f d\tau$ non-zero although the formal selection rules are broken.

Transitions which are spin-forbidden are observed due to spin-orbit coupling; these bands are weak, especially for 3d-complexes (4 and 5d complexes exhibit larger spin-orbit coupling effects). ε is small for spin-forbidden transitions, Table 1.3.

Transitions which are forbidden are observed due to vibronic coupling, coupling of the vibrational states of the complex with the electronic states. Ψ may be written as $(\Psi_e)(\Psi_v)$, where Ψ_v is the vibrational component of the wavefunction. As the ground vibrational state always has the fully symmetric representation the symmetry of

$(\Psi_e)_i \mu (\Psi_e)_f (\Psi_v)_f$ must span the fully symmetric representation for a transition to be vibronically allowed.

In tetrahedral complexes the lack of inversion centre means that the t_2 d-orbitals have the same symmetry as the p-orbitals and can interact. The Laporte rule is thereby relaxed as transitions are no longer pure d $\longrightarrow$ d transitions. Laporte-forbidden transitions have a larger ε in tetrahedral complexes than in octahedral complexes, Table 1.3.

Charge transfer transitions where the electronic occupation moves from ligand to metal or vice versa do not contravene either the parity or Laporte selection rules and thus have larger ε values than any d $\longrightarrow$ d transitions, Table 1.3.

1.4.6 Ligand exchange thermochromism

Linert *et al.* define chromotropism as the "reversible variation of colour under differing physical or chemical conditions such as temperature, pressure, light and solvent."[91] Thermochromism is a subset of chromotropism where the colour change is induced by a change in temperature.

There are several known mechanisms by which thermochromism may occur. For example VO_2 has a solid-solid phase change at 68 °C, below the transition the material transmits IR light, which is reflected above the transition temperature.[92] Some iron(II) complexes (often called spin-crossover complexes) undergo changes in spin state through thermally induced electron promotion, causing colour changes.[93]

LETC (ligand exchange thermochromism) is the changing of colour on heating due to the identity of the ligands in a d-block metal complex changing. As discussed in section Section 1.4.3 the structures and energy levels of the valence MOs - and therefore the magnitude of Δ_{oct} - in a d-block metal complex are strongly influenced by the type of ligand involved. Ligand exchange then is expected to cause a change in colour. At a low temperature these systems contain the metal complex with ligand A, in a solution which contains ligand B. As the temperature increases ligand A and ligand B are exchanged, such that ligand A is in the solvent part of the solution and ligand B in the metal complex.

The simplest example of such a system contains the following equilibrium: (M = Ni(II), Co(II))

$$[M(H_2O)_6]^{2+} + 4\,Cl^- \rightleftharpoons [MCl_4]^{2-} + 6\,H_2O \tag{1.2}$$
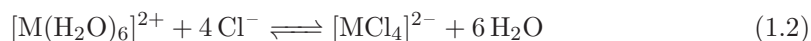
The mechanism of the ligand exchange, and the identity of the intermediate complexes

which must form is not addressed in the literature. The left hand side, octahedral complex, predominates at lower temperatures, and the right hand side, tetrahedral complex, is increasingly formed as temperature increases.[94,95] For M = Co(II) the solution is pink at low temperatures (20 °C) and blue at high temperatures (50 °C) and for M = Ni(II) the solution is yellow-green at low temperatures (20 °C) and blue at high temperatures (50 °C).

1.4.7 Nickel(II) complexes

This section will take a more specific view of the complexes of nickel (and other related 3d metals) with Cl and 1,2-ethanediol (Eg) ligands, the complexes involved in the nickel HMDES system that will be investigated in chapter 3.

Electron configurations and spin states

Ni(II) has a 3d orbital occupation of d^8. In Ni(II) complexes either 0 or 2 electron are unpaired, giving spin values of 0 or 1, and corresponding multiplicities of 1 and 3. The spin state for a given complex is determined by the complex geometry and the identity of the complexing ligands. In some cases the energy difference between the two spin states is particularly marginal, and crystal structures containing both high and low spin metal centres in the same unit cell have been characterised.[88]

1,2-ethanediol containing complexes

Antti *et al.* investigated a series of d-block metal complexes with Eg ligands, with both $[SO_4]^{2-}$ and Cl^- anions, via X-ray diffraction studies.[96–98] Across the series Eg coordinates in a bidentate fashion though the O atoms. The hydrogen atoms bound to
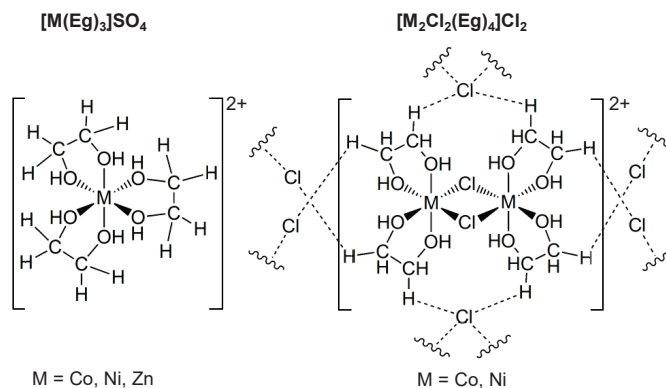
Figure 1.27: The structures of $[M(Eg)_3][HSO_4]$ and $[M_2Cl_2(Eg)_4]Cl_2$ as determined via X-ray diffraction studies by Antti *et al.*[96–98]

the Eg O atoms form H-bonding interactions between the cationic metal complexes and the anions ($[SHO_4]^-$ or Cl^-), see Fig. 1.27.

When the anion is $[SO_4]^{2-}$ the homoleptic, single metal centre complex $[M(Eg)_3]^{2+}$ (M = Co, Ni, Zn) is formed, Fig. 1.27. The metals are octahedrally coordinated with some distortion present. M = Zn is more symmetric with less distortion, as may be expected due to its "more symmetric" electronic structure with full d orbital occupancy.

Gruden-Pavlovic *et al.* used multideterminental DFT to perform a detailed investigation on the Jahn-Teller distortions present in the analogous complex $[Cu(Eg)_3]^{2+}$.[99] The authors concluded that the larger Jahn-Teller relaxation energies calculated for $[M(Eg)_3]^{2+}$ than for $[M(en)_3]^{2+}$ (en = 1,2-ethanediamine) were due to the synergy of intramolecular H-bonding and Jahn-Teller distortions which favour the H-bonding. It is unclear what the effect of H-bonding to external molecules such as $[HSO_4]^-$ may be on the intramolecular H-bonds and the extent of Jahn-Teller distortions.

The Cl^- anion results in a markedly different complex structure with two metal centres and 2 bridging Cl atoms, $[M_2Cl_2(Eg)_4]^{2+}$ (M = Co, Ni), Fig. 1.27. Small distortions to the octahedral centres are again noted.

1.4.8 Nickel(II) complexes in ionic liquids

Nickel containing ionic liquids were first achieved by adding $NiCl_2$ to a chloroaluminate ionic liquid system: $AlCl_3$-1-butlypyridinium chloride.[103] More recent studies have added $NiCl_2$ to a similar $AlCl_3$-$[C_2C_1Im]Cl$ system.[101,102] The nickel coordination in the $AlCl_3$-$[C_2C_1Im]Cl$ system was detected via EXAFS, and found to be dependent upon the aluminium and chloride species present.

$\chi_{\textbf{AlCl}_3} = \textbf{0.33, "basic"}$ $2\,[C_2C_1Im]Cl + AlCl_3 \longrightarrow [C_2C_1Im]Cl + [C_2C_1Im][AlCl_4]$
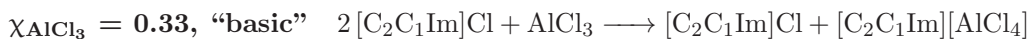
When $NiCl_2$ is added EXAFS shows that the nickel atom is surrounded by a single shell of 4 chlorine atoms:

$2\,Cl^- + NiCl_2 \longrightarrow [NiCl_4]^{2-}$
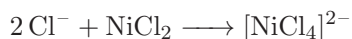
The dianion is anticipated to associate with 2 $[C_2C_1Im]^+$ cations.

$\chi_{\textbf{AlCl}_3} = \textbf{0.54, "neutral"}$ $[C_2C_1Im]Cl + AlCl_3 \longrightarrow [C_2C_1Im][AlCl_4]$

When $NiCl_2$ is added a single EXAFS peak reveals that nickel atom is surrounded by a single shell of 6 chlorine atoms:

$8\,[AlCl_4]^- + NiCl_2 \longrightarrow [NiCl_6]^{4-} + 4\,[Al_2Cl_7]^-$
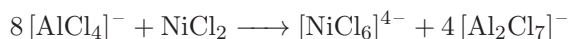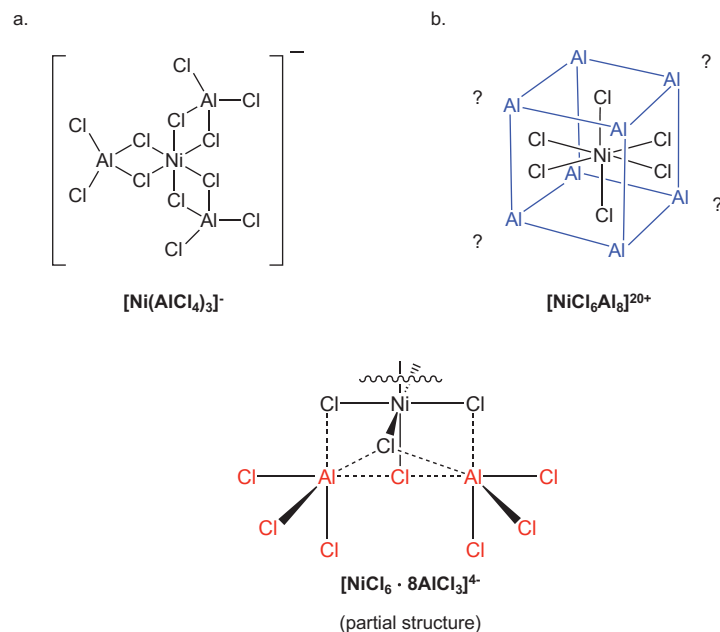
Figure 1.28: a. The coordination of Ni in acidic solutions as proposed in initial EXAFS studies by Dent *et al.*[100] b. Coordination of Ni by a first shell of 6 Cl atoms and a second shell of 8 Al atoms, as detected via EXAFS in later studies.[101,102] The formal equation of this coordination is $[NiCl_6Al_8]^{20+}$. c. 20+ is a large charge and it is likely additional coordination of Cl atoms occurs. For example $[NiCl_6 \cdot 8\,AlCl_3]^{4-}$ may be produced by the interaction of 4 $[Al_2Cl_7]^-$ anions with $NiCl_2$. In this scheme one Cl atom from each $[Al_2Cl_7]^-$ (coloured red) becomes coordinated to the Ni(II) centre. Each Al atom remains singly bonded to 3 Cl atoms, and interacts weakly with 3 Cls coordinated to the Ni atom.

$[NiCl_6]^{4-}$ is a highly charged anion and compounds including it are not reported in the wider crystallographic literature. It may be that a proportion of the Cl atoms are shared with another species in solution, reducing the effective charge of the nickel based anion. The reported EXAFS data are not sufficient to distinguish between Cl atoms in chemically different environments and discern the exact speciation of the solution.

$\chi_{AlCl_3} = 0.6$, "acidic" $[C_2C_1Im]Cl + 2\,AlCl_3 \longrightarrow [C_2C_1Im][Al_2Cl_7]$

3 studies on the addition of $NiCl_2$ to $AlCl_3$-$[C_2C_1Im]Cl$ with $\chi_{AlCl_3} = 0.6$ have been published, all utilising EXAFS to determine the coordination of the nickel atoms. The earliest study by Dent *et al.*[100] proposed that the nickel atoms in solution have a first coordination shell of 6 Cl atoms, followed by 3 Al atoms. They propose that the species formed is $[Ni(AlCl_4)_3]^-$, Fig. 1.28.a. One may write an equation for the formation of this species as follows:

$$2\,[Al_2Cl_7]^- + NiCl_2 \longrightarrow [Ni(AlCl_4)_3]^- + [AlCl_4]^-$$
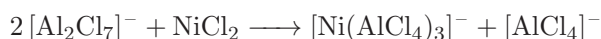
Two later authors found different results, with 8 Al atoms in the second coordination layer around the $NiCl_6$ core, Fig. 1.28 b.[101,102] The extremely large positive charge on a $[NiCl_6Al_8]^{20+}$ ion seems to indicate further coordination of the 8 Al atoms

by Cl is likely. A conceivable equation for the formation of such a species is:

$$4\,[\mathrm{Al_2Cl_7}]^- + \mathrm{NiCl_2} \longrightarrow [\mathrm{NiCl_6} \cdot 8\,\mathrm{AlCl_3}]^{4-}$$

Each Al atom would be in a octahedral-like environment with 3 strongly coordinated terminal Cl atoms, and 3 weaker interactions with 3 Cls complexed to the nickel centre, Fig. 1.28.c.

The conflicting results between studies may be due to experimental or analytical error in the earlier study; later authors have not had access to the raw data or analysis in order to verify the methods used. It is also possible that the difference in concentration of $\mathrm{NiCl_2}$ between the studies (0.05M in Dent *et al.* and 0.03M in O'Grady and Roeper *et al.*) had an effect on the speciation present.
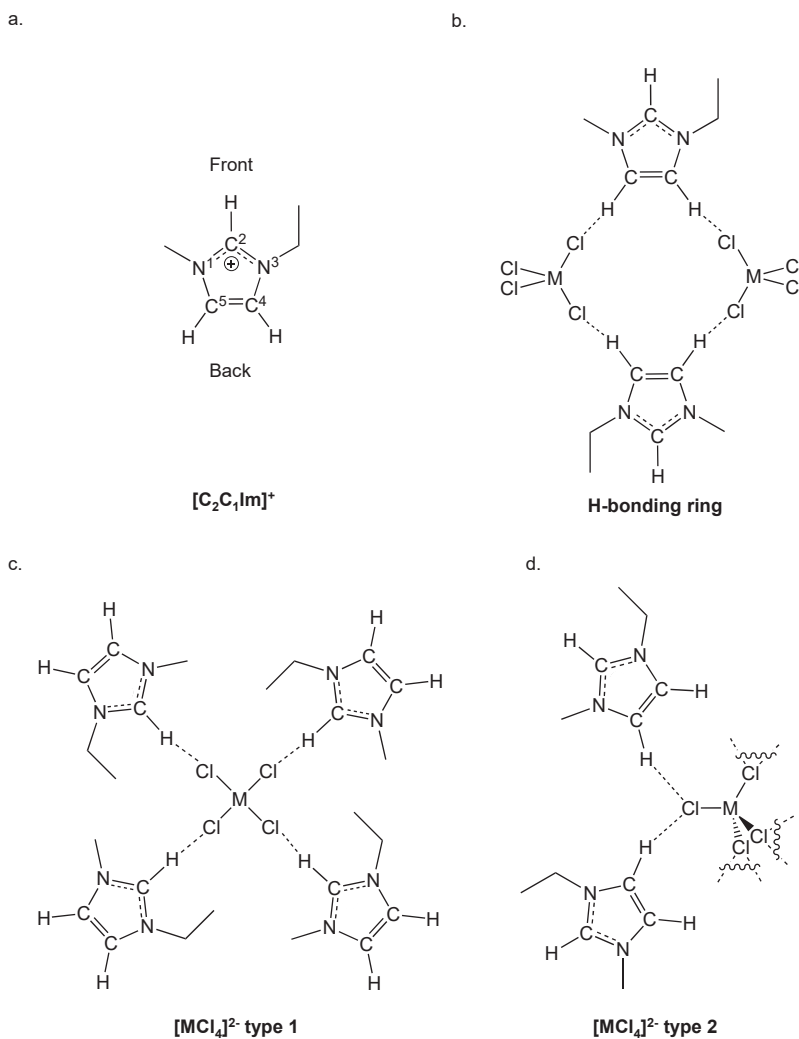
Figure 1.29: a. Atom numbering in $[\mathrm{C_2C_1Im}]^+$. b. H-bonding rings formed in $[\mathrm{C_2C_1Im}]_2[\mathrm{NiCl_4}]$. c and d. H-bonding motifs around the two anion types in crystalline $[\mathrm{C_2C_1Im}]_2[\mathrm{NiCl_4}]$. Figures b-d are schematic interpretations of crystal structures presented by Hitchcock *et al.*[104] In b-d charges are omitted for clarity.

EXAFS was also applied to determine that when $NiCl_2$ is added to $[C_2C_1Im]Cl$ alone the anion species formed is $[NiCl_4]^{2-}$.[104,105] $[C_2C_1Im]_2[NiCl_4]$ and $[C_4C_1Im]_2[NiCl_4]$ are solid at room temperature, and have therefore been studied via X-ray crystallography.[104,106]

Hitchcock *et al.* characterised the structure of $[C_2C_1Im]_2[MCl_4]$, M = Co and Ni, Fig. 1.29. H-bonding between the Cl atoms and the H^2, H^4, and H^5 is shown to direct the crystal structures which are almost identical with respect to changing the metal centre between Ni and Co. The dianion $[MCl_4]^{2-}$ is tetrahedral and exists in two types. In the first type each Cl in $[MCl_4]^{2-}$ is H-bonded to two $[C_2C_1Im]^+$ cations via the H^4, and H^5 hydrogen atoms (Fig. 1.29 d.) forming three dimensional H-bonding rings (Fig. 1.29 b.). The second type of $[MCl_4]^{2-}$ anion is H-bonded to one $[C_2C_1Im]^+$ cation per Cl atom, at the H^2 hydrogen, Fig. 1.29 c.

Zhong *et al.* studied $[C_4C_1Im]_2[MCl_4]$ for M including Cu, Ni, Mn, Fe, Co, and Zn.[106] Similar crystal structures were elucidated for each M, with all anions in the tetrahedral conformation. H-bonding networks are present with every Cl involved in at least one H-bond with H^2, H^4, H^5 or one of the H atoms bonded to the first carbon of the butyl chain. The hydrogen atoms on the methyl group were not involved in forming H-bonds. The crystal structures are similar across all M, with the butyl chain having the same conformation for all M except Ni. Two types of cation-cation interaction are present: $C-H\cdots\pi$ (imidazolium ring), and $\pi\cdots\pi$ stacking interactions.

Meredith *et al.* were able to synthesise room temperature ionic liquids with relatively low viscosities by combining $[C_nC_1Im]Cl$ (n = 5, 7, 8 and a mixture of n = 4 and 6) with $NiCl_2$.[107] The authors hypothesised that $[C_nC_1Im]_2[NiCl_4]$ was formed in solution for all n, however later studies found evidence via EXAFS experiments that the nickel containing species in n=6 and n=8 compositions is $[NiCl_3]^-$.[79,108] A reason suggested for the change in apparent anion from $[NiCl_4]^{2-}$ in $[C_2C_1Im]Cl$ to $[NiCl_3]^-$ in $[C_6C_1Im]Cl$ and $[C_8C_1Im]Cl$ is that the longer alkyl chains better stabilise a lower charged species. Similar behaviour was observed when copper systems rather than nickel were examined.[79]

Room temperature ionic liquids exhibiting thermochromic behaviour were synthesised and incorporated into plastic films by Wei *et al.*.[109,110] $[C_4C_1Im]_2[NiCl_4]$ was dissolved into $[C_nOHC_1Im][anion]$, where n = 2 or 3, and anion = $[BF_4]^-$, $[PF_6]^-$, and $[OCl_4]^-$. All the ionic liquids displayed thermochromic behaviour, due to an equilibrium between green octahedral nickel complexes involving the counter cations $[C_nOHC_1Im]^+$

and blue tetrahedral $[NiCl_4]^{2-}$, Fig. 1.30

Mixed chloride and -OH ligand complexes were also observed in ionic liquids by Hartley *et al.* via EXAFS.[79] When $NiCl_2 \cdot 6H_2O$ was added to $[C_6C_1Im]Cl$ an EXAFS peak indicating three chlorine atoms was reported, and the authors concluded that the nickel containing species was $[NiCl_3]^-$. When extra water (5% w/w) was added two EXAFS peaks corresponding to three Cl atoms and 3 O atoms were generated, indicating formation of $[NiCl_3(H_2O)_3]^-$. This finding shows the delicate balance between forming chloride only complexes, and complexes including -OH ligands in nickel ionic liquid systems. Mild changes in conditions lead to quite different complexes forming; this aspect of nickel - ionic liquid systems allows thermochromism to occur.

1.4.9 Nickel(II) complexes in deep eutectic solvents

Hartley *et al.* studied the speciation of MCl_2 (M = Co, Cu, Fe, Mn, Pd, Pt, Sn, Zn and Ni) dissolved in deep eutectic solvent systems formed of a 1:2 ratio of choline chloride
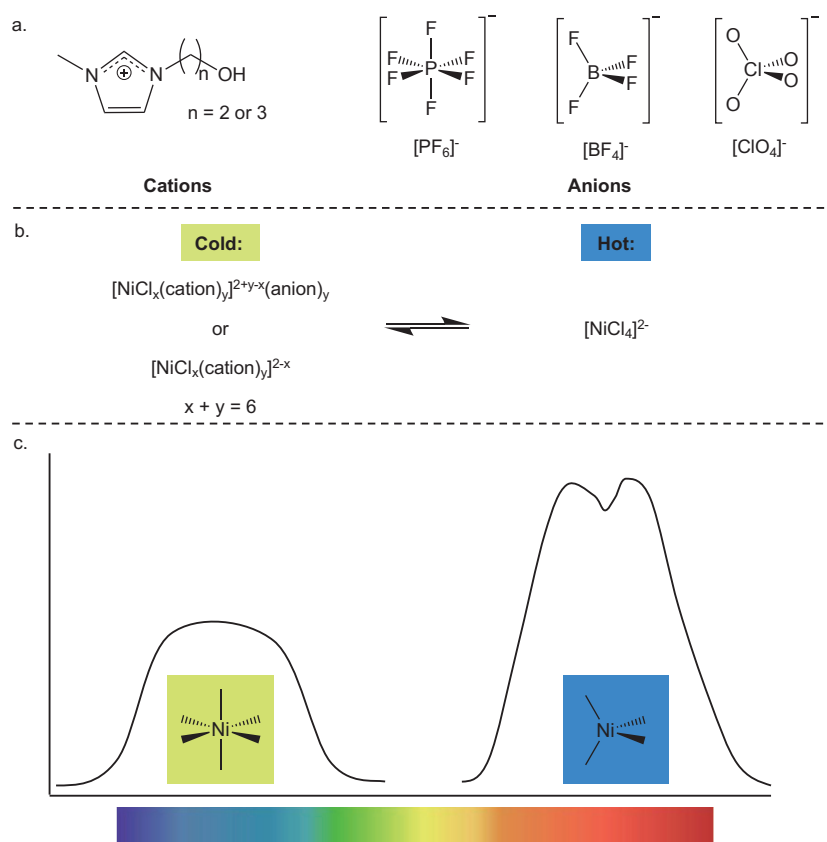
Figure 1.30: Summary of thermochromic equilibria of nickel(II) complexes in functionalised ionic liquids as reported by Wei *et al.*[109,110] a. Structures of the cations and anions included in the ionic liquids. b. Equation of the equilibria between species in solution. c. Sketch of UV-vis absorption spectra peaks arising from nickel complexes in tetrahedral and octahedral co-ordinations.

and 1,2-ethanediol (Eg) - a solution known as ethaline.[79] All M^{II} except nickel formed $[MCl_4]^{2-}$ - speciation confirmed via EXAFS. Nickel formed cationic $[Ni(Eg)_3]^{2+}$, with each 1,2-ethanediol co-ordinating in a bidentate fashion. When 1,2-ethanediol was replaced with 1,2-propanediol (1,2-pg) the same modality was observed; $[Ni(1,2-pg)_3]^{2+}$ formed. 1,3-propanediol does not have the correct bite angle to from a chelated complex, but the nickel containing species in a 1,3-propanediol system was similar to that observed in the other diols - an octahedral, 2+ complex is formed, with 6 oxygen atoms co-ordinating to the nickel center. The 1,3-propanediol is likely to coordinate in a monodentate manner; a second peak in the EXAFS spectrum was not sharp enough to resolve the exact complex geometry, and more conformational disorder is expected around the nickel centre than in the systems with bidentate ligands. All three solutions are thermochromic; green/yellow at room temperature becoming blue as the temperature is increased - indicating that $[NiCl_4]^{2-}$ may be forming in solution.

Nickel halide speciation in ethaline has been of interest to several other authors: Abbott *et al.* investigated improvements in nickel electrodeposition from the ethaline system vs. a standard method using an aqueous solution (Watts bath). Electrodeposition from the ethaline system was strongly affected by temperature, with an 80°C procedure obtaining a much flatter, shinier surface than the same procedure at 25°C. UV-vis spectra at temperatures from 25°to 80°C give further insight into the equilibrium between octahedral and tetrahedral complexation.[75]

Protsenko *et al.* investigated the physical properties of the same system including the effect of changing water concentration. Added water reduced viscosity and increased conductivity.[76] Kityk *et al.* discussed further the electrochemical and physical properties of the nickel chloride - ethaline system, in particular the impact of changing nickel(II) concentration and temperature.[77]

Overall the research into the ethaline-$NiCl_2$ system has focused on physical and electrochemical properties. The underlying chemical speciation, reactions, and intermolecular interactions have only been investigated by one study, and theoretical methods have not been applied.[79]

Bibliography

[1] T. Welton, *Chemical Reviews*, 1999, **99**, 2071–2084.

[2] J. P. Hallett and T. Welton, *Chemical Reviews*, 2011, **111**, 3508–76.

[3] N. V. Plechkova and K. R. Seddon, *Chemical Society Reviews*, 2008, **37**, 123–150.

[4] Q. Zhang, K. De Oliveira Vigier, S. Royer and F. Jérôme, *Chemical Society Reviews*, 2012, **41**, 7108.

[5] J. Estager, J. D. Holbrey and M. Swadźba-Kwaśny, *Chemical Society Reviews*, 2014, **43**, 847–86.

[6] V. I. Pârvulescu and C. Hardacre, *Chemical reviews*, 2007, **107**, 2615–65.

[7] M. V. Fedorov and A. a. Kornyshev, *Chemical Reviews*, 2014.

[8] R. Prado and C. C. Weber, *Application, Purification, and Recovery of Ionic Liquids*, 2016, **7**, 1–58.

[9] P. Sun and D. W. Armstrong, *Analytica Chimica Acta*, 2010, **661**, 1–16.

[10] K. S. Egorova, E. G. Gordeev and V. P. Ananikov, *Chemical Reviews*, 2017, **117**, 7132–7189.

[11] N. MacDowell, N. Florin, A. Buchard, J. Hallett, A. Galindo, G. Jackson, C. S. Adjiman, C. K. Williams, N. Shah and P. Fennell, *Energy and Environmental Science*, 2010, **3**, 1645–1669.

[12] X. Sun, H. Luo and S. Dai, *Chemical Reviews*, 2012, **112**, 2100–2128.

[13] H. Wang, G. Gurau and R. D. Rogers, *Chemical Society Reviews*, 2012, **41**, 1519–1537.

[14] H. Niedermeyer, C. Ashworth, A. Brandt, T. Welton and P. a. Hunt, *Physical Chemistry Chemical Physics*, 2013, **15**, 11566–78.

[15] E. F. Borra, O. Seddiki, R. Angel, D. Eisenstein, P. Hickson, K. R. Seddon and S. P. Worden, *Nature*, 2007, **447**, 979–981.

[16] T. L. Greaves and C. J. Drummond, *Chemical Reviews*, 2008, **108**, 206–237.

[17] D. Zhao, Z. Fei, H. A. Wee, R. Scopelliti and P. J. Dyson, *European Journal of Inorganic Chemistry*, 2007, 279–284.

[18] V. Ganesan, *Molecular Systems Design and Engineering*, 2019, **4**, 280–293.

[19] D. Tabor, *Gases, liquids, and solids : and other states of matter*, Cambridge ; New York : Cambridge University Press, New York, 3rd edn, 1991.

[20] S. M. Murray, R. A. O'Brien, K. M. Mattson, C. Ceccarelli, R. E. Sykora, K. N. West and J. H. Davis, *Angewandte Chemie - International Edition*, 2010, **49**, 2755–2758.

[21] P. A. Hunt, C. R. Ashworth and R. P. Matthews, *Chemical Society Reviews*, 2015, **44**, 1257.

[22] A. Frontera, P. Gamez, M. Mascal, T. J. Mooibroek and J. Reedijk, *Angewandte Chemie - International Edition*, 2011, **50**, 9564–9583.

[23] P. A. Hunt, B. Kirchner and T. Welton, *Chemistry - A European Journal*, 2006, **12**, 6762–6775.

[24] I. Skarmoutsos, D. Dellis, R. P. Matthews, T. Welton and P. A. Hunt, *The Journal of Physical Chemistry B*, 2012, **116**, 4921–4933.

[25] R. P. Matthews, T. Welton and P. A. Hunt, *Physical Chemistry Chemical Physics*, 2014, **16**, 3238.

[26] R. Hayes, G. G. Warr and R. Atkin, *Chemical Reviews*, 2015, **115**, 6357–6426.

[27] J. P. Hallett, C. L. Liotta, G. Ranieri and T. Welton, *Journal of Organic Chemistry*, 2009, **74**, 1864–1868.

[28] R. P. Matthews, C. Ashworth, T. Welton and P. a. Hunt, *Journal of Physics: Condensed Matter*, 2014, **26**, 284112.

[29] J. N. Canongia Lopes and A. A. Pádua, *The Journal of Physical Chemistry B*, 2006, **110**, 3330–3335.

[30] N. E. Cousens, L. J. Taylor Kearney, M. T. Clough, K. R. J. Lovelock, R. G. Palgrave and S. Perkin, *Dalton Transactions*, 2014, **43**, 10910–9.

[31] S. Takahashi, L. Curtiss, D. Gosztola and M.-L. Saboungi, *Inorganic Chemistry*, 1995, **34**, 2990–2993.

[32] C. Hardacre, R. W. Murphy, K. R. Seddon, G. Srinivasan and M. Swadźba-Kwaśny, *Australian Journal of Chemistry*, 2010, **63**, 845.

[33] D. C. Apperley, C. Hardacre, P. Licence, R. W. Murphy, N. V. Plechkova, K. R. Seddon, G. Srinivasan, M. Swadźba-Kwaśny and I. J. Villar-Garcia, *Dalton Transactions*, 2010, **39**, 8679–87.

[34] K. Dong and S. Zhang, *Chemistry - A European Journal*, 2012, **18**, 2748–2761.

[35] H. H. H. H. Li, Y. Chang, W. Zhu, W. Jiang, M. Zhang, J. Xia, S. Yin and H. H. H. H. Li, *The Journal of Physical Chemistry B*, 2015, **119**, 5995–6009.

[36] E. A. Pidko, V. Degirmenci, R. A. van Santen and E. J. M. Hensen, *Inorganic Chemistry*, 2010, **49**, 10081–10091.

[37] R. Lü, H. Tangbo and Z. Cao, *Journal of Natural Gas Chemistry*, 2007, **16**, 70–77.

[38] E. I. Izgorodina, Z. L. Seeger, D. L. Scarborough and S. Y. Tan, *Chemical Reviews*, 2017, **117**, 6696–6754.

[39] K. Dong, Y. Song, X. Liu, W. Cheng, X. Yao and S. Zhang, *The Journal of Physical Chemistry B*, 2012, **116**, 1007–1017.

[40] G. J. Mains, E. A. Nantsis and W. R. Carper, *The Journal of Physical Chemistry A*, 2001, **105**, 4371–4378.

[41] J. D. Andrade, E. Böes and H. Stassen, *The Journal of Physical Chemistry B*, 2002, **106**, 3546–3548.

[42] J. D. Andrade, E. S. Bo and H. Stassen, *The Journal of Physical Chemistry B*, 2002, **106**, 13344–13351.

[43] A. Chaumont and G. Wipff, *Chemistry - A European Journal*, 2004, **10**, 3919–30.

[44] B. Kirchner and A. Seitsonen, *Inorganic Chemistry*, 2007, 73–75.

[45] J. D. Andrade, E. Boes and H. Stassen, *The Journal of Physical Chemistry B*, 2008, **112**, 8966–8974.

[46] W. Wu, Y. Lu, H. Ding, C. Peng and H. Liu, *Physical Chemistry Chemical Physics*, 2015, **17**, 1339–1346.

[47] Q. Wang, Q. Zhang, X. Lu and S. Zhang, *Ionics*, 2017, **23**, 2449–2455.

[48] F. Parveen, T. Patra and S. Upadhyayula, *New Journal of Chemistry*, 2018, **42**, 1423–1430.

[49] Y. Liu and J. Wang, *Molecules*, 2018, **23**, year.

[50] E. R. Schreiter, J. E. Stevens, M. F. Ortwerth and R. G. Freeman, *Inorganic Chemistry*, 1999, **38**, 3935–3937.

[51] M. S. Sitze, E. R. Schreiter, E. V. Patterson and R. G. Freeman, *Inorganic Chemistry*, 2001, **40**, 2298–2304.

[52] K. Thiel, T. Klamroth, P. Strauch and A. Taubert, *Physical Chemistry Chemical Physics*, 2011, **13**, 13537–43.

[53] A. García-Saiz, I. de Pedro, P. Migowski, O. Vallcorba, J. Junquera, J. A. Blanco, O. Fabelo, D. Sheptyakov, J. C. Waerenborgh, M. T. Fernández-Díaz, J. Rius, J. Dupont, J. A. Gonzalez and J. R. Fernández, *Inorganic Chemistry*, 2014, **53**, 8384–8396.

[54] K. Wang, A. K. Chinnam, N. Petrutik, E. P. Komarala, Q. Zhang, Q. L. Yan, R. Dobrovetsky and M. Gozin, *Journal of Materials Chemistry A*, 2018, **6**, 22819–22829.

[55] R. Kore, P. Berton, S. P. Kelley, P. Aduri, S. S. Katti and R. D. Rogers, *ACS Catalysis*, 2017, **7**, 7014–7028.

[56] W. W. Ewing, J. D. Brandner, C. B. Slichter and W. K. Griesinger, *Journal of the American Chemical Society*, 1933, **55**, 4822–4824.

[57] E. L. Smith, A. P. Abbott and K. S. Ryder, *Chemical Reviews*, 2014, **114**, 11060–11082.

[58] P. Liu, J. W. Hao, L. P. Mo and Z. H. Zhang, *RSC Advances*, 2015, **5**, 48675–48704.

[59] D. V. Wagle, H. Zhao and G. A. Baker, *Accounts of Chemical Research*, 2014, **47**, 2299–2308.

[60] G. García, S. Aparicio, R. Ullah and M. Atilhan, *Energy and Fuels*, 2015, **29**, 2616–2644.

[61] F. Pena-Pereira and J. Namieśnik, *ChemSusChem*, 2014, **7**, 1784–1800.

[62] A. P. Abbott, G. Capper, D. L. Davies, R. K. Rasheed and V. Tambyrajah, *Chemical Communications*, 2003, **0**, 70–71.

[63] A. P. Abbott, D. Boothby, G. Capper, D. L. Davies and R. K. Rasheed, *Journal of the American Chemical Society*, 2004, **126**, 9142–9147.

[64] M. C. Gutiérrez, F. del Monte, D. Carriazo, M. C. Serrano and M. L. Ferrer, *Chemical Society Reviews*, 2012, **41**, 4996.

[65] H. Sun, Y. Li, X. Wu and G. Li, *Journal of Molecular Modeling*, 2013, **19**, 2433–2441.

[66] G. García, M. Atilhan and S. Aparicio, *Chemical Physics Letters*, 2015, **634**, 151–155.

[67] S. Zahn, B. Kirchner and D. Mollenhauer, *ChemPhysChem*, 2016, **17**, 3354–3358.

[68] C. R. Ashworth, R. P. Matthews, T. Welton and P. A. Hunt, *Physical Chemistry Chemical Physics*, 2016, **18**, 18145–18160.

[69] S. Zhu, H. Li, W. Zhu, W. Jiang, C. Wang, P. Wu, Q. Zhang and H. Li, *Journal of Molecular Graphics and Modelling*, 2016, **68**, 158–175.

[70] D. V. Wagle, C. A. Deakyne and G. A. Baker, *The Journal of Physical Chemistry B*, 2016, **120**, 6739–6746.

[71] R. Stefanovic, M. Ludwig, G. B. Webber, R. Atkin and A. J. Page, *Physical Chemistry Chemical Physics*, 2017, **19**, 3297–3306.

[72] A. Abbott and G. Capper, *Inorganic chemistry*, 2004, **43**, 3447–3452.

[73] R. F. Bader, *Atoms in Molecules: A Quantum Theory*, Oxford University Press, 1994.

[74] M. Palusiak and T. M. Krygowski, *Chemistry - A European Journal*, 2007, **13**, 7996–8006.

[75] A. P. Abbott, A. Ballantyne, R. C. Harris, J. A. Juma, K. S. Ryder and G. Forrest, *Electrochimica Acta*, 2015, **176**, 718–726.

[76] V. S. Protsenko, A. A. Kityk, D. A. Shaiderov and F. I. Danilov, *Journal of Molecular Liquids*, 2015, **212**, 716–722.

[77] A. A. Kityk, D. A. Shaiderov, E. A. Vasil'eva, V. S. Protsenko and F. I. Danilov, *Electrochimica Acta*, 2017, **245**, 133–145.

[78] H. Wang, Y. Jia, X. Wang, Y. Yao and Y. Jing, *Journal of Thermal Analysis and Calorimetry*, 2014, **115**, 1779–1785.

[79] J. M. Hartley, C. M. Ip, G. C. H. Forrest, K. Singh, S. J. Gurman, K. S. Ryder, A. P. Abbott and G. Frisch, *Inorganic Chemistry*, 2014, **53**, 6280–6288.

[80] F. S. Ghareh Bagh, F. S. Mjalli, M. A. Hashim, M. K. O. Hadj-Kali and I. M. Alnashef, *Industrial and Engineering Chemistry Research*, 2013, **52**, 11488–11493.

[81] S. D. Stranks and H. J. Snaith, *Nature Nanotechnology*, 2015, **10**, 391–402.

[82] S. A. Adonin, M. N. Sokolov and V. P. Fedin, *Coordination Chemistry Reviews*, 2016, **312**, 1–21.

[83] G. A. Fisher and N. C. Norman, *Advances in Inorganic Chemistry*, 1994, **41**, year.

[84] B. Liu, L. Xu, G. C. Guo and J. S. Huang, *Journal of Solid State Chemistry*, 2006, **179**, 1611–1617.

[85] J. Zhai, R. L. Sang and L. Xu, *Journal of Molecular Structure*, 2011, **1006**, 553–558.

[86] J. Estager, P. Nockemann, K. R. Seddon, M. Swadźba-Kwaśny and S. Tyrrell, *Inorganic chemistry*, 2011, **50**, 5258–71.

[87] Z.-P. Wang, J.-Y. Wang, J.-R. Li, M.-L. Feng, G.-D. Zou and X.-Y. Huang, *Chemical Communications*, 2015, **51**, 3094–3097.

[88] J. Cirera, P. Alemany and S. Alvarez, *Chemistry - A European Journal*, 2004, **10**, 190–207.

[89] J. Cirera, E. Ruiz and S. Alvarez, *Inorganic Chemistry*, 2008, **47**, 2871–2889.

[90] Y. Tanabe and S. Sugano, *Journal of the Physical Society of Japan*, 1954, **9**, 766–779.

[91] W. Linert, Y. Fukuda and A. Camard, *Coordination Chemistry Reviews*, 2001, **218**, 113–152.

[92] A. S. Barker, H. W. Verleur and H. J. Guggenheim, *Physical Review Letters*, 1966, **17**, 1286–1289.

[93] P. Gutlich, A. Horner and H. Spiering, *Angewandte Chemie International Edition*, 1994, **33**, 2024–2054.

[94] T. R. Griffiths and R. K. Scarrow, *Transactions of the Faraday Society*, 1969, **65**, 1727–1733.

[95] D. Lavabre, J. C. Micheau and G. Levy, *Journal of Chemical Education*, 1988, **65**, 274.

[96] B.-M. Antti, *Acta Chemica Scandinavica A*, 1976, **30**, 24–30.

[97] B.-M. Antti, *Acta Chemica Scandinavica A*, 1976, **30**, 103–108.

[98] B.-M. Antti, *Acta Chemica Scandinavica A*, 1975, **29**, 76–88.

[99] M. Gruden-Pavlović, M. Zlatar, C. W. Schläpfer and C. Daul, *Journal of Molecular Structure: THEOCHEM*, 2010, **954**, 80–85.

[100] A. J. Dent, K. R. Seddon and T. Welton, *Journal of the Chemical Society, Chemical Communications*, 1990, 315–316.

[101] W. E. O'Grady, D. F. Roeper, K. I. Pandya and G. T. Cheek, *Powder Diffraction*, 2011, **26**, 171–175.

[102] D. F. Roeper, K. I. Pandya, G. T. Cheek and W. E. O'Grady, *Journal of The Electrochemical Society*, 2011, **158**, F21.

[103] R. J. Gale, B. Gilbert and R. A. Osteryoung, *Inorganic Chemistry*, 1979, **18**, 2723–2725.

[104] P. B. Hitchcock, K. R. Seddon and T. Welton, *Journal of the Chemical Society, Dalton Transactions*, 1993, 2639–2643.

[105] A. Carmichael and C. Hardacre, *Analytical Chemistry*, 1999, 4572–4574.

[106] C. Zhong, T. Sasaki, A. Jimbo-Kobayeshi, E. Fujiwara, A. Kobayashi, M. Tada and Y. Iwasawa, *Bulletin of the Chemical Society of Japan*, 2007, **80**, 2365–2374.

[107] M. B. Meredith, C. H. McMillen, J. T. Goodman and T. P. Hanusa, *Polyhedron*, 2009, **28**, 2355–2358.

[108] A. W. Taylor, S. Men, C. J. Clarke and P. Licence, *RSC Advances*, 2013, **3**, 9436–9445.

[109] X. Wei, L. Yu, D. Wang, X. Jin and G. Z. Chen, *Green Chemistry*, 2008, **10**, 296.

[110] X. Wei, L. Yu, X. Jin, D. Wang and G. Z. Chen, *Advanced Materials*, 2009, **21**, 776–780.

Chapter 2

Theoretical background

This chapter provides the theoretical background to DFT, the method used for the theoretical work presented in this thesis. The chapter follows the standard textbook approach to the topic, beginning with the Hamiltonian energy operator, then considering many electron wavefunctions before discussing the rigourous foundation of DFT.[1]

2.1 The Hamiltonian operator

Schrödinger's equation shows how the Hamiltonian operator, H, acts on the wavefunction, Ψ, to give the system energy as an eigenvalue, E.

$$H\Psi = E\Psi \tag{2.1}$$

The Hamiltonian for a molecule in a simple situation (no external electric or magnetic fields, no relativistic effects) is a sum of the following components:

kinetic energy of electrons

kinetic energy of nuclei

potential energy of electron-nuclei attraction

potential energy of electon-electon repulsion

potential energy of nuclei-nuclei repulsion.

The functional form of this sum is:

$$H = -\sum_i \frac{\hbar^2}{2m_e}\nabla_i^2 - \sum_k \frac{\hbar^2}{2m_k}\nabla_k^2 - \sum_i\sum_k \frac{e^2 Z_k}{r_{ik}} + \sum_{i<j} \frac{e^2}{r_{ij}} + \sum_{k<l} \frac{e^2 Z_k Z_l}{r_{kl}} \tag{2.2}$$

$$\nabla_i^2 = \frac{\partial^2}{\partial x_i^2} + \frac{\partial^2}{\partial y_i^2} + \frac{\partial^2}{\partial z_i^2}$$

i, j: indices which run over electrons

k, l: indices which run over nuclei

m_e: mass of an electron

m_k: mass of nucleus k

e: charge of an electron

Z: atomic number

r_{ab}: distance from a to b

The potential energy terms are the same as in classical mechanics, but the kinetic energy terms are the kinetic energy operator T:

$$T = -\frac{\hbar^2}{2m}\nabla^2 \tag{2.3}$$

Ψ is a function of $3N$ coordinates, where N is the number of particles.

2.1.1 Calculating E

Equation (2.1) has many acceptable eigenfunctions Ψ for a given molecule, each with a different eigenvalue, E. Therefore a set of Ψ_i with associated E_i exists. For ease of manipulation we will assume that these Ψ_i are orthonormal. For a one-particle system with a 3-coordinate Ψ:

$$\int\int\int \Psi_i\Psi_j dxdydz = \delta_{ij} \tag{2.4}$$

δ_{ij}: Kronecker delta function, 1 for $i = j$ (normal), 0 for $i \neq j$ (orthogonal)

Replacing the multiple integrals for a single integral over $3N$ dimensional volume:

$$\int \Psi_i\Psi_j d\vec{r} = \delta_{ij} \tag{2.5}$$

Take Eq. (2.1) for Ψ_i, multiply by Ψ_j, and integrate both sides:

$$\int \Psi_j H\Psi_i d\vec{r} = E\int \Psi_j\Psi_i d\vec{r} \tag{2.6}$$

Combining with Eq. (2.5) we have:

$$\int \Psi_j H\Psi_i d\vec{r} = E\delta_{ij} \tag{2.7}$$

Given a suitable wavefunction Eq. (2.7) allows calculation of the energy be solving the integral on the RHS since when i=j we have:

$$\int \Psi_i H \Psi_i d\vec{r} = E_i \tag{2.8}$$

2.1.2 Variational principle

So far we have no way of obtaining the set of (complete, orthonormal) Ψ_i. However, assume we can pick a function ϕ which is an appropriate function on which to operate H. Since our set of Ψ_i is complete ϕ must be a linear combination of Ψ_i, with coefficients c_i:

$$\phi = \sum_i c_i \Psi_i \tag{2.9}$$

The normality of ϕ constrains c_i:

$$\int \phi^2 d\vec{r} = 1 = \int \sum_i c_i \Psi_i \sum_j c_j \Psi_j d\vec{r}$$

$$1 = \sum_{ij} c_i c_j \int \Psi_i \Psi_j d\vec{r}$$

$$1 = \sum_{ij} c_i c_j \delta_{ij}$$

$$1 = \sum_i c_i^2 \tag{2.10}$$

Applying H to both sides of Eq. (2.9) we have:

$$H\phi = H \sum_i c_i \Psi_i \tag{2.11}$$

By squaring both sides and integrating:

$$\int \phi H \phi d\vec{r} = \int (\sum_i c_i \Psi_i) H (\sum_j c_j \Psi_i) d\vec{r}$$

$$\int \phi H \phi d\vec{r} = \sum_{ij} c_i c_j \int \Psi_i H \Psi_j d\vec{r}$$

$$\int \phi H \phi d\vec{r} = \sum_{ij} c_i c_j E_j \delta_{ij}$$

77

$$\int \phi H \phi d\vec{r} = \sum_i c_i^2 E_i \tag{2.12}$$

The energy of a system with the generic wavefunction ϕ is determined by c_i and their associated E_i. The values of c_i and E_i are still unknown, however the set of E_i has a lowest value which we call E_0. From Eq. (2.10) we have:

$$E_0 \int \phi^2 d\vec{r} = E_0 \sum_i c_i^2 \tag{2.13}$$

Subtracting from both sides of Eq. (2.12):

$$\int \phi H \phi d\vec{r} - E_0 \int \phi^2 d\vec{r} = \sum_i c_i^2 E_i - E_0 \sum_i c_i^2$$

$$\int \phi H \phi d\vec{r} - E_0 \int \phi^2 d\vec{r} = \sum_i c_i^2 (E_i - E_0) \tag{2.14}$$

Since each c_i^2 and $(E_i - E_0)$ must be ≥ 0 the RHS must also be ≥ 0, giving:

$$\int \phi H \phi d\vec{r} - E_0 \int \phi^2 d\vec{r} \geq 0$$

$$\frac{\int \phi H \phi d\vec{r}}{\int \phi^2 d\vec{r}} \geq E_0 \tag{2.15}$$

Now since $\int \phi H \phi d\vec{r}$ is the E of ϕ, and $\int \phi^2 d\vec{r}$ is 1 (due to normalisation) we have:

$$E \geq E_0 \tag{2.16}$$

This is the variational principle. It means that we can judge the quality of any generated ground state wavefunction by the associated energy value - the lower the energy, the more accurate the wavefunction. This is a powerful principle: It allows us to construct wavefunctions in any manner we find appropriate, and it means calculus may be used to minimise the energy of a wavefunction.

2.1.3 The clamped nuclei and Born-Oppenheimer approximations

The molecular Hamiltonian for a many-particle system (Eq. (2.2)) is mathematically complex, including pairwise repulsive and attractive terms. This means that each particle's movements are "correlated" with all the others. The complexity may be

reduced substantially without significant loss of accuracy by considering a system with nuclei at fixed positions. This clamped nuclei approximation is justified by the relative masses of nuclei and electrons - electrons are orders of magnitude lighter than nuclei, and therefore move much faster. From the point of view of an electron the position of a nucleus is almost constant. The Schrödinger equation for a molecule with fixed nuclei (the "electronic Schrödinger equation") may be expressed as follows:

$$(H_e + V_N)\Psi_{el}(\vec{q_i} : \vec{q_k}) = E_{el}\Psi_{el}(\vec{q_i} : \vec{q_k}) \tag{2.17}$$

$H_e = -\sum_i \frac{\hbar^2}{2m_e}\nabla_i^2 - \sum_i \sum_k \frac{e^2 Z_k}{r_{ik}} + \sum_{i<j} \frac{e^2}{r_{ij}}$: The purely electronic Hamiltonian, H_e, is composed of the kinetic energy of the electrons and the potential energies of the electron-nuclear attraction and the electron-electron repulsion

V_N: nuclear-nuclear potential energy (constant)

$\vec{q_i}$: electronic coordinates

$\vec{q_k}$: nuclear coordinates

$(\vec{q_i} : \vec{q_k})$: a function of the electronic coordinates, which depend parametrically on the nuclear coordinates

E_{el}: electronic energy

Correlation in the nuclear-electronic potential energy term in the molecular Hamiltonian (Eq. (2.2)) is eliminated and nuclear-nuclear potential energy becomes a constant calculated for a given geometry. Wavefunctions are invariant for constants in the Hamiltonian so in practice Eq. (2.17) is solved without V_N, providing the pure electronic energy E_e, to which V_N is added to give E_{el}.

The Born-Oppenheimer approximation is the supposition that the molecular wavefunction Ψ may be expressed as a product of the electronic wavefunction Ψ_{el} and the nuclear wavefunction Ψ_N:

$$\Psi(\vec{q_i}, \vec{q_k}) \approx \Psi_{el}(\vec{q_i} : \vec{q_k})\Psi_N(\vec{q_i}) \tag{2.18}$$

From now on the clamped nuclei and Born-Oppenheimer approximations will be applied and Ψ shall be used to mean Ψ_{el}, and H and E to mean $H_{el} = H_e + V_N$ and E_{el}.

2.2 Construction of trial wavefunctions

Although we have neglected electron-nuclear correlation in the construction of the electronic Schrödinger equation, electron-electron correlation is still present. Initially a single electron system is considered, avoiding electron-electron correlation. From Eq. (2.17) the electronic wavefunction is only dependent on the fixed coordinates of the nucleus and the coordinates of the single electron. From now on all wavefunctions referred to are electronic wavefunctions. We will denote the many-electron wavefunction simply as Ψ, and the single-electron wavefunction as ψ.

We will call the eigenfunctions of the electronic Schrödinger equation MOs (molecular orbitals). The energy of an electron in an MO is the pure electronic energy eigenvalue. Experimentally this corresponds to ionisation energy.

2.2.1 LCAO basis set approach

We may construct wavefunctions in any fashion - and compare them via their energy eigenvalues. So how to form the wavefunctions? A common mathematical approach to represent an arbitrary function is via a combination of convenient functions - a basis set.

The electronic Schrödinger equation is exactly soluble for a system of 1 nucleus and 1 electron, yielding the hydrogenic AOs as eigenfunctions. These AOs (or approximations thereof) are used as basis sets for constructing wavefunctions for systems with more than 1 electron. The basis set is combined to build a guess wavefunction, ϕ, as follows:

$$\phi = \sum_{i=1}^{N} a_i \varphi_i \tag{2.19}$$

As N in Eq. (2.19) is increased the basis set initially gets closer to spanning the full space - however increasing N too much leads to linear dependency, decreasing the quality of the description.

Combining Eq. (2.19) and Eq. (2.15) gives an expression for E in terms of the basis functions and their coefficients:

$$E = \frac{\int (\sum_i a_i \varphi_i) H (\sum_j a_j \varphi_j) d\vec{r}}{\int (\sum_i a_i \varphi_i)(\sum_j a_j \varphi_j) d\vec{r}}$$

$$E = \frac{\sum_{ij} a_i a_j \int \varphi_i H \varphi_j d\vec{r}}{\sum_{ij} a_i a_j \int \varphi_i \varphi_j d\vec{r}}$$

$$E = \frac{\sum_{ij} a_i a_j H_{ij}}{\sum_{ij} a_i a_j S_{ij}} \tag{2.20}$$

$H_{ij} = \int \varphi_i H \varphi_j d\vec{r}$ is the resonance integral

$S_{ij} = \int \varphi_i H \varphi_j d\vec{r}$ is the overlap integral

Physically the overlap integral S_{ij} is the extent of phase matched spatial overlap between basis functions φ_i and φ_j. Note that basis functions are not orthonormal to one another. The resonance integral H_{ij} is less intuitive, though it tends to increase with S_{ij}. H_{ii} is the ionisation potential of a single electron occupying basis function φ_i. Both H_{ij} and S_{ij} are called matrix elements.

From the variational principal, to get closer to the true wavefunction we must minimise the energy of our guess wavefunction. Now that we have selected our basis set E is a function of the basis function coefficients, a_i. When the energy is minimised we have:

$$\frac{\partial E}{\partial a_k} = 0 \qquad \forall k \tag{2.21}$$

$\forall k$ means for all k

Partially differentiating Eq. (2.20) for each of the N variables a_k gives N equations which must be satisfied simultaneously in order that Eq. (2.21) holds and E is minimised:

$$\sum_{i=1}^{N} a_i (H_{ki} - E S_{ki}) = 0 \qquad \forall k \tag{2.22}$$

A set of N equations with N unknowns is soluble if and only if the determinant formed from coefficients $(H_{ki} - S_{ki})$ equals 0:

$$\begin{vmatrix} H_{11} - E S_{11} & H_{12} - E S_{12} & \cdots & H_{1N} - E S_{1N} \\ H_{21} - E S_{21} & H_{22} - E S_{22} & \cdots & H_{2N} - E S_{2N} \\ \vdots & \vdots & \ddots & \vdots \\ H_{N1} - E S_{N1} & H_{N2} - E S_{N2} & \cdots & H_{NN} - E S_{NN} \end{vmatrix} = 0 \tag{2.23}$$

Equation (2.23) is the secular equation. There are N roots E_j which satisfy the secular equation. Each value of E_j corresponds to a different MO. Each E_j gives a different set of the coefficients a_i, termed a_{ij}. a_{ij} are found by solving Eq. (2.22). For each E_j the wavefunction for its MO is ϕ_j and is defined by:

$$\phi_j = \sum_{i=1}^{N} a_{ij}\varphi_i \qquad (2.24)$$

For a one electron system the lowest energy MO defines the ground state.

The summarised process to find the optimal one electron wavefunction is:

1. Select a set of N basis functions.

2. Determine H_{ij} and S_{ij} for all N values of i and j.

3. Calculate the N roots E_j of the secular equation.

4. For each root solve Eq. (2.22) to find the coefficient a_{ij} for that MO

   MOs found via this process are orthogonal.

2.3 Many electron wavefunctions

2.3.1 Hartree-product wavefunctions

When one electron is considered the only terms in the Hamiltonian are the one electron kinetic energy term and the one electron nuclear attraction potential energy term. With only these terms present H is separable:

$$H = \sum_{i=1}^{N} h_i \qquad (2.25)$$

N is the total number of electrons

h_i is the one electron Hamiltonian

In AU we express h_i as:

$$h_i = -\frac{1}{2}\nabla_i{}^2 - \sum_{k=1}^{m} \frac{Z_k}{r_{ik}} \qquad (2.26)$$

m is the total number of nuclei

Eigenfunctions of h_i must satisfy the corresponding one electron Schrödinger equation:

$$h_i \psi_i = \varepsilon_i \psi_i \tag{2.27}$$

H is separable so we may construct its many electron wavefunctions out of products of one electron wavefunctions:

$$\Psi_{HP} = \psi_1 \psi_2 \psi_3 \ldots \psi_N \tag{2.28}$$

The wavefunction Ψ_{HP} thus formed is called the Hartree-product wavefunction. It can be shown that the energy eigenvalue of Ψ_{HP} is the sum of the one electron energies, ε_i. Starting with combining the Schrödinger equation and Eq. (2.28):

$$E\Psi_{HP} = H\Psi_{HP} = H\psi_1 \psi_2 \psi_3 \ldots \psi_N \tag{2.29}$$

From Eq. (2.25):

$$E\Psi_{HP} = \sum_{i=1}^{N} h_i \psi_1 \psi_2 \psi_3 \ldots \psi_N \tag{2.30}$$

Expanding the sum:

$$E\Psi_{HP} = (h_1\psi_1)\psi_2 \ldots \psi_N + \psi_1(h_2\psi_2)\psi_3 \ldots \psi_N + \cdots + \psi_1\psi_2 \ldots (h_N\psi_N) \tag{2.31}$$

Using the one electron Schrödinger equation (Eq. (2.27)):

$$E\Psi_{HP} = (\varepsilon_1\psi_1)\psi_2 \ldots \psi_N + \psi_1(\varepsilon_2\psi_2)\psi_3 \ldots \psi_N + \cdots + \psi_1\psi_2 \ldots (\varepsilon_N\psi_N)$$

$$E\Psi_{HP} = \sum_{i=1}^{N} \varepsilon_i \psi_1 \psi_2 \ldots \psi_N$$

$$E\Psi_{HP} = \left(\sum_{i=1}^{N} \varepsilon_i\right)\Psi_{HP}$$

$$E = \sum_{i=1}^{N} \varepsilon_i \tag{2.32}$$

2.3.2 The Hartree Hamiltonian

The Hamiltonian defined by the sum of one electron Hamiltonians does not include electron - electron repulsive potential energy. Calculating electron - electron repulsion is complex due to its dependence on many simultaneous pairwise interactions.

We take the approach of using Ψ_{HP} to compute energies from the full Hamiltonian, finding MOs ψ_i which minimise $\langle \Psi_{HP} | H | \Psi_{HP} \rangle$ (where H is the true Hamiltonian). Via variational calculus (not included here) it can be shown that each such ψ_i (which multiply to give the Ψ_{HP} which minimises $\langle \Psi_{HP} | H | \Psi_{HP} \rangle$) is an eigenfunction of its corresponding h_i, expressed as:

$$h_i = \frac{1}{2}\nabla_i^2 - \sum_{k=1}^{m} \frac{Z_k}{r_{ik}} + \sum_{j \neq k} \int \frac{\rho_j}{r_{ij}} d\vec{r} \tag{2.33}$$

We will refer to this Hamiltonian as the "many electron Hamiltonian", however it is not the true Hamiltonian H. The many electron Hamiltonian (Eq. (2.33)) differs from the one electron Hamiltonian (Eq. (2.26)) by the addition of the electron electron repulsive term. This repulsive potential energy term is expressed analogously to the nuclear electron attractive term, except that the nuclei are treated as point charges and the electrons as spread out charge density, which is therefore integrated over all space.

To calculate our one electron wavefunctions ψ_i from the many electron Hamiltonian we need to calculate the electron electron repulsion, which depends on our wavefunctions. This recursive dependence is solved using the SCF (self-consistent field) iterative method proposed by Hartree:
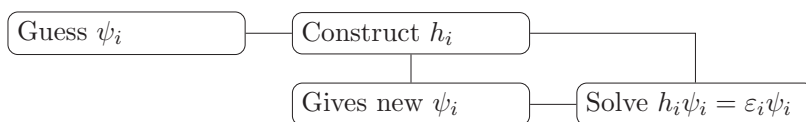
When a set of ψ_i is sufficiently (by some arbitrary criteria) close to the previous set of ψ_i we take the final set as the converged SCF orbitals.

From Eq. (2.32) the sum of h_i gives a separable Hamiltonian H for which Ψ_{HF} is an eigenvalue. In this "non-interacting" Hamiltonian each electron sees a constant potential (derived in an average sense from the electron density) but is not interacting in an instantaneous pairwise manner.

The non-interacting Hamiltonian double-counts electron interactions: h_i and h_j both include the full repulsive potential energy of the ij electron pair. To correct this double-counting we compute $E = \langle \Psi_{HP} | H | \Psi_{HP} \rangle$ as:

$$E = \sum_i \varepsilon_i - \frac{1}{2} \sum_{i \neq j} \int \int |\psi_i|^2 |\psi_j|^2 d\vec{r_i} d\vec{r_j} \qquad (2.34)$$

$\int \int |\psi_i|^2 |\psi_j|^2 d\vec{r_i} d\vec{r_j}$ is the Coulomb integral J_{ij}

Now we have a Hartree-product wavefunction. How do we go about filling the MOs generated with electrons?

2.3.3 Electron spin and antisymmetry

When Einstein's theory of relativity is included in quantum mechanics the result is relativistic quantum mechanics. When applied to electrons the concept of spin and the Pauli exclusion principle (no two electrons may have the same set of quantum numbers) are generated.

Electrons have spin quantum numbers, eigenvalues of the electron spin function which is an eigenfunction of the spin operator S_z. The two eigenvalues are $S_z \alpha \frac{+\hbar}{2}$ and $S_z \beta \frac{-\hbar}{2}$, where α and β denote the orthonormal spin eigenfunctions.

We might guess that a ground state Hartree-product wavefunction for a molecule with two electrons of spin α could be written as:

$$^3\Psi_{HP} = \psi_a(1)\alpha(1)\psi_b(2)\alpha(2) \qquad (2.35)$$

$^3\Psi_{HP}$ denotes the Hartree-product wavefunction for a triplet electronic state where triplet denotes the multiplicity, equal to $2S + 1$, where $S =$ total spin.

ψ_a and ψ_b are different (both electrons have the same spin number so they cannot have all other quantum numbers the same). ψ_a and ψ_b are orthonormal.

It turns out that although this formulation satisfies the Pauli exclusion principle it violates a further result of relativistic quantum field theory. Electronic wavefunctions must change sign when the coordinates of two electrons are switched. This makes the wavefunction antisymmetric.

We can express the Pauli principle for N electrons as follows:

$$P_{ij}\Psi[\vec{q_1}(1), \dots, \vec{q_i}(i), \dots, \vec{q_j}(j), \dots, \vec{q_N}(N),]$$

$$= \Psi[\vec{q_1}(1), \dots, \vec{q_j}(j), \dots, \vec{q_i}(i), \dots, \vec{q_N}(N),]$$

$$= -\Psi[\vec{q_1}(1), \ldots, \vec{q_i}(i), \ldots, \vec{q_j}(j), \ldots, \vec{q_N}(N),] \tag{2.36}$$

P_{ij} is the interchange operator

$\vec{q}$ includes both the Cartesian coordinates and the spin function

We can alter $^3\Psi_{HP}$ such that it satisfies Eq. (2.36):

$$^3\Psi_{SD} = \frac{1}{\sqrt{2}}[\psi_a(1)\alpha(1)\psi_b(2)\alpha(2) - \psi_a(2)\alpha(2)\psi_b(1)\alpha(1)] \tag{2.37}$$

The SD subscript stands for Slater determinant

Integrating $|^3\Psi_{SD}|^2$ over all space, and using the orthonormality of the MOs and spin functions to simplify (ω is a spin integration variable):

$$\int |^3\Psi_{SD}|^2 d\vec{r_1} d\vec{\omega_1} d\vec{r_2} d\vec{\omega_2}$$

$$= \frac{1}{2}[\int |\psi_a(1)|^2|\alpha(1)|^2|\psi_b(2)|^2|\alpha(2)|^2 d\vec{r_1} d\vec{\omega_1} d\vec{r_2} d\vec{\omega_2}$$

$$-2\int \psi_a(1)\psi_b(1)|\alpha(1)|^2\psi_b(2)\psi_a(2)|\alpha(2)|^2 d\vec{r_1} d\vec{\omega_1} d\vec{r_2} d\vec{\omega_2}$$

$$+\int |\psi_a(2)|^2|\alpha(2)|^2|\psi_b(1)|^2|\alpha(1)|^2 d\vec{r_1} d\vec{\omega_1} d\vec{r_2} d\vec{\omega_2}]$$

$$= \frac{1}{2}[1 - 0 + 1] = 1 \tag{2.38}$$

From Eq. (2.38) we see that the $\frac{1}{\sqrt{2}}$ in Eq. (2.37) normalises $|^3\Psi_{SD}|^2$.

2.3.4 Slater determinants

We can express our new wavefunction $^3\Psi_{SD}$ as a matrix determinant:

$$^3\Psi_{SD} = \frac{1}{\sqrt{2}} \begin{vmatrix} \psi_a(1)\alpha(1) & \psi_b(1)\alpha(1) \\ \psi_a(2)\alpha(2) & \psi_b(2)\alpha(2) \end{vmatrix} \tag{2.39}$$

It is a general property of matrix determinants that when a pair of rows or columns are switched the sign of the determinant changes. When the permutation

operator (which switches two sets of electron coordinates) is applied the effect is to switch two rows in the Slater Determinant. To generalise:

$$\Psi_{SD} = \frac{1}{\sqrt{N!}} \begin{vmatrix} \chi_1(1) & \chi_2(1) & \cdots & \chi_N 1 \\ \chi_1(2) & \chi_2(2) & \cdots & \chi_N 2 \\ \vdots & \vdots & \ddots & \vdots \\ \chi_1(N) & \chi_2(N) & \cdots & \chi_N N \end{vmatrix} \quad (2.40)$$

In compacted form, with implicit $\frac{1}{\sqrt{N!}}$ prefactor:

$$\Psi_{SD} = |\chi_1 \chi_2 \chi_3 \ldots \chi_N\rangle \quad (2.41)$$

If an orbital is doubly occupied by electrons 1 and 2 then their spin orbitals χ_1 and χ_2 only differ in the spin eigenfunction. In this case $\chi_1 \chi_2$ is denoted as ψ_1^2, where the 2 denotes double occupation. Ψ_{SD} could then be expressed:

$$\Psi_{SD} = |\psi_1^2 \chi_3 \ldots \chi_N\rangle \quad (2.42)$$

In Slater determinants the indistinguishability of electrons is maintained (unlike in Hartree-product wavefunctions). Every electron appears in every spin-orbital at some point.

Quantum mechanical exchange is also manifest in Slater determinants. To evaluate the energy of the interelectronic repulsion for $^3\Psi_{SD}$ as expressed in Eq. (2.37) we must evaluate the following integral:

$$\int {}^3\Psi_{SD} \frac{1}{r_{12}} {}^3\Psi_{SD} d\vec{r_1} d\vec{\omega_1} d\vec{r_2} d\vec{\omega_2}]$$

$$= \frac{1}{2} [\int |\psi_a(1)|^2 |\alpha(1)|^2 \frac{1}{r_{12}} |\psi_b(2)|^2 |\alpha(2)|^2 d\vec{r_1} d\vec{\omega_1} d\vec{r_2} d\vec{\omega_2}$$

$$- 2 \int \psi_a(1)\psi_b(1)|\alpha(1)|^2 \frac{1}{r_{12}} \psi_b(2)\psi_a(2)|\alpha(2)|^2 d\vec{r_1} d\vec{\omega_1} d\vec{r_2} d\vec{\omega_2}$$

$$+ \int |\psi_a(2)|^2 |\alpha(2)|^2 \frac{1}{r_{12}} |\psi_b(1)|^2 |\alpha(1)|^2 d\vec{r_1} d\vec{\omega_1} d\vec{r_2} d\vec{\omega_2}]$$

$$= \frac{1}{2} [\int |\psi_a(1)|^2 \frac{1}{r_{12}} |\psi_b(2)|^2 d\vec{r_1} d\vec{r_2}$$

$$-2 \int \psi_a(1)\psi_b(1)\frac{1}{r_{12}}\psi_b(2)\psi_a(2)d\vec{r_1}d\vec{r_2}$$

$$+ \int |\psi_a(2)|^2 \frac{1}{r_{12}}|\psi_b(1)|^2 d\vec{r_1}d\vec{r_2}$$

$$= \frac{1}{2}(J_{ab} - 2 \int \psi_a(1)\psi_b(1)\frac{1}{r_{12}}\psi_b(2)\psi_a(2)d\vec{r_1}d\vec{r_2} + J_{ab})$$

$$= J_{ab} - K_{ab} \tag{2.43}$$

$K_{ab} = \int \psi_a(1)\psi_b(1)\frac{1}{r_{12}}\psi_b(2)\psi_a(2)d\vec{r_1}d\vec{r_2}$ is called the exchange integral.

If we did the same process for a system with two electrons of opposite spin we find that the interelectronic repulsion is simply J_{ab}. This means that the interelectronic repulsion energy is less by K_{ab}, the exchange integral, when electrons spins are parallel. This is due to the Fermi hole which surrounds each electron - a region where the probability of finding another electron of the same spin is reduced. Since the positions of electrons with the same spin are correlated in this way, the interelectronic repulsion energy is reduced.

2.3.5   The Hartree-Fock Self-Consistent Field method

Hartree's SCF procedure was extended to SD wavefunctions by Fock. When HF MOs are used the interaction of each electron with the static field of all the other electrons includes the exchange effect outlined above.

Here the RHF (restricted Hartree-Fock) equations are presented. Restricted means all electrons are spin-paired, with two electrons per occupied MO.

The one electron Fock operator is expressed for electron i as follows:

$$f_i = -\frac{1}{2}\nabla_i^2 - \sum_{k}^{nuclei} \frac{Z_k}{r_{ik}} + V_i^{HF}\{j\} \tag{2.44}$$

$V_i^{HF}\{j\} = 2J_i - K_i$ is the HF potential

J_i and K_i are operators which compute the Coulomb and exchange integrals

Roothaan developed matrix algebraic methods to allow MOs to be represented by basis sets to be used in HF calculations. In this procedure, given a set of N basis functions we first solve the secular equation for its roots E_j:

$$\begin{vmatrix} F_{11} - ES_{11} & F_{12} - ES_{12} & \cdots & F_{1N} - ES_{1N} \\ F_{21} - ES_{21} & F_{22} - ES_{22} & \cdots & F_{2N} - ES_{2N} \\ \vdots & \vdots & \ddots & \vdots \\ F_{N1} - ES_{N1} & F_{N2} - ES_{N2} & \cdots & F_{NN} - ES_{NN} \end{vmatrix} = 0 \qquad (2.45)$$

F and S are calculated explicitly. S are the overlap matrix elements. We denote a general matrix element F as $F_{\mu\nu}$, where the lower-case greek letter μ refers to the basis function, and the lower-case roman letter ν refers to the MO.

To calculate $F_{\mu\nu}$:

$$F_{\mu\nu} = \langle \mu | -\frac{1}{2}\nabla^2 | \nu \rangle - \sum_k^{nuclei} \langle \mu | \frac{1}{r_k} | \nu \rangle + \sum_{\lambda\sigma} P_{\lambda\sigma} [(\mu\nu|\lambda\sigma) - \frac{1}{2}(\mu\lambda|\nu\sigma)] \qquad (2.46)$$

$\langle \mu | g | \nu \rangle$ where g is some operator denotes a one electron integral:

$$\langle \mu | g | \nu \rangle = \int \phi_\mu (g\phi_\nu) d\vec{r} \qquad (2.47)$$

$(\mu\nu|\lambda\sigma)$ gives the Coulomb integral:

$$(\mu\nu|\lambda\sigma) = \int \int \phi_\mu(1)\phi_\nu(1)\frac{1}{r_{12}}\phi_\lambda(2)\phi_\sigma(2)d\vec{r}(1)d\vec{r}(2) \qquad (2.48)$$

where ϕ_μ and ϕ_ν represent the probability density of one electron and ϕ_λ and ϕ_σ the other. $(\mu\lambda|\nu\sigma)$ similarly gives the exchange integral.

In the final term of Eq. (2.46) the exchange integral is halved because it only applies when both electrons have the same spin.

P is the density matrix, representing the amount a basis function contributes to the many electron wave function. The final term therefore weights the energy contribution of a basis function according to its relative importance in the wavefunction. Elements of P are calculated as follows:

$$P_{\lambda\sigma} = 2 \sum_i^{occupied} a_{\lambda i} a_{\sigma i} \qquad (2.49)$$

where the coefficients $a_{\zeta i}$ specify the contribution of basis function ζ to the MO.

Like the Hartree method HF is self-referential so the SCF procedure is applied:

Choose basis set

Choose geometry $q^{(0)}$

Calculate overlap, one electron and two electron integrals

Guess initial density matrix $P^{(0)}$

Solve HF secular equation

Replace $P^{(n-1)}$ with $P^{(n)}$

Construct $P^{(n)}$ from MOs

NO

Is $P^{(n)}$ sufficiently similar to $P^{(n-1)}$?

Generate $q^{(n+1)}$

YES

NO

Does $q^{(n)}$ satisfy geometry optimisation criteria?

YES

Output data for optimised molecule
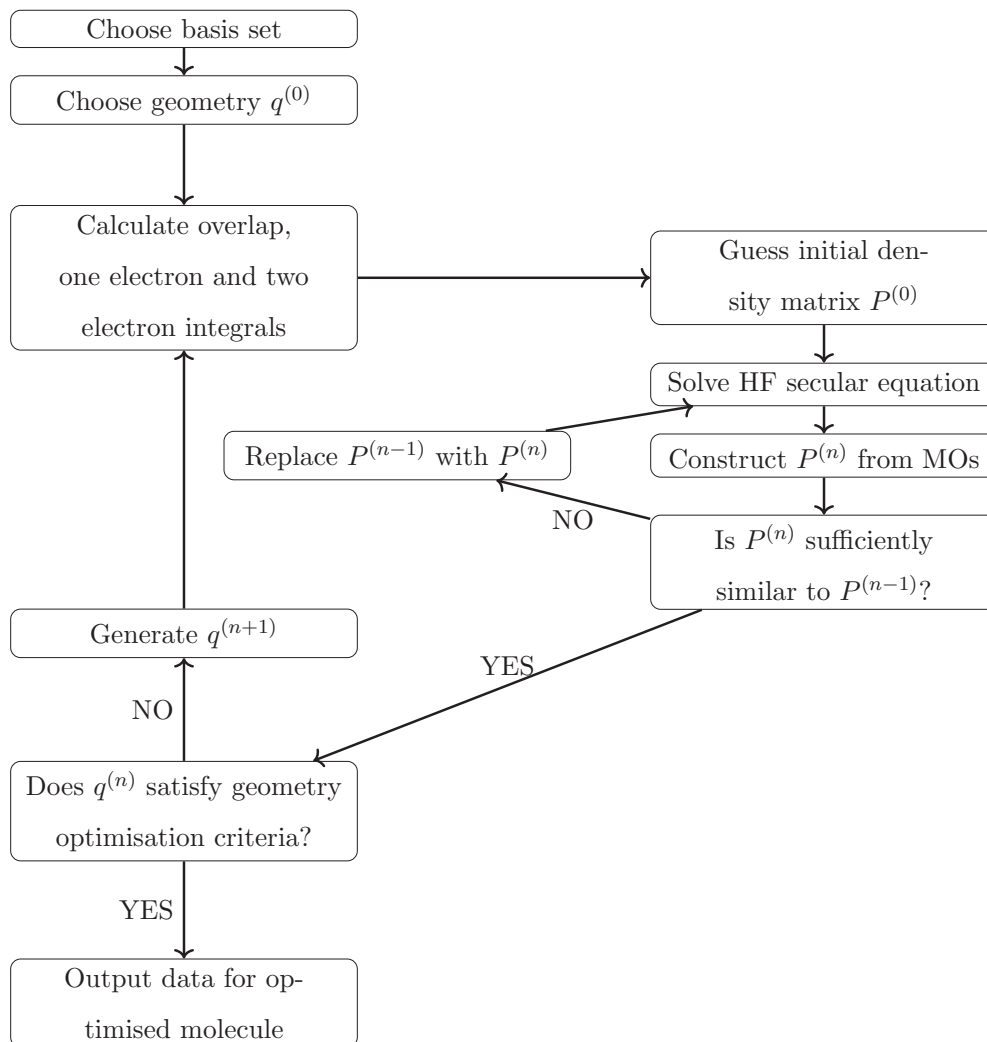
The HF energy of a molecule is well defined and may be converged to the basis set limit. However, the Fock operator is a one-electron operator; the HF energy is the energy of a system of N electrons which do not interact amongst themselves but instead experience an effective potential. Whilst the exchange energy is fully accounted for in this model, all other sources of electron correlation energy are not. We define the electron correlation energy as the difference between the HF energy of a system and the exact solution to the non-relativistic Schrödinger equation of that system (where the clamped nuclei approximation and Born-Oppenheimer ansatz are included in defining the system).

HF theory is limited in its application by its large scaling in computational time requirements with respect to the number of basis functions, N. This is due to the need to evaluate 4-index integrals where each index increments over all N basis functions, giving N^4 scaling in number of integrals to calculate.

2.4 Density Functional Theory (DFT)

2.4.1 Theoretical motivation

Wavefunctions produced from MO theories are complex, many dimensional and unintuitive. The function depends on the three geometric coordinates and one spin number for each electron. Accurate measurements of observables are achieved, but the wavefunction itself is not observable.

A more intuitive feature to work with is electron density, ρ. ρ is a physical observable (albeit difficult to observe directly), and it contains all the information required (positions and atomic numbers of nuclei, total number of electrons) to specify the Hamiltonian.

Integrated over all space, ρ gives the total number of electrons, N:

$$N = \int \rho(\vec{r})d\vec{r} \tag{2.50}$$

Nuclear positions, and atomic numbers correspond to local maxima in ρ.

It follows that given a known density, the Hamiltonian may be formed, the Schrödinger equation solved and the wavefunctions and energy eigenvalues determined.

To calculate molecular energy from electron density, separate energy into kinetic and potential parts. Considering the system to be classical the potential parts may be formulated as follows:

Electron density - nuclear attraction:

$$V_{ne}[\rho(\vec{r})] = \sum_k^{nuclei} \int \frac{Z_k}{|\vec{r} - \vec{r_k}|}\rho(\vec{r})d\vec{r} \tag{2.51}$$

Classical self-repulsion of the electron density:

$$V_{ee}[\rho(\vec{r})] = \frac{1}{2} \int \int \frac{\rho(\vec{r_1})\rho(\vec{r_2})}{|\vec{r_1} - \vec{r_2}|}d\vec{r_1}d\vec{r_2} \tag{2.52}$$

where $d\vec{r_1}$ and $d\vec{r_2}$ indicate that integration runs over all space.

Fermion statistical mechanics was used by Thomas and Fermi in 1927 to derive the kinetic energy for the "uniform electron gas"; a system having infinite electrons moving in an infinitely large space with a uniformly distributed positive charge.

$$T_{ueg}[\rho(\vec{r})] = \frac{3}{10}(3\pi^2)^{\frac{2}{3}} \int \rho^{\frac{5}{3}}(\vec{r})d\vec{r} \tag{2.53}$$

In Eqs. (2.51) to (2.53) T and V are functions of ρ, itself a function of $\vec{r}$. A function of a function is a functional, making T and V "density functionals".

Equations (2.51) to (2.53) (along with a variational principle) make up Thomas-Fermi DFT. In this first iteration of DFT all molecules are unstable relative to dissociation into individual atoms.

Equation (2.52) contains a large approximation - all correlation effects are ignored. We introduce a hole function, h, to correct the classical energy:

$$\langle \Psi | \sum_{i<j}^{electrons} \frac{1}{r_{ij}} = \frac{1}{2} \int \int \frac{\rho(\vec{r_1})\rho(\vec{r_2})}{|\vec{r_1} - \vec{r_2}|} d\vec{r_1} d\vec{r_2} + \frac{1}{2} \int \int \frac{\rho(\vec{r_1})h\rho(\vec{r_2})}{|\vec{r_1} - \vec{r_2}|} d\vec{r_1} d\vec{r_2} \qquad (2.54)$$

So the exact quantum mechanical electronic repulsion (LHS) is equal to the classical value minus some correction via the hole function h, which would include exchange, all other correlation, and self-interaction energies. The exact form of h is indeterminate for many-electron systems.

HF theory does not have self-interaction error and has exact exchange. But the exact exchange is slow to calculate so Slater adopted a simple approximation for the exchange energy $E_x[\rho(\vec{r})]$, with a spherical exchange hole:

$$E_x[\rho(\vec{r})] = -\frac{9\alpha}{8}(\frac{3}{\pi})^{\frac{1}{3}} \int \rho^{\frac{4}{3}}(\vec{r}) d\vec{r} \qquad (2.55)$$

When $\alpha = 1$ the equation is for "Slater's exchange". Bloch and Dirac had already derived the same equation from the uniform electron gas, except with $\alpha = \frac{2}{3}$. Combining that expression with Eqs. (2.51) to (2.53) gives the Thomas-Fermi-Dirac model (still highly inaccurate).

Due to α being given different values it began to be treated as an empirical constant, with subsequent calculations being termed Xα calculations. $\alpha = \frac{3}{4}$ tended to give the most accurate computations.

2.4.2 Rigorous foundation

The above approach is much simpler than the wavefunction based methods, and though it proved too inaccurate for most molecular focused chemists, solid state physicists found many uses for it in their much larger systems.

The Hohenberg-Kohn theorems

Existence theorem   The external potential (and hence the total energy) is a unique functional of the electron density.

Variation theorem   The functional that delivers the ground state energy of the system gives the lowest energy if and only if the input density is the true ground state density.

Notes on the existence theorem   We aim to establish that the energy depends on the electron density. In order to do this we must prove that the Hamiltonian is uniquely determined by electron density. Integration of the electron density gives the number of electrons so to complete the Hamiltonian we need only the external potential. In molecular DFT the external potential is the charge and position of each nucleus.

The existence theorem may be proved via *reductio ad absurdum* by assuming its opposite - that two different external potentials can have the same electron density. This gives the result (steps not shown here) that the energy of system a, E_a, plus the energy of system b, E_b is less than itself:

$$E_a + E_b < E_a + E_b \qquad (2.56)$$

This is clearly nonsensical, proving the existence theorem.

Thus the ground state density determines the Hamiltonian which determines both the ground state and all excited state wavefunctions.

Notes on the variational theorem   Assume a candidate electron density which integrates to give the correct number of electrons. The existence theorem shows that the density determines a candidate wavefunction and Hamiltonian, giving a candidate energy:

$$\langle \Psi_{cand} | H_{cand} | \Psi_{cand} \rangle = E_{cand} \geq E_0 \qquad (2.57)$$

By the variational principle of MO theory E_{cand} is $\geq$ the true ground state energy.

These two theorems provide a basis for, but no prescription to, using electron density to determine molecular systems. We can guess different densities and know which is closest to correct but these is no method to systematically improve our candidate densities. Also we would like to determine the energy directly from the density, without going through a wavefunction.

2.4.3 Kohn-Sham Self Consistent Field methodology

The above is no significant improvement on MO theory, since the final step still uses a wavefunction and the Hamiltonian to solve the Schrödinger equation. This is prohibitively difficult in most cases, due to the electron - electron interaction term in the correct Hamiltonian. Kohn and Sham conceived of a simpler Hamiltonian - for a non-interacting system of electrons. The non-interacting Hamiltonian is a sum of one-electron operators, its eigenfunctions are Slater determinants of the one-electron eigenfunctions and eigenvalues which are the sum of the one-electron eigenvalues.

The procedure to make use of this simplified Hamiltonian is to take a real system of interest (with interacting electrons) and create an analogous non-interacting system which has the same electron density as the real system. We then express the energy functional as a sum of parts whose evaluation is facilitated by this approach:

$$E[\rho(\vec{r})] = T_{ni}[\rho(\vec{r})] + V_{ne}[\rho(\vec{r})] + V_{ee}[\rho(\vec{r})] + \Delta T[\rho(\vec{r})] + \Delta V_{ne}[\rho(\vec{r})] \qquad (2.58)$$

$T_{ni}[\rho(\vec{r})]$: kinetic energy of the non-interacting electrons (sum of individual kinetic energies)

$V_{ne}[\rho(\vec{r})]$: nuclear electron interaction

$V_{ee}[\rho(\vec{r})]$: classical electron-electron repulsion

$\Delta T[\rho(\vec{r})]$: correction to kinetic energy due to electron interaction

$\Delta V_{ne}[\rho(\vec{r})]$: all non-classical corrections to electron-electron repulsion

Using an orbital expression for density we can rewrite Eq. (2.58) as:

$$E[\rho(\vec{r})] = \sum_i^N (\langle \chi_i | -\frac{1}{2}\nabla_i^2|\chi_i\rangle - \langle \chi_i | \sum_k^{nuclei} \frac{Z_k}{|\vec{r_i} - \vec{r_k}|}|\chi_i\rangle) \qquad (2.59)$$

$$+ \sum_i^N \langle \chi_i | \frac{1}{2} \int \frac{\rho(\vec{r'})}{|\vec{r_i} - \vec{r'}|} d\vec{r'}|\chi_i\rangle + E_{xc}[\rho(\vec{r})] \qquad (2.60)$$

N: number of electrons

χ_i Slater determinantal wavefunction, an exact eigenfunction for the non-interacting system

$\rho = \sum_{i=1}^N \langle \chi_i | \chi_i \rangle$ is the density

$E_{xc}[\rho(\vec{r})] = \Delta T[\rho(\vec{r})] + \Delta V_{ne}[\rho(\vec{r})]$

$E_{xc}[\rho(\vec{r})]$ is usually termed the exchange-correlation energy - it includes the

quantum mechanical exchange and correlation, the correction for the classical self-interaction energy and the correction to the kinetic energy on moving from the non-interacting system to the real one.

The next step is to find orbitals χ which minimise E. It is found that such orbitals satisfy the pseudoeigenvalue equations, where h_i^{KS} is the Kohn-Sham one-electron operator:

$$h_i^{KS}\chi_i = \varepsilon_i\chi_i \tag{2.61}$$

$$h_i^{KS} = -\frac{1}{2}\nabla_i^2 - \sum_k^{nuclei} \frac{Z_k}{|\vec{r_i} - \vec{r_k}|} + \int \frac{\rho(\vec{r'})}{|\vec{r_i} - \vec{r'}|} d\vec{r'} + V_{xc} \tag{2.62}$$

$$V_{xc} = \frac{\delta E_{xc}}{\delta\rho} \tag{2.63}$$

V_{xc} is the one-electron operator for which the expectation value of the KS Slater determinant is E_{xc}.

The E (from Eq. (2.58)) to which we are minimising is exact, therefore the orbitals provide the exact density. To determine the KS orbitals the same approach as that applied to MO theory is used - they are expressed with a basis set of functions $\{\phi\}$. Then a secular equation analogous to that used in HF theory is solved to find the coefficients of each basis function in each orbital.

$$K_{\mu\nu} = \langle\phi_\mu| -\frac{1}{2}\nabla_i^2 - \sum_k^{nuclei} \frac{Z_k}{|\vec{r_i} - \vec{r_k}|} + \int \frac{\rho(\vec{r'})}{|\vec{r_i} - \vec{r'}|} d\vec{r'} + V_{xc}|\phi_\nu\rangle \tag{2.64}$$

If the same basis functions are used then the kinetic energy, nuclear-electron attraction, and classical electron repulsion components are identical for DFT and HF. DFT as derived so far is an exact theory, however its equations must be solved approximately due to not knowing the exact form of E_{xc}. HF is an approximate theory, however its equations may be solved exactly.

2.4.4 Exchange-correlation functionals

To repeat, in theory E_{xc} accounts for both the difference between classical and quantum mechanical electron-electron repulsion, and the difference in kinetic energy between the real and non-interacting systems.

Modern functionals usually do not explicitly compute the kinetic energy term,

instead incorporating it into a hole function analogous to that in Eq. (2.54). If empirical parameters from experiments are used then these will contain some kinetic energy correction by default.

It is conventional to express the dependence of the E_{xc} function on electron density as follows:

$$E_{xc}[\rho(\vec{r})] = \int \rho(\vec{r}) \varepsilon_{xc}[\rho(\vec{r})] d\vec{r} \qquad (2.65)$$

where ε_{xc} is the energy density (also dependent on the electron density) expressed per particle (electron density is expressed per unit volume). ε_{xc} is treated as a sum of individual exchange and correlation contributions.

Combining Eq. (2.55) and Eq. (2.65) we may express the Slater exchange energy density:

$$-\frac{9\alpha}{8}(\frac{3}{\pi})^{\frac{1}{3}} \int \rho^{\frac{4}{3}}(\vec{r}) d\vec{r} = \int \rho(\vec{r}) \varepsilon_{xc}[\rho(\vec{r})] d\vec{r} \qquad (2.66)$$

$$-\frac{9\alpha}{8}(\frac{3}{\pi})^{\frac{1}{3}} \rho^{\frac{4}{3}}(\vec{r}) = \rho(\vec{r}) \varepsilon_{xc}[\rho(\vec{r})] \qquad (2.67)$$

$$\varepsilon_{xc}[\rho(\vec{r})] = -\frac{9\alpha}{8}(\frac{3}{\pi})^{\frac{1}{3}} \rho^{\frac{1}{3}}(\vec{r}) \qquad (2.68)$$

Another convention is to express the electron density in terms of the radius of a sphere (r_s) which would contain exactly one electron if the density at the centre of the sphere was maintained throughout the sphere:

$$r_s(\vec{r}) = (\frac{3}{4\pi\rho(\vec{r})})^{\frac{1}{3}} \qquad (2.69)$$

If the density is high at $\vec{r}$ (the centre of the sphere) then r_s is small and vice versa.

Spin is included in DFT simply by using separate functionals for the α and β densities. The spin densities at any point are conventionally expressed using the normalised spin polarisation function ($\zeta(\vec{r})$):

$$\zeta(\vec{r}) = \frac{\rho^{\alpha}(\vec{r}) - \rho^{\beta}(\vec{r})}{\rho(\vec{r})} \qquad (2.70)$$

$$\rho^{\alpha}(\vec{r}) = \frac{1}{2}\rho(\vec{r})(\zeta(\vec{r}) + 1) \qquad (2.71)$$

$$\rho^{\beta}(\vec{r}) = \frac{1}{2}\rho(\vec{r})(1 - \zeta(\vec{r})) \tag{2.72}$$

Local density approximation (LDA)

LDA was originally defined as any functional where $\varepsilon_{xc}(\vec{r})$ was determined only from the value or properties of $\rho(\vec{r})$ at the same position, $\vec{r}$. ie. not from any property of ρ at any other position in space. However LDA now often refers only to those functionals which derive from analysis of the uniform electron gas where $\rho(\vec{r})$ is constant. For example the exchange energy for a uniform electron gas is given by Eq. (2.68) with $\alpha = \frac{2}{3}$, and this is termed LDA, but the same formula with the same local dependence on ρ is used in both the Slater ($\alpha = 1$) and Xα ($\alpha = \frac{3}{4}$) methods which are not referred to as LDA.

LDA, Slater and Xα methods can all be extended to spin polarised systems:

$$\varepsilon_x[\rho(\vec{r}), \zeta(\vec{r})] = \varepsilon_x^0[\rho(\vec{r})] + \{\varepsilon_x'[\rho(\vec{r})] - \varepsilon_x^0[\rho(\vec{r})]\}[\frac{(1+\zeta)^{\frac{4}{3}} + (1-\zeta)^{\frac{4}{3}} - 2}{2(2^{\frac{1}{3}} - 1)}] \tag{2.73}$$

ε_x^0 is given by Eq. (2.68), ε_x' is an analogous expression for the exchange energy density of a uniform electron gas with all electrons having the same spin.

In an unpolarised system (closed-shell) ζ is 0 everywhere, and so is the second term on the RHS. For open-shell systems the above formalism must be used and is often termed LSDA (local spin density approximation).

The correlation energy density ε_c has not been analytically derived even for a uniform electron gas, except for the limits at 0 and ∞ electron density. An empirical approach has was therefore taken, with Ceperley and Alder (1980) computing the total energies for uniform electron gases at several densities, using quantum Monte Carlo techniques to a high numerical accuracy. The correlation energy was then obtained by subtracting the analytical exchange energies. Vosko, Wilk and Nusair (1980) created local functionals of the density fitting to these results. Several forms of ε_c were expressed as a function of r_s rather than of density. Four empirical constants are contained within the express and their values are different for ε_c^0 and ε_c'. The most widely used forms are VWN and VWN5. LSDA calculations using Slater exchange and VWN correlation are termed SVWN. The steps involved in a LSDA calculation are summarised below:
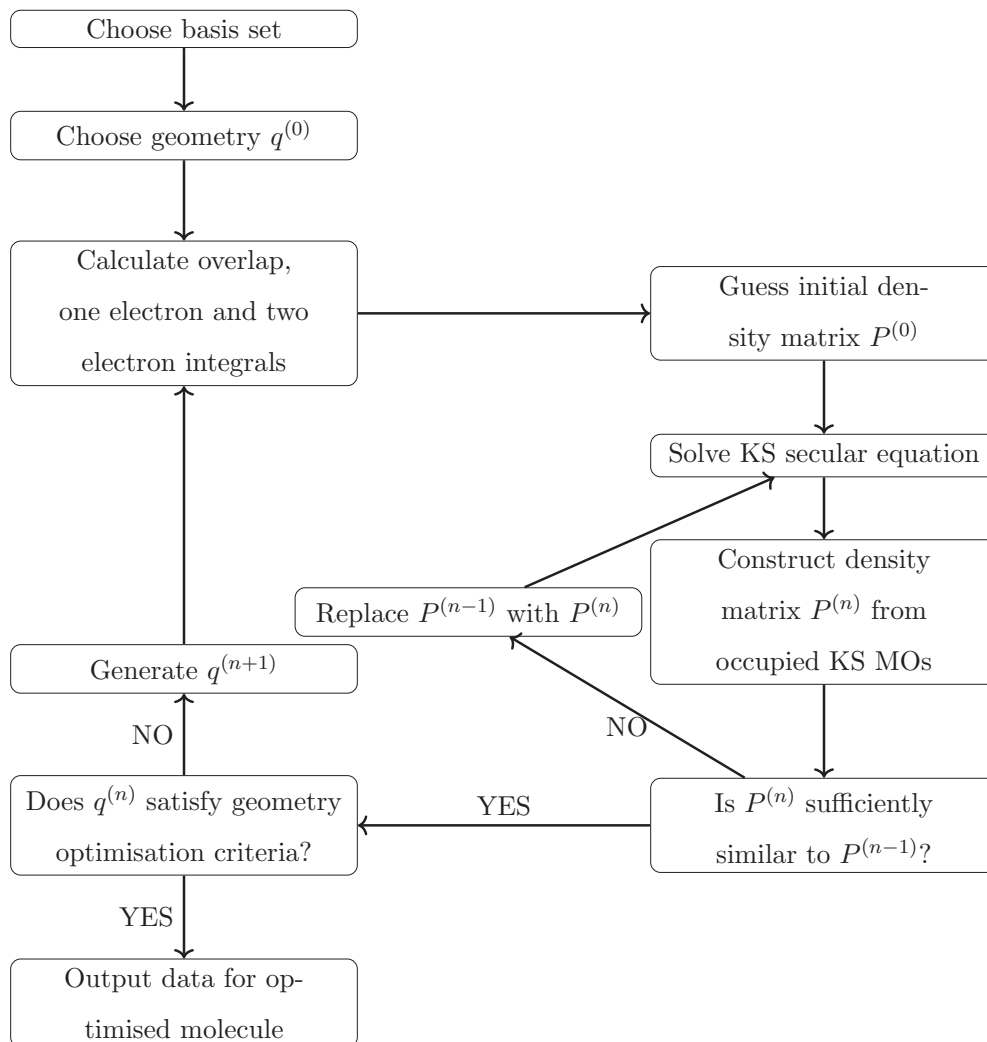
Once a satisfactory density matrix P is achieved the energy is computed directly from the density via Eq. (2.58).

A note on how the LSDA approximation is applied in molecules:

It is not assumed that the electron density is constant across space in the molecule. It is assumed that the ε_{xc} at position $\vec{r}$ in a molecule with electron density ρ is equal to the ε_{xc} in a uniform electron gas of electron density ρ.

Density gradient and kinetic energy density corrections

The LDA approximation can be upgraded by considering not only the electron density at a given point but also its gradient when constructing the correlation functional. This approach is called the GGA (generalised gradient approximation). GGA functionals usually consist of an LDA functional with a corrective terms added on:

$$\varepsilon_{X/C}^{GGA}[\rho(\vec{r})] = \varepsilon_{X/C}^{LSD}[\rho(\vec{r})] + \Delta\varepsilon_{X/C}[\frac{|\nabla\rho(\vec{r})|}{\rho^{\frac{4}{3}}(\vec{r})}] \qquad (2.74)$$

The first widely used GGA exchange functional was B by Becke, which incorporated a single empirical parameter fitted to the exact exchange energies of the noble gases He - Rn. Similar approaches by others produced functionals such as CAM, FT17, O, PW, mPW and X (B and PW combined).

Alternative GGA exchange functionals based on expansions of the reduced gradient include no empirical parameters: B86, LG, P, PBE and mPBE.

GGA correlation functionals following Eq. (2.74) include B88, P86 and P91.

The LYP correlation functional does not improve on an LDA expression but computes the whole correlation energy at once. It contains four empirical parameters fitted to the helium atom. It is the only functional mentioned here with exactly cancels the self-interaction energy in one-electron systems.

Combinations of exchange and correlation functionals to specify a full method are named using the exchange initials followed by the correlation, e.g. BLYP.

Meta-GGA (MGGA) functionals which include dependence on the second derivative of the density (the Laplacian) were proposed for exchange (BR) and correlation (Lap).

The Laplacian was found to be somewhat numerically unstable and an alternative MGGA formalism was conceived; where a dependence on τ is included in the functional. Where τ is the kinetic energy density and ϕ_i are the Kohn-Sham orbitals:

$$\tau(\vec{r}) = \sum_{i}^{occupied} \frac{1}{2}|\nabla\psi_i|^2 \qquad (2.75)$$

MGGA functionals for exchange, correlation, or both are: B95, B98, ISM, KCIS, PKZB, τHCTH, TPSS, VSXC.

Adiabatic connection methods

The adiabatic connection model underlies the widely used modern hybrid functionals, including that used in this work; B3LYP. In this model a dial smoothly increasing the electron-electron interactions from the non-interacting Kohn-Sham reference system to the real system is imagined.

The Hellman-Feynman theorem can be used to show that the E_{xc} can be computed as:

$$E_{xc} = \int_0^1 \langle \Psi(\lambda)|V_{xc}(\lambda)|\Psi(\lambda)\rangle d\lambda \qquad (2.76)$$

where λ is the extent of electron-electron interaction, from 0 (none) to 1 (exact).
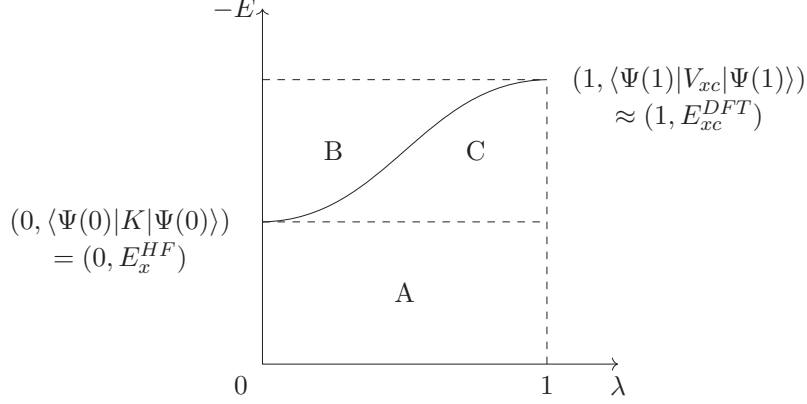
The area under the curve is the integral in Eq. (2.76). We do not know how Ψ and V vary as functions of λ in general, but we can evaluate the left end-point of the curve. In the non-interacting limit V is entirely composed of exchange due to the antisymmetry of the wavefunction. The Slater determinant of Kohn-Shan orbitals is the exact wavefunction for the non-interacting Hamiltonian. Thus $(0, \langle \Psi(0)|K|\Psi(0)\rangle) = E_x^{HF}$, which is the exact HF exchange for the non-interacting system, computed with Kohn-Sham orbitals. If the right hand endpoint of the line is approximately calculated using some DFT functional, giving E_{xc}^{DFT}, a parameterisation approach can be taken to find E_{xc}, the area under the curve:

$$\text{Area of whole square (A + B + C)} = E_{xc}^{DFT} \qquad (2.77)$$

$$\text{Area of A} = E_x^{HF} \qquad (2.78)$$

$$\text{Area of B + C} = E_{xc}^{DFT} - E_x^{HF} \qquad (2.79)$$

$$\text{Area under curve} = E_{xc} = E_x^{HF} + z(E_{xc}^{DFT} - E_x^{HF}) \qquad (2.80)$$

In this formulation z can be varied to improve E_{xc}. Usually this relation is formulated in terms of the parameter a instead:

$$E_{xc} = (1 - a)E_{xc}^{DFT} + aE_x^{HF} \qquad (2.81)$$

This approach (called "hybrid exchange") combined with a GGA correction to

exchange $(b\Delta E_x^B)$ was used to formulate the popular B3LYP functional, along with a similar approach to the correlation component:[2,3]

$$E_{xc}^{B3LYP} = (1-a)E_x^{LSDA} + aE_x^H + b\Delta E_x^B + (1-c)E_c^{LSDA} + cE_c^{LYP} \qquad (2.82)$$

The parameters found to perform best are $a = 0.20$, $b = 0.72$, and $c = 0.81$. The B3LYP functional was chosen for the work in this thesis due to good performance for a relatively inexpensive functional, and also the retained efficacy across a range of organic and inorganic systems.

2.5 Thermodynamic analysis

The DFT calculations reported in this thesis were completed using the Gaussian computational package.[4] This section clarifies the origin of the thermochemical quantities relied upon in the remainder of this work. Several thermochemical quantities are printed directly in the .log file produced by the Gaussian09 program when a frequency calculation is completed, Table 2.1. E_{elec} is the total electronic energy of the system. The zero point energy correction (zpe) is the correction applied to E_{elec} to account for the vibrational effects present at 0 K:

$$E_0 = E_{elec} + \text{zpe} \qquad (2.83)$$

The sum of E_{elec} and zpe is the total energy of the system at 0 K, E_0. To generate thermochemical parameters for standard conditions, 298.15 K and 1 Atm, a further vibrational, rotational and translational correction (E_{vrt}) is required:

$$E = E_0 + E_{vrt} \qquad (2.84)$$

Thermochemical quantity	Relevant Gaussian09[4] string
Electronic energy (E_{elec})	E(UB3LYP)
Zero point energy correction (zpe)	Zero-point correction
Energy (E)	Sum of electronic and thermal Energies
Enthalpy (H)	Sum of electronic and thermal Enthalpies
Gibbs free energy (G)	Sum of electronic and thermal Free Energies

Table 2.1: Thermochemical quantities printed by Gaussian09[4] in frequency .log files.

Enthalpy (H) and Gibbs free energy (G) values at standard conditions may then be calculated by Gaussian09 as follows:

$$H = E + RT \tag{2.85}$$

$$G = H - TS \tag{2.86}$$

where T is temperature, S is entropy, and R is the universal gas constant.

Substituting Eqs. (2.83) to (2.85) into Eq. (2.86) clarifies the individual contributions to G:

$$G = E_{elec} + zpe + E_{vrt} + RT - TS \tag{2.87}$$

For calculations using all-electron basis sets (rather than pseudopotentials) E_{elec} is the largest contribution to G. The other factors (zpe, E_{vrt}, RT and TS) are all 5 or more orders of magnitude smaller.

When comparing the stability of different configurations of a system (e.g. different conformers of a molecule, or atoms arranged into different molecules) the relevant parameter is ΔG, the difference in G between the configurations. From Eq. (2.87) it is apparent that ΔG is split into contributions from ΔE_{elec}, Δzpe, ΔE_{vrt}, and $-T\Delta S$:

$$\Delta G = \Delta E_{elec} + \Delta zpe + \Delta E_{vrt} - T\Delta S \tag{2.88}$$

ΔRT is always zero as RT has the same value for all configurations. E_{elec} is much larger than zpe and $-$TS, however ΔE_{elec} and $-T\Delta S$ are usually of the same order of magnitude, with ΔE_{vrt} and Δzpe making contributions an order of magnitude smaller. The majority of contributions to E_{elec} within a system are due to the interactions among nuclei and core electrons, which are not affected by configurational changes. Therefore ΔE_{elec} values tend to be very small fractions of E_{elec}, but $-T\Delta S$ can be of the same order of magnitude as $-$TS.

Bibliography

[1] C. J. Cramer, *Essentials of computational chemistry*, 2003.

[2] A. D. Becke, *The Journal of Chemical Physics*, 1993, **98**, 5648.

[3] C. Lee, W. Yang and R. G. Parr, *Physical Review B*, 1988, **37**, 785–789.

[4] M. J. Frisch, G. W. Trucks, H. B. Schlegel, G. E. Scuseria, M. A. Robb, J. R.

Cheeseman, G. Scalmani, V. Barone, B. Mennucci, G. A. Petersson, H. Nakatsuji, M. Caricato, X. Li, H. P. Hratchian, A. F. Izmaylov, J. Bloino, G. Zheng, J. L. Sonnenberg, M. Hada, M. Ehara, K. Toyota, R. Fukuda, J. Hasegawa, M. Ishida, T. Nakajima, Y. Honda, O. Kitao, H. Nakai, T. Vreven, J. Montgomery, J. A., J. E. Peralta, F. Ogliaro, M. Bearpark, J. J. Heyd, E. Brothers, K. N. Kudin, V. N. Staroverov, R. Kobayashi, J. Normand, K. Raghavachari, A. Rendell, J. C. Burant, S. S. Iyengar, J. Tomasi, M. Cossi, N. Rega, M. J. Millam, M. Klene, J. E. Knox, J. B. Cross, V. Bakken, C. Adamo, J. Jaramillo, R. Gomperts, R. E. Stratmann, O. Yazyev, A. J. Austin, R. Cammi, C. Pomelli, J. W. Ochterski, R. L. Martin, K. Morokuma, V. G. Zakrzewski, G. A. Voth, P. Salvador, J. J. Dannenberg, S. Dapprich, A. D. Daniels, Ö. Farkas, J. B. Foresman, J. V. Ortiz, J. Cioslowski and D. J. Fox, *Gaussian 09, Revision D.01*, 2009.

Chapter 3

Bismuth halides in ionic liquids

3.1 Introduction

This chapter is a theoretical investigation into recently synthesised bismuth containing HMILs.[1] These liquids are dense, air stable, and thermally stable. The chapter begins with a brief description of the theoretical and experimental methods used, including the parameterisation of an SMD model for the Bi HMIL system. The results and discussion section begins by describing the optimised structures of a range of anions and ion-pairs. The anionic speciation for a range of compositions is then predicted in a computationally inexpensive manner. Finally experimental valence band XPS (unpublished, private communication) and UV-Vis spectra (this work) are compared to theoretical predictions, validating the theoretical methods utilised. The research questions this chapter investigates are:

- What is the anionic speciation of Bi containing HMILs - which anions are present across the range of compositions and halides?

- What is the nature of the anion-cation interactions?

- Can DFT calculations reproduce valence band XPS and colour properties of Bi containing HMILs?

3.2 Theoretical methods

The Gaussian 09 (revision D01) suite of programs was utilised to run all DFT calculations.[2] The functional B3LYP-GD3BJ was selected: Becke's three parameter exchange functional,[3] along with Lee, Yang and Parr's correlation functional,[4] and the

D3 version of Grimme's dispersion correction, with Becke-Johnson damping.[5-7] This functional is relatively inexpensive, widely used, and retains efficacy across organic and inorganic ground state systems. The aug-cc-pVDZ basis sets were applied to H, C, N, and Cl atoms.[8,9] The cc-pVDZ-pp pseudo potentials and aug-cc-pVDZ associated basis sets (including additional diffuse functions) were applied to Br, I and Bi atoms.[10,11] The cc-pVDZ-pp pseudo potentials accurately recover both scalar and spin-orbit relativistic effects.

Optimisation calculations used a pruned (99,590) integration grid, 99 radial shells and 590 points per shell (int=ultrafine). For all calculations an improved SCF convergence criterion was applied (scf=conver=9): Root mean squared change in the elements of the density matrix between consecutive cycles of less than 10^{-9}, maximum density element change of less than 10^{-7}, and an energy change of less than 10^{-7}. Structures were fully optimized and no symmetry constraints were applied. Vibrational analysis confirmed each reported structure as a minimum. MOs visualisations use a standard iso value of 0.02, unless otherwise noted.

To calculate a valence band XPS of $[C_2C_1Im]_2[Bi_2Br_8]$ the optimised cluster was analysed via Mulliken population analysis, which provides the contribution of each basis function or AO to each MO. To calculate the peak generated by the contribution of a single AOs to a single MO the contribution of the AO to the MO is multiplied by the photoionisation cross-section value for that AO.[12] A Gaussian-Lorenztian (70% Gaussian) broadening function is then applied to generate a peak shape. This process was carried out for all AO contributions to each MO, summing all the contributions generated results in a computed valence band XPS.

UV-vis spectra were calculated via TD-DFT (time dependent density functional theory). 10 triplet and 10 singlet excitations were obtained for each conformer. The spectra were generated in Gaussview 5.[13]

3.2.1   Solvation environment

The SMD model was utilised to provide a generalised solvation environment.[14] Solvation models give the free energy of solvation for a solute (the molecule being explicitly considered) from the gas phase to a liquid solution. The SMD model uses certain solvent descriptors which allow customization of the model to include ionic liquid solvents. These are: dielectric constant ϵ, index of refraction n, macroscopic surface tension γ, Abraham hydrogen bond acidity $\Sigma\alpha_2^H$, Abraham hydrogen bond basicity $\Sigma\beta_2^H$, the

fraction of non-hydrogen atoms that are aromatic carbon atoms ϕ, and the fraction of non-hydrogen atoms that are electronegative halogen atoms ψ.

The use of the model for ionic liquids has been tested and detailed by Barnales et al, who also provided experimentally determined solvent descriptor values for twelve ionic liquids.[15] It was found that a version of the model called SMD-GIL (GIL stands for general ionic liquid) also gave accurate results. In SMD-GIL most solvent descriptors are set to the average of the available values for the twelve ionic liquids, but ϕ and ψ are calculated for the particular ionic liquid assigned as the solvent.

For this work solvent descriptors were selected to emulate the ionic liquid $[C_2C_1Im][BiCl_4]$. Experimentally determined descriptors were not available for $[C_2C_1Im][BiCl_4]$ therefore average values were used, or the parameter was calculated. Parameters were set as follows: ϵ, n, and γ use the average values for ionic liquids collated by Bernales et al. (11.5, 1.43, 61.24).[15] ϕ and ψ are simply calculated from the molecular formula (0.231, 0.308). $\Sigma\alpha_2^H$ and $\Sigma\beta_2^H$ were derived computationally. First Kamlet and Taft α and β parameters were generated using a previously published method (0.65, -0.03).[16] These values were then converted into Abraham $\Sigma\alpha_2^H$ and Abraham $\Sigma\beta_2^H$ values via an empirical conversion formula derived from experimental data (0.275, 0.070).[15] Utilising average values for some of the SMD parameters and specifically calculated values for others was termed SMD-PGP (partial generic parameters), and was found to perform similarly to SMD parameterised specifically for the solvent.

The ϵ parameter is important for calculating the bulk electrostatic component of the solvation energy via the PCM (polarized continuum model).[17] The rest of the solvent descriptors are involved in computing the non-bulk-electrostatic component. This component depends on the exposed surface area of the solute atoms. The solvent descriptors contribute to the atomic and molecular surface tensions.

For some systems with flat potential energy surfaces small imaginary frequencies were retained when a solvent continuum model was applied, or the optimisation convergence criteria were not met after optimisation calculations had reached a plateau. In these cases a manual determination of structure convergence was applied, taking into account factors such as the size of the imaginary frequencies, the energy profile of the optimisation, and whether the structure was a confirmed minimum in the gas phase.

3.3 Molecular structure

3.3.1 Monomeric anions

Comprehensive conformational searches were carried out in both the gas phase and IL-SMD on $[BiX_n]^{(3-n)}$, n = 3, 4, 5, 6, X = Cl, Br, I. This section begins with a detailed description of $[BiCl_4]^-$, before continuing to discuss the remaining species.

$[BiCl_4]^-$ was optimised in the gas phase and in solution using the parameterised IL-SMD. In both environments square planar, tetrahedral, sawhorse and trigonal pyramidal starting structures were optimised and all lead to a single stable conformer, see the dashed box in Fig. 3.2. In the gas phase the anion is tetrahedral, with Bi-Cl bond lengths of 2.63Å. This structure results from simple valence pair repulsion as the distance between the negatively charged ligands is maximised in the tetrahedral environment. In the IL-SMD a sawhorse structure was obtained, with axial and equatorial bond lengths of 2.71Å and 2.55Å respectively. The IL-SMD stabilises the charge anisotropy of the sawhorse structure, shown via mapping the ESP (electrostatic potential) to electron density iso-surfaces in Fig. 3.1. Sawhorse $[BiCl_4]^-$ has a dipole moment of 4.08 Debye, whereas the tetrahedral structure has 0 dipole moment. The IL-SMD stabilises higher dipole moment conformations due to the charges located on the cavity surface.

Full conformational searches were undertaken on BiX_3, $[BiX_4]^-$, $[BiX_5]^{2-}$ and $[BiX_6]^{3-}$. For each anion X = Cl, Br and I were investigated. In each case several starting structures were tested: trigonal planar and trigonal pyramidal for BiX_3, square planar, tetrahedral, sawhorse and trigonal pyramidal for $[BiX_4]^-$, trigonal bipyramidal and square based pyramid for $[BiX_5]^{2-}$, and octahedral and trigonal prismatic for
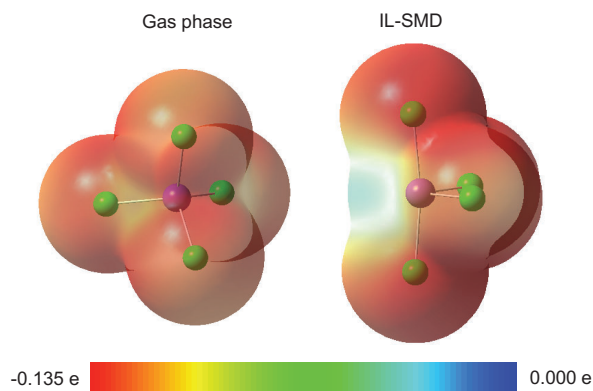
Figure 3.1: ESP values mapped onto the electron density iso-surface ($\rho = 0.0004$ a.u.) of $[BiCl_4]^-$. In the gas phase a tetrahedral conformer is obtained. With the IL-SMD applied the optimised structure is sawhorse.

$[BiX_6]^{3-}$. Where the structures obtained were symmetric small distortions were manually applied to reduce the point group to C_1, and the structures were reoptimised to ensure that this was the lowest energy structure.

In the gas phase exactly one stable conformer was located for every monomeric anion. Highly symmetric structures were obtained (Fig. 3.2): BiX_3 is trigonal pyramidal, C_{3v}, $[BiX_4]^-$ is tetrahedral, T_d, $[BiX_5]^{2-}$, is bipyramidal, D_{3h}, and $[BiX_6]^{3-}$ is octahedral, O_h. Bond lengths increase as the number of halide atoms and therefore the amount of negative charge in the complex increases. Bi-Cl bond lengths increase from 2.47Å in $BiCl_3$ to 2.83Å in $[BiCl_6]^{3-}$. Bond lengths also increase as the halide size increases: Bi-X is 2.63, 2.79, and 3.00Å in $[BiCl_4]^-$, $[BiBr_4]^-$ and $[BiI_4]^-$ respectively.

Anion structures were altered significantly within the IL-SMD environment, Fig. 3.2. BiX_3 (X = Cl, Br, I) retained trigonal pyramidal geometries. $[BiX_6]^{3-}$ remained octahedral, however the geometry is slightly distorted and the O_h point group reduced to C_1. For $[BiX_5]^{2-}$ adding the solvation environment changed the shape of the PES. In the gas phase there is no minimum at the square based pyramid (SBP) geometry, and in the IL-SMD there is no bipyramidal minimum. $[BiI_5]^{2-}$ gives a symmetric square based pyramid, point group C_{4v}. $[BiCl_5]^{2-}$ and $[BiBr_5]^{2-}$ are also square based pyramids but unlike $[BiI_5]^{2-}$ are slightly distorted.

$[BiX_4]^-$ shows the most variation in geometry when the solvation environment and halide are changed. $[BiBr_4]^-$ and $[BiI_4]^-$ have two energetically similar minima in the solvated state: sawhorse, and tetrahedral. Both sawhorse geometries are closer to
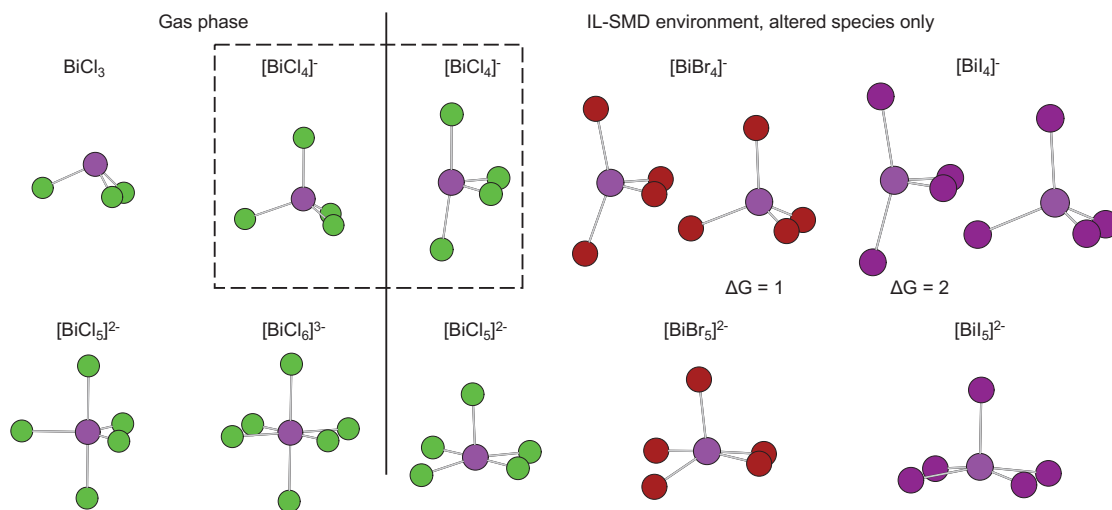
Figure 3.2: The conformers of BiX_3, $[BiX_4]^-$, $[BiX_5]^{2-}$, $[BiX_6]^{3-}$; X = Cl, Br, I. The gas phase conformers where X = Cl are representative of those where X = Br, I. BiX_3 and $[BiX_6]^{3-}$ structures are only shown in the gas phase as the IL-SMD conformers are similar. ΔG values are given in kJ mol^{-1}.

tetrahedral than the $[BiCl_4]^-$ IL-SMD geometry; the axial $X-Bi-X$ angle is $171°$, $151°$, and $156°$ for $X = Cl$, Br, I respectively.

A search of the CSD (Cambridge Structural Database) yielded only di- or poly-meric $[BiX_4]^-$ and $[BiX_5]^{2-}$ structures. However, monomeric $[PCl_4]^-$ and $[PBr_4]^-$ have sawhorse structures, not tetrahedral.[18] $K_2[SbCl_5]$ is a rare example of a group 5 monomeric $[EX_5]^{2-}$ anion, and has SBP geometry, not trigonal bipyramidal.[18] Overall solvated structures are more similar to the crystal structures than gas phase structures.

Mixed halide anions: $[BiX_2Y_2]^-$

Cousens et al. synthesised bismuth ILs with mixed halides in several ratios of Cl, Br and I.[1] Mass spectroscopy detected all permutations of anion for a given combination of halide, i.e. for Cl and Br $[BiCl_4]^-$, $[BiCl_3Br]^-$, $[BiCl_2Br_2]^-$, $[BiClBr_3]^-$ and $[BiBr_4]^-$ were reported.[1]

To investigate the mixed halide anions theoretically a series of three simple anions of the form $[BiX_2Y_2]^-$ was chosen: $[BiCl_2Br_2]^-$, $[BiCl_2I_2]^-$, $[BiBr_2I_2]^-$. Conformational searches in the gas phase and IL-SMD started from four conformers: tetrahedral, sh_small_axial (sawhorse with the smaller halide atom in the axial positions), sh_large_axial (with the larger halide atom in the axial positions) and sh_mixed_axial (with one smaller halide and one larger halide atom in the axial positions).

In the gas phase only tetrahedral conformers were located, Fig. 3.3. With the IL-SMD applied all 3 sawhorse conformers were found to be minima and are within 8 kJ mol^{-1} of one another. The ΔG of $2[BiX_2Y_2]$ vs $[BiX_4]^- + [BiY_4]^-$ was computed and found to be less than 4 kJ mol^{-1} in all cases. Therefore rapid interconversion between both conformers and species is expected in solution.
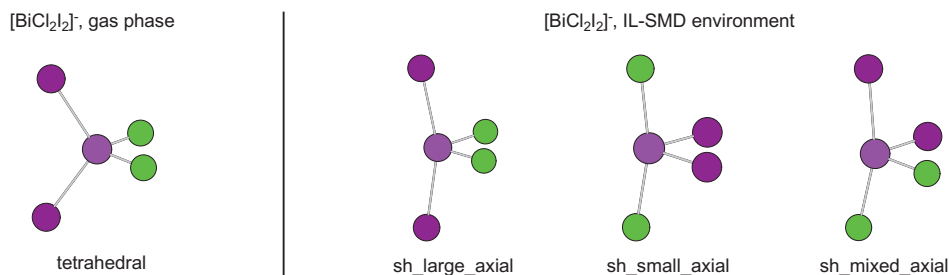
Figure 3.3: Optimised $[BiCl_2I_2]^-$ conformers in the gas phase and with the IL-SMD solvation environment applied. Analogous conformers were located for $[BiCl_2Br_2]^-$ and $[BiBr_2I_2]^-$. Sh in conformer names stands for sawhorse.

3.3.2   Dimeric anions

Three dimeric anions were investigated: $[Bi_2X_7]^-$, $[Bi_2X_8]^{2-}$ and $[Bi_2X_9]^{3-}$ (X = Cl, Br, I). Fig. 3.4 shows an example structure for each conformer located. $[Bi_2Cl_7]^-$ is only present in polymeric form on the CSD.[19] No monomeric group 5 $[E_2X_7]^-$ complexes are known according to comprehensive reviews by Fisher and Norman.[18] From group 3 $[Al_2Cl_7]^-$ is present in Al-Cl halometallate ILs.[20] Isolated $[Bi_2X_8]^{2-}$ is known in both the sbp_sbp_a and sbp_sbp_b forms.[18,19] Isolated $[Bi_2X_9]^{3-}$ has only been reported in the oct_oct conformation.[18,19]

Comprehensive conformational searches were undertaken for $[Bi_2X_7]^-$, $[Bi_2X_8]^{2-}$ and $[Bi_2X_9]^{3-}$ (X = Cl, Br, I). 21, 9, and 8 starting structures were optimised for $[Bi_2X_7]^-$, $[Bi_2X_8]^{2-}$ and $[Bi_2X_9]^{3-}$ respectively, in both gas and IL-SMD environments. The same initial structures were used for X = Cl, Br, I, in both gas and IL-SMD environments. Structures with 1, 2, and 3 bridging halide atoms were included for each species. Conformers with tetrahedral and sawhorse coordination were included where a Bi centre was coordinated by 4 halide atoms. Square based pyramid and bipyramidal coordination were considered for Bi centres surrounded by 5 halide atoms.

The most stable $[Bi_2X_7]^-$ conformer located is sh_sh_a for X = Cl, Br, I in both environments, Fig. 3.4. a., Table 3.1. Sh_sh_a has a single bridging X atom, and both Bi atoms are in sawhorse configurations. sh_sh_b and sh_sh_c are similar conformers, with different relative orientations of the two sawhorse moieties. sh_sh_b is located for each environment/halide combination except for X = Cl in the IL-SMD environment. ΔG values of below 5 kJ mol^{-1} were obtained in every case. The sh_sh_c conformer was only found for X = I in IL-SMD solvation. Sh_sbp, a conformer with two bridging X atoms, one Bi atom in a sawhorse conformation and the other in a square based pyramidal coordination pattern, was found for each environment/halide combination except for X = I in the gas phase. ΔG values of below 12 kJ mol^{-1} were obtained in every case. A further, higher energy conformer, sbp_sbp, was obtained for X = Cl in both

Conformer	Cl		Br		I	
	Gas	IL-SMD	Gas	IL-SMD	Gas	IL-SMD
Sh_sh_a	0	0	0	0	0	0
Sh_sh_b	5	-	4	5	2	4
Sh_sh_c	-	-	-	-	-	33
Sh_sbp	4	7	3	12	-	12
Sbp_sbp	37	24	35	-	-	-

Table 3.1: Relative Gibbs free energies (ΔG in kJ mol^{-1}) of $[Bi_2X_7]^-$ conformers (X = Cl, Br, I), in the gas phase and with IL-SMD applied.

a. [Bi₂X₇]⁻ conformers

sh_sh_a   sh_sh_b   sh_sh_c

sh_sbp   sbp_sbp

b. [Bi₂X₈]²⁻ conformers

sbp_sbp_a   sbp_sbp_b   sbp_sbp_c

oct_sbp   sbp_bipy

c. [Bi₂X₉]³⁻ conformer
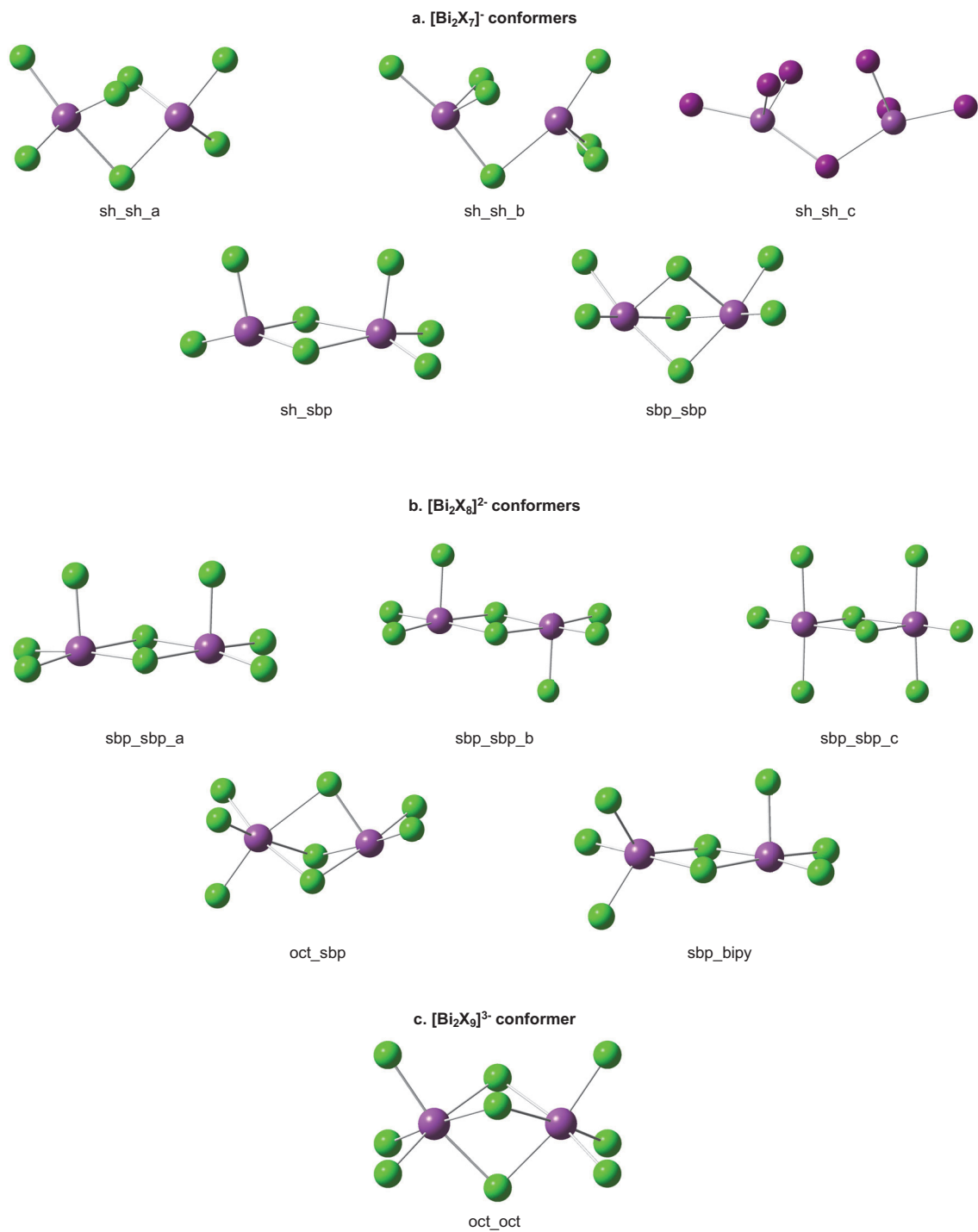
oct_oct

Figure 3.4: Conformers of $[Bi_2Cl_7]^-$, $[Bi_2Cl_8]^{2-}$ and $[Bi_2Cl_9]^{3-}$. In conformer names the following abbreviations are used: sh = sawhorse, sbp = square based pyramid, oct = octahedral, and bipy = bipyramidal.

environments and for X = Br in the gas phase.

Al based HMILs are highly studied and have a main group metal in the +3 oxidation state, making them a useful comparison to Bi based HMILs. In Al-based HMILs $[Al_2Cl_7]^-$ forms, an analogous anion to $[Bi_2X_7]^-$.[21] A crystal structure of $[Al_2Cl_7]^-$ in solid $[Te_4][Al_2Cl_7]_2$ has been published.[22] The $[Al_2Cl_7]^-$ structure is most similar to the sh_sh_a conformer located in the bismuth anions, however the Al centres are tetrahedrally coordinated rather than sawhorse.

The most stable $[Bi_2X_8]^{2-}$ conformer is oct_sbp across environments and halides, except for X = Br in SMD, Fig. 3.4. b., Table 3.2. The oct_sbp conformer has 3 bridging halides. One Bi atom is octahedrally coordinated and the other is coordinated in a square based pyramid position. As far as we are aware the oct_sbp structure has not been reported in the literature for group 5 metal halide anions. For X = Cl in the IL-SMD four further conformers are located, including the sbp_sbp_a (also found for X = Br in IL-SMD) and sbp_sbp_b, both of which are reported in $[Bi_2X_8]^{2-}$ crystal structures.[18,19].

A single conformer, oct_oct, was located for $[Bi_2X_9]^{3-}$, Fig. 3.4. c. The structure has 3 bridging X atoms, and both Bi atoms are octahedrally coordinated. The oct_oct structure is found in crystal structures of $[Bi_2X_9]^{3-}$.[18,19] The most stable $[Bi_2X_8]^{2-}$ conformer oct_sbp is essentially the $[Bi_2X_9]^{3-}$ oct_oct structure with a vacancy at one of the terminal positions. The most stable $[Bi_2X_7]^-$ conformers sh_sh_a and sh_sh_b are also close to oct_oct structures, but with two terminal positions vacant.

Similarly to the monomeric species bond lengths are increased as more halides are added to a structure. The shortest Bi-Cl lengths in $[Bi_2Cl_7]^-$ and $[Bi_2Cl_9]^{3-}$ are 2.52 and 2.63Å respectively. Again larger halides also increase bond lengths, the shortest Bi-I length in $[Bi_2I_9]^{3-}$ is 3.04Å. A wide variation in bond lengths is found within structures - terminal bonds being much shorter than bridging contacts. In $[Bi_2Br_8]^{2-}$, sbp_sbp_e the shortest bond length is 2.71Å and the longest is 3.07Å.

| | Cl | | Br | | I | |
Conformer	Gas	IL-SMD	Gas	IL-SMD	Gas	IL-SMD
Oct_sbp	0	0	0	-	0	0
Sbp_sbp_a	-	10	-	0	-	-
Sbp_sbp_b	-	4	-	-	-	-
Sbp_bipy	-	13	-	-	-	-
Sbp_sbp_c	-	48	-	-	-	32

Table 3.2: Relative Gibbs free energies (ΔG in kJ mol^{-1}) of $[Bi_2X_8]^{2-}$ conformers (X = Cl, Br, I), in the gas phase and with IL-SMD applied.

3.3.3 Neutral ion clusters

[C$_2$C$_1$Im]Cl

A conformational search was carried out for the ion pair [C$_2$C$_1$Im]Cl. Optimisations in the gas phase and with the IL-SMD applied were began with the Cl$^-$ ion in seven positions around the [C$_2$C$_1$Im]$^+$ cation: front_me, front, front_eth, side_eth, back, side_me, and top. (See Fig. 3.5 for position naming scheme and optimised conformers.)

In the gas phase stable minima were obtained for all positions except for the front position, matching the results of previous studies on [C$_4$C$_1$Im]Cl.[23,24] Rotating the ethyl group and reoptimising revealed two further top conformers. The front_me and front_eth contain the shortest Cl$---$H contacts; a H-bond between Cl and the C^2 H atom forms in both cases. The Cl$^-$ is situated such that a secondary interaction with an alkyl H atom may also form. The front_me and front_eth conformers are the most stable, followed by the three top conformers, then the side conformers, then the back conformer.

With an IL-SMD environment applied the energy ordering of conformers is preserved but compressed, Fig. 3.5. In contrast to the two gas phase front structures which contain two Cl$---$H interactions in the IL-SMD only one front conformer was located, with a single H-bond to the C^2 H atom. No top conformer was optimised in the IL-SMD environment; all attempts at optimising the three gas phase top structures gave only the front conformer with the IL-SMD applied.

[C$_2$C$_1$Im][BiCl$_4$]

A detailed conformational search on [C$_2$C$_1$Im][BiCl$_4$] was carried out. Initial test optimisations begun with tetrahedral and sawhorse [BiCl$_4$]$^-$ always resulted in sawhorse [BiCl$_4$]$^-$, the shape obtained for the lone anion in the IL-SMD environment. The presence of either [C$_2$C$_1$Im]$^+$ or the IL-SMD solvation environment produces sawhorse [BiCl$_4$]$^-$, whereas a tetrahedral conformer is located for the lone anion in the gas phase. This result indicates that the IL-SMD environment reproduces the effect of an explicit cation on [BiCl$_4$]$^-$.

53 starting structures with sawhorse [BiCl$_4$]$^-$ were optimised in the gas phase and in the IL-SMD environment. The conformers located for [C$_2$C$_1$Im]Cl were used as the basis for drawing the input structures. Structures with one Cl atom in the front (17), front_me (7), front_eth (7), side_me (4), side_eth (4), and top (3) positions were included, as were 5 structures with the whole anion in the top position as opposed to a single Cl atom. Structures with axial Cl atoms and structures with equatorial Cl atoms in the key

a. Front conformers

Gas phase

front_me | front_eth

2.65 Å | 1.95 Å

0 | 0

SMD

front

2.30 Å

0

b. Top conformers

Gas phase

top_a | top_b | top_c

5 | 6 | 8

SMD

c. Side conformers

Gas phase | SMD

side_eth | side_me | side_eth | side_me

33 | 35 | 15 | 17

d. Back conformers

Gas phase | SMD

back | back

56 | 18
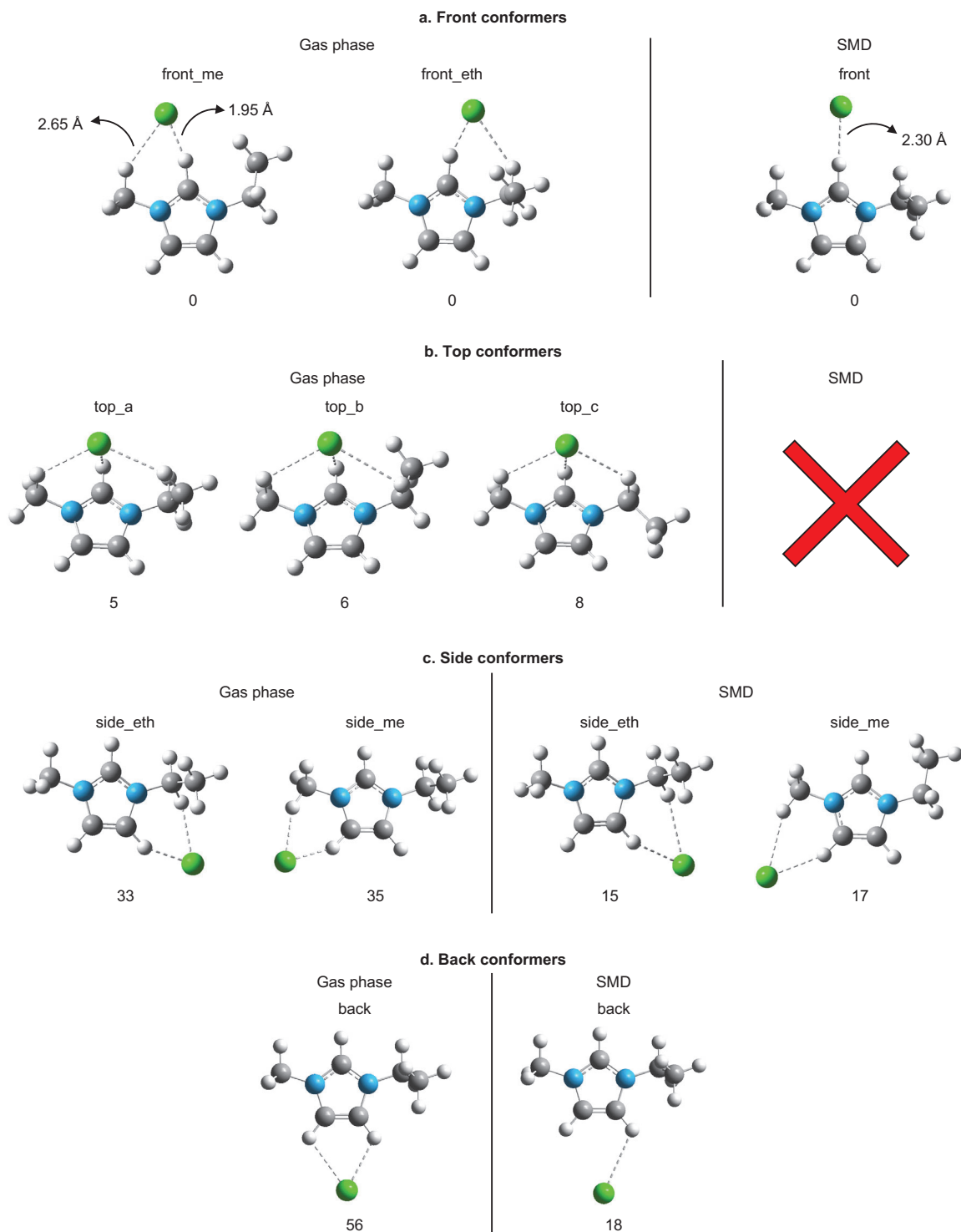
Figure 3.5: Gas phase and IL-SMD optimised conformers of $[C_2C_1Im]Cl$. $Cl---H$ contacts of less than 3 Å are indicated by dashed bonds. The ΔG values are given below each conformer in kJ mol^{-1}.

position were included. Various anion orientations and ethyl group rotations were also explored for each group of starting structures. Although a large number of starting structures have been examined it is unlikely that all potential energy surface minima

have been located, due to the complexity of the system. Instead, a representative sample of structures has been produced by the conformational search procedure. It is expected that any additional minima will only have small ΔG values relative to the identified structures.

In the gas phase the 53 optimisations yielded 8 conformers, all with ΔG values 10 kJ mol^{-1} of the most stable structure, Fig. 3.6. The conformers are named with a letter indicating their relative stability; a for the lowest energy structure, b for the second lowest and so on. Secondly the Cl atom closest to one of the positions defined for $[C_2C_1Im]Cl$ is considered: if that Cl atom is in an axial position this is denoted by "ax", or equatorial by "eq". The conformer name a_ax_front_me therefore indicates the lowest energy structure which has an axial Cl atom in the front_me position. If none of the Cl atoms are positioned closely to a defined position the ax or eq identifier is absent and the position identifier refers to the placement of the entire anion. For example conformers f to h are simply "back" conformers as the entire anion is toward the back of the ring but no individual Cl atom occupies a position defined by the $[C_2C_1Im]Cl$ conformers.

The four lowest energy gas phase conformers all have Cl atoms in the front_me or front_eth positions. None of the structures contain Cl atoms in the front, side, or back positions. All have one Cl atom close to the top position but further away from the ring
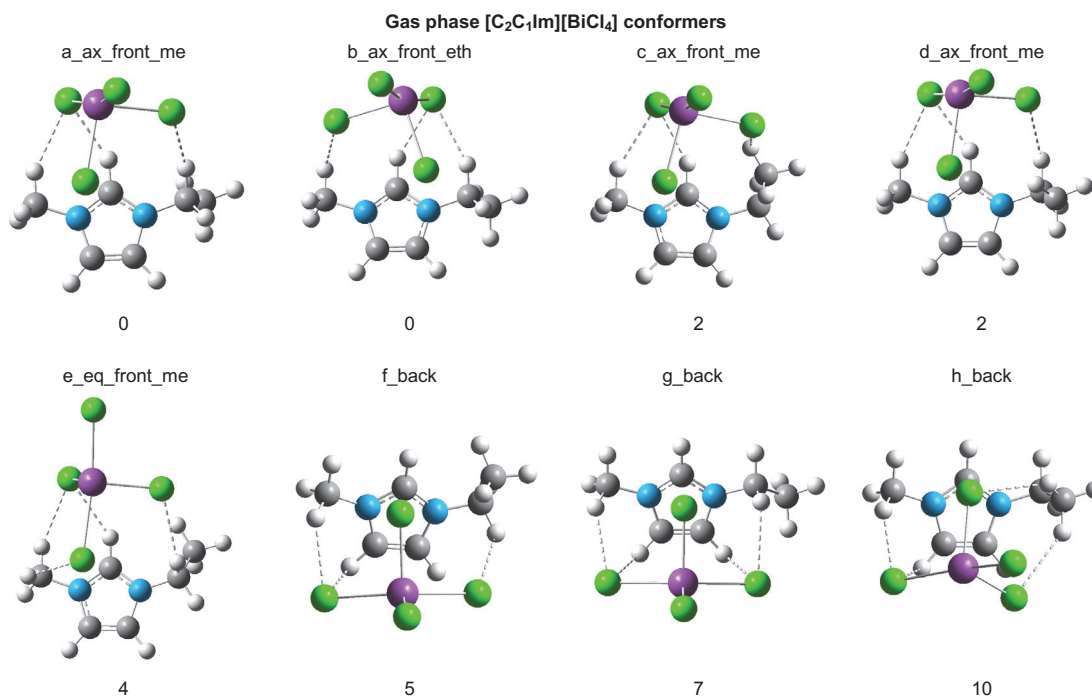
Figure 3.6: Gas phase $[C_2C_1Im][BiCl_4]$ conformers, with ΔG values in kJ mol^{-1} below each structure. Cl−−−H contacts of less than 3 Å are indicated by dashed bonds.

115

than seen in $[C_2C_1Im]Cl$. Short $Cl---H$ contacts are common; every structure has either three or four below 3 Å. (3 Å is the sum of the Van der Waals radii of Cl and H.) The shortest contacts are $Cl---H-C^2$ interactions, the shortest in all the conformers is found in c_ax_front_me at 2.32 Å. The $Bi-Cl$ bond length is significantly increased by the interaction, it is 2.80 Å. The $Bi-Cl$ bond length is 2.59 Å for the other axial Cl atom which is oriented away from the cation, and therefore does not interact with the cation.

With the IL-SMD environment applied optimisation of the same 53 intial structures led to 17 minima, all within 14 kJ mol^{-1}, and 15 within 10 kJ mol^{-1} of the most stable conformer, Fig. 3.7. Wider structural variation is observed in the IL-SMD conformers; the four most stable conformers are of ax_front_eth, back, and eq_front_me types whereas the four most stable gas phase conformers are all ax_front_eth and ax_front_me. Similarly to the gas phase structures most contain a Cl atom close to the top position observed for $[C_2C_1Im]Cl$, but further from the imidazolium ring. As in the gas phase no conformer contains Cl atoms in the side or back positions. Unlike the gas phase two conformers were located with Cl atoms in the front position. $Cl---H$ contacts below 3 Å are found in every structure; one conformer (j_ax_front_me) has four short contacts, four conformers have three, seven have two, and five have only one. None of the gas phase conformers have fewer than three short $Cl---H$ contacts. The $Cl---H$ distances are generally longer with the IL-SMD applied; the conformer h_ax_front_me is analogous to the gas phase conformer c_ax_front_me, and has a $Cl---H-C^2$ length of 2.56 Å (2.32 Å in the gas phase). In contrast to the gas phase the $Bi-Cl$ length is unaffected by the $Cl---H-C^2$ interaction; with the IL-SMD applied the $Bi-Cl$ distance is 2.75 Å for both the H-bonding and non-interacting axial Cl atoms.

$[C_2C_1Im][BiX_4]$

The 17 $[C_2C_1Im][BiCl_4]$ IL-SMD conformers located were optimised in the IL-SMD environment with the Cl atoms replaced by Br and I atoms. This is a limited survey compared to the 53 structures optimised for $[C_2C_1Im][BiCl_4]$, and many more conformers likely exist, yet the structures obtained allow analysis into how changing the halide affects the cation-anion interactions. Six $[C_2C_1Im][BiBr_4]$ conformers (within 7 kJ mol^{-1}) and seven $[C_2C_1Im][BiI_4]$ conformers (within 10 kJ mol^{-1}) were located, Figs. 3.8 and 3.9.

Conformers of the type ax_front_me were found for both $[C_2C_1Im][BiBr_4]$ and $[C_2C_1Im][BiI_4]$. This allows a direct comparison across the series $[C_2C_1Im][BiCl_4]$,

a_ax_front_eth

0

b_back

0

c_back

1

d_eq_front_me

3

d_ax_front

3

e_back

5

f_back

5

g_eq_front_me

6

h_ax_front_me

7

i_eq_front_eth

7

j_ax_front_me

7

k_ax_front_eth

8

l_eq_front_eth

10

m_top

10

n_back

10

o_top

11

p_ax_front

14
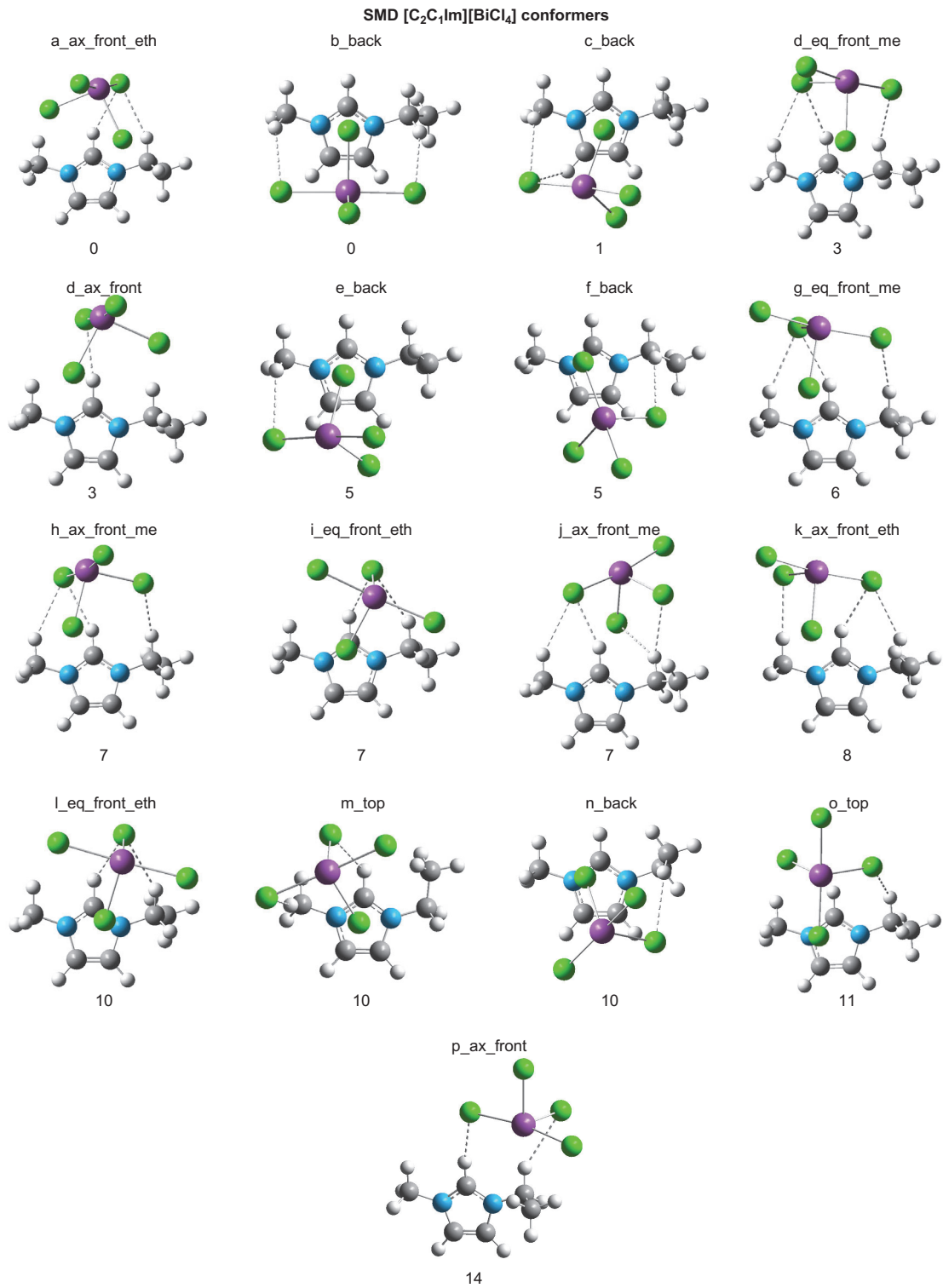
Figure 3.7: IL-SMD [C$_2$C$_1$Im][BiCl$_4$] conformers, with ΔG values in kJ mol^{-1} below each structure. Cl−−−H contacts of less than 3 Å are indicated by dashed bonds.
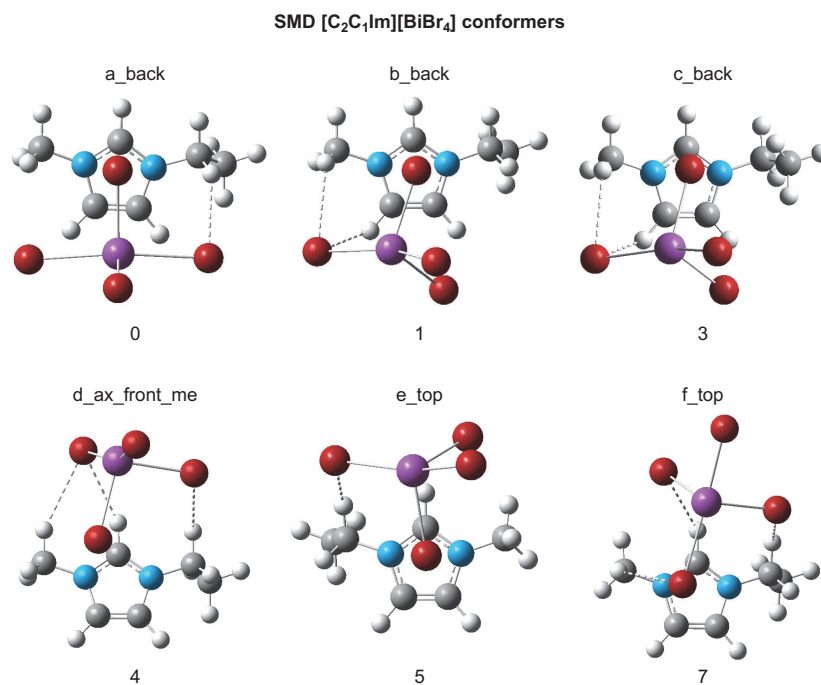
Figure 3.8: IL-SMD [C$_2$C$_1$Im][BiBr$_4$] conformers, with ΔG values in kJ mol^{-1} below each structure. Br$---$H contacts of less than 3.1 Å are indicated by dashed bonds.
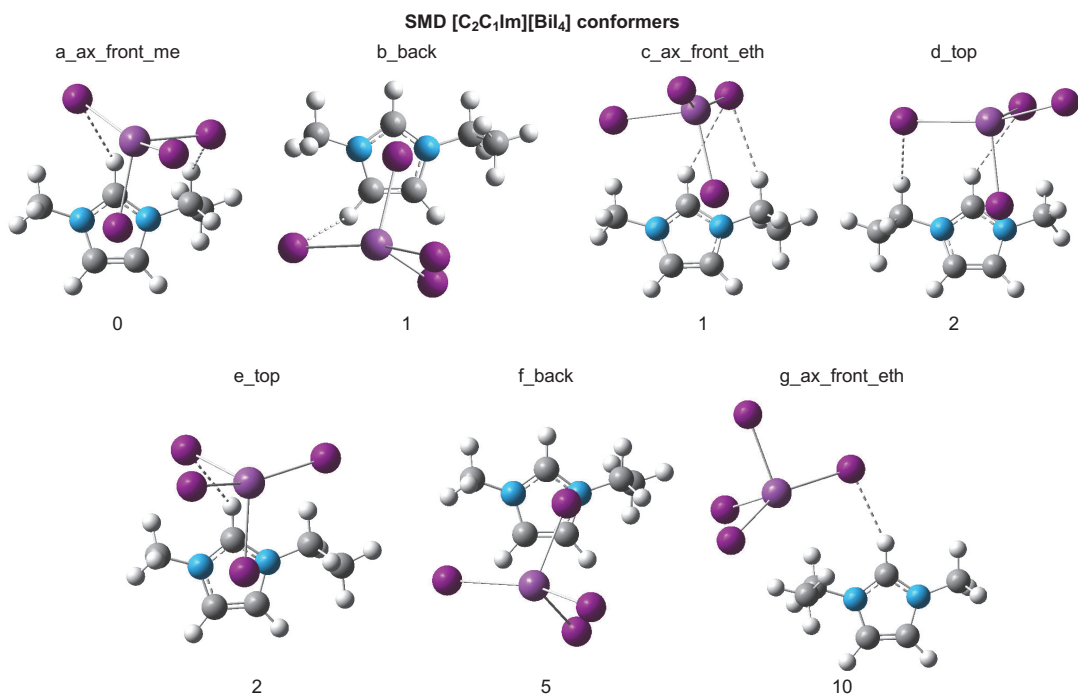
Figure 3.9: IL-SMD [C$_2$C$_1$Im][BiI$_4$] conformers, with ΔG values in kJ mol^{-1} below each structure. I$---$H contacts of less than 3.2 Å are indicated by dashed bonds.

$[C_2C_1Im][BiBr_4]$, $[C_2C_1Im][BiI_4]$. The H-bonding between X and the C^2 H atom was investigated for the series of ax_front_me structures, Table 3.3. The $Cl----H-C^2$ length increases with the size of halide. The $Cl----H-C^2$ length as a proportion of the sum of the Van der Waals radii of X and H also increases with halide size, indicating a reduced H-bonding interaction from Cl to Br to I. This follows the trend of reducing electronegativity down group seven. The shape of the anion is sawhorse in all cases but the axial $X-Bi-X$ angle decreases slightly across the across the series, as observed for the lone anions with SMD applied.

Similarly to the $[C_2C_1Im][BiCl_4]$ conformers most of the $[C_2C_1Im][BiBr_4]$ and $[C_2C_1Im][BiI_4]$ structures have one halide atom close to the top position, and none have halides in the side or back positions. All but one (X = I) conformer contain short $X---H$ contacts.

$[C_2C_1Im][Bi_2Cl_7]$

The dimeric anion $[M_2X_7]^-$ is known to form in HMILs containing Al, Ga and Fe chlorides.[25] A conformational search was carried out on the analogous ion pair $[C_2C_1im][Bi_2Cl_7]$. The starting points were the 8 $[C_2C_1Im]Cl$ gas phase conformers. In each case the Cl was replaced by either a bridging or terminal Cl atom in the $[Bi_2Cl_7]^-$ anion. The anion conformer used was sh_sh_a, as this was the most stable conformer located in the lone anion conformer search. The anion was then oriented either away or towards the cation. This process yielded 8 x 2 x 2 = 32 starting structures. In the gas phase 20 minima were confirmed, and six had ΔG values below 15 kJ mol^{-1}, Fig. 3.10. The three most stable conformers have Cl atom in the positions most favourable for bifurcated H-bonding with the cation, the front_eth and front_me positions. As with the $[C_2C_1Im][BiX_4]$ structures no low energy conformer contains Cl atoms in the side positions. The eq_front_eth conformers (e and f) have an interesting structure where one of the Bi atoms is over the centre of the ring. The Bi atom is in an octahedral

X	$X----H-C^2$	% of $\Sigma(VdW)$	$Bi-X---H$	$Bi-X$	$\Delta(Bi-X)$	$\angle X-Bi-X$
Cl (Gas)	2.32	79	2.80	2.59	0.21	164
Cl (SMD)	2.56	87	2.75	2.68	0.07	170
Br (SMD)	2.77	91	2.91	2.82	0.09	159
I (SMD)	3.13	98	3.13	3.07	0.06	156

Table 3.3: Structural parameters in $[C_2C_1Im][BiX_4]$ ax_front_me conformers. Bond distances are given in Å, and bond angles in degrees. "% of $\Sigma(VdW)$" is the $X---H-C^2$ distance as a percentage of the sum of the Van der Waals radii of X and H. "$\Delta(Bi-X)$" is the difference between the H-bonding and non H-bonding axial $Bi-X$ bond lengths.

Gas phase [C$_2$C$_1$Im][Bi$_2$Cl$_7$] conformers

a_ax_front_eth

0

b_ax_front_me

5

c_ax_front_me

6

d_top

12

e_eq_front_eth

13

f_ eq_front_eth

14

SMD [C$_2$C$_1$Im][Bi$_2$Cl$_7$] conformers

a_ax_front

0

b_top

3

c_back

7

f_bridge_side_eth

16
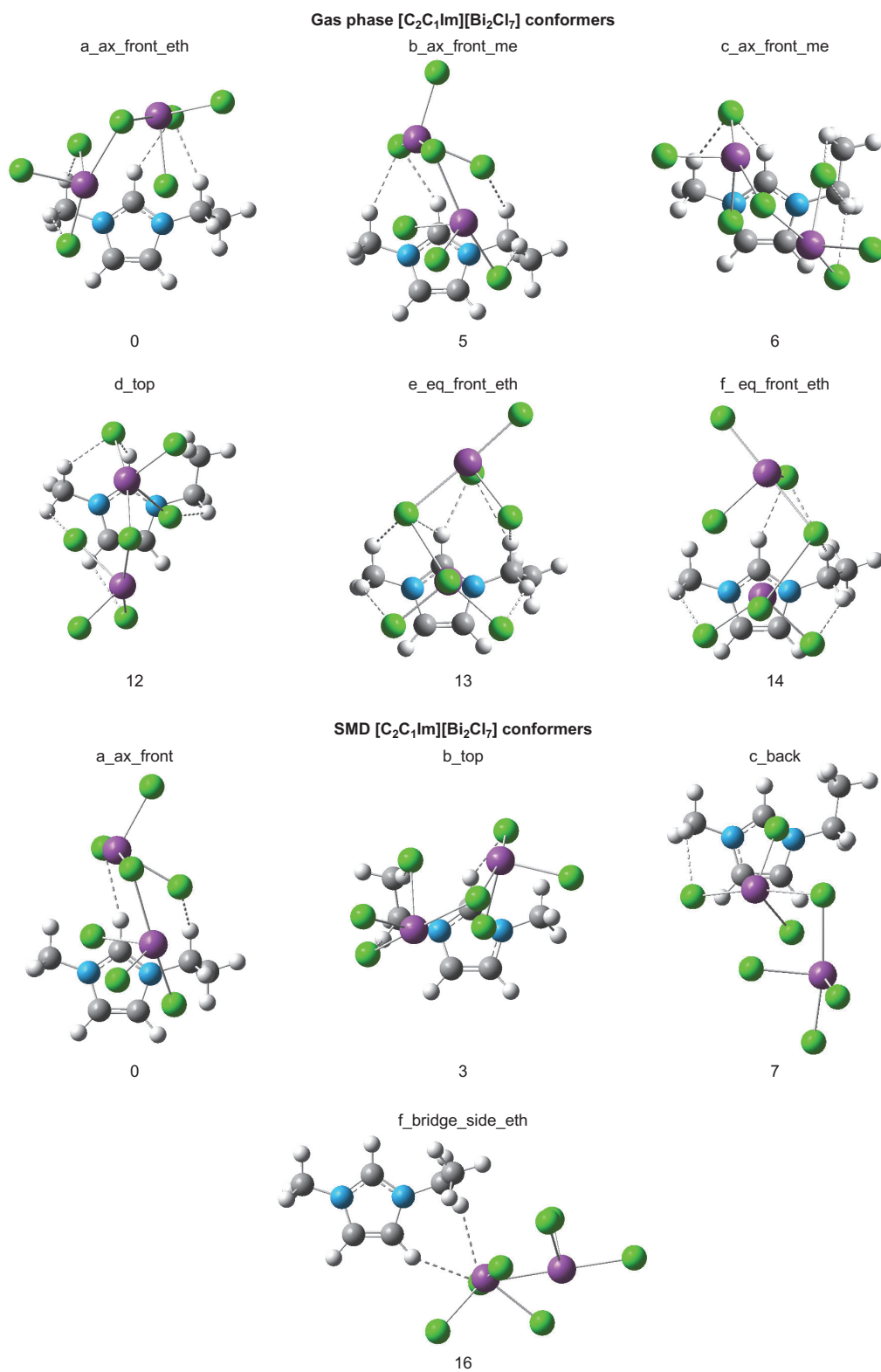
Figure 3.10: Gas phase and IL-SMD [C$_2$C$_1$Im][Bi$_2$Cl$_7$] conformers, with ΔG values in kJ mol^{-1} below each structure. Cl−−−H contacts of less than 3.0 Å are indicated by dashed bonds.

environment with five Cl atoms and the imidazolium ring coordinating it.

In the IL-SMD four conformers were located, all with ΔG values below 17 kJ mol^{-1}. None of the conformers in the IL-SMD match any of the gas phase conformers. Fewer short contacts between Cl and H atoms were found in the IL-SMD conformers. H-bonding still impacts energy ordering; the two most stable conformers contain short contacts between a Cl atom and the $C^{2-}H$ atom.

$[C_2C_1Im]_2[Bi_2Cl_8]$

A conformational study was performed on the charge neutral cluster $[C_2C_1im]_2[Bi_2Cl_8]$. The three most stable $[Bi_2Cl_8]^{2-}$ conformers (sbp_sbp_a, sbp_sbp_b and sbp_oct) were included in the initial structures as well as various combinations of cation positions and orientations around the anion. Although a wide range of initial structures were optimised (24 in total), due to the size and complexity of the cluster it is likely that not all possible conformers were obtained. The conformational searches completed on the previous ion pairs have shown that conformers are generally close together in energy and show similar anion-cation interactions, MOs and NBO charges. Therefore we assume that the $[C_2C_1Im]_2[Bi_2Cl_8]$ conformers located (Fig. 3.11) are a representative sample of structures.

18 gas phase (11 with ΔG below 20 kJ mol^{-1}) and 12 IL-SMD (11 with ΔG below 20 kJ mol^{-1}) conformers were located. Fig. 3.11 shows the six most stable conformers in each environment. In both environments conformers with sbp_sbp_a, sbp_sbp_b and sbp_oct anions were all among the minima located. The most stable conformer is similar between the gas phase and IL-SMD environments, and has an sbp_sbp_b anion. In the gas phase the axial Cl atoms are in front_eth positions and have short contacts with H atoms. In the IL-SMD the cations are rotated slightly such that the axial Cl atoms are out of the plane of the ring and have no short contacts with H atoms.

3.3.4   Association energy

Applying the IL-SMD model is a good approximation to the solvation environment of these liquids and is able to recover the anion-cation interactions well. In the gas phase the association energy ($G_{ionpair}$ - [G_{cation} + G_{anion}]) is 270 kJmol^{-1} for $[C_2C_1Im][BiCl_4]$. This large value, common in ionic liquids, is representative of the strong Coulombic cation-anion interactions. With IL-SMD the association energy of $[C_2C_1Im][BiCl_4]$ is very low at -1 kJ mol^{-1}, Table 3.4. In this case the association energy is not a direct

Gas phase [C₂C₁Im]₂[Bi₂Cl₈] conformers

a_sbp_sbp_b

0

b_ sbp_sbp_b

9

c_ sbp_sbp_b

9

d_eq_oct_sbp

14

e_ sbp_sbp_a

16

f_sbp_sbp_a

17

SMD [C₂C₁Im]₂[Bi₂Cl₈] conformers

a_ sbp_sbp_b

0

b_oct_sbp

6

c_ sbp_sbp_b

8

d_oct_sbp

9

e_oct_sbp

10

f_oct_sbp

11
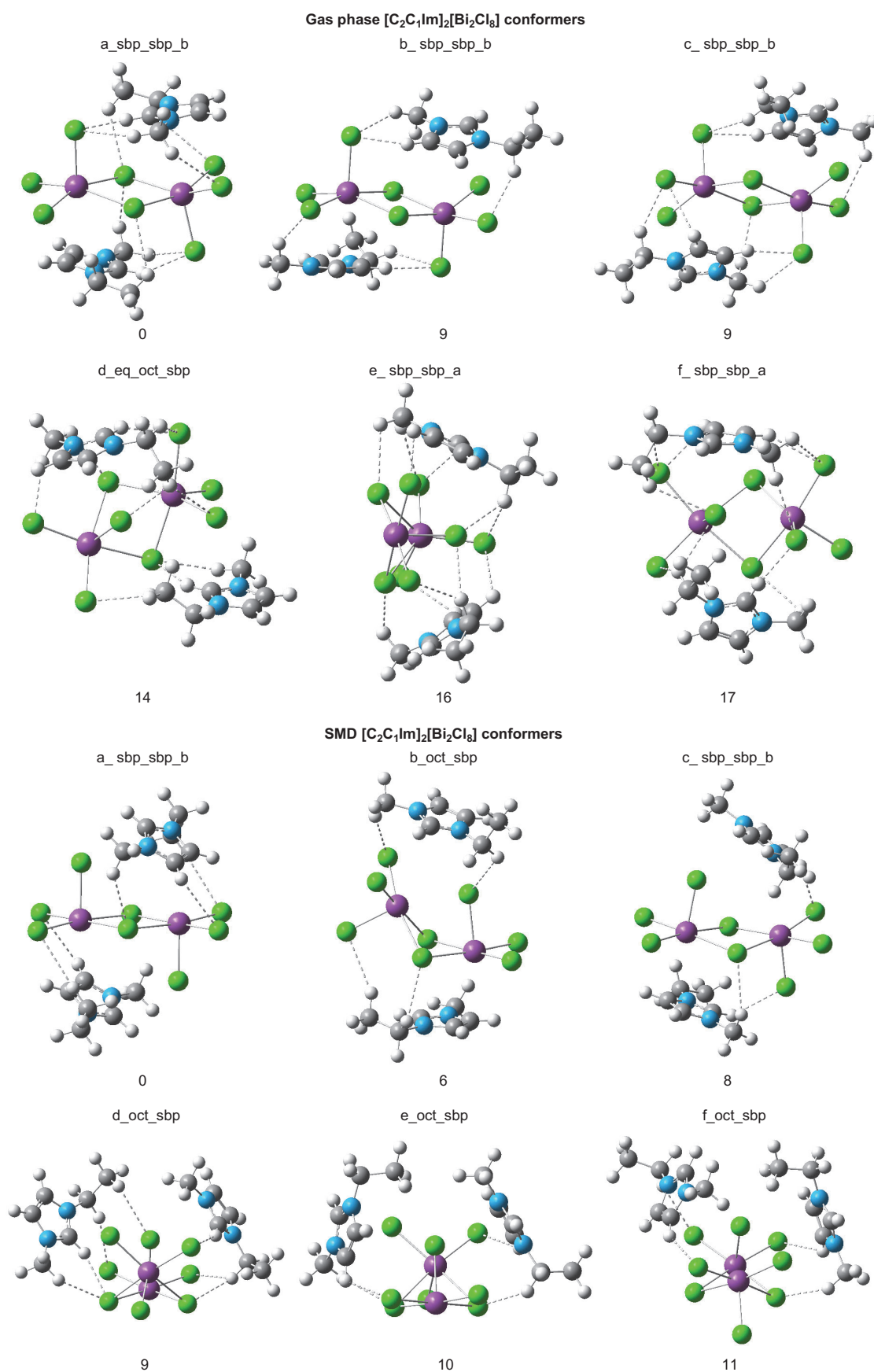
Figure 3.11: Gas phase and IL-SMD $[C_2C_1Im]_2[Bi_2Cl_8]$ conformers, with ΔG values in kJ mol^{-1} below each structure. Cl−−−H contacts of less than 3.0 Å are indicated by dashed bonds.

Ion pair	Association energy/kJ mol^{-1}
$[C_2C_1Im]Cl$	16
$[C_2C_1Im][BiCl_4]$	-1
$[C_2C_1Im][BiBr_4]$	-2
$[C_2C_1Im][BiI_4]$	10
$[C_2C_1Im]_2[Bi_2Cl_8]$	21

Table 3.4: Association energies in the ionic liquid IL-SMD are very low.

measure of the absolute strength of the anion-cation interaction. Instead, see Fig. 3.12, the energy value represents the difference between the IL-SMD modelled interaction (lone ions) and explicit interaction (ionpair).

Low IL-SMD association energies were calculated for a range of ionpairs, Table 3.4. The low values mean that the IL-SMD environment is reproducing the explicit anion-cation interactions well. Since the IL-SMD model only produces generalised, Coulombic interactions we conclude that these are the key interactions present in the liquid. Specific interactions such as H-bonds therefore are not making a significant contribution to the association of ions in solution.

The low association energies found for a range of ionpairs in the IL-SMD environment allow us to assume that results from lone pairs in an IL-SMD environment will approximate those from ionpair calculations. Thus we have a computationally viable method to investigate the anionic speciation of these liquids via a large survey of anionic species in an IL-SMD environment.
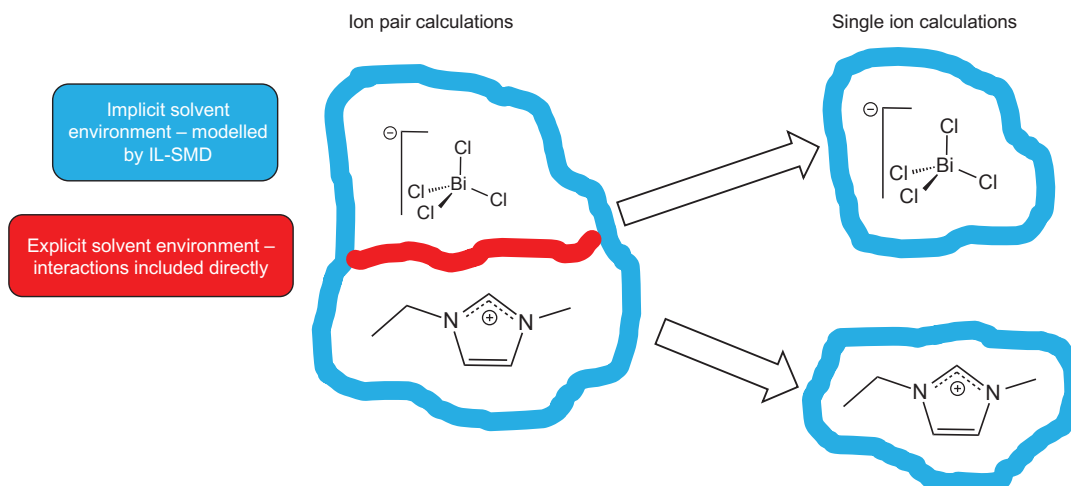
Figure 3.12: Association energy gives a measure of the effectiveness of the IL-SMD at replicating anion-cation interactions.

3.3.5 Anionic speciation

In order to gain insight into which anionic species may be present, four specific mole fractions (χ_{BiCl_3}) of bismuth halide have been studied, and the relative energies of different combinations of anions were compared. The results for all four ratios are summarised in Fig. 3.13, and are compared with the well know speciation profile of $[C_4C_1Im]Cl-AlCl_3$.[26] For a ratio of components $x[C_2C_1Im]Cl + yBiCl_3$, e.g. $2[C_2C_1Im]Cl + 1BiCl_3$:

$$\chi_{BiCl_3} = \frac{y}{x+y} = \frac{1}{1+2} \approx 0.33$$

At the basic χ_{BiCl_3} of 0.67 both Bi and Al have a single predominant species in solution, $[M_2X_7]^-$. In the bismuth systems this anion persists at the neutral 0.5 χ_{BiCl_3}, and is joined by 4 other anions, however for aluminium $[Al_2Cl_7]^-$ is completely replaced by $[AlCl_4]^-$ only. X^- and $[MX_4]^-$ are formed at a χ_{BiCl_3} of 0.33 in both systems. In the Al system no other anions are observed, in contrast to the 5 species in equilibrium in the Bi IL.

To obtain the speciation outlined in Fig. 3.13 a range of species were first optimised, with the IL-SMD model applied: Bi^{3+}, $[BiX]^{2+}$, $[BiX_2]^+$, BiX_3, $[BiX_4]^-$, $[BiX_5]^{2-}$, $[BiX_6]^{3-}$, $[Bi_2X_7]^-$, $[Bi_2X_8]^{2-}$, $[Bi_2X_9]^{3-}$, X^-. $X = Cl$, Br, I. Two of the IL-SMD parameters were derived from calculations on $[C_2C_1Im][BiCl_4]$, which may be slightly different than those corresponding to clusters containing the other halides. An error introduced by this is likely to be small as small changes in SMD parameters have
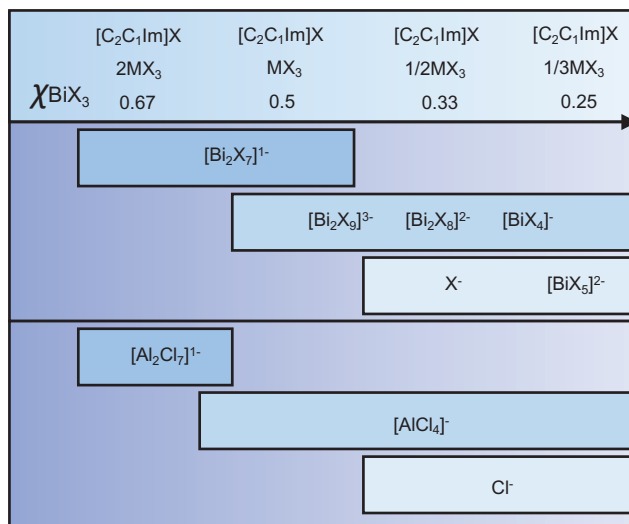
Figure 3.13: Calculated speciation of $[C_2C_1Im]X-BiX_3$, compared to literature values for the speciation of $[C_4C_1Im]Cl-AlCl_3$ taken from Estager et al.[25]

an insignificant effect on the results. For three ratios of $[C_2C_1Im]Cl$ to $BiCl_3$ the energy of every possible combination of the bismuth halide species listed was calculated. Only the combinations with energies low enough to be accessible at room temperature are included in the tables. The largest calculated IL-SMD association energy is 21 kJ mol^{-1} for $[C_2C_1Im]_2[Bi_2Cl_8]$. This value is an indication of the accuracy of the lone ion approximation to ion pairs. We therefore set the threshold for inclusion of a system at 30 kJ mol^{-1}. Any system below this value potentially has a high concentration in solution. The combinations containing cationic bismuth halide species were all very high in energy at every ratio and therefore are not included in the discussion.

The simplest system is 1:1 $[C_2C_1Im]Cl : BiCl_3$, $\chi_{BiCl_3} = 0.5$. To synthesise this system $[C_2C_1Im]Cl$ and $BiCl_3$ are combined in equal parts. Reactive dissolution occurs: the Cl^- combines with the $BiCl_3$ to form $[BiCl_4]^-$, as shown in reaction A, Fig. 3.14. Two $[BiCl_4]^-$ anions may then combine to form $[Bi_2Cl_8]^{2-}$, reaction B.

The relative Gibbs free energies (ΔG) for each system are shown in Fig. 3.14. The system of 2 individual species $BiCl_3 + Cl$ has a large ΔG (ΔG_1 in Fig. 3.14) so is not expected to be present in solution. $0.5[Bi_2Cl_8]^{2-}$ is the lowest energy species so it becomes the reference species with a ΔG_3 of 0 and will be the predominant species.

A variety of reactions are possible in the solution and an equilibrium of different anionic systems is formed, Fig. 3.15. The lower the ΔG of a system the higher its proportion in the ionic liquid. (In Fig. 3.15 the stoichiometry of the reactions is doubled compared to Fig. 3.14, therefore the ΔG values are also doubled.) Table 3.5 summarises the ΔG values of the systems in equilibrium for X = Cl, Br, I. To demonstrate the process used to obtain the values in Tables 3.5 to 3.7, Eq. (3.1) gives the calculation used to generate the value in the "Cl" column, and "$0.25[Bi_2X_7]^- + 0.25[Bi_2X_9]^{3-}$" row of Table 3.5.
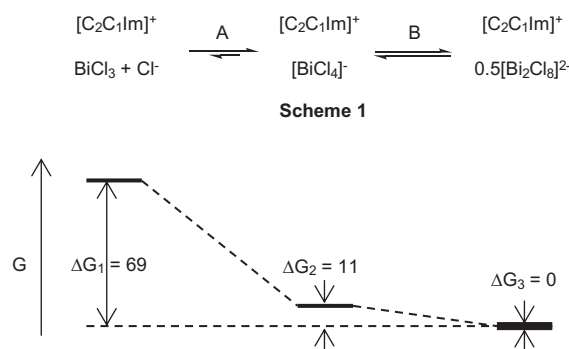
Figure 3.14: The synthesis of $[C_2C_1Im][BiCl_4]$, and the associated Gibbs free energy plot.
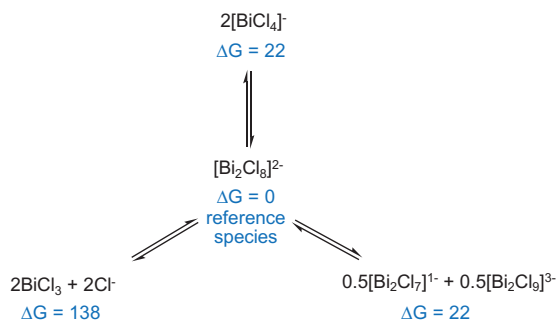
Figure 3.15: The equilibria between various anionic systems present in χ_{BiCl_3} 0.5.

$$\Delta\text{G}(0.25\,[\text{Bi}_2\text{Cl}_7]^- + 0.25\,[\text{Bi}_2\text{Cl}_9]^{3-})$$

$$= \text{G}(0.25\,[\text{Bi}_2\text{Cl}_7]^- + 0.25\,[\text{Bi}_2\text{Cl}_9]^{3-}) - \text{G}(0.5\,[\text{Bi}_2\text{Cl}_8]^{2-}) \tag{3.1}$$

The results (Table 3.5) at χ_{BiCl_3} 0.5 are similar for each halide. Four species are stable in solution: $0.5\,[\text{Bi}_2\text{X}_8]^{2-}$ (predominant species), $[\text{BiX}_4]^-$, $[\text{Bi}_2\text{X}_7]^-$ and $[\text{Bi}_2\text{X}_9]^{3-}$. At this ratio we do not see free halide in the stable systems.

$[\text{C}_2\text{C}_1\text{Im}]\text{X} : \text{BiX}_3$	Cl	Br	I
$[\text{BiX}_3] + \text{X}^-$	69	80	49
$[\text{BiX}_4]^-$	11	2	11
$0.5\,[\text{Bi}_2\text{X}_8]^{2-}$	0	0	0
$0.25\,[\text{Bi}_2\text{X}_7]^- + 0.25\,[\text{Bi}_2\text{X}_9]^{3-}$	11	16	5

Table 3.5: ΔG (relative Gibbs free energy) in kJ mol^{-1} of lowest energy anionic systems in 1:1 $[\text{C}_2\text{C}_1\text{Im}]\text{Cl}$: BiCl_3

If more BiX_3 is added 1:2 $[\text{C}_2\text{C}_1\text{Im}]\text{X} : \text{BiX}_3$, m$\chi_{BiCl_3}$ 0.66 is created. At this "acidic" ratio $[\text{Bi}_2\text{X}_7]^-$ predominates for all X, see Table 3.6 A small amount of dissociation into $\text{BiX}_3 + [\text{BiX}_4]^-$ or $\text{BiX}_3 + 0.5\,[\text{Bi}_2\text{X}_8]^{2-}$ may occur, especially for X = Cl. Similarly to the 1:1 ratio no free halide is expected to form.

$[\text{C}_2\text{C}_1\text{Im}]\text{X} : 2\,\text{BiX}_3$	Cl	Br	I
$[\text{Bi}_2\text{X}_7]^-$	0	0	0
$\text{BiX}_3 + [\text{BiX}_4]^-$	19	29	34
$\text{BiX}_3 + 0.5\,[\text{Bi}_2\text{X}_8]^{2-}$	14	28	29

Table 3.6: ΔG (relative Gibbs free energy) in kJ mol^{-1} of lowest energy anionic systems in 1:2 $[\text{C}_2\text{C}_1\text{Im}]\text{Cl}$: BiCl_3

Adding *less* BiX_3 gives the "basic" ratio 2:1 $[\text{C}_2\text{C}_1\text{Im}]\text{X} : \text{BiX}_3$, Table 3.7. The results are broadly similar across the halides, and free X^- is stable for all X. For X = Br six anionic systems have very similar energies, <6 kJ mol^{-1} apart. Therefore an

equilibrium is expected between all six systems, which include five anions: X^-, $[BiBr_5]^{2-}$, $[Bi_2Br_9]^{3-}$, $[Bi_2Br_8]^{2-}$ and $[BiBr_4]^-$. For $X = I$ the only difference is the relatively high energy of $[BiI_5]^{2-}$; at 25 kJ mol^{-1} this species may still be present but likely in a lower proportion than for $X = Br$. With $X = Cl$ only the system $2\,[BiX_4]^- + 2\,X^-$ has an increased energy at 17 kJ mol^{-1}, however since both anions are also included in lower energy systems all five anions are likely to be present in solution.

Decreasing the χ_{BiCl_3} of BiX_3 further to 0.25 effectively increases the number of X^- ions in the stoichiometry. Each anionic system in Table 3.7 ($\chi_{BiCl_3}n = 0.33$) has an additional $2\ X^-$ ions added at $\chi_{BiCl_3} = 0.25$. For example $2\,[BiX_5]^{2-}$ becomes $2\,[BiX_5]^{2-} + 2\ X^-$. As $2\ X^-$ anions are added to every system in equilibrium the relative energies of the systems remain the same. Therefore the same five anions are expected to be in solution at $\chi_{BiCl_3} = 0.25$ as $\chi_{BiCl_3} = 0.33$, with a larger proportion of free halide ions present than at $\chi_{BiCl_3} = 0.25$.

$4\,[C_2C_1Im]X : 2\,BiX_3$	Cl	Br	I
$2\,[BiX_5]^{2-}$	5	0	25
$[Bi_2X_9]^{3-} + X^-$	0	6	0
$[Bi_2X_8]^{2-} + 2\,X^-$	5	1	0
$2\,[BiX_4]^- + 2\,X^-$	17	2	11
$0.5\,[Bi_2X_8]^{2-} + 0.5\,[Bi_2X_9]^{3-} + 1.5\,X^-$	3	3	0
$[BiX_4]^- + 0.5\,[Bi_2X_9]^{3-} + 1.5\,X^-$	8	4	6

Table 3.7: ΔG (relative Gibbs free energy) in kJ mol^{-1} of lowest energy anionic systems in 2:1 $[C_2C_1Im]Cl$: $BiCl_3$

3.4 Halide exchange mechanism

When mixed halide Bi HMILs were synthesised mass spectroscopy and UV-vis measurements indicate that anions with each possible combination of mixed halides occur, i.e. for the HMIL $[C_2C_1Im]Cl + BiBr_3$ results corresponding to Cl only anions, Br only anions and species with mixed halide coordination were reported. This indicates that halide exchange between anions is continuous in solution. To model this process the following equilibrium has been investigated:

$$[BiCl_4]^- + [BiBr_4]^- \rightleftharpoons [BiCl_3Br]^- + [BiClBr_3]^-$$
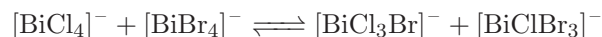
A dissociative mechanism for this process can be conceived:

$$[BiCl_4]^- + [BiBr_4]^- \rightleftharpoons BiCl_3 + Cl + BiBr_3 + Br \rightleftharpoons [BiCl_3Br]^- + [BiClBr_3]^-$$

However in the preceding study on speciation it was concluded that in 1:1 $[C_2C_1Im]Cl:BiX_3$ the lowest energy anionic species are $[Bi_2X_8]^{2-}$ and $[BiX_4]^-$, and the species X^- and BiX_3 are high in energy. Therefore an associative mechanism is proposed, whereby two $[BiX_4]^-$ come together to form $[Bi_2X_8]^{2-}$ and then disassociate back into four coordinate species having exchanged a pair of halide atoms:

$$[BiCl_4]^- + [BiBr_4]^- \rightleftharpoons [Bi_2Cl_4Br_4]^{2-} \rightleftharpoons [BiCl_3Br]^- + [BiClBr_3]^-$$

Relaxed scans were performed to investigate this mechanism. In a relaxed scan the parameter scanned (e.g. the distance between two atoms) is changed by a set amount each step. At each step the remaining geometric parameters are optimised. A simple example of a PES (potential energy surface) formed by two parameters is shown in Fig. 3.16.a. Green contour lines indicate low energies and red lines indicate high energies. Starting at the lower left of Fig. 3.16.a. a relaxed scan of parameter A is carried out. The first (leftmost) black dot is the optimised intial structure which is at a local minimum in both parameter A and parameter B. To get to the second black dot parameter A is incremented by a set amount, and parameter B is optimised, reaching a local minimum in parameter B. This process continues, producing minor variations in parameter B at each point, and a smooth energy profile, Fig. 3.16.b. At the blue arrow a large change in parameter B is required to reach an energy minimum, creating a discontinuity in the energy profile. After the discontinuity the scan continues and a local minima in both A and B is reached. In Fig. 3.16.c. a relaxed scan in the opposite direction results in a different pathway between the two minima. A discontinuity also occurs in the energy profile of the backwards scan, Fig. 3.16.d. Plotting both the forwards and backwards scans on a single energy profile (Fig. 3.16.e.) shows the difference the effect of scan direction on the energy profile. This type of behaviour can be due to multiple PESs crossing and coupling thus there are multiple surfaces the molecule can track along. The accessibility of the lower energy surface from the higher energy surface dictates the presence of discontinuities in the scan.

Due to the requirement for a geometry optimisation at each step relaxed scans are computationally expensive. In choosing an appropriate method both the number of optimisation steps necessary and the cost of each step were taken into account. A gas phase method without dispersion correction was chosen (B3LYP) in order to avoid the flattening of the PES which occurs when SMD and dispersion corrections are applied; this flattening effect is undesirable in a scan as the number of optimisation steps required

Discontinuites and PES crossing regions in relaxed scans

a. Scanning parameter A **forwards**, parameter B is optimised

PES formed by parameter A and B, low energy regions are green, high energy regions are purple.

Parameter B

Parameter A

b. Scanning parameter A **backwards**, parameter B is optimised

Parameter B

Parameter A

c. Scanning parameter A **forwards**, energy profile contains discontinuity

Energy

Parameter A

d. Scanning parameter A **backwards**, energy profile contains discontinuity

Energy

Parameter A

e. Forwards and **backwards** scans superimposed

Energy

Parameter A

PES crossing regions contain discontinuities and the energy profile is dependent upon the direction of the scan, and the precise part of the PES explored.

Figure 3.16: Relaxed scans in a PES crossing region.

at each point are significantly increased. Quantitative accuracy is compromised by choosing this method, but productive investigation into the qualitative features of the reaction pathway is possible. The basis sets used were 6-311G(d,p) for H, C, N, and Cl.[27] Stuttgart pseudo potentials, and the corresponding basis sets were utilised for Bi (ECP78MWB) and Br (ECP28MWB) atoms.[28]

Initially an anion only model was used. $[BiCl_4]^-$ and $[BiBr_4]^-$ were optimised separately, giving tetrahedral structures. A relaxed scan started at structure a. with the two tetrahedral anions set with Bi atoms 9.5 Å apart, Fig. 3.17. The Bi-Bi distance was reduced by 0.1 Å each step, initially the energy steadily increases as the anions approach, with a trigonal plane on each anion oriented towards the other anion. Fig. 3.17. Between b. and c. a discontinuity occurs where the $[BiBr_4]^-$ anion rotates so that one Br atom forms a bridge between the two Bi atoms. The Cl–Bi–Br angle then decreases from c. to e. with a transition state at d. A frequency calculation at d. confirmed the point as a transition state, the red arrows indicate the primary atom translations of the imaginary frequency. The magnitude of the imaginary frequency is low, at -10 cm^{-1}. At e. a minimum energy point corresponding to the sbp_sbp_b conformer of $[Bi_2Cl_4Br_4]^{2-}$ was reached. From structure e. a new relaxed scan increasing the Bi–Bi distance was carried out. An equivalent transition state to that at point d. on the inwards scan was located on the outwards scan at point f. Similarly to point d. the imaginary frequency at point f. is small at -16 cm^{-1}. The energy decreases gradually from the transition state to point g. where a discontinuity occurs as the molecule switches from the single bridging atom surface to the planes surface.

The lowest energy $[C_2C_1Im]_2[Bi_2Cl_8]$ SMD conformer was altered to $[C_2C_1Im]_2[Bi_2Cl_4Br_4]$ and optimised. A relaxed scan was performed, in which the Bi–Bi distance was increased by 0.1 Å per step, Fig. 3.18. Point c. was confirmed as a transition state via a frequency analysis which found a single negative frequency of -20 cm^{-1}. The negative frequency corresponds to the same atom movement as found in the anion only system. The Bi atoms are coordinated in a sawhorse fashion rather the tetrahedral shape observed in the anion only model. After the transition state at point c. a discontinuity in the energy profile is generated by a rotation of the $[BiCl_3Br]^-$ anion. From point d. onwards the anion orientations are different from those observed in the anion only model. Between structure e. and f. a further discontinuity occurs, corresponding to the rotation of both anions such that the equatorial halides face inwards towards the opposite anion. Overall the results indicate that halide exchange
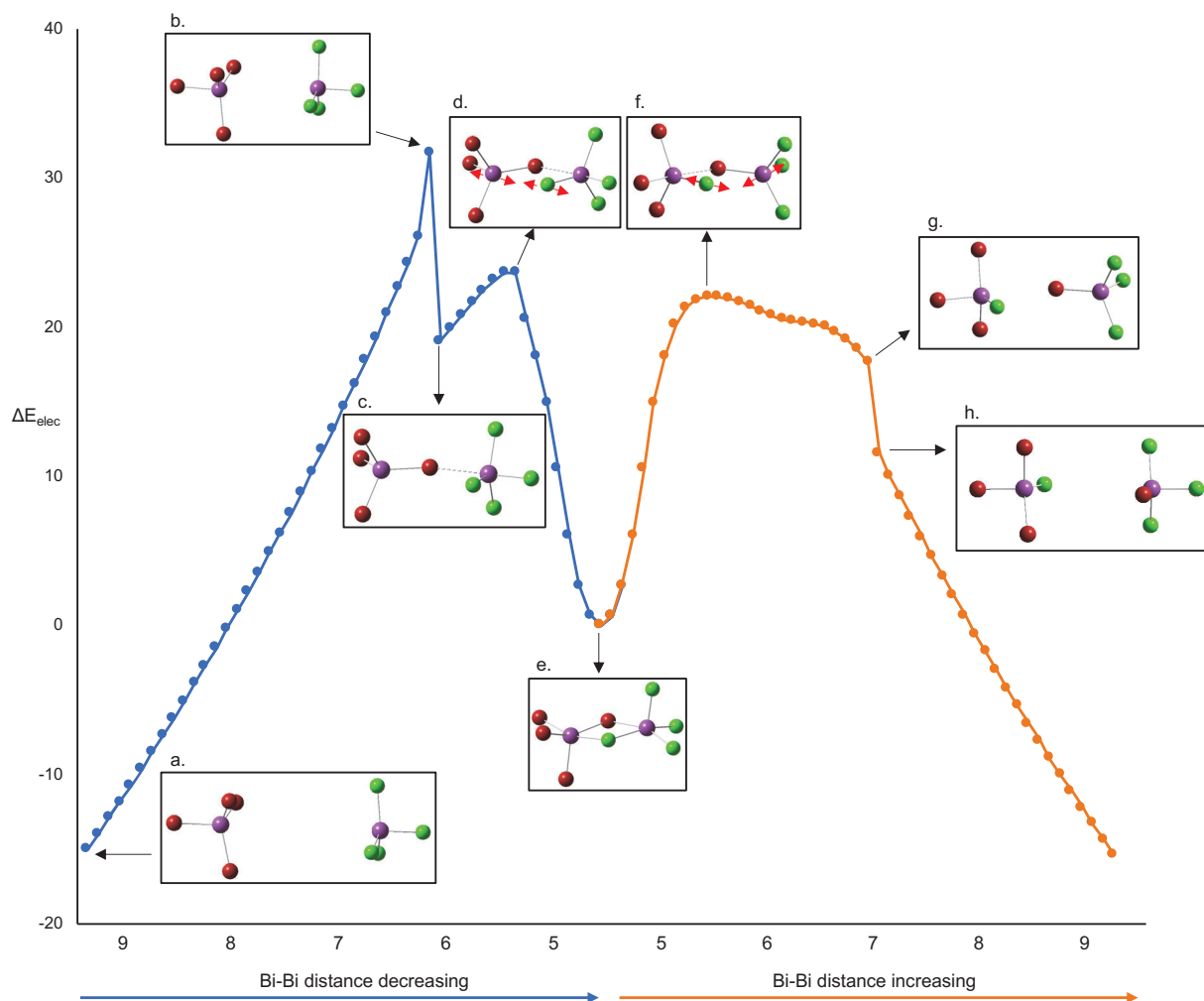
Figure 3.17: Relaxed scans of $[BiCl_4]^- + [BiBr_4]^- \longrightarrow [Bi_2Cl_4Br_4]^{2-}$ and $[Bi_2Cl_4Br_4]^{2-} \longrightarrow [BiCl_3Br]^- + [BiClBr_3]^-$. Energy values are in kJ mol^{-1}
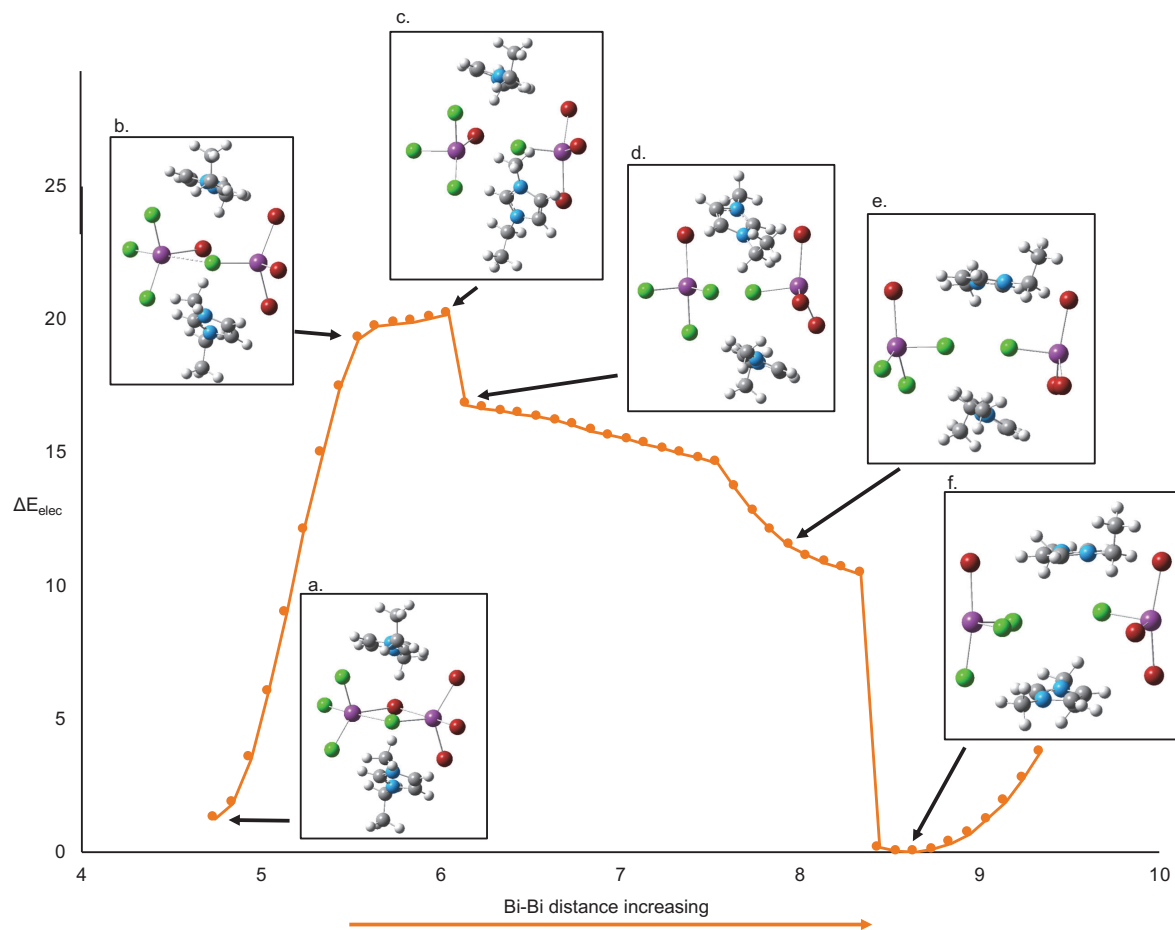
Figure 3.18: Relaxed scans of $[BiCl_4]^- + [BiBr_4]^- \longrightarrow [Bi_2Cl_4Br_4]^{2-}$ and $[Bi_2Cl_4Br_4]^{2-} \longrightarrow [BiCl_3Br]^- + [BiClBr_3]^-$. Energy values are in kJ mol^{-1}

between anions via dimerisation is facile with a barrier of approximately 20 kJ mol^{-1}. Cation coordination did not significantly affect the reaction barrier or transition state geometry, indicating weak cation-anion interactions.

In this section anion structure, anion-cation cluster structure, anion speciation and halide exchange have been investigated. In the following section the electronic structure of anions and cation-anion clusters will be analysed. Concluding remarks on the work presented over the full chapter will be made at the end of the chapter.

3.5 Results and discussion - electronic structure

3.5.1 XPS valence band spectra

Valence band XPS probes the electronic structure of ionic liquids.[29,30] Core level XPS were published in the work concerning the initial synthesis of bismuth HMILs.[1] Valence band XPS experiments were also carried out, and the unpublished spectrum of [C$_2$C$_1$Im][BiBr$_4$] (Fig. 3.19) was provided via private communication. Full experimental details are provided in the published work.[1]

The calculated spectrum has been systematically shifted and normalised to match the position and height of peak one in the experimental data. The peak shape is closely matched to that in the experimental spectrum, as is the shape, position and intensity of the second peak. In the experimental data the background level begins to increase near the third peak, partially obscuring peaks 3 and 4. The match between experimental and theoretical data is still clearly visible for both peaks, although the relative position of peak 4 in the calculated spectrum has drifted slightly away from the experimental peak.

The calculated spectrum is overall a good match to the experimental data which allows use of the calculated contributions of orbitals to assign the experimental peaks, Fig. 3.19. The first two peaks are dominated by Br 4p orbitals, with a small Bi 5d contribution. The third peak is a combination of Bi 6s and Br 4p MOs, and the fourth can be assigned to Br 4s MOs.

3.5.2 Synthesis and experimental UV-vis

To investigate the effect of halide selection on the electronic properties of bismuth ILs a series of ILs was synthesised: [C$_4$C$_1$Im][BiCl$_4$], [C$_4$C$_1$Im][BiCl$_2$Br$_2$], [C$_4$C$_1$Im][BiBr$_4$], [C$_4$C$_1$Im][BiCl$_2$I$_2$], [C$_4$C$_1$Im][BiBr$_2$I$_2$], [C$_4$C$_1$Im][BiI$_4$]. Each IL was synthesised in a 1:1 molar ratio with [C$_4$C$_1$Im][Tf$_2$N] in order to reduce the viscosity of the liquids produced.
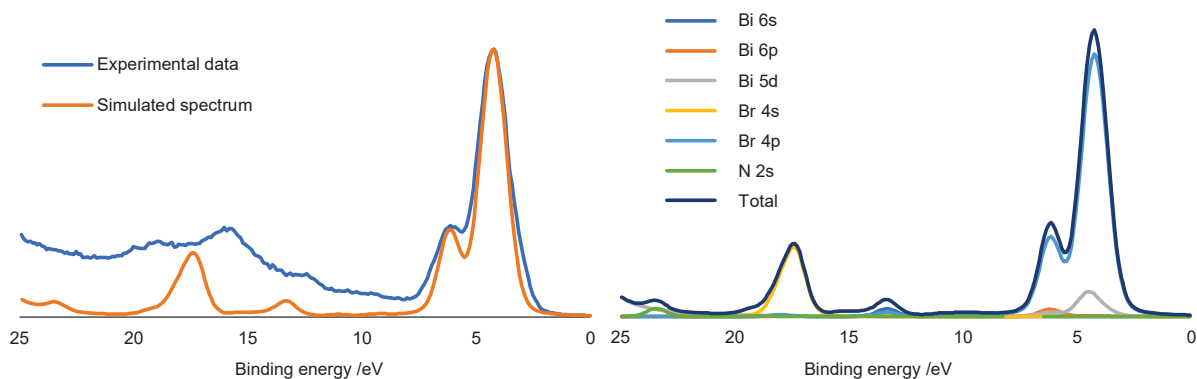
Figure 3.19: Theoretical and experimental valence band XPS of $[C_2C_1Im]_2[Bi_2Br_8]$.
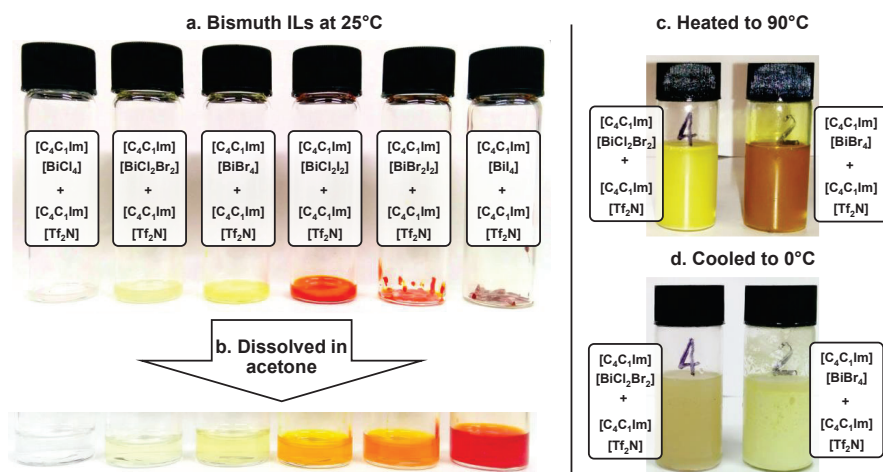
Figure 3.20: Bismuth containing ionic liquids.

For monohalide species the molecular ratio of the components was: 1 $[C_4C_1Im]X$: 1 BiX_3 : 1 $[C_4C_1Im][Tf_2N]$. For bihalide species the components were: 1 $[C_4C_1Im]X$: 1 $[C_4C_1Im]Y$: 1 BiX_3 : 1 BiY_3 : 2 $[C_4C_1Im][Tf_2N]$. All starting materials were purchased from Merck. The liquid/low melting components ($[C_4C_1Im][Tf_2N]$ and $[C_4C_1Im]X$) were dried under vacuum and confirmed pure via ^1H and ^{13}C NMR analysis. To synthesise the ILs all starting materials for each IL were added to a sample vial, which was agitated by hand then magnetically stirred and heated for 30-60 minutes. ILs containing I were heated at 140°C. ILs without I were heated at 90°C.

1 $[C_4C_1Im][BiCl_4]$: 1 $[C_4C_1Im][Tf_2N]$ is a white, semi-opaque liquid at room temperature, and doesn't change colour within the range of temperatures 0-90°C, Fig. 3.20a. 1 $[C_4C_1Im][BiCl_2Br_2]$: 1 $[C_4C_1Im][Tf_2N]$ is a grey-yellow liquid at room temperature, but is bright yellow at 90°C, Fig. 3.20a, c, d. The colour transition is gradual and continuous. 1 $[C_4C_1Im][BiBr_4]$: 1 $[C_4C_1Im][Tf_2N]$ is a clear orange/brown liquid at 90°C, but is opaque and a much paler colour at room temperature, Fig. 3.20a,

c, d. The colour change is sharp, non-continuous. If left overnight the ionic liquid separates into 2 phases, presumably a $[C_4C_1Im][Tf_2N]$ rich phase and a $[C_4C_1Im][BiBr_4]$ rich phase. 1 $[C_4C_1Im][BiCl_2I_2]$: 1 $[C_4C_1Im][Tf_2N]$ is a viscous red liquid at room temperature, Fig. 3.20a. 1 $[C_4C_1Im][BiBr_2I_2]$: 1 $[C_4C_1Im][Tf_2N]$ is a red solid at room temperature, Fig. 3.20a. 1 $[C_4C_1Im][BiI_4]$: 1 $[C_4C_1Im][Tf_2N]$ is a dark purple solid at room temperature, Fig. 3.20a.

Viscosity and melting point are increased across the series as the molecular weight of the halide is increased.

In order to generate UV-vis spectra of the ILs they were dissolved in acetone. The colour series is maintained when acetone is added to the samples, Fig. 3.20b; therefore we assume that dilution in acetone does not significantly alter the electronic properties of Bi ILs. All samples were diluted significantly further in an *ad hoc* manner in order to obtain UV-vis spectra with peak absorbances between 0.2 and 3. UV-vis spectra were run on a Perkin-Elmer LAMBDA 650 UV/Vis Spectrophotometer, with a pure acetone reference sample. A wavelength range of 250-800nm was used, with 1 nm increments, Fig. 3.21.

The resulting experimental UV-vis spectra were normalised in 2 ways; first the spectra were shifted vertically so that the lowest recorded absorbances are plotted at 0, secondly the absorbance values were multiplied such that the heights of the highest wavelength peak in each spectrum are equal.

The spectra obtained for 1 $[C_4C_1Im][BiI_4]$: 1 $[C_4C_1Im][Tf_2N]$ and 1 $[C_4C_1Im][BiBr_2I_2]$: 1 $[C_4C_1Im][Tf_2N]$ have two visible peaks, in contrast to the other
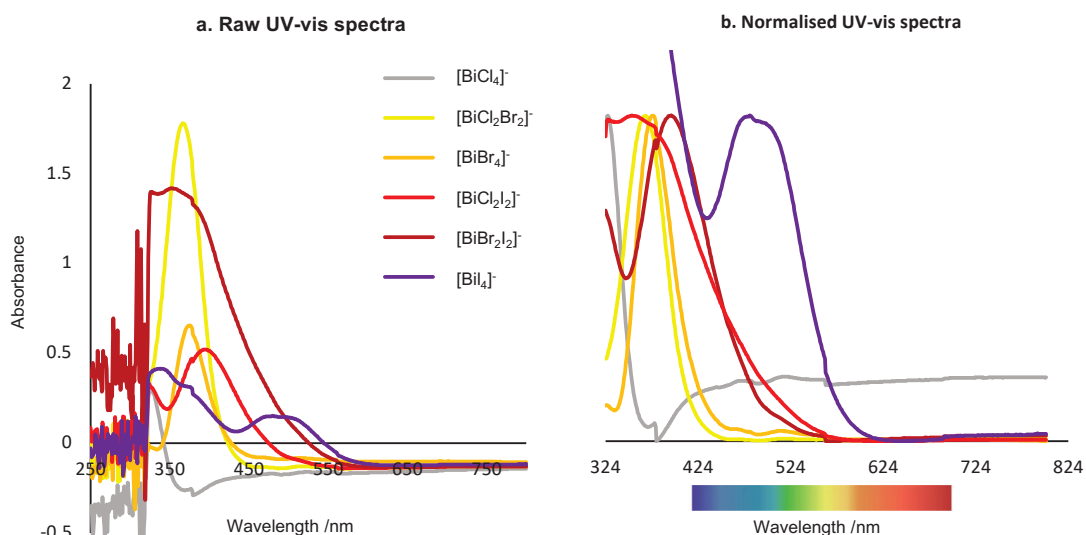
Figure 3.21: UV-vis experimental spectra.

135

samples which only have one. The other samples may also have these peaks at a higher energy than the cut-off for the spectrometer used.

The ordering of the low energy peaks in each spectrum is consistent with the colours seen in Fig. 3.20a. The peak for 1 $[C_4C_1Im][BiCl_4]$: 1 $[C_4C_1Im][Tf_2N]$ is the highest in energy compared to the other samples and is outside the visible region, as expected for a colourless liquid. The peaks for 1 $[C_4C_1Im][BiCl_2Br_2]$: 1 $[C_4C_1Im][Tf_2N]$ and 1 $[C_4C_1Im][BiBr_4]$: 1 $[C_4C_1Im][Tf_2N]$ are very close together and begin in the blue region of the visible spectrum, giving yellow coloured liquids. The peaks in the 1 $[C_4C_1Im][BiCl_2I_2]$: 1 $[C_4C_1Im][Tf_2N]$ and 1 $[C_4C_1Im][BiBr_2I_2]$: 1 $[C_4C_1Im][Tf_2N]$ spectra are also close together and extend to the green region giving orange colours. 1 $[C_4C_1Im][BiI_4]$: 1 $[C_4C_1Im][Tf_2N]$ is absorbing strongly everywhere in the visible spectrum except the red region, giving a dark red colour.

The peaks obtained are broader for ILs containing larger halides, and also for ILs with mixed halides. The broadest peak is within the spectrum for 1 $[C_4C_1Im][BiCl_2I_2]$: 1 $[C_4C_1Im][Tf_2N]$, this is likely to be due to the presence of a mixture of anions containing different ratios of Cl and I halides resulting in several overlapping peaks which combine to form a broad absorbance.

3.5.3 Theoretical UV-Vis

Bismuth containing HMILs are highly coloured, with the hue changing from light yellow to red to purple depending on which halides are incorporated, see Fig. 3.20. We
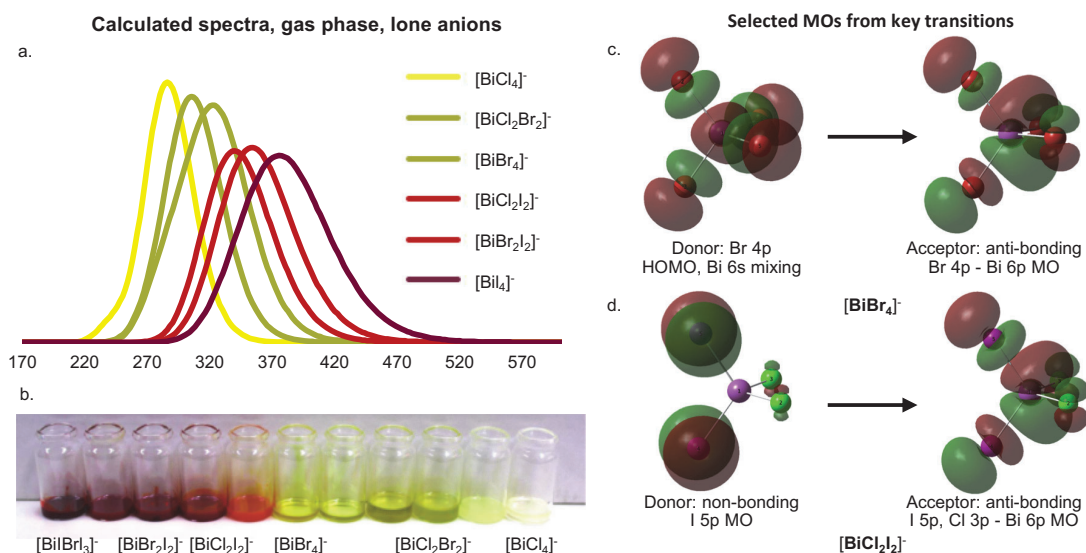
Figure 3.22: a. Time dependent DFT generated UV-Vis spectra, from lone anions in the gas phase. b. Selected MOs involved in the key transitions for $[BiBr_4]^-$ and $[BiCl_2I_2]^-$.

136

attempted to reproduce this series using time-dependent DFT (TD-DFT) in order to validate our theoretical results against the properties observed experimentally. A sequence of anions, $[BiCl_4]^-$, $[BiCl_2Br_2]^-$, $[BiBr_4]^-$, $[BiCl_2I_2]^-$, $[BiBr_2I_2]^-$, $[BiI_4]^-$, were optimised in both the gas phase and with the SMD applied, Section 3.3.1. TD-DFT was applied in the gas phase and ionic liquid SMD to calculate 10 triplet and 10 singlet excitations for each conformer.

In the gas phase single peaks were produced for each anion. As larger halides were incorporated the peaks increased in wavelength, decreased in intensity and became broader, Fig. 3.22 a. Two groups of transitions account for the spectra produced. A group of 3 transitions with main contributions from the HOMO to the LUMO, LUMO+1 and LUMO+2 gives rise to the main peak, Fig. 3.22 c. A much less intense transition from several MOs below the HOMO to the LUMO - LUMO+2 MOs comes at a lower wavelength causing a small increase in peak width, Fig. 3.22 d. The peak positions are consistent with the decrease in energy (and increase in wavelength) as halide size increases of the calculated HOMO-LUMO gaps, Fig. 3.27.

The gas phase lone anion calculation results qualitatively reproduce the key features of the experimental data; the peaks are ordered correctly, and the peaks broaden as halide weight increases. However accurate quantitative data is not expected from this method, and the theoretical peak positions are offset from the experimental peaks by -65nm ($[BiCl_4]^-$) to -130nm ($[BiI_4]^-$). The large width of the experimental peaks for mixed species, especially $[BiCl_2I_2]^-$ are also not reproduced; experimentally several species ($[BiCl_4]^-$, $[BiI_3Cl]^-$ etc) will be present, leading to wider peaks than calculated for the single $[BiCl_2I_2]^-$ anion. The second, higher energy peaks experimentally observed for 1 $[C_4C_1Im][BiI_4]$: 1 $[C_4C_1Im][Tf_2N]$ and 1 $[C_4C_1Im][BiBr_2I_2]$: 1 $[C_4C_1Im][Tf_2N]$ are not present in the gas phase lone anion calculations.

When the TD-DFT calculations were repeated within an SMD environment large conformational effects resulted, Fig. 3.23. Gas phase geometries gave similar spectra to the gas phase TD-DFT calculations. Using optimised SMD geometries resulted in changes to the spectra. For $[BiCl_4]^-$ and $[BiBr_4]^-$ sawhorse geometries are stable minima in the SMD environment, and give different spectra to the tetrahedral species; the spectra for the sawhorse geometries contain double peaks, Fig. 3.23 b. $[BiX_2Y_2]^-$ anions have 4 possible geometries; tetrahedral (minima in gas phase), sawhorse - small halide axial, sawhorse - large halide axial, and sawhorse mixed halides axial. Peak positions and intensities vary significantly across the conformers, Fig. 3.23. The

a. All calculated spectra, smd, gas phase geometry

b. [BiX₄]⁻ Calculated spectra, smd, sawhorse geometry

[BiCl₄]⁻
[BiCl₂Br₂]⁻
[BiBr₄]⁻
[BiCl₂I₂]⁻
[BiBr₂I₂]⁻
[BiI₄]⁻
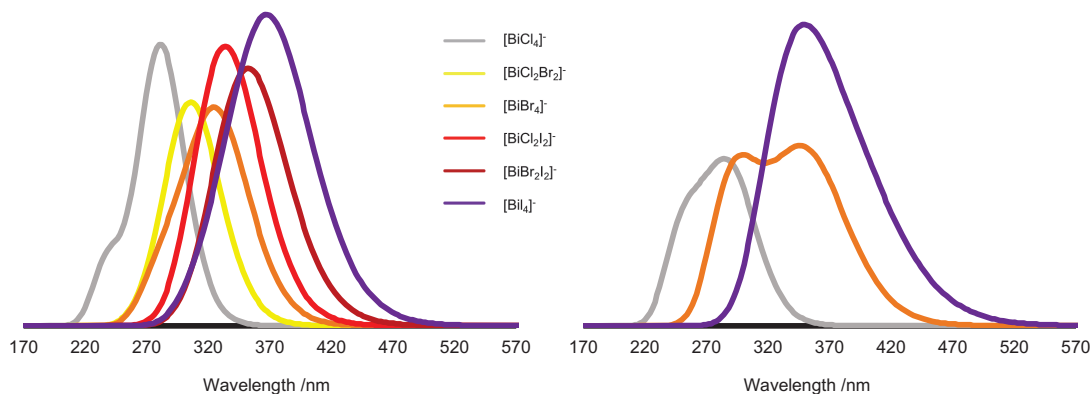
c. [BiX₂Y₂]⁻ Calculated spectra, smd

Gas phase geometry (tetrahedral)
Sawhorse, both halides axial
Sawhorse, small halide axial
Sawhorse, large halide axial
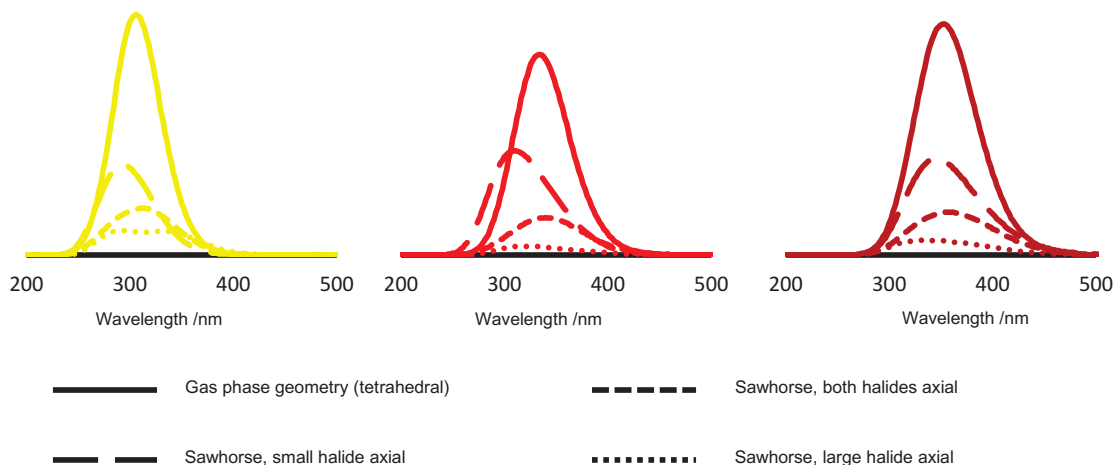
Figure 3.23: Time dependent DFT generated UV-Vis spectra, from lone anions in an SMD. a. All species, gas phase geometry. b. $[BiX_4]^-$ anions in sawhorse geometry. c. $[BiX_2Y_2]^-$ anions in gas phase geometry and 3 sawhorse conformers.

computed transitions and relevant MOs are similar across the conformers so it is not clear where the large conformational variation originates.

3.5.4 MO analysis

$[BiX_4]^-$

A basic insight into the bonding interactions within bismuth halide anions is obtained by considering the MO diagram of tetrahedral $[BiCl_4]^-$ in the gas phase, Fig. 3.24. The four Cl 3s AOs combine to form a single fully bonding MO, and 3 triply degenerate antibonding MOs. The single fully bonding MO is fully symmetric and therefore interacts with the Bi 6s AO to form a bonding MO a. and an antibonding MO b. The Bi
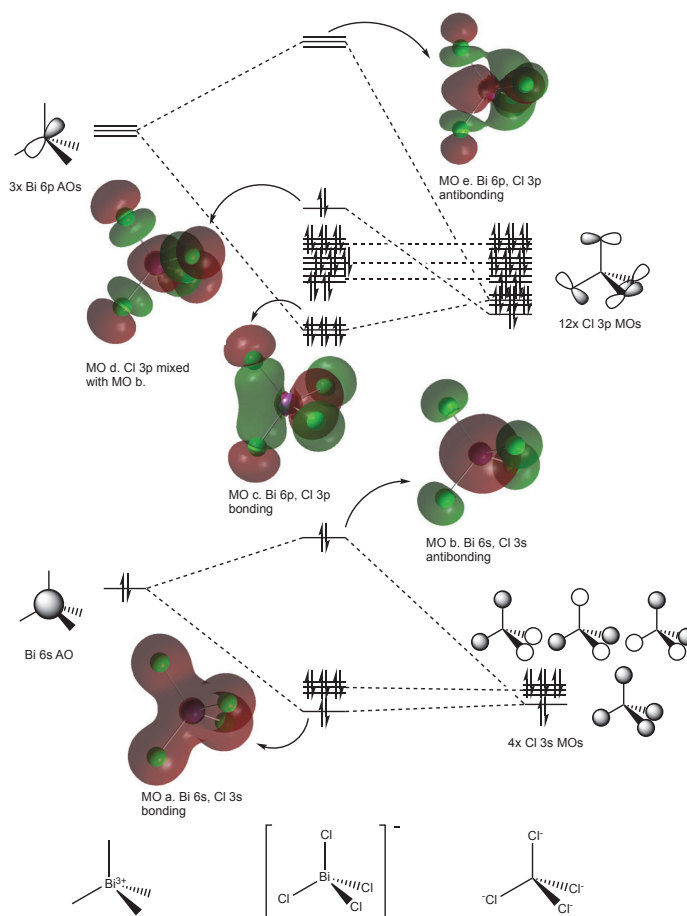
Figure 3.24: MO diagram of tetrahedral $[BiCl_4]^-$ in the gas phase.

6s AO has a larger contribution to the antibonding MO, and the Cl 3s AOs have a larger contribution to the bonding MO.

The four sets of Cl 3p AOs combine to form 3 triply degenerate MOs, 1 doubly degenerate MO, and a single, fully symmetric MO. One of the triply degenerate sets combines with the 3 Bi 6p AOs to form triply degenerate bonding and antibonding MOs (MO c. and MO e.). MO e. is the LUMO $[BiCl_4]^-$. MO d. the single Cl 3p fully symmetric MO undergoes significant mixing with MO b. and is raised up in energy above the non-bonding Cl 3p MOs to become the HOMO. Therefore both HOMO and LUMO have both Bi and Cl contributions.

MOs (molecular orbitals) of the two conformers have similar atomic contributions, see Fig. 3.25. The MOs are arranged from highest energy at the top of the figure (MO d.) to the lowest energy MO at the bottom (MO a.). MOs a. and b. are formed by the combination of Cl 3s AOs with the Bi 6s AO. In MO a. the two components combine in phase, forming a bonding MO. MO b. is the anti-bonding MO with the Bi 6s component

139
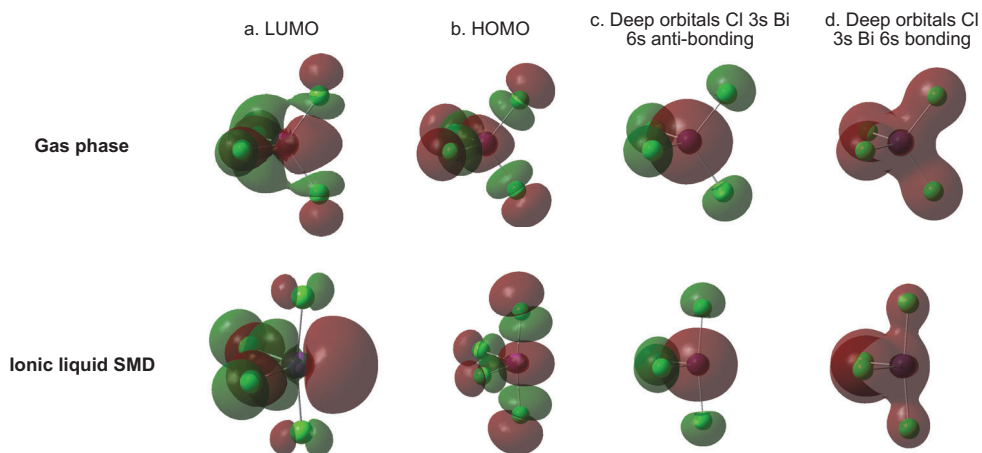
Figure 3.25: Comparision of [BiCl$_4$]$^-$ MOs in the gas phase (tetrahedral) and ionic liquid SMD (sawhorse).

out of phase with the Cl 3s part.

The Bi 6p AOs and some Cl 3p MOs also interact, forming 3 bonding-antibonding pairs - one for each Bi 6p AO. The 3 bonding MOs are occupied, and the three antibonding MOs are not. In the gas phase tetrahedral [BiCl$_4$]$^-$ the three bonding MOs are triply degenerate, as are the three antibonding MOs - which are the LUMO, see Fig. 3.25. d. In the sawhorse structure the analogous sets of 3 bonding and 3 antibonding MOs are not degenerate, but are close in energy.

In both tetrahedral (gas phase) and sawhorse (SMD) conformers the HOMO (Fig. 3.25 c.) is formed via mixing between a fully bonding Cl 3p orbital and the Cl 3s, Bi 6s antibonding MO - MO b. This mixing increases the energy of the fully bonding Cl 3p orbital, raising it above all other occupied orbitals. The degree of this mixing therefore has a large impact on the HOMO-LUMO gap; increased mixing raises the energy of the HOMO further and reduces the energy gap between the HOMO and the LUMO.

[BiCl$_4$]$^-$ has a sawhorse structure in the ionic liquid SMD environment. Fig. 3.26 shows the correlation between the gas phase and SMD MO energy levels. The ordering of the MOs is unchanged by the change in environment and structure, as are the AO contributions to the MOs. The relative energies of the MOs are also similar between the gas phase and SMD structures. Every MO is stabilised on moving from the gas phase to the SMD; NBO analysis gives values of -0.53 a.u. for the Bi 6s AO in the gas phase, and -0.63 a.u. when the SMD is applied. Symmetry breaking occurs as the symmetry is reduced from tetrahedral in the gas phase to C$_{2v}$ with the SMD applied. The gas phase triply degenerate MOs become sets of doubly degenerate and single MOs in the SMD,
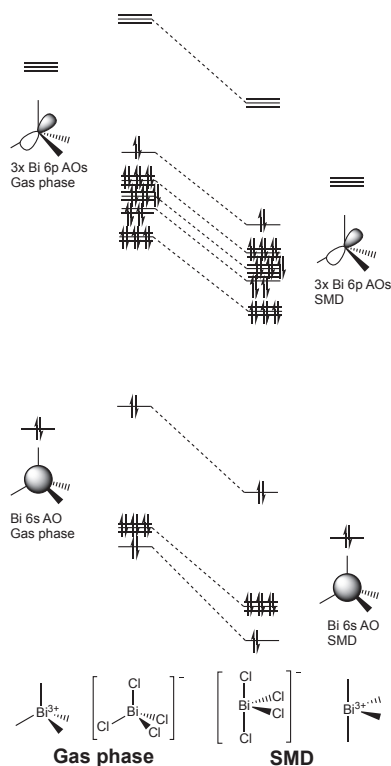
Figure 3.26: The relative energies of the MOs of gas phase, tetrahedral, $[BiCl_4]^-$ vs ionic liquid SMD, sawhorse, $[BiCl_4]^-$. NBO analysis gives values of -0.53 a.u. for the Bi 6s AO in the gas phase, and -0.63 a.u. when the SMD is applied.

however the MOs are still very tightly grouped in energy so this effect is not visible on the correlation diagram, Fig. 3.26.

Across the series of halides: $[BiCl_4]^-$, $[BiBr_4]^-$, $[BiI_4]^-$ the same bonding and mixing interactions remain and the order of the MOs produced is retained, Fig. 3.27. Across the series the Bi 6p - X np bonding MO shifts up in energy, and the Bi 6p - X np antibonding MO shifts down. The Bi 6p AOs remain in the middle and make similar contributions to the bonding and antibonding MOs across the series. Anion size is increased across the series due to increased Bi-X bond lengths, as well as increased diffusivity in the X AOs.

$[C_2C_1Im][BiCl_4]$

The HOMO and LUMO of the ion pairs is identical to the HOMO and LUMO of the lone anion, with no added cation contribution, Fig. 3.28.

The anion - cation π star interaction is more pronounced in the gas phase conformers than the SMD. Charge transfer values for the front conformer in both environments were calculated using NBO analysis. In the gas phase charge transfer was

141
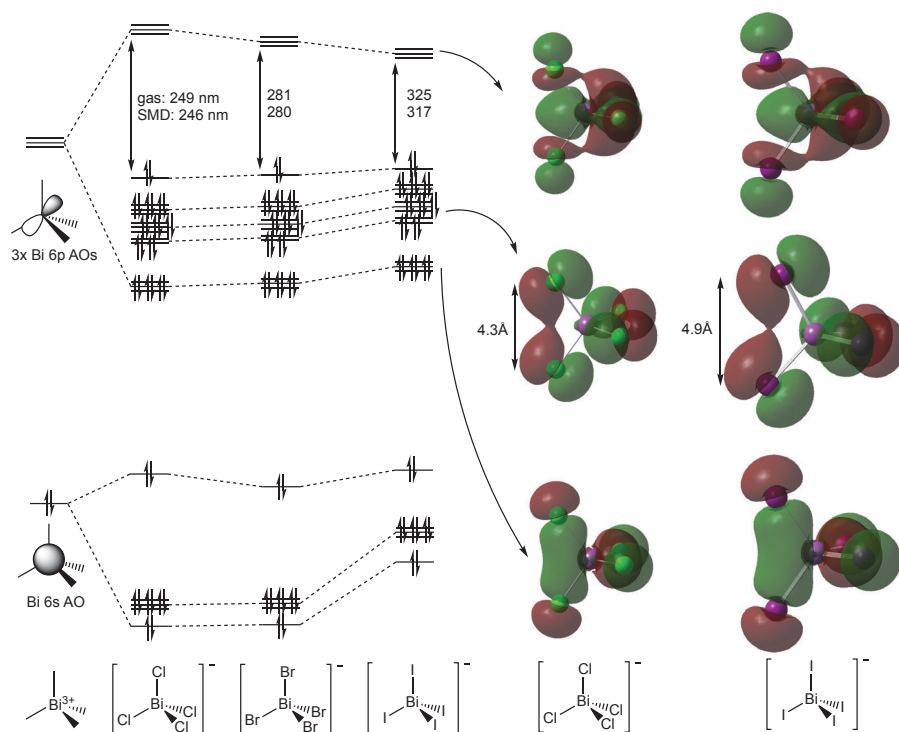
Figure 3.27: The relative energies of the MOs in gas phase, tetrahedral, $[BiCl_4]^-$, $[BiBr_4]^-$, $[BiI_4]^-$. The wavelength corresponding to the energy of the HOMO-LUMO gap is provided for each anion in nm. The energy levels obtained in the SMD ionic liquid environment are not shown, but are very similar to the gas phase levels. The SMD HOMO-LUMO gaps are also given in nm.

0.15e, and the SMD structure gave a significantly lower value of 0.05e, also indicating weaker anion-cation interactions.
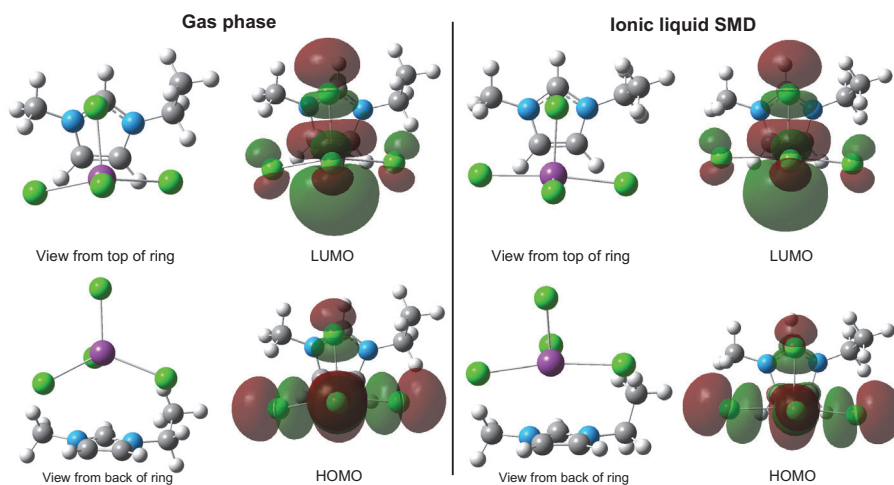
Figure 3.28: Structures and images of the HOMO and LUMO of the equatorial_top $[C_2C_1Im][BiCl_4]$ conformer in gas phase and ionic liquid SMD.
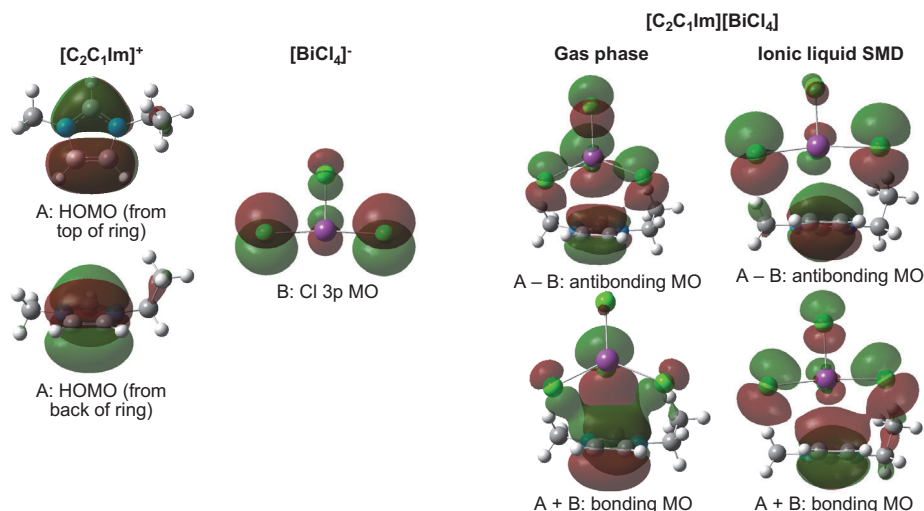
Figure 3.29: The HOMO of $[C_2C_1Im]^+$ interacting with a $[BiCl_4]^-$ Cl 3p MO in gas phase and ionic liquid SMD.

3.6 Conclusions

The anionic speciation in Bi containing HMILs has been predicted using DFT, and the SMD solvation model. Six anions: $[Bi_2X_7]^-$, $[Bi_2X_8]^{2-}$, $[Bi_2X_9]^{3-}$, $[BiX_5]^{2-}$, $[BiX_4]^-$, X^- are accessible via changing the mole fraction of BiX_3 added to the liquid. The calculations have been validated via comparison to experimental valence band XPS and experimentally observed colour trends were correctly predicted. Insight has also been provided into the types of anion - cation interactions present in Bi HMILs, and how they vary from gas phase to solvated systems.

Bibliography

[1] N. E. Cousens, L. J. Taylor Kearney, M. T. Clough, K. R. J. Lovelock, R. G. Palgrave and S. Perkin, *Dalton Transactions*, 2014, **43**, 10910–9.

[2] M. J. Frisch, G. W. Trucks, H. B. Schlegel, G. E. Scuseria, M. A. Robb, J. R. Cheeseman, G. Scalmani, V. Barone, B. Mennucci, G. A. Petersson, H. Nakatsuji, M. Caricato, X. Li, H. P. Hratchian, A. F. Izmaylov, J. Bloino, G. Zheng, J. L. Sonnenberg, M. Hada, M. Ehara, K. Toyota, R. Fukuda, J. Hasegawa, M. Ishida, T. Nakajima, Y. Honda, O. Kitao, H. Nakai, T. Vreven, J. Montgomery, J. A., J. E. Peralta, F. Ogliaro, M. Bearpark, J. J. Heyd, E. Brothers, K. N. Kudin, V. N. Staroverov, R. Kobayashi, J. Normand, K. Raghavachari, A. Rendell, J. C. Burant, S. S. Iyengar, J. Tomasi, M. Cossi, N. Rega, M. J. Millam, M. Klene, J. E. Knox,

J. B. Cross, V. Bakken, C. Adamo, J. Jaramillo, R. Gomperts, R. E. Stratmann, O. Yazyev, A. J. Austin, R. Cammi, C. Pomelli, J. W. Ochterski, R. L. Martin, K. Morokuma, V. G. Zakrzewski, G. A. Voth, P. Salvador, J. J. Dannenberg, S. Dapprich, A. D. Daniels, Ö. Farkas, J. B. Foresman, J. V. Ortiz, J. Cioslowski and D. J. Fox, *Gaussian 09, Revision D.01*, 2009.

[3] A. D. Becke, *The Journal of Chemical Physics*, 1993, **98**, 5648.

[4] C. Lee, W. Yang and R. G. Parr, *Physical Review B*, 1988, **37**, 785–789.

[5] S. Grimme, S. Ehrlich and L. Goerigk, *Journal of Computational Chemistry*, 2011, **32**, 1456–1465.

[6] A. D. Becke, *Physical Review A*, 1988, **38**, 3098–3100.

[7] P. J. Stephens, F. J. Devlin, C. F. Chabalowski and M. J. Frisch, *The Journal of Physical Chemistry*, 1994, **98**, 11623–11627.

[8] T. H. Dunning, *The Journal of Chemical Physics*, 1989, **90**, 1007.

[9] D. E. Woon and T. H. Dunning, *The Journal of Chemical Physics*, 1993, **98**, 1358.

[10] K. A. Peterson, D. Figgen, E. Goll, H. Stoll and M. Dolg, *The Journal of Chemical Physics*, 2003, **119**, 11113–1123.

[11] K. A. Peterson, *The Journal of Chemical Physics*, 2003, **119**, 11099–11112.

[12] J. Yeh and I. Lindau, *Atomic Data and Nuclear Data Tables*, 1985, **32**, 1–155.

[13] R. Dennington, T. Keith and J. Millam, *GaussView, Version 5.*, 2009.

[14] A. V. Marenich, C. J. Cramer and D. G. Truhlar, *The Journal of Physical Chemistry B*, 2009, **113**, 6378–96.

[15] V. S. Bernales, A. V. Marenich, R. Contreras, C. J. Cramer and D. G. Truhlar, *The Journal of Physical Chemistry B*, 2012, **116**, 9122–9129.

[16] H. Niedermeyer, C. Ashworth, A. Brandt, T. Welton and P. a. Hunt, *Physical Chemistry Chemical Physics*, 2013, **15**, 11566–78.

[17] J. Tomasi, B. Mennucci and E. Cancès, *Journal of Molecular Structure: THEOCHEM*, 1999, **464**, 211–226.

[18] G. A. Fisher and N. C. Norman, *Advances in Inorganic Chemistry*, 1994, **41**, year.

[19] S. A. Adonin, M. N. Sokolov and V. P. Fedin, *Coordination Chemistry Reviews*, 2016, **312**, 1–21.

[20] S. Takahashi, L. Curtiss, D. Gosztola and M.-L. Saboungi, *Inorganic Chemistry*, 1995, **34**, 2990–2993.

[21] H. Øye, M. Jagtoyen, T. Oksefjell and J. Wilkes, *Materials Science Forum*, 1991, **73-75**, 183–190.

[22] T. W. Couch, D. A. Lokken and J. D. Corbett, *Inorganic Chemistry*, 1972, **11**, 357–362.

[23] P. A. Hunt and I. R. Gould, *The Journal of Physical Chemistry A*, 2006, **110**, 2269–2282.

[24] P. A. Hunt, B. Kirchner and T. Welton, *Chemistry - A European Journal*, 2006, **12**, 6762–6775.

[25] J. Estager, J. D. Holbrey and M. Swadźba-Kwaśny, *Chemical Society Reviews*, 2014, **43**, 847–86.

[26] J. Estager, P. Nockemann, K. R. Seddon, M. Swadźba-Kwaśny and S. Tyrrell, *Inorganic chemistry*, 2011, **50**, 5258–71.

[27] A. McLean and G. Chandler, *The Journal of Chemical Physics*, 1980, **72**, 5639.

[28] W. Küchle, M. Dolg, H. Stoll and H. Preuss, *Molecular Physics*, 1991, **74**, 1245–1263.

[29] M. Reinmöller, A. Ulbrich, T. Ikari, J. Preiß, O. Höfft, F. Endres, S. Krischok and W. J. D. Beenken, *Physical Chemistry Chemical Physics*, 2011, **13**, 19526.

[30] K. R. J. Lovelock, I. J. Villar-Garcia, F. Maier, H.-P. Steinruck and P. Licence, *Chemical Reviews*, 2010, **110**, 5158–5190.

Chapter 4

Nickel complexes in ionic liquids and deep eutectic solvents

4.1 Introduction

In the previous chapter the molecular structure, speciation, and electronic properties of a main group HMIL were investigated. Similar aspects of a d-block HMDES will be studied in this chapter. The HMDES system has additional complexities compared to the HMIL system: there is more than one potential ligand species in solution, and the d-block metal complexes studied are open shell systems.

The system investigated here is nickel(II) chloride dissolved in ethaline. Ethaline is a popular DES consisting of 2 parts H-bond donor ethylene glycol (1,2-ethanediol, Eg) to 1 part choline chloride (2-Hydroxy-N,N,N-trimethylethan-1-aminium, [Ch]Cl). The system has been studied experimentally by several authors, as have analogous systems with other transition metals, Section 1.4.9.[1–3] The ethaline-NiCl$_2$ HMDES system is of particular interest due to the applications (e.g. in smart windows,[2] electrodeposition[3] and metal-metal separation[4]). Studying ethaline-MCl$_2$ will develop understanding of the anomalous chemical behaviour of nickel compared to other d-block metals when added to ethaline.

4.2 Methods

4.2.1 Program used and theoretical method

Calculations were run in Gaussian 09 (revision D01).[5] The functional B3LYP-GD3BJ was employed: Becke's three parameter exchange functional,[6] with Lee, Yang and Parr's

correlation functional,[7] and the D3 Grimme dispersion correction with Becke-Johnson damping.[8–10] The B3LYP-GD3BJ functional is relatively inexpensive, widely used, and retains efficacy across organic and inorganic ground state systems. Aug-cc-pVDZ basis sets were applied.[11,12] Optimisation calculations used a pruned (99,590) integration grid, 99 radial shells and 590 points per shell (int=ultrafine). For all calculations an improved SCF convergence criterion was applied (scf=conver=9): Root mean squared change in the elements of the density matrix between consecutive cycles of less than 10^{-9} au, maximum density element change of less than 10^{-7} au, and an energy change of less than 10^{-7} au. Structures were fully optimised under no symmetry constraints. Vibrational analysis confirmed each reported structure as a minimum. MO (molecular orbital) pictures use a standard iso value of 0.02, unless otherwise noted. All thermochemical values reported are calculated at standard conditions of 298.15 K and 1 atm.

Unrestricted B3LYP (UB3LYP) was utilised for calculations on open shell d block complexes. (UB3LYP and B3LYP are exactly equivalent for closed shell systems.) Testing of high and low spin states was carried out for $[MCl_4]^{2-}$ and $[M(Eg)_3]^{2+}$, M = Fe, Co, Ni, Cu. Each complex was optimised in both low and high spin states and the relative energies were computed. In every case the high spin complex was lower in energy by approximately 100 kJ mol^{-1}. Therefore all complexes discussed in this chapter were calculated in the high spin state, with multiplicities as follows: m = 5 (Fe), m = 4 (Co), m = 3 (Ni), and m = 2 (Cu).

Non-covalent interactions were visualised with the NCI (non-covalent interactions) method, implemented via the AIMALL suite.[13–15] NCIs are identified in terms of electron density (ρ) and its reduced gradient ($S = \frac{1}{(2(3\pi^2)^{1/3})} \frac{|\nabla\rho|}{\rho^{4/3}}$). Regions with low electron density (< 0.05a.u.) and low S (0.5) indicate NCIs. The sign of λ_2, the second of the three eigenvalues of the second derivative matrix of ρ ($\nabla^2\rho = \lambda_1 + \lambda_2 + \lambda_3$) quantifies the type and strength of the interaction. Large, negative values of sign(λ_2)ρ are associated with attractive NCIs (dipole-dipole or H-bonding), large, positive, values with regions of weakly repulsive overlap, and values near 0 with weak van der Waals interactions.

4.2.2   SMD model parameterisation

The SMD model was utilised to provide a solvation environment.[16] The solvent parameters chosen correspond to Eg. In ethaline there is a 2:1 ratio of Eg molecules to [Ch]Cl pairs, so Eg is the most abundant species. Solvent parameters are also readily available for Eg, which is not the case for [Ch]Cl or ethaline itself. Eg is also a pragmatic

choice due to its chemical similarities to the other organic molecules in solution: H_2O and $[Ch]^+$. To test the effect of different solvent parameters on Gibbs free energy, an example ionpair ($[Ch]Cl$) was optimised in both the Gaussian internally specified water SMD and in the chosen Eg SMD. ΔG between the two calculations was 4 kJ mol^{-1}. The Eg parameters were manually specified as tabulated by in the Minnesota solvent descriptor database:[17]

Dielectric constant ϵ: 40.245

Index of refraction n: 1.4318

Macroscopic surface tension γ: 69.07

Abraham's hydrogen bond acidity and basicity parameters for the solvent when treated as a solute $\Sigma\alpha_2^H$ and $\Sigma\beta_2^H$: 0.58, 0.78

Fraction of non-hydrogen atoms that are aromatic carbon atoms ϕ: 0.0

Fraction of non-hydrogen atoms that are electronegative halogen atoms ψ: 0.0

For some structures with flat potential energy surfaces small imaginary frequencies were retained when a solvent continuum model was applied, or the optimisation convergence criteria were not met after optimisation calculations had reached a plateau. In these cases a manual determination of structure convergence was applied: any imaginary frequencies must be below 60 cm^{-1}, and the energy profile of the optimisation must have reached a plateau with energy oscillations below 1 kJ mol^{-1}.

4.3 $[MCl_4]^{2-}$ vs $[M(Eg)_3]^{2+}$, M = Fe, Co, Ni, Cu, Zn

Hartley *et al.* studied HMDESs formed of MCl_2 salts added to ethaline (2Eg:1[Ch]Cl), Section 1.4.9.[1] The metals added to the ethaline DES included the 3d series: Fe, Co, Ni, Cu, Zn. The authors used EXAFS (extended X-ray absorption fine structure) to analyse the coordination of the metal centres at room temperature. The HMDESs containing Fe, Co, Cu, and Zn gave single EXAFS peaks corresponding to 4±0.4 Cl atoms at a distance of 2.3±0.03 Å from the metal centres. The EXAFS data was used to assign the metal containing species as $[MCl_4]^{2-}$ for M = Fe, Co, Cu, Zn, Fig. 4.1. In contrast the EXAFS spectrum for M = Ni contained two peaks, one for 6 O atoms at 2.08 Å and one for 5±2 C atoms at 2.9 Å. The complex $[Ni(Eg)_3]^{2+}$ was assigned from the EXAFS results, Fig. 4.1. At temperatures above 50 °C the ethaline-$NiCl_2$ HMDES changes colour from yellow to blue and two additional peaks appear in the UV-vis spectrum. These observations have been attributed to the formation of $[NiCl_4]^{2-}$.[3]

In this section a simple equilibrium between $[M(Eg)_3]^{2+}$ and $[MCl_4]^{2-}$ is modeled
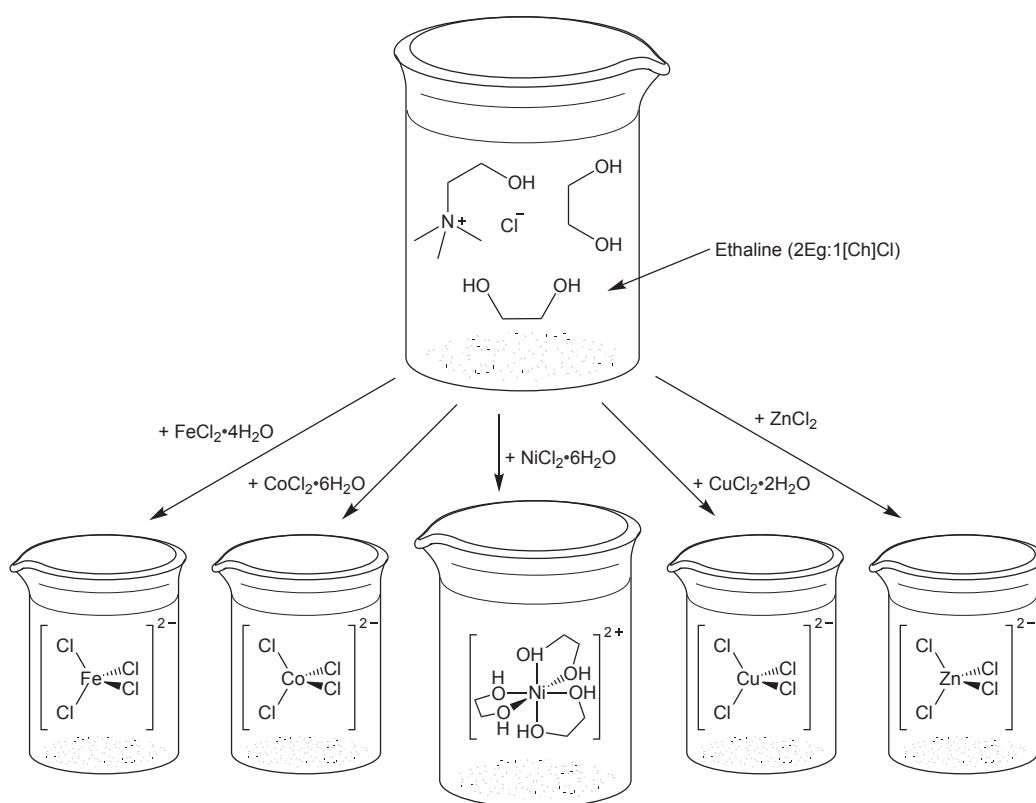
Figure 4.1: Five HMDESs synthesised by Hartley *et al.*[1] Fe, Co, Ni, Cu, and Zn chloride salts were added to ethaline. The metal containing species (in the lower beakers) were assigned via EXAFS.

for M = Fe, Co, Ni, Cu, Zn:

$$[M(Eg)_3]^{2+} + 4\,Cl^- \rightleftharpoons [MCl_4]^{2-} + 3\,Eg \tag{4.1}$$
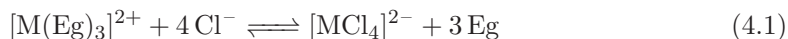
The molecule Eg, anion Cl^-, and complexes $[MCl_4]^{2-}$ and $[M(Eg)_3]^{2+}$ were optimised in separate calculations, Fig. 4.2. A conformational search at the B3LYP-GD3/6-311++G(d,p) level on the Eg molecule is available in the literature.[18] In this work the lowest energy conformer from the literature was redrawn by eye (as molecule coordinates were not available) and reoptimised.

Initially the structures of $[MCl_4]^{2-}$ and $[M(Eg)_3]^{2+}$ in the gas phase and with an SMD environment applied are discussed. An energetic analysis of the equilibrium in Eq. (4.1) is then presented. Energies of each side of the equilibrium are calculated via simple addition of the energies of the species shown in Fig. 4.2.

4.3.1 $[MCl_4]^{2-}$ structures

All $[MCl_4]^{2-}$ structures (Fig. 4.3 and Table 4.1) were optimised from the same two starting geometries: a tetrahedral structure with the point group T_d, and a slightly distorted tetrahedral structure with the point group C_1. In every case the two optimisations gave identical final structures.

All gas phase structures are tetrahedral, with varying degrees of Jahn-Teller distortion towards other geometries. For M = Zn and Co the structures are fully tetrahedral, and $[FeCl_4]^{2-}$ shows only a minimal distortion. In crystal field theory M = Fe, Co and Zn all have half or fully occupied t_2 levels, meaning a geometric distortion
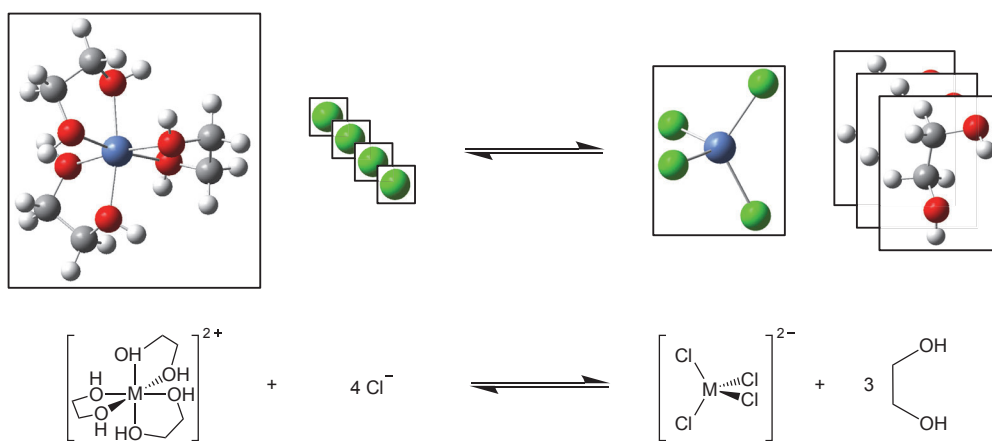
Figure 4.2: The $[M(Eg)_3]^{2+} + 4\,Cl^- \rightleftharpoons [MCl_4]^{2-} + 3\,Eg$ equilibrium was modeled by optimising Eg, Cl^-, $[MCl_4]^{2-}$, and $[M(Eg)_3]^{2+}$ separately.

150
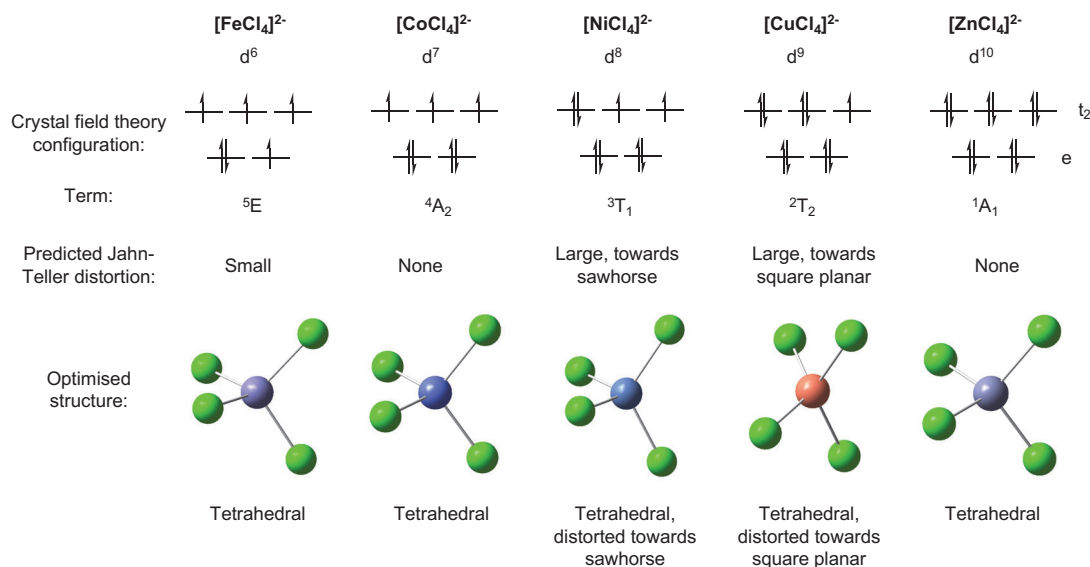
Figure 4.3: Gas phase optimised $[MCl_4]^{2-}$ structures for M = Fe, Co, Ni, Cu, Zn.

Metal	Parameter	Gas phase	Eg SMD
Fe(II)	Point group	S_4, approx D_{2d}	C_1
	$M-Cl$ distance	All 2.39	3 x 2.36, 2.37
	$Cl-M-Cl$ angle	4 x 111, 2 x 106	112, 3 x 111, 2 x 106
Co(II)	Point group	T_d	T_d
	$M-Cl$ distance	All 2.36	All 2.33
	$Cl-M-Cl$ angle	All 109	All 109
Ni(II)	Point group	C_1, approx C_{2v}	C_s, approx C_{2v}
	$M-Cl$ distance	2 x 2.33, 2 x 2.36	2 x 2.32, 2 x 2.31
	$Cl-M-Cl$ angle	121, 108, 4 x 107	124, 107, 4 x 106
Cu(II)	Point group	D_{2d}	D_{2d}
	$M-Cl$ distance	All 2.34	All 2.31
	$Cl-M-Cl$ angle	2 x 131, 4 x 100	2 x 134, 4 x 99
Zn(II)	Point group	T_d	C_1, approx T_d
	$M-Cl$ distance	All 2.36	3 x 2.33, 2.32
	$Cl-M-Cl$ angle	All 109	3 x 109, 3 x 110

Table 4.1: Structural parameters in $[MCl_4]^{2-}$ optimised in the gas phase and with SMD solvation (solvent = Eg) applied. Bond distances are given in Å, and all bond angles in degrees.

which splits the t_2 level is not favoured.[19] $[NiCl_4]^{2-}$ has one doubly occupied t_2 MO, and two singly occupied, encouraging a distortion towards the sawhorse geometry which stabilises one former t_2 MO and destabilises the other two. $[CuCl_4]^{2-}$ undergoes a large distortion towards the square planar structure; with two t_2 MOs doubly occupied and the other singly occupied a conformation which stabilises two former t_2 MOs and destabilises one former t_2 MO is strongly favoured.

The SMD and gas phase structures are broadly similar, Table 4.1, with a slight increase in the Jahn-Teller distortion away from tetrahedral for $[NiCl_4]^{2-}$ and $[CuCl_4]^{2-}$. The SMD environment stabilises increased dipole moments compared to the gas phase, leading to the lower symmetry structures being favoured when SMD is applied.

4.3.2 $[M(Eg)_3]^{2+}$ structures

The bidentate ligand Eg may bind to a metal in either the δ or λ conformations, Fig. 4.4. The combination of the ligand conformations gives 4 optically distinct stereoisomers. The high symmetry forms of these isomers have the point groups D_3 for $\delta\delta\delta$ and $\lambda\lambda\lambda$, and C_2 for $\delta\delta\lambda$ and $\delta\lambda\lambda$. The four $[M(Eg)_3]^{2+}$ conformers were optimised in the gas phase and with SMD applied for M = Fe, Co, Ni, Cu, Zn. Both a high symmetry and a C_1 structure for each conformer were used as starting points for optimisations. Overall 8 optimisations were completed in the gas phase and 8 with SMD applied, for each of the five metals. For each conformer optimising the C_1 and high symmetry input structures produced the same optimised structure.

The relative Gibbs free energies (ΔG) of the four conformers are the sum of the
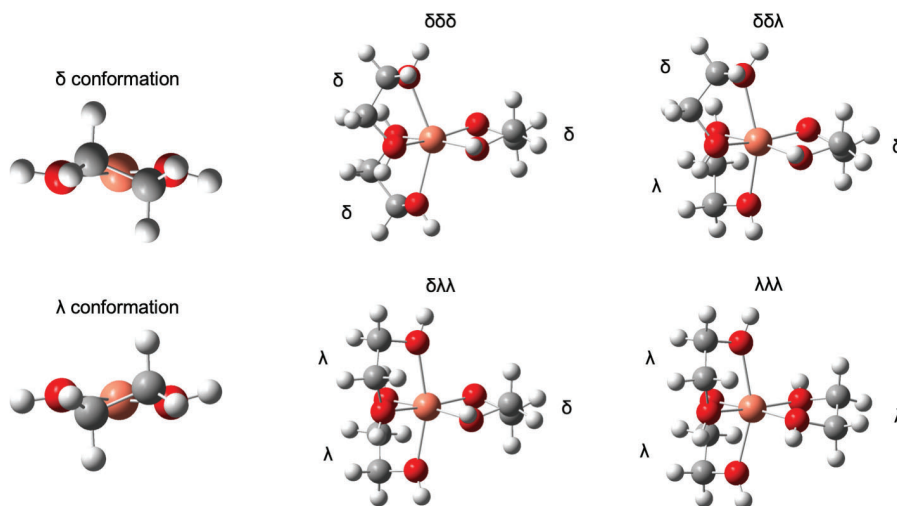
Figure 4.4: Gas phase optimised $[Cu(Eg)_3]^{2+}$ structures.

relative enthalpies (ΔH) and the relative entropy terms ($-$TΔS):

$$\Delta G = \Delta H - T\Delta S \qquad (4.2)$$

Figure 4.5.a. explains how the ΔH and $-$TΔS contributions to ΔG are visualised using data from $[\text{Ni}(\text{Eg})_3]^{2+}$ as an example. In the first pane the ΔH values are graphed in blue. ΔH is referenced to the conformer with the lowest H, the $\delta\delta\delta$ conformer. In the second pane $-$TΔS is plotted in yellow, and the values are referenced to the conformer with the lowest -TS, the $\lambda\lambda\lambda$. Referencing ΔH to the lowest H conformer and $-$TΔS to the lowest -TS conformer is mathematically equivalent to referencing both ΔH and $-$TΔS to the same conformer, with the advantage that only positive values are produced. In the third pane the ΔH and $-$TΔS values are plotted in stacked columns, producing ΔG overall, as demonstrated in the fourth pane. The fifth pane shows the ΔG values referenced to the conformer with the lowest ΔG. The representation of the contributions to ΔG from ΔH and $-$TΔS in the third pane is useful to visualise the relative sizes of the differences in enthalpy and entropy between conformers. ΔG for the four gas phase conformers of $[\text{M}(\text{Eg})_3]^{2+}$, M = Fe, Co, Ni, Cu, Zn. is plotted in Fig. 4.5.b., and Fig. 4.5.c. shows the ΔH and $-$TΔS contributions to ΔG.

The $\delta\delta\delta$ $[\text{M}(\text{Eg})_3]^{2+}$ conformer is the most stable for all five metals calculated, with the lowest ΔG and ΔH, Fig. 4.5. For M = Fe, Ni, Cu, Zn ΔH increases as the number of ligands in the λ conformation increases. M = Co has different ΔH behavior; the $\delta\delta\lambda$, and $\delta\lambda\lambda$ conformers have the highest ΔH. Across all five metals $-$TΔS is similar between the $\delta\delta\delta$, $\delta\delta\lambda$, and $\delta\lambda\lambda$ conformers, and is 0 for the $\lambda\lambda\lambda$ conformer. $-$TΔS and ΔH run counter to each other for M = Fe, Ni, Cu, and Zn, reducing ΔG between conformers to $\leq$ 10 kJ mol^{-1}, when ΔH values are up to 17 kJ mol^{-1}.

The factors which determine ΔH values between conformers include: intramolecular H-bonding between ligands, steric clashes between ligands, Van der Waals forces between ligands, and positioning of the O atoms relative to the preferred coordination sphere of the metal.

The most stable conformer ($\delta\delta\delta$) will now be discussed. The structures of the $\delta\delta\delta$ $[\text{M}(\text{Eg})_3]^{2+}$ conformers are similar for M = Fe, Co, Ni, and Zn, Fig. 4.6. Crystal field theory analysis does not predict significant Jahn-Teller distortion for octahedral complexes of Fe(II), Co(II), Ni(II), and Zn(II). The calculated structures do not show Jahn-Teller effects; 6 equivalent M$-$O bond distances were obtained in each case. The trans-O$-$M$-$O angles deviate from 180° due to the constrained ligand geometry, rather
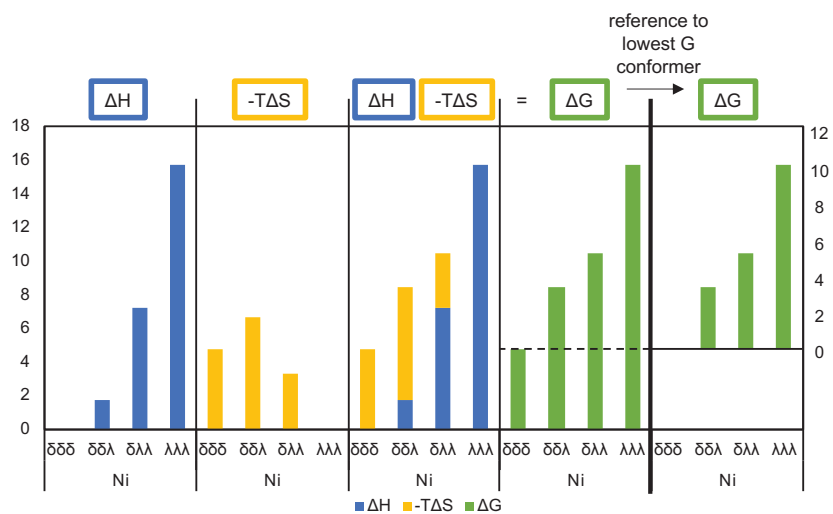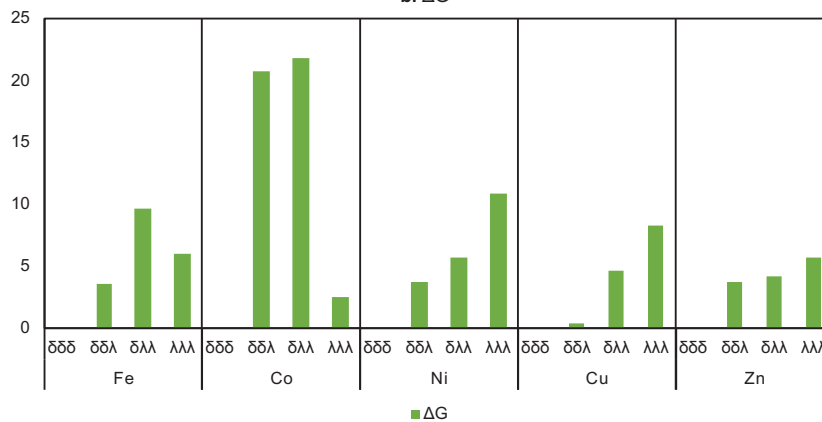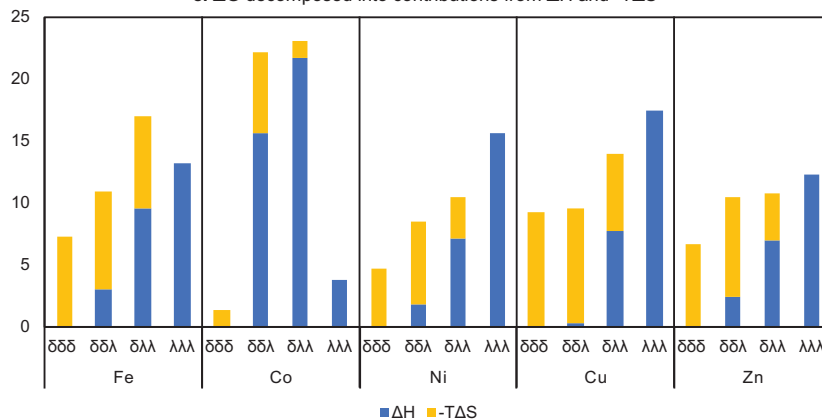
Figure 4.5: a. Explanation of how ΔG may be plotted as the sum of ΔH and $-T\Delta S$. b. ΔG of the $\delta\delta\delta$, $\delta\delta\lambda$, $\delta\lambda\lambda$, and $\lambda\lambda\lambda$ conformers of $[M(Eg)_3]^{2+}$, M = Fe, Co, Ni, Cu, Zn, calculated in the gas phase. c. ΔG split into contributions from ΔH and $-T\Delta S$. Energies are given in kJ mol^{-1}.

than Jahn-Teller effects. In contrast crystal field theory predicts a large distortion towards the square-planar geometry in Cu(II) complexes. $[Cu(Eg)_3]^{2+}$ has four shorter M$-$O bond distances and two longer with a significant difference of 0.33 Å between the two.

The smaller trans-O$-$M$-$O angle calculated in the $[Cu(Eg)_3]^{2+}$ $\delta\delta\delta$ is due to intramolecular H-bonding between adjacent ligands rather than Jahn-Teller effects, Fig. 4.7. There are two short O$--$H$-$O contacts of 2.57 Å in the $\delta\delta\delta$ conformer and no contacts below 2.72 Å (the sum of the Van der Waals radii of O and H) in the $\lambda\lambda\lambda$ conformer. Intramolecular H-bonding between Eg groups in $\delta\delta\delta$-$[Cu(Eg)_3]^{2+}$ has been proposed in the literature as the cause the stability of the $\delta\delta\delta$ conformer.[20] In this work H-bonding in $\delta\delta\delta$-$[Cu(Eg)_3]^{2+}$ was visualised using the non-covalent interactions (NCI) method, implemented via the AIMALL suite.[13–15]

To visualise NCIs values of $\text{sign}(\lambda_2)\rho$ were colour-mapped onto an isosurface of S = 0.5 with maximum $\rho = 0.02$ a.u. The red regions indicate attractive non-covalent interactions. The red regions in gas phase $\delta\delta\delta$-$[Cu(Eg)_3]^{2+}$ are assigned as H-bonds due to their location between O and H atoms with a short contact distance. In the gas phase $\delta\delta\delta$-$[Cu(Eg)_3]^{2+}$ has two clear H-bonds, while $\lambda\lambda\lambda$-$[Cu(Eg)_3]^{2+}$ does not display any non-covalent interactions, Fig. 4.7. AIM analysis did not locate bond critical points (BCP) for the two H-bonds visualised, due to the reduced density gradient not dropping all the way to 0 at these points. This has also been discussed in the literature, for

	$[FeEg_3]^{2+}$	$[CoEg_3]^{2+}$	$[NiEg_3]^{2+}$	$[CuEg_3]^{2+}$	$[ZnEg_3]^{2+}$	
	d^6	d^7	d^8	d^9	d^{10}	
Crystal field theory configuration:						
Term:	$^5T_{2g}$	$^4T_{1g}$	$^3A_{2g}$	^2E_g	$^1A_{1g}$	
Predicted Jahn-Teller distortion:	Small	Small	None	Large	None	
Optimised structure:						
O-M distances:	2.15	2.12	2.09	4 x 2.01 / 2 x 2.34	2.12	
O-M-O angles:	158	166	163	2 x 163 / 146	160	

Figure 4.6: Electronic configurations, gas phase optimised structures, and key geometric parameters for $[M(Eg)_3]^{2+}$, M = Fe, Co, Ni, Cu, Zn. Angles are given in degrees and distances in Å.

Visulasing H-bonding in [Cu(Eg)₃]²⁺

Gas phase optimised structure

H-bond, 2.57 Å

H-bond, 2.57 Å

Alkyl chains removed for clarity
δδδ (ΔH = 0)

Gas phase – with NCI visualisation

H-bond

146°

H-bond

δδδ (ΔH = 0)

No H-bond

157°

λλλ (ΔH = 17)

SMD applied

No H-bond

160°

δδδ (ΔH = 0)

attractive non-covalent interactions (H-bond or dipole-dipole)

very weak van der Waals interactions

non-bonding, repulsive overlap

-0.012   0   +0.012

Figure 4.7: NCI visualisation of gas phase $\delta\delta\delta$-[Cu(Eg)₃]²⁺ and $\lambda\lambda\lambda$-[Cu(Eg)₃]²⁺, and SMD $\delta\delta\delta$-[Cu(Eg)₃]²⁺. Values of sign(λ_2)ρ are colour-mapped onto an isosurface of S = 0.5 with maximum $\rho = 0.02$ a.u. Energies are given in kJ mol⁻¹.

example a lone Eg molecule was considered to have a H-bond though no BCP was present, through the use of NCI analysis.[21] Although the electron density continuously decreases away from the O atom it decreases less (the gradient reduces) in the region where a BCP would be located in a H-bond with a BCP. Analysis of $\delta\lambda\lambda$ and $\delta\delta\lambda$ conformers (not shown) concluded that H-bonds were only formed between δ ligands and not between two λ ligands or one δ and one λ ligand.

In the SMD environment the shortest O−−−H distance in $\delta\delta\delta$-[Cu(Eg)₃]²⁺ is 2.86Å. The NCI visualisation applied to gas phase $\delta\delta\delta$-[Cu(Eg)₃]²⁺ was applied to the same conformer in the SMD environment, Fig. 4.7, and the H-bonding is "switched off" due to the interaction of the molecule with the implicit solvent. The Jahn-Teller effect increases in the SMD environment (similarly to the earlier finding for [MCl₄]²⁻) with axial and equatorial average M−O bond lengths of 2.48 and 2.04Å respectively. The axial O−M−O angles of gas phase and SMD $\delta\delta\delta$-[Cu(Eg)₃]²⁺, and gas phase $\lambda\lambda\lambda$-[Cu(Eg)₃]²⁺ are highlighted in Fig. 4.7. The angle is significantly reduced in the H-bonding gas phase $\delta\delta\delta$ structure. In the SMD $\delta\delta\delta$ and the gas phase $\lambda\lambda\lambda$ structures the axial O−M−O angles are in line with those observed for the other metals. This confirms the hypothesis that the change in angle is due to the H-bonding and not to the Jahn-Teller effect.

No evidence of similar H-bonding interactions was found for M = Fe, Co, Ni, or Zn in the gas phase, or for any metal in the SMD environment, via O−−H lengths below 2.72 Å or NCI analysis. The O−−−H bond distance in the two H-bonds in $\delta\delta\delta$-[Cu(Eg)₃]²⁺ is 2.57Å, whereas the shortest O−−−H distances in gas phase

$\delta\delta\delta$-[M(Eg)$_3$]$^{2+}$ are 3.09, 3.13, 2.99, and 3.01 for M = Fe, Co, Ni, and Zn respectively. The H-bonding in the $\delta\delta\delta$ and $\delta\delta\lambda$ [Cu(Eg)$_3$]$^{2+}$ conformers is therefore a weak effect as ΔH of $\lambda\lambda\lambda$-[Cu(Eg)$_3$]$^{2+}$ is only increased by between 2 and 5 kJ mol^{-2} compared to $\lambda\lambda\lambda$-[M(Eg)$_3$]$^{2+}$, M = Fe, Ni, Zn, where no H-bonding is observed.

To investigate causes (other than H-bonding) of the increase in ΔH with the number of λ ligands further structural and NCI analysis was completed on the gas phase [Ni(Eg)$_3$]$^{2+}$ conformers, Fig. 4.8. Steric clashes between O atoms are visible in blue. Nine of these clashes are found in the high energy $\lambda\lambda\lambda$ conformer and six in the low energy $\delta\delta\delta$ conformer. By analysing the four [Ni(Eg)$_3$]$^{2+}$ conformers it was determined that the least steric clashes occur between neighbouring δ ligands, an intermediate amount between one δ and one λ ligand, and the most between neighbouring λ ligands. This observation explains the increase in energy for conformers with additional λ ligands for M = Fe, Ni, Cu, and Zn.

The [Co(Eg)$_3$]$^{2+}$ gas phase conformers follow a different trend, which appears to be related to the degree of distortion to the octahedral ligand environment around the metal center. In the lower energy conformers, $\delta\delta\delta$-[Co(Eg)$_3$]$^{2+}$ and $\lambda\lambda\lambda$-[Ni(Eg)$_3$]$^{2+}$, all three trans-O$-$Co$-$O angles are close to equal. In the two high energy mixed ligand complexes one angle is significantly different to the other two angles. The size of the three angles was averaged and the difference between the average angle and the angle the furthest from average was calculated for each conformer. This measure of distortion correlates well with ΔH with an R^2 value of 0.92. (The number of values evaluated is

Visualising steric clashes in gas phase [Ni(Eg)$_3$]$^{2+}$

Figure 4.8: NCI visualisation of gas phase $\delta\delta\delta$-[Ni(Eg)$_3$]$^{2+}$ and $\lambda\lambda\lambda$-[Ni(Eg)$_3$]$^{2+}$. Values of sign(λ_2)ρ are colour-mapped onto an isosurface of S = 0.8 with maximum ρ = 0.01 a.u. Energies are given in kJ mol^{-1}.

small thus R^2 is only indicative, not quantitative.)

The relative energies between conformers in the SMD environment are reduced, and the ΔH vs -TΔS contributions are more broadly spread between conformers with no obvious pattern across the five metals, Fig. 4.9. Overall the conformational effects are small in the solvation environment, especially for M = Ni and Fe. $[Cu(Eg)_3]^{2+}$ is an exception and retains a large ΔG for the $\lambda\lambda\lambda$ conformer, due to it having the highest ΔH and -TΔS contributions to ΔG. For the other four metals the ΔH and -TΔS contributions run counter to one another resulting in low overall ΔG values.

4.3.3 Energetic analysis of the $[MCl_4]^{2-}$ vs $[M(Eg)_3]^{2+}$ equilibrium

The conformers with the lowest ΔE, ΔH, and ΔG values were selected for each species to calculate the ΔE, ΔH, and ΔG values for the following reaction:

$$[MCl_4]^{2-} + 3\,Eg \rightleftharpoons [M(Eg)_3]^{2+} + 4\,Cl^- (M = Fe, Co, Ni, Cu, Zn)$$
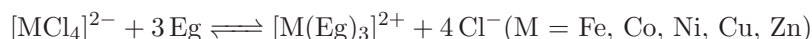
Using ΔG as an example the relative energies were calculated as follows:

$$\Delta G^{reaction} = [G([M(Eg)_3]^{2+}) + 4G(Cl^-)] - [G([MCl_4]^{2-}) + 3G(Eg)]$$

A positive value of $\Delta G^{reaction}$ means that the $[MCl_4]^{2-} + 3\,Eg$ side of the reaction is lower in energy and a negative value that the $[M(Eg)_3]^{2+} + 4\,Cl^-$ side is lower.

In the gas phase $\Delta E_{elec}^{reaction}$ values are large and positive for each metal; $[MCl_4]^{2-} + 3\,Eg$ is the favoured side of the equilibrium, Fig. 4.10. Gas phase electronic energies are typically stabilised by a reduction in overall charge on the molecules calculated, therefore the side of the equilibrium with one 2- complex and 3 neutral species is lower in energy than the side with a 2+ complex and 4 1- ions. The stability of $[M(Eg)_3]^{2+} + 4\,Cl^-$ is significantly higher for M = Ni than for the other metals in the series. $\Delta H^{reaction}$ values follow the same trend but are offset to higher energies. Since H = E_{elec} + zpe + E_{vrt} the increase in energy from $\Delta E_{elec}^{reaction}$ to $\Delta H^{reaction}$ indicates that the zpe and E_{vrt} contributions to H favour the $[MCl_4]^{2-} + 3\,Eg$ side of the reaction. $\Delta G^{reaction}$ values follow the same trend as $\Delta H^{reaction}$ but are offset to higher energies thus we can conclude that entropy factors also favour the $[MCl_4]^{2-} + 3\,Eg$ side.

Similar energetic trends were observed in the SMD solvation environment, with all values shifted significantly lower in energy due to the solvent environment stabilising the charged species. $\Delta E_{elec}^{reaction}$ for M = Ni is negative, reproducing the experimental
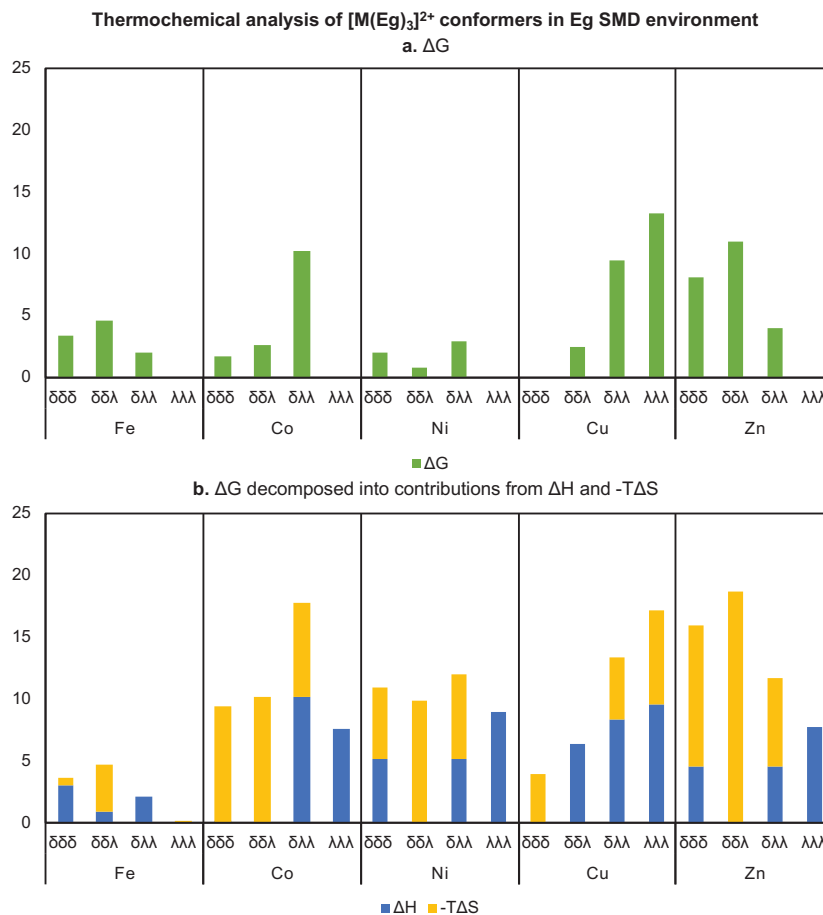
Figure 4.9: a. ΔG of the $\delta\delta\delta$, $\delta\delta\lambda$, $\delta\lambda\lambda$, and $\lambda\lambda\lambda$ conformers of $[M(Eg)_3]^{2+}$, M = Fe, Co, Ni, Cu, Zn, calculated in Eg SMD solvation. b. ΔG split into contributions from ΔH and $-T\Delta$S. Energies are given in kJ mol^{-1}.
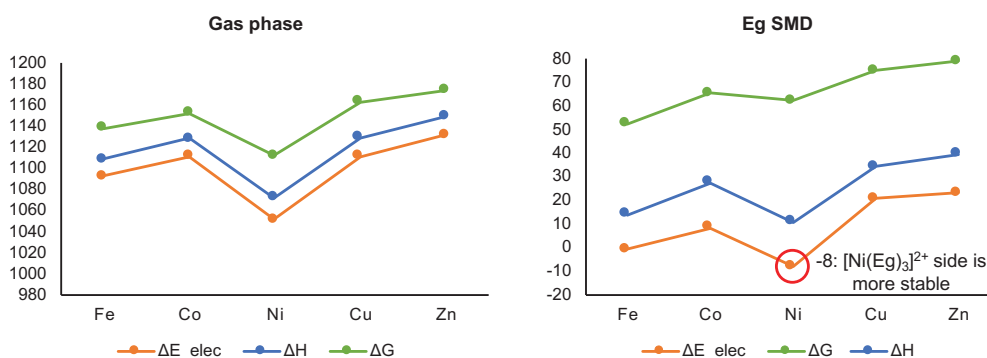
Figure 4.10: $\Delta E_{elec}^{reaction}$, $\Delta H^{reaction}$, and $\Delta G^{reaction}$ values for the reaction: $[MCl_4]^{2-} + 3\,Eg \rightleftharpoons$ $[M(Eg)_3]^{2+} + 4\,Cl^-$ (M = Fe, Co, Ni, Cu, Zn) in the gas phase and with SMD applied. Energies are given in kJ mol^{-1}.

finding that the $[M(Eg)_3]^{2+} + 4\,Cl^-$ side of the reaction is favoured for M = Ni, and the $[MCl_4]^{2-} + 3\,Eg$ side is favoured for M = Fe, Co, Cu and Zn, Fig. 4.1.[1] The $\Delta H^{reaction}$ and $\Delta G^{reaction}$ values follow the same trend as $\Delta E_{elec}^{reaction}$ but are offset to higher values such that the $[MCl_4]^{2-} + 3\,Eg$ side is favoured for the full series of metals. The shift to

higher energy for ΔH and ΔG indicate it is ΔE which underpins the stability of $[\text{Ni}(\text{Eg})_3]^{2+}$ relative to $[\text{NiCl}_4]^{2-}$.

To investigate further the difference between nickel and the other metals in the series in calculations and experiment the complexation energies for $[\text{MCl}_4]^{2-}$ and $[\text{M}(\text{Eg})_3]^{2+}$ were calculated, Fig. 4.11. The complexation energy is the energy of the complex relative to the energy of its separate components.

$$\Delta\text{H}^{\text{complexation}}([\text{MCl}_4]^{2-}) = \text{H}([\text{MCl}_4]^{2-}) - \text{H}(\text{M}^{2+} + 4\,\text{Cl}^-)$$

$$\Delta\text{H}^{\text{complexation}}([\text{M}(\text{Eg})_3]^{2+}) = \text{H}([\text{M}(\text{Eg})_3]^{2+}) - \text{H}(\text{M}^{2+} + 3\,\text{Eg})$$
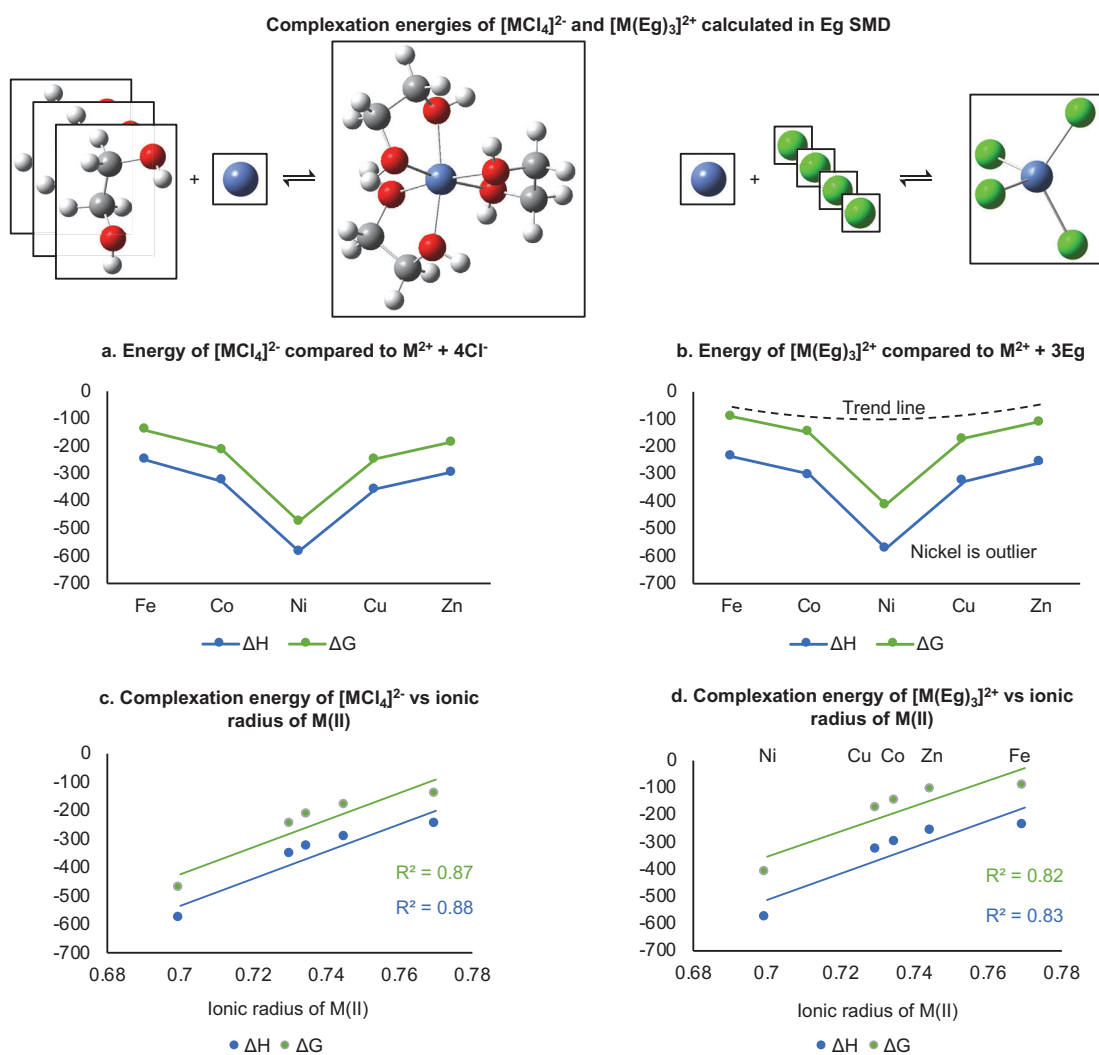
Figure 4.11: $\Delta\text{H}^{\text{complexation}}$ and $\Delta\text{G}^{\text{complexation}}$ values for: $\text{M}^{2+} + 4\,\text{Cl}^- \longrightarrow [\text{MCl}_4]^{2-}$ and $\text{M}^{2+} + 3\,\text{Eg} \longrightarrow [\text{M}(\text{Eg})_3]^{2+}$ (M = Fe, Co, Ni, Cu, Zn) in the gas phase and with SMD applied. ($\Delta\text{H}^{\text{complexation}}([\text{M}(\text{Eg})_3]^{2+}) = \text{H}([\text{M}(\text{Eg})_3]^{2+}) - \text{H}(\text{M}^{2+} + 3\,\text{Eg})$) Energies are given in kJ mol^{-1}.

Complexation energies are large and negative as they contain the energy of formation of all the bonds in the complexes, Fig. 4.11.a-b. $\Delta G^{complexation}$ values are smaller than $\Delta H^{complexation}$ because the uncomplexed side of the reaction has more free molecules than the complexed side and is therefore entropically favoured. The entropy effect is larger for $[M(Eg)_3]^{2+}$ than $[MCl_4]^{2-}$.

Similar trends across the metal series were obtained for $[MCl_4]^{2-}$ and $[M(Eg)_3]^{2+}$, Fig. 4.11.a-b. For the metals which are not nickel, the series form relatively shallow U-shaped curves with M = Fe and Zn having smaller complexation energies, and M = Co and Cu slightly larger values. At M = Ni the values drop sharply to lower energies; both complexes are significantly more stabilised relative to the separate species compared to the other metals. The complexation energies of $[MCl_4]^{2-}$ correlate with the experimental values of ionic radii of M(II) obtained from Shannon *et al.*, Fig. 4.11.c-d.[22]

4.4   Complexation of nickel(II) in ethaline DES

The complexation of Ni(II) in the ethaline-$NiCl_2 \cdot 6\,H_2O$ system was investigated in more detail via a survey of the different nickel containing complexes which could potentially form in solution, Fig. 4.12. The aim is to understand the relative stabilities of different species, and the relationship between stability and type and number of ligands included in a complex. A comprehensive set of nickel containing complexes was selected using several assumptions:
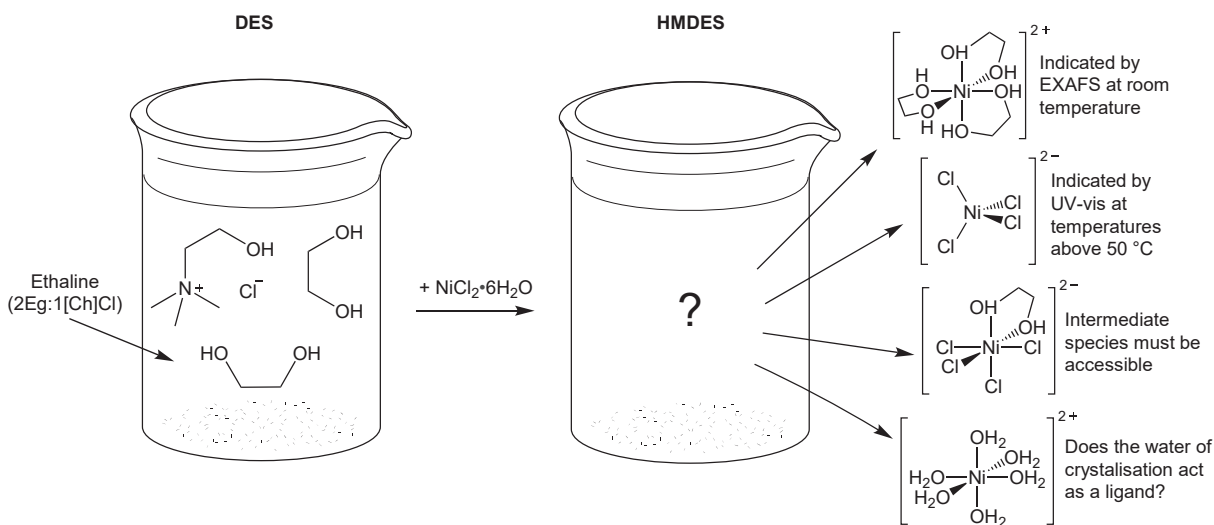
Figure 4.12: The ethaline-$NiCl_2 \cdot 6\,H_2O$ HMDES contains Ni(II) and several potential ligand species. Experimental evidence for $[NiCl_4]^{2-}$ and $[Ni(Eg)_3]^{2+}$ is reported, and intermediate complexes with a mixture of Cl and Eg ligands will be investigated.[1] The water of crystallisation may also act as a ligand.

1. Potential ligands are Cl^-, H_2O, and Eg.

2. Eg coordinates as a neutral bidentate ligand.

3. In complexes with mixed coordination the coordination number is assumed to be 6.

4. If all ligands are the same then complexes with coordination of 4 and 6 ligands were included.

These assumptions generate 19 complexes to consider, Fig. 4.13. The 19 complexes were optimised and analysed in terms of relative stability, geometric structure and electronic structure. Further, neutralised versions of the charged complexes were constructed by the addition of appropriate numbers of Cl^- ions to positively charged complexes and Ch^+ cations to negatively charged complexes. The effects of neutralising the complexes on the relative stability, geometric structure and electronic structure were analysed, as well as the non-covalent interactions present between the neutralising anions/cations and the nickel complexes. Previously low spin (multiplicity = 1) $[NiCl_4]^{2-}$ and $[Ni(Eg)_3]^{2+}$ complexes were found to be >100 kJ mol^{-1} higher in energy than the corresponding high spin (multiplicity = 3) complexes. Based on this result all
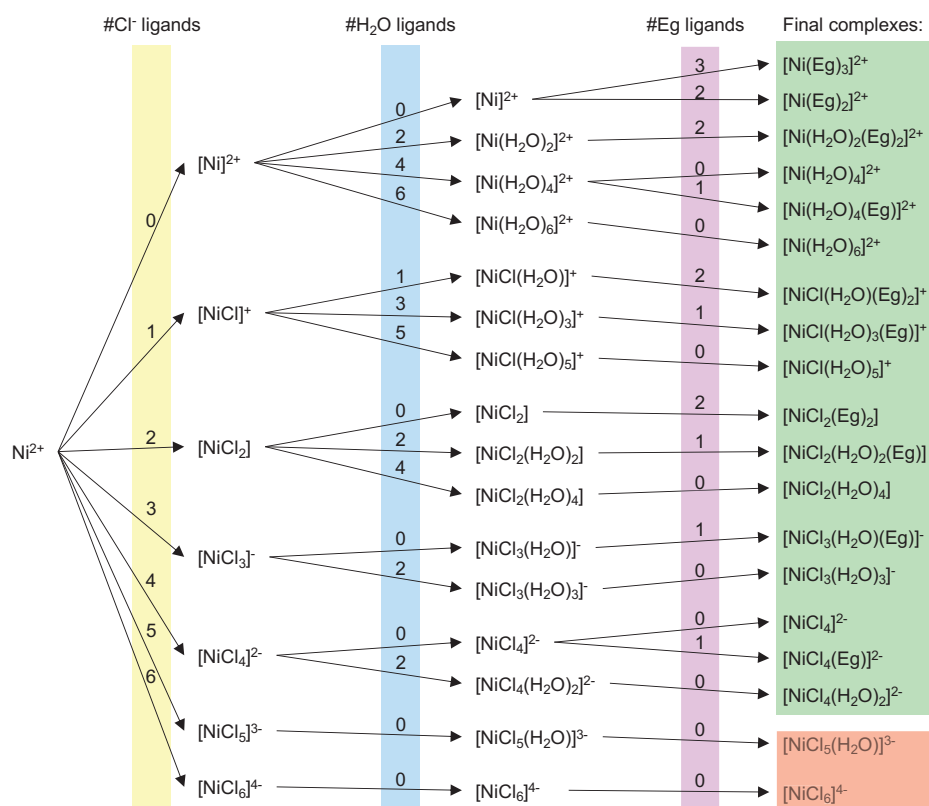
Figure 4.13: Nickel containing species included in the intial survey. $[NiCl_6]^{4-}$ and $[NiCl_5(H_2O)]^{3-}$ are highlighted in red as calculations on these species failed due to spontaneous dissociation, and they are not considered further.

subsequent nickel complexes were calculated with multiplicity values of 3. The small energy differences between conformers in $[Ni(Eg)_3]^{2+}$ informed the decision not to investigate conformers with differing Eg conformations for the series of discrete complexes. For each complex a single conformer for each different ligand configuration was optimised. The direct coordination of Ch^+ to the nickel centre was tested via optimisation of $[NiCl_4]Ch_2$ and $[NiCl_4Ch_2]$ in the SMD environment, Fig. 4.14.a. The configuration with Ch^+ acting as a ligand is significantly higher in energy thus Ch^+ was not further considered as a ligand. A scan of the rotation of a single water ligand in $[Ni(H_2O)_6]^{2+}$ revealed that the energy barrier to water rotation is low, Fig. 4.14.b. Therefore conformational searches included only a single water ligand orientation.

Testing

a. Direct coordination of Ch⁺ to Ni is disfavoured

$[NiCl_4]Ch_2$

Av. Ni-Cl distance:
2.31 Å

$\Delta G = 0$

$[NiCl_4Ch_2]$

Av. Ni-Cl distance:
2.47 Å

$\Delta G = 38$ kJ mol⁻¹

b. Rotation of water ligands is facile

Optimisation from any water orientation leads to the global minimum
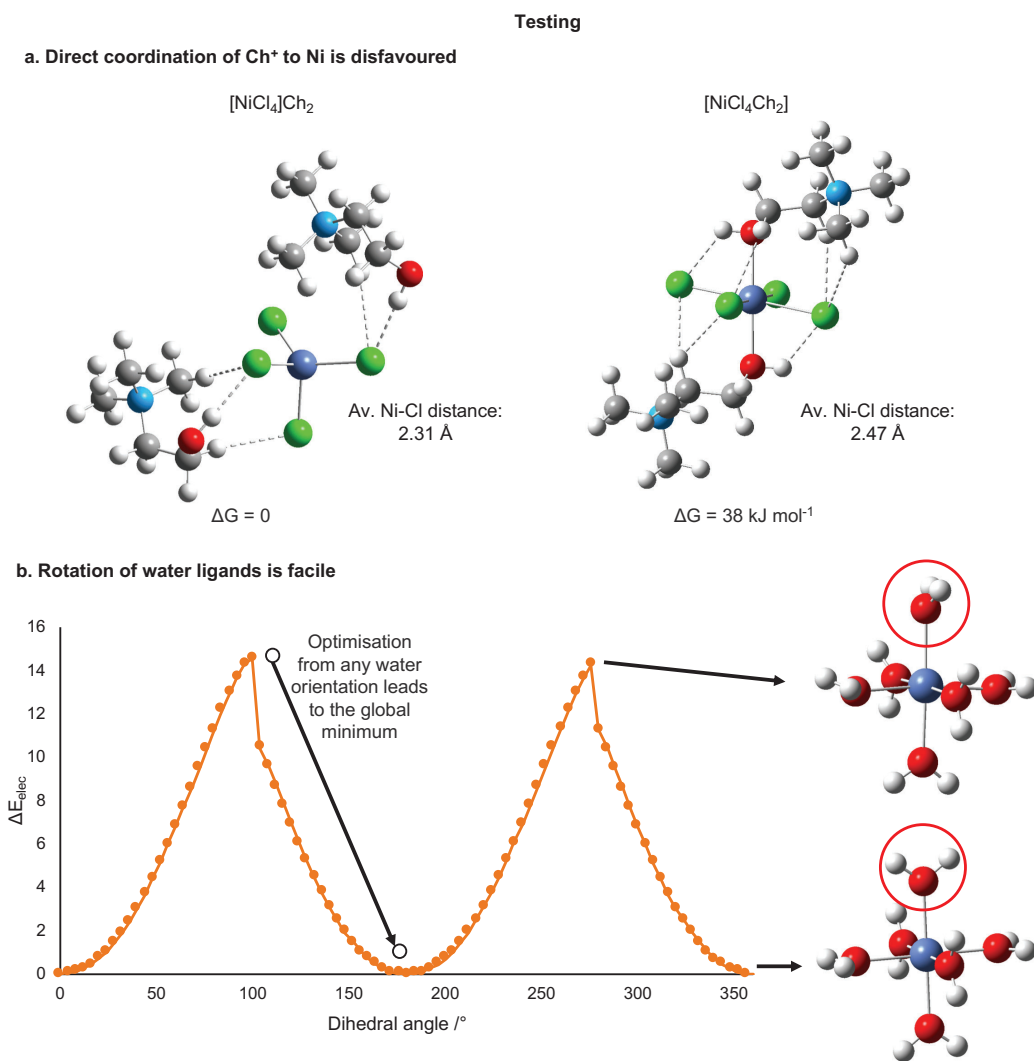
Figure 4.14: a. $[NiCl_4]Ch_2$ is significantly lower in energy than $[NiCl_4Ch_2]$ in the SMD environment. b. Rotation of water ligands in $[Ni(H_2O)_6]^{2+}$ is facile in the gas phase.

4.4.1 Structure of discrete complexes

The structures of $[NiCl_4]^{2-}$ and $[Ni(Eg)_3]^{2+}$ were discussed in Section 4.3.1 and Section 4.3.2. It was not possible to optimise $[NiCl_6]^{4-}$ or $[NiCl_5(H_2O)]^{3-}$ structures in the gas phase or SMD environment, likely due to the high charges on the complexes and repulsion between Cl^- ligands, which resulted in dissociated structures. The remaining 15 complexes were optimised in the gas phase, Fig. 4.15 and employing SMD environment, Fig. 4.16.

In the gas phase (but not when SMD was applied) cis-$[NiCl_2(Eg)_2]$, $[NiCl_4(Eg)]^{2-}$, and trans-$[NiCl_3(H_2O)(Eg)]^-$ experienced ligand dissociation during the optimisation process. The optimised structures generated in the SMD environment were reoptimised in the gas phase, also resulting in ligand dissociation. The released ligands formed partial second coordination shells with $Cl--O-H$ H-bonds to the former ligand. The obtained structures are shown in red boxes, Fig. 4.15. Relative energies of dissociated conformers are not given and their energies are not considered further, as they are no longer considered to be discrete complexes.

Most structures obtained in the SMD environment are similar to those in the gas phase. In both cases free energy differences between conformers with different ligand configurations are small. In the gas phase the average ΔG between the highest and lowest energy conformer of a complex is 6, and the largest is 14 kJ mol^{-1} for $[NiCl_2(H_2O)_4]$. When the SMD is applied the average is 2.9 and the largest is 8 kJ mol^{-1} for $[NiCl_4(H_2O)_2]$.

The structures of the homogeneously coordinated discrete complexes follow the patterns found for $[NiCl_4]^{2-}$ and $[Ni(Eg)_3]^{2+}$. $[Ni(Eg)_2]^{2+}$ is sawhorse shaped in both gas and SMD. In the SMD the structure is closer to an ideal sawhorse than in the gas phase with axial and equatorial $O-Ni-O$ angles of 157° and 115° (gas) and 170° and 99° (SMD). $Ni-O$ bond lengths are slightly longer when the SMD is applied (2.00-2.02Å) than in the gas phase (1.97-1.99Å), an observation which holds across the series of discrete complexes.

The shape of $[Ni(H_2O)_4]^{2+}$ is also affected by the solvation environment: in the gas phase it is a distorted tetrahedron with four $O-Ni-O$ angles of 119° and two of 93°, when the SMD is applied the complex is sawhorse with axial and equatorial $O-Ni-O$ angles of 157° and 108°.

The shape of octahedral complexes are less affected by solvation environment than four coordinate complexes; likely due to more constraints on shape from steric

Homogenous coordination

$[Ni(Eg)_2]^{2+}$　　$[Ni(H_2O)_4]^{2+}$　　$[Ni(H_2O)_6]^{2+}$

Mixed H$_2$O and Eg coordination

$[Ni(H_2O)_4(Eg)]^{2+}$　　$[Ni(H_2O)_2(Eg)_2]^{2+}$

trans, +0.3　　cis

Mixed H$_2$O and Cl coordination

$[NiCl(H_2O)_5]^+$　　$[NiCl_2(H_2O)_4]$　　$[NiCl_3(H_2O)_3]^-$　　$[NiCl_4(H_2O)_2]^{2-}$

trans, +13.7　　cis　　trans　　cis, +0.3　　trans, +12.9　　cis

Mixed Eg and Cl coordination

$[NiCl_2(Eg)_2]$　　　　$[NiCl_4(Eg)]^{2-}$

trans　　dissosciated　　dissosciated

Mixed H$_2$O, Eg, and Cl coordination

$[NiCl(H_2O)_3(Eg)]^+$　　$[NiCl(H_2O)(Eg)_2]^+$

trans　　cis, +9.5　　trans　　cis, +0.4

$[NiCl_2(H_2O)_2(Eg)]$　　$[NiCl_3(H_2O)(Eg)]^-$

trans(Cl)　　trans(H$_2$O), +0.4　　cis, +7.7　　dissosciated　　cis

Figure 4.15: Gas phase optimised structures of potential nickel containing complexes in the ethaline-NiCl$_2 \cdot 6$ H$_2$O system. For complexes with multiple ligand configurations ΔG values in kJ mol^{-1} are given for the higher energy structures. The structures of $[NiCl_4]^{2-}$ and $[Ni(Eg)_3]^{2+}$ were discussed in Section 4.3.1 and Section 4.3.2. The structures in red boxes are those for which ligand dissociation occurred during the optimisation. Dashed bonds indicate Cl$--$H distances of ≤ 3.00 Å, and O$--$H distances of ≤ 2.72 Å.

Homogenous coordination

[Ni(Eg)$_2$]$^{2+}$ [Ni(H$_2$O)$_4$]$^{2+}$ [Ni(H$_2$O)$_6$]$^{2+}$

Mixed H$_2$O and Eg coordination

[Ni(H$_2$O)$_4$(Eg)]$^{2+}$ [Ni(H$_2$O)$_2$(Eg)$_2$]$^{2+}$

trans, +5.2   cis

Mixed H$_2$O and Cl coordination

[NiCl(H$_2$O)$_5$]$^+$ [NiCl$_2$(H$_2$O)$_4$]   [NiCl$_3$(H$_2$O)$_3$]$^-$ [NiCl$_4$(H$_2$O)$_2$]$^{2-}$

trans   cis, +0.3   trans, +0.0   cis   trans, +7.6   cis

Mixed Eg and Cl coordination

[NiCl$_2$(Eg)$_2$]   [NiCl$_4$(Eg)]$^{2-}$

trans, +6.0   cis

Mixed H$_2$O, Eg, and Cl coordination

[NiCl(H$_2$O)$_3$(Eg)]$^+$ [NiCl(H$_2$O)(Eg)$_2$]$^+$

trans   cis, 3.3   trans   cis, 0.6

[NiCl$_2$(H$_2$O)$_2$(Eg)]   [NiCl$_3$(H$_2$O)(Eg)]$^-$

trans(Cl), +1.9   trans(H$_2$O), +1.0   cis   trans, +1.2   cis

Figure 4.16: SMD optimised structures of potential nickel containing complexes in the ethaline–NiCl$_2$ · 6 H$_2$O system. The structures of [NiCl$_4$]$^{2-}$ and [Ni(Eg)$_3$]$^{2+}$ were discussed in Section 4.3.1 and Section 4.3.2. The complexes in black boxes are those which underwent ligand dissociation when optimised in the gas phase. For complexes with multiple ligand configurations ΔG values in kJ mol^{-1} are given for the higher energy structures. Dashed bonds indicate Cl−−H distances of ≤ 3.00 Å, and O−−H distances of ≤ 2.72 Å.

repulsion between ligands. Also the electronic configuration of Ni(II), d^8, lends itself to Jahn-Teller distortion for tetrahedral complexes but not octahedral complexes, Figs. 4.3 and 4.6. Therefore $[Ni(H_2O)_6]^{2+}$ is close to ideal octahedral conformation in both the gas phase (trans $O-Ni-O$ angles of 180°, Ni$-$O bond lengths of 2.08Å) and in the SMD environment (trans $O-Ni-O$ angles of 177°, Ni$-$O bond lengths of 2.08-2.09Å).

Distortions away from ideal octahedral structure are seen in the mixed complexes, seemingly in order to facilitate intramolecular H-bonding between Cl ligands and H atoms on either water or Eg ligands. A representative example is $[NiCl_4(H_2O)_2]^{2-}$, which forms four H-bonds in the gas phase and two when SMD was utilised, Fig. 4.17. The H-bonding was analysed via structural parameters, AIM analysis, and NCI visualisation. The complexes are almost symmetrical in both environments and the water ligands are equivalent to one another. In the gas phase each water ligand has two H-bonds which are both shorter than the single H-bond to each water ligand in the SMD complex. Compression of the $O-Ni-Cl$ angles between H-bonding ligands is present in both environments but reduced upon application of the SMD. Electron density (ρ) at the BCPs of the H-bonds was also reduced in the SMD. To visualise the H-bonding values of $sign(\lambda_2)\rho$ were colour-mapped onto an isosurface of S = 0.5 with maximum $\rho = 0.05$ a.u. , Fig. 4.17. The Ni$-$ligand bonds are relatively weak with ρ at the BCPs in the same range as at the strong H-bonding BCPs. Therefore the NCI visualisation also shows the covalent Ni$-$ligand bonds, as ρ at the covalent bonds is within the maximum value required to visualise the H-bonding. The geometric distortion of complexes to form intramolecular H-bonds is seen across the series of complexes with Cl ligands, as is the weakening of the H-bonds when SMD is applied. Weaker H-bonding in the Eg SMD environment is expected due to the interaction of the atoms with the SMD cavity which weakens the other interactions present.

4.4.2 Energetic analysis of discrete complexes

To enable comparison between complexes a minimal model system of the following species was conceived:

$$Ni^{2+} : 4\,Cl^- : 2\,Ch^+ : 6\,H_2O : 3\,Eg$$

The energy of a given system was calculated by adding the energy of the relevant complex to that of the molecules not already present in the nickel complex, Fig. 4.18. Any Cl$^-$ anions not coordinated to the nickel atom were assumed to pair with any

Gas phase [NiCl$_4$(H$_2$O)$_2$]$^{2-}$ contains four H-bonds to Cl ligands

80°

76°

2.26 Å

2.15 Å

SMD [NiCl$_4$(H$_2$O)$_2$]$^{2-}$ contains two H-bonds to Cl ligands

86°

79°

2.61 Å

2.32 Å

Optimised structures

Moderate H-bond, ρ = 0.024 a.u.

Weak covalent bond, ρ = 0.039 a.u.

Strong H-bond, ρ = 0.030 a.u.

Weak interaction, no bcp

Moderate H-bond, ρ = 0.022 a.u.

Optimised structures with NCIs mapped

Covalent bonding	Non-covalent bonding interactions	very weak van der Waals interactions	non-bonding, repulsive overlap

-0.04　　　　　　0　　　　　　+0.04

Figure 4.17: H-bonding in [NiCl$_4$(H$_2$O)$_2$]$^{2-}$ in the gas phase and with an SMD environment applied. AIM BCPs are indicated by bonds drawn between atoms; solid lines for BCPs with $\rho \geq 0.03$, dashed lines for BCPs with $\rho < 0.03$. NCI visualisations were created using Aimall.[14,23] Values of sign(λ_2)ρ are colour-mapped onto an isosurface of S = 0.5 with maximum $\rho = 0.05$ a.u.

available Ch^+ cations. For example the free energy of $[Ni(Eg)_3]^{2+}$ in the discrete complex (DC) model $(G(DC\text{-}[Ni(Eg)_3]^{2+}))$ was calculated as follows:

$$G(DC\text{-}[Ni(Eg)_3]^{2+}) = G([Ni(Eg)_3]^{2+}) + 2G([ChCl]) + 2G(Cl^-) + 6G(H_2O)$$

Relative thermochemical parameters for all complexes were then calculated, using $DC\text{-}[Ni(Eg)_3]^{2+}$ as the reference level, for example:

$$\Delta G(DC\text{-}complex) = G(DC\text{-}complex) - G(DC\text{-}[Ni(Eg)_3]^{2+})$$

The relative thermochemical values for the 17 systems of nickel complexation shown in Fig. 4.13 were calculated in the gas phase, Fig. 4.19. In the gas phase $\Delta G(DC\text{-}complex)$ and $\Delta E_{elec}(DC\text{-}complex)$ are well correlated with a coefficient of determination (R^2) of 0.99, therefore electronic effects dominate the thermodynamic stability of complexes within the gas phase DC model.

The charge on the nickel complex (determined by the number of Cl^- ligands) accounts for most of the variation in energy between systems, with neutral complexes being the most stable. This result is explained by systems with two Cl^- ligands in the
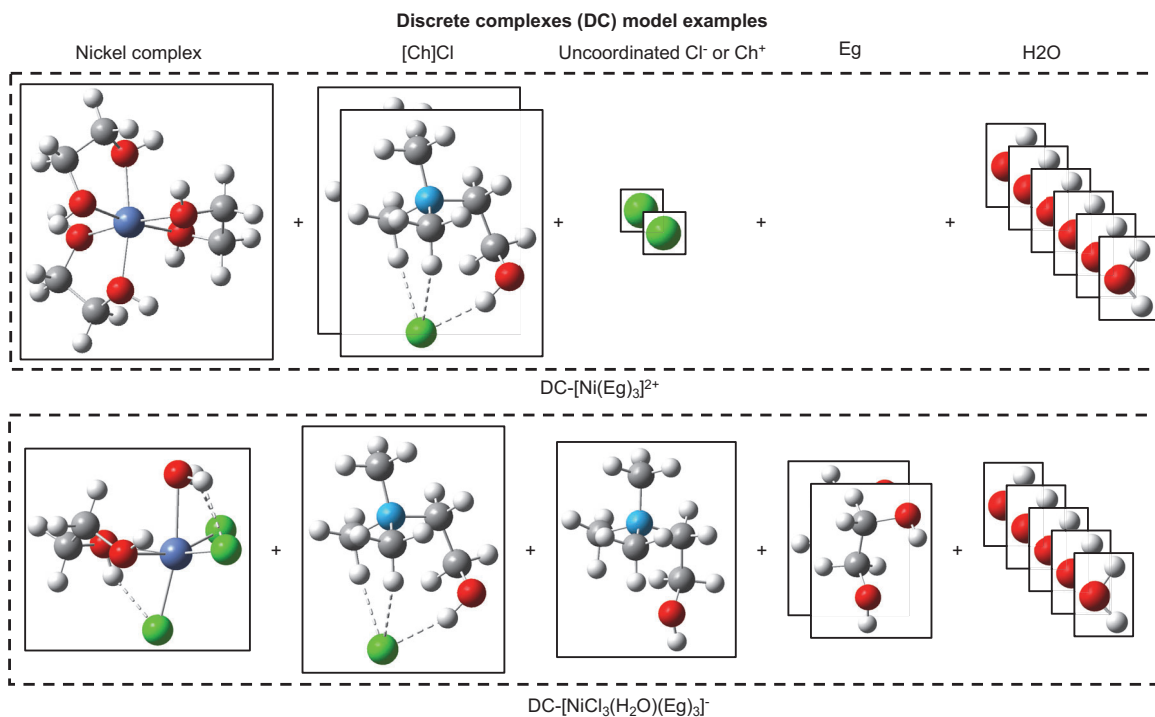
Figure 4.18: Pictorial example of the discrete complexes (DC) model for DC-$[Ni(Eg)_3]^{2+}$ and DC-$[NiCl_3(H_2O)(Eg)]^-$.

complex being composed of entirely neutral species, since the complexes are neutral and both Cl^- ligands not in the complex are coordinated to Ch^+. The lowest energy system is DC-[NiCl$_2$(H$_2$O)$_4$]. The entropy contribution (-TΔS) to ΔG is an order of magnitude smaller than the electronic contribution, so has no significant effect on ΔG. -TΔS is not correlated with the charge on the nickel complex but with the number of water ligands coordinated to the Ni atom. Systems with more water molecules coordinated to the ligand have a lower S than those with fewer water ligands and therefore a higher -TΔS.

In the SMD environment ΔH follows the same trend as in the gas phase; the lowest energy systems are those with neutral nickel complexes, Fig. 4.20. Whilst following the same trend as in the gas phase, the SMD ΔH values are significantly reduced in magnitude with the SMD applied. The -TΔS values correlate with the number of water ligands coordinated to the nickel centre, and have values close to those calculated in the gas phase. ΔG values are dominated by the entropic contribution and also increase as the number of water molecules coordinated to the nickel centre increases. The lowest ΔG value is for [NiCl$_4$]$^{2-}$. No correlation between relative energies and number of Eg ligands in the complex is evident.

4.4.3   Structure of neutralised complexes

In the discrete complexes model the relative energies of the complexes were largely determined by the charge on the complex, with neutral complexes lowest in ΔG and ΔH

Figure 4.19: Gas phase DC-*complex* thermochemical parameters calculated relative to DC-[Ni(Eg)$_3$]$^{2+}$. Values are reported in kJ mol^{-1}.
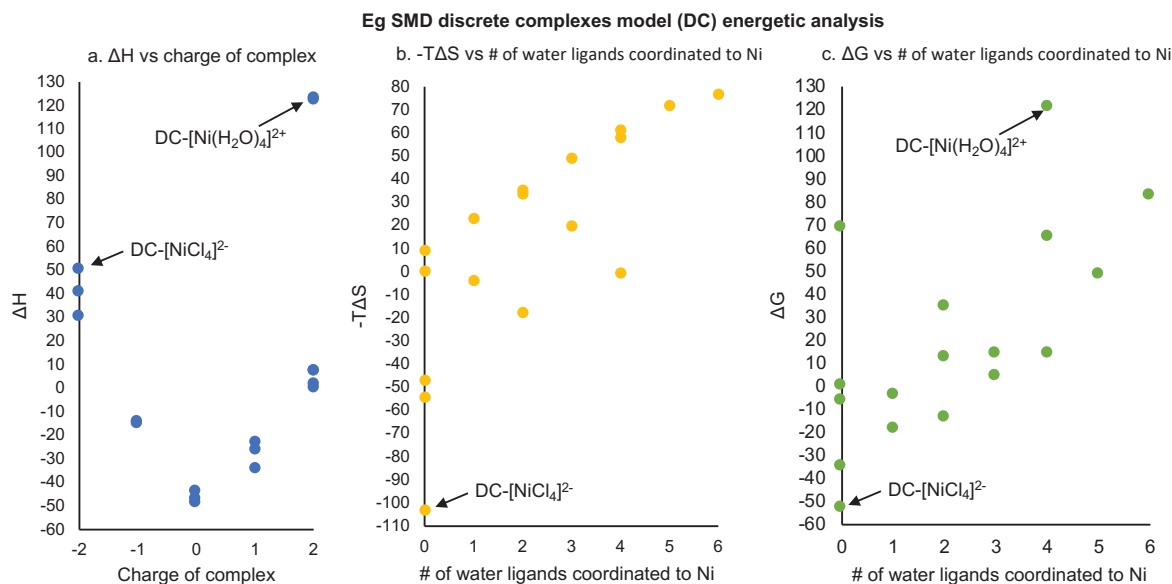
Figure 4.20: Eg SMD DC-*complex* thermochemical parameters calculated relative to DC-[Ni(Eg)$_3$]$^{2+}$. Values are reported in kJ mol^{-1}.

in the gas phase, and in ΔH in the SMD environment. Therefore the neutralised complexes (NC) model was formulated, in which each nickel complex is neutralised by the addition of Cl$^-$ or Ch$^+$.

A single conformer was optimised for each species with the additional Cl$^-$ or Ch$^+$ ions positioned to maximise Cl$-$$-$H hydrogen bonding, Figs. 4.21 and 4.22. Choosing to optimise only a single conformer for each species reduces both the computational and human resources required to complete the survey, however a potential error is introduced. The conformer chosen may not be the lowest energy conformer which could affect the calculated energies. The size of this error is likely to be small as the potential binding sites around each complex are chemically similar. The NC systems will be referred to as NC-*complex*; for example "the NC-[Ni(Eg)$_3$]$^{2+}$ system" means [Ni(Eg)$_3$]Cl$_2$ + 2ChCl + 6H$_2$O.

All neutralised complexes contain multiple short ($\leq$ 3.00) Cl$-$$-$H contacts. Gas and SMD structures are similar for all complexes, with SMD structures containing slightly fewer short Cl$-$$-$H contacts. Intramolecular (ligand-ligand) interactions are reduced compared to the non-neutralised complexes, and the shortest contacts are intermolecular (Cl$^-$ or Ch$^+$ to ligand).

A detailed analysis of the H-bonding in the representative system [NiCl$_4$(H$_2$O)$_2$]Ch$_2$ was completed, utilising geometrical data, AIM analysis and NCI visualisation, Fig. 4.23. In the gas phase each axial Cl atom has three BCPs with

Cl coordination

[NiCl$_4$]Ch$_2$

Gas   SMD

Mixed Eg and Cl coordination

[NiCl$_4$(Eg)]Ch$_2$

Gas   SMD

Mixed H$_2$O and Cl coordination

[NiCl$_3$(H$_2$O)$_3$]Ch   [NiCl$_4$(H$_2$O)$_2$]Ch$_2$

Gas   SMD   Gas   SMD

Mixed H$_2$O, Eg, and Cl coordination

[NiCl$_3$(H$_2$O)(Eg)]Ch

Gas   SMD

Figure 4.21: The gas and SMD optimised structures of negatively charged complexes, neutralised by the addition of Ch$^+$ ions. Dashed bonds indicate Cl−−H distances of >3.00Å, or O−−H distances of >2.72Å.

Eg coordination

$[Ni(Eg)_3]Cl_2$

Gas   SMD

$[Ni(Eg)_2]Cl_2$

Gas   SMD

H₂O coordination

$[Ni(H_2O)_4]Cl_2$

Gas   SMD

$[Ni(H_2O)_6]Cl_2$

Gas   SMD

Mixed H₂O and Eg coordination

$[Ni(H_2O)_4(Eg)]Cl_2$

Gas   SMD

$[Ni(H_2O)_2(Eg)_2]Cl_2$

Gas   SMD

Mixed H₂O and Cl coordination

$[NiCl(H_2O)_5]Cl$

Gas   SMD

Mixed H₂O, Eg, and Cl coordination

$[NiCl(H_2O)_3(Eg)]Cl$

Gas   SMD

$[NiCl(H_2O)(Eg)_2]Cl$

Gas   SMD

Figure 4.22: The gas and SMD optimised structures of positively charged complexes, neutralised by the addition of Cl^- ions. Dashed bonds indicate $Cl--H$ distances of >3.00Å, or $O--H$ distances of >2.72Å.

173

Gas phase [NiCl$_4$(H$_2$O)$_2$]Ch$_2$ contains three H-bonds to Cl ligands

2.19 Å   2.46 Å

79°

2.32 Å

SMD [NiCl$_4$(H$_2$O)$_2$]Ch$_2$ contains two H-bonds to Cl ligands

2.15 Å

80°

2.39 Å

Optimised structures

Strong H-bond, $\rho = 0.026$ a.u.

Weak H-bond, $\rho = 0.016$ a.u.

Moderate H-bond, $\rho = 0.022$ a.u.

Weak H-bond, $\rho = 0.019$ a.u.

Strong H-bond, $\rho = 0.028$ a.u.

Optimised structures with NCIs mapped

Covalent bonding	Non-covalent bonding interactions	very weak van der Waals interactions	non-bonding, repulsive overlap

-0.04   0   +0.04

Figure 4.23: H-bonding in [NiCl$_4$(H$_2$O)$_2$]Ch$_2$ in the gas phase and with an SMD environment applied. AIM BCPs are indicated by bonds drawn between atoms; solid lines for BCPs with $\rho \geq 0.03$, dashed lines for BCPs with $0.015 < \rho < 0.03$. NCI visualisations were created using Aimall.[14,23] Values of sign(λ_2)ρ are colour-mapped onto an isosurface of S $= 0.5$ with maximum $\rho = 0.05$ a.u.

$0.015 < \rho < 0.03$ indicating non covalent interactions with close H atoms. The strongest interaction is with the $-OH$ group attached to the Ch^+, and the weakest with an alkyl H atom from the Ch^+. The H_2O-Cl intramolecular H-bond observed in $[NiCl_4(H_2O)_2]^{2-}$ is retained but weakened by the additional interactions with the Cl atom present in the neutralised cluster. In the SMD environment each axial Cl atom has two BCPs with $0.015 < \rho < 0.03$, reduced from three in the gas phase. The *intra*molecular H-bond is weaker than that found in the gas phase, but the *inter*molecular H-bond with the $-OH$ group attached to the Ch^+ is stronger. Overall fewer H-bonds were formed in the SMD environment than the gas phase, and most H-bonds were weakened by the SMD, but a single stronger interaction also occurred.

4.4.4 Energetic analysis of neutralised complexes

The relative thermochemical values of each NC-*complex* system have been calculated, relative to NC-$[Ni(Eg)_3]^{2+}$, in both the gas phase and in the SMD environment, Fig. 4.24. For example, to determine the ΔG of NC-$[NiCl_4]^{2-}$ the following calculation was carried out:

Figure 4.24: Pictorial example of the neutralised complexes (NC) model for NC-$[Ni(Eg)_3]^{2+}$ and NC-$[NiCl_3(H_2O)(Eg)]^-$.

Gas phase neutralised complexes model (NC) energetic analysis
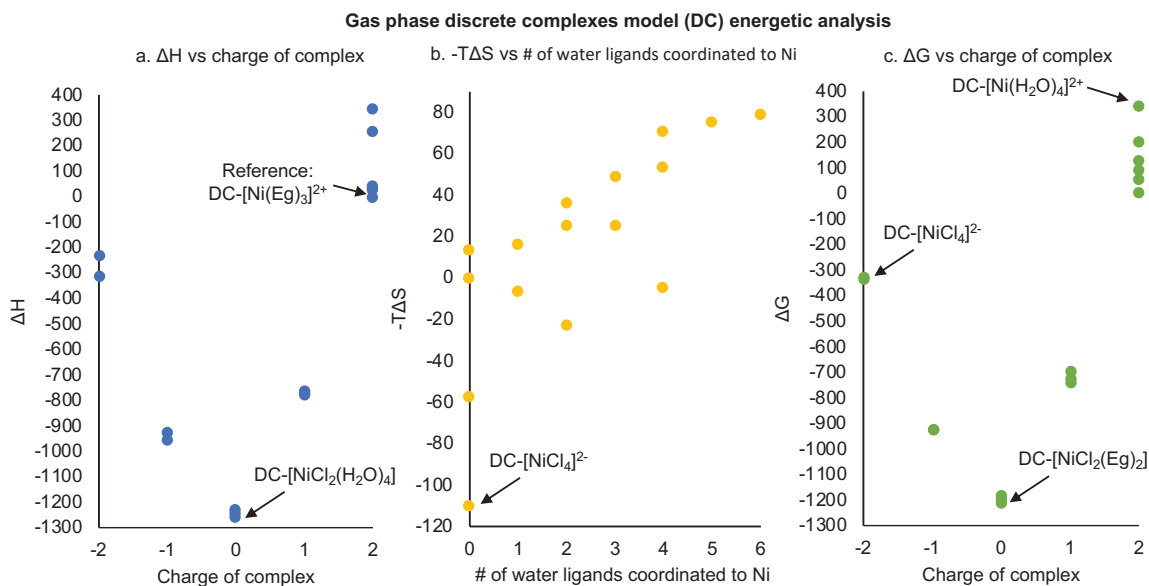
Figure 4.25: Gas phase NC-*complex* thermochemical parameters calculated relative to NC-[Ni(Eg)$_3$]$^{2+}$. Values are reported in kJ mol^{-1}.

$$\Delta G(\text{NC-[NiCl}_4]^{2-}) = G(\text{NC-[NiCl}_4]^{2-}) - G(\text{NC-[Ni(Eg)}_3]^{2+})$$

$$G(\text{NC-[Ni(Eg)}_3]^{2+} = G([\text{Ni(Eg)}_3]\text{Cl}_2) + 2G(\text{ChCl}) + 6G(\text{H}_2\text{O})$$

$$G(\text{NC-[NiCl}_4]^{2-}) = G([\text{NiCl}_4]\text{Ch}_2) + 6G(\text{H}_2\text{O}) + 6G(\text{Eg})$$
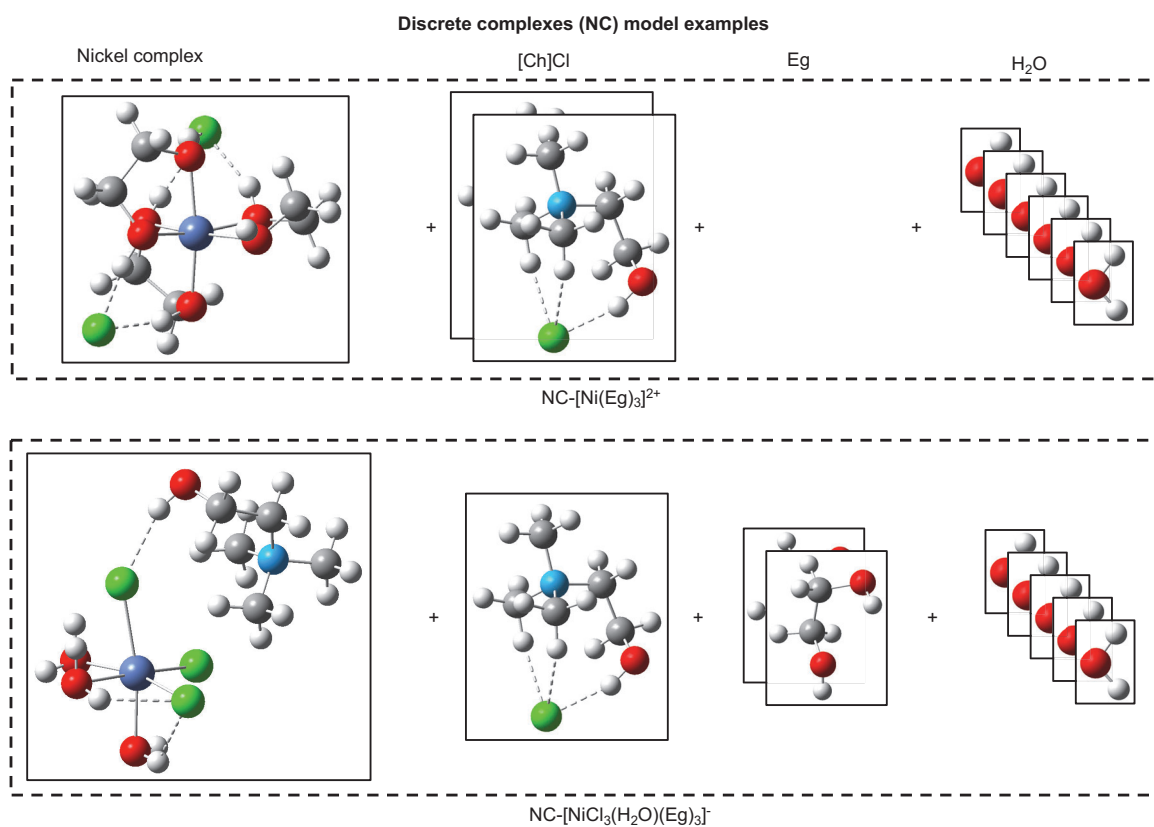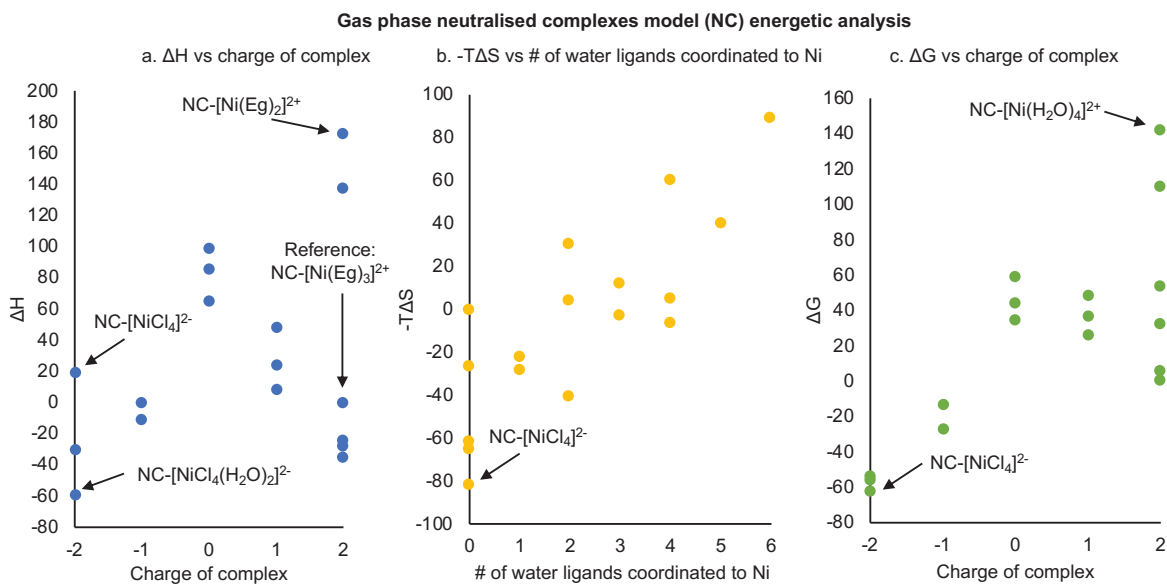
In the gas phase significant changes to the relative thermochemical values of the complexes occurred upon applying the NC model, Fig. 4.25. ΔH values correlate with the charge on the nickel containing complex, in an inversion of the trend in the DC model, Fig. 4.19. Higher charged complexes are lower in enthalpy in the NC model where Cl$^-$ or Ch$^+$ are added to create a neutral cluster. The decrease in enthalpy for charged complexes can be attributed to strong Coulombic forces and doubly ionic H-bonds between molecules in the clusters. The higher the charge on the nickel complex the more neutralising species are added to the complex, increasing the intermolecular interactions and reducing the total enthalpy of the system. This effect is more pronounced for the negatively charged complexes than those with positive charges. The only exceptions to this trend are NC-[Ni(Eg)$_2$]$^{2+}$ and NC-[Ni(H$_2$O)$_4$]$^{2+}$ both of which are high energy systems due to the nickel centre being undercoordinated. The ΔH values are significantly reduced in magnitude compared to those calculated for the gas phase DC model. A similar trend occurs in the SMD NC model ΔH values, Fig. 4.26.a, with the difference that the systems with negatively charged complexes are not stabilised relative to the neutral complex systems. Small enthalpy differences between complexes of

176

the same charge indicate that the H_2O–Ni and Eg–Ni interactions are similar in strength. These interactions also seem to be similar in magnitude to the Cl–Ni bond due to the small enthalpy differences between the systems containing neutral complexes and negatively charged complexes.

Similarly to the DC model the NC -TΔS correlates strongly with the number of water ligands coordinated to the nickel centre in both the gas phase and with the SMD environment applied. In the gas phase the enthalpic contribution to ΔG dominates the entropic effects and ΔG follows a similar trend to ΔH. The exception to this is the most stable system in the gas phase, NC-$[NiCl_4]^{2-}$, which has the lowest -TΔS of all the systems and therefore the lowest ΔG despite having a ΔH of + 80 kJ mol^{-1} compared to the lowest enthalpy system. In the SMD NC model ΔH values have a smaller magnitude and entropic effects have a significant impact on ΔG. Overall NC-$[NiCl_2(Eg)_2]$ is the most stable system with NC-$[Ni(Eg)_3]^{2+}$ very close in energy. Due to the entropic effects NC-$[NiCl_4]^{2-}$ is also low in energy. These results align with the experimental literature on ethaline-$NiCl_2 \cdot 6H_2O$, Fig. 4.12. $[Ni(Eg)_3]^{2+}$ is reported at low temperatures, and $[NiCl_4]^{2-}$ at elevated temperatures. The results of the NC model show that $[NiCl_4]^{2-}$ is favoured entropically, and as the entropy contribution to ΔG is -TΔS the relative stability of $[NiCl_4]^{2-}$ is increased as temperature increases.
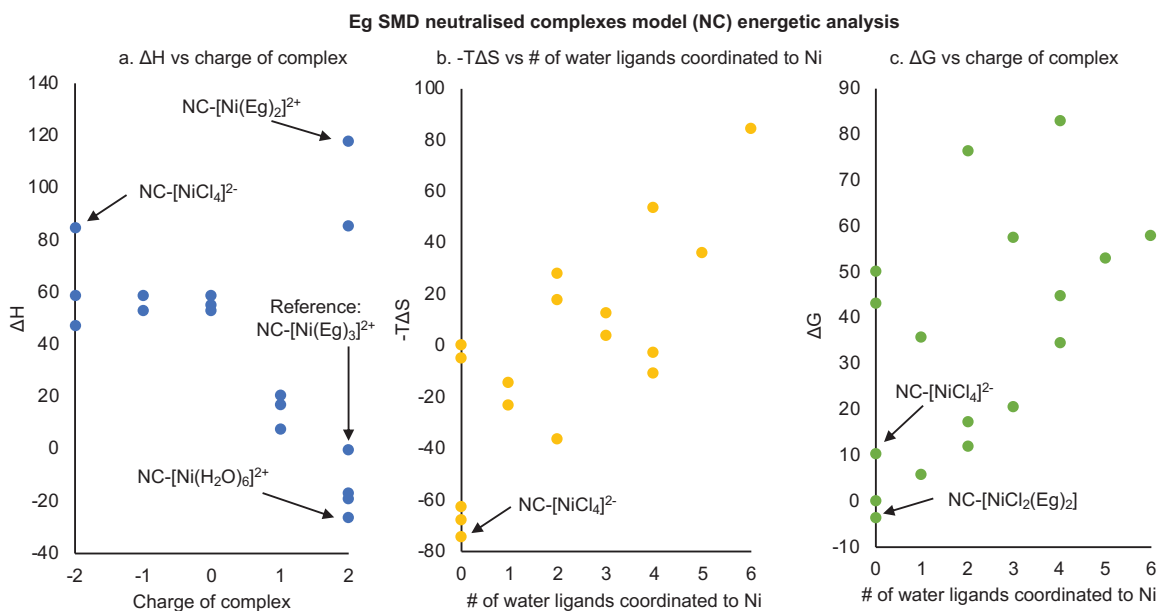
Figure 4.26: SMD NC-*complex* thermochemical parameters calculated relative to NC-$[Ni(Eg)_3]^{2+}$. Values are reported in kJ mol^{-1}.

4.5 Electronic structure

The electronic structure of $[NiCl_4]^{2-}$, $[Ni(Eg)_3]^{2+}$ and the octahedral intermediate species $[NiCl_2(Eg)_2]$ and $[NiCl_4(Eg)]^{2-}$ were investigated via visualisation of the MOs and TD-DFT calculations. The approach taken here is to rationalise the MO contributions for the simple example of Td $[CoCl_4]^{2-}$ and then analyse $[NiCl_4]^{2-}$ in terms of distortion from the Td complex. $[CoCl_4]^{2-}$ is d^7, simple crystal field theory predicts an $(e)^4(t_2)^3$ configuration. Jahn-Teller distortion is not observed, as the t_2 level is evenly occupied and therefore splitting of the level would not stabilise the complex. The ground state is non-degenerate.

The $1t_2$ level in $[CoCl_4]^{2-}$ is formed of contributions from the Co $3d_{xy}$, d_{xz}, and d_{yz} AOs (atomic orbitals) and the Cl 3p AOs, Fig. 4.27. The antibonding counterparts are the partially occupied $1t_2^*$ levels. The a_1 and a_1^* levels arise from the interaction of the Co 4s AO with the fully symmetrical Cl 3p ligand orbital. The Co $3d_{z^2}$ and $d_{x^2-y^2}$ MOs interact with a pair of Cl 3p ligand orbitals to form the e and e* levels. The Co 4p MOs also interact with the Cl 3p ligand orbitals, giving the $2t_2$ and $2t_2^*$ levels. A non-bonding set of Cl 3p ligand orbitals (t_1) sits between the $2t_2$ and e* levels.

$[NiCl_4]^{2-}$ has C_2v symmetry; it undergoes a Jahn-Teller distortion away from an ideal tetrahedron towards a sawhorse structure. The orbitals in $[NiCl_4]^{2-}$ are similar to those in $[CoCl_4]^{2-}$, with some differences, Fig. 4.28. The Co complex $1t_2$ level is split into one higher energy and two lower energy MOs in the Ni complex (MOs 34-36). The Co e MOs are stabilised significantly in the Ni complex (MO 37-38) and become lower in energy than the Ni 4s - Cl 3p bonding MO (MO 39). The Ni 3p AOs interact with different Cl 3p ligand orbitals to those in the Co complex but the energies of the resulting MOs are not significantly affected. The Co t_1, e*, and $1t_2^*$ levels all experience mixing when the symmetry is lowered in the Ni complex. MOs 43 and 44 correspond directly to the Co e* level; they are stabilised below the ligand MOs 45-47 which have some Co 3d character after mixing.

TD-DFT calculations were carried out on both $[NiCl_4]^{2-}$ and $[CoCl_4]^{2-}$, Fig. 4.29. The peaks and corresponding transitions are similar, as expected given the similar ligand-metal interactions observed in the MOs of the species. Two sets of allowed transitions are calculated for each species: one higher energy peak arising from LMCT (ligand to metal charge transfer), and one lower energy d $\longrightarrow$ d peak.

The $[CoCl_4]^{2-}$ LMCT transition is from the α t_2^* to the α a_1^* level. The α t_2^* MOs have large contributions from the ligand orbitals, whereas the α a_1^* MO has

Figure 4.27: a. MO diagram of α MOs of $[CoCl_4]^{2-}$. Levels are plotted to scale, electrons are neglected for clarity. b. The occupied α MOs of $[CoCl_4]^{2-}$. Levels are plotted to scale.
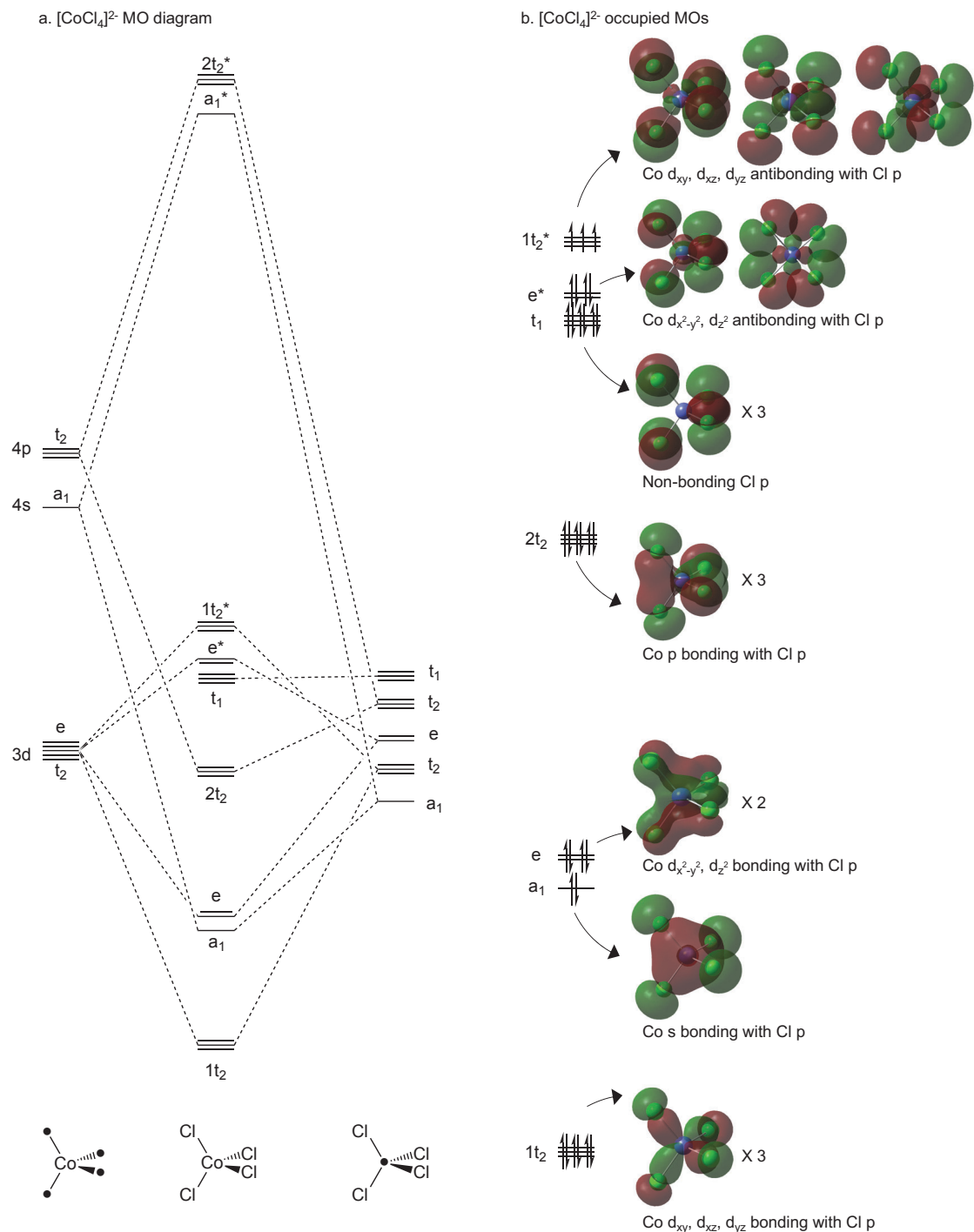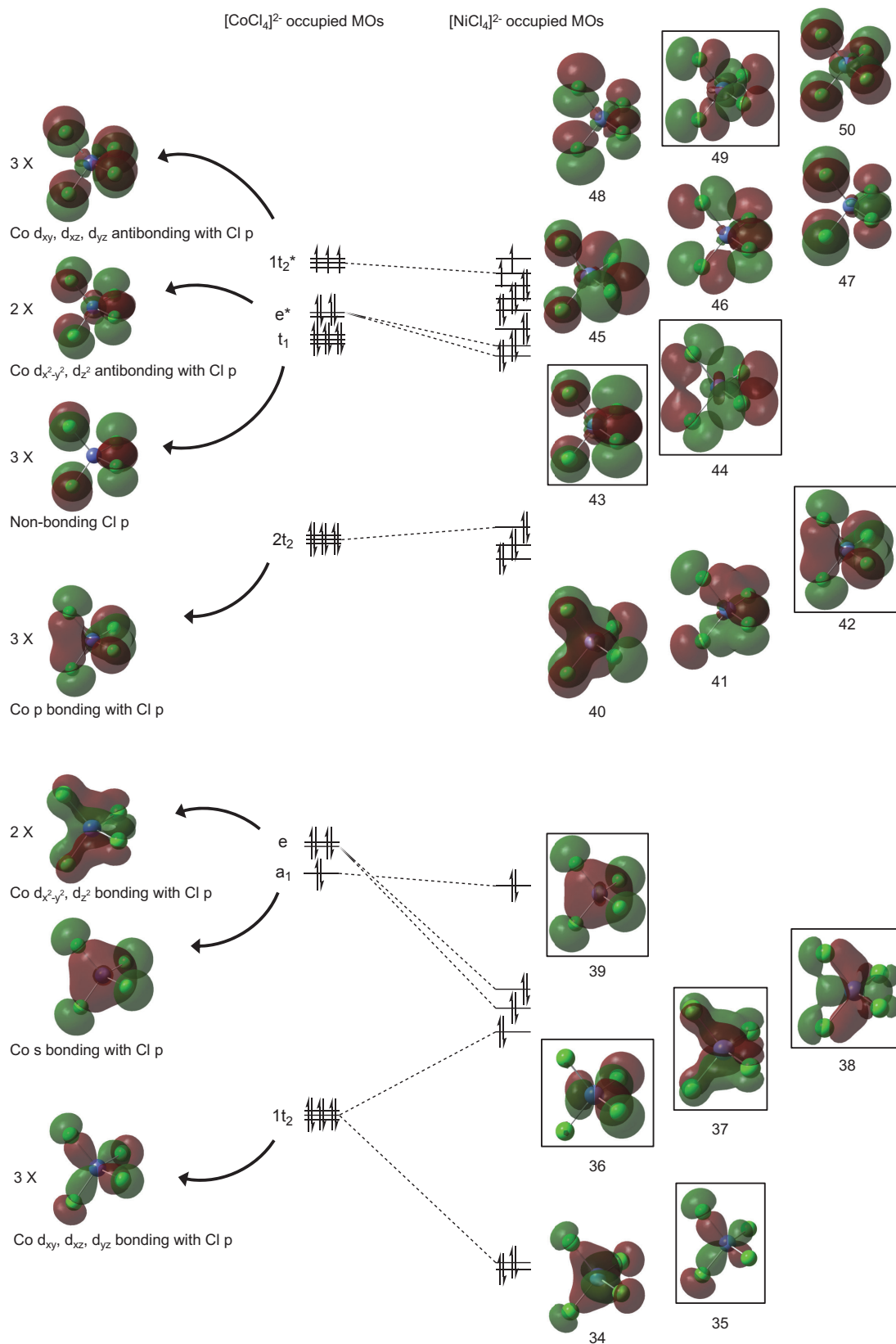
Figure 4.28: Correlation between the occupied α MOs of [CoCl$_4$]$^{2-}$ and [NiCl$_4$]$^{2-}$. Levels are plotted to scale. Black boxes indicate [NiCl$_4$]$^{2-}$ MOs which correspond directly to [CoCl$_4$]$^{2-}$ MOs.
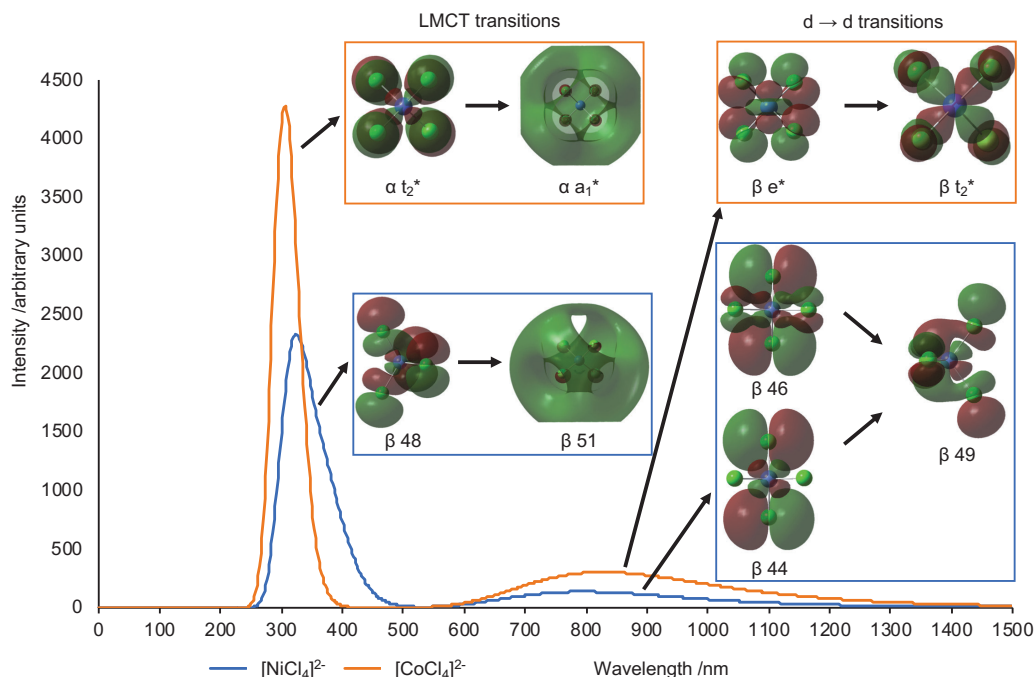
Figure 4.29: TD-DFT generated UV-vis spectra of $[NiCl_4]^{2-}$ and $[CoCl_4]^{2-}$. The MOs with the largest contributions to the transitions causing each peak are visualised. MOs are visualised at an iso value of 0.02 except for the Co α a_1* and Ni β 51 MOs which are shown at an iso value of 0.01.

predominantly Co 4s character. The $[NiCl_4]^{2-}$ LMCT transition is between similar MO; the β HOMO and MO 51, the first level unoccupied by either α or β electrons. In general LMCT peaks are more intense than peaks arising from d $\longrightarrow$ d transitions. LMCT transitions are fully allowed while d $\longrightarrow$ d transitions are Laporte-forbidden. The expected increased intensity is present in the calculated spectra.

From crystal field theory (d-orbitals in a strong ligand field) the d $\longrightarrow$ d transition in a d^7 tetrahderal complex is $(e)^4(t)^3 \longrightarrow (e)^3(t)^4$ in terms of electron configuration, and can be expressed in term symbols as $^4A_2 \longrightarrow {}^4T_1$. For a d^8 tetrahedral complex we have $(e)^4(t)^4 \longrightarrow (e)^3(t)^5$, $^3T_1 \longrightarrow {}^3T_1 + {}^3T_2$. d $\longrightarrow$ d transitions in d^7 and d^8 tetrahedral complexes are spin-allowed, and symmetry allowed, but formally Laporte-forbidden.

The calculated $[CoCl_4]^{2-}$ d $\longrightarrow$ d transition is predominantly from the β e* to the β t_2* level. Again similar MOs contribute to the transitions in $[NiCl_4]^{2-}$. The Laporte rule is partially relaxed due to the interaction of the ligand orbitals with the metal d-orbitals, as well as mixing between the metal p-orbital levels ($2t_2$) and the $1t_2$* level. These effects both reduce the d $\longrightarrow$ d character of the transition, meaning they are partially allowed and resulting in a low intensity transition, as calculated.

Experimental UV-vis spectra of $[NiCl_4]^{2-}$ evidence two peaks: a high energy

charge transfer peak with onset at 350 nm,[24] and a split lower energy peak assigned to d $\longrightarrow$ d transitions at 655 and 705 nm.[2,3,24] A range of hybrid functionals with different levels of HF (Hartree-Fock) exchange were used in TD-DFT calculations on $[NiCl_4]^{2-}$, Fig. 4.30.a. $[NiCl_4]^{2-}$ was optimised and confirmed as a minima via frequency analysis for each functional. The LMCT absorption maxima are inversely correlated with the amount of HF exchange included in the functional. This effect has been reported previously.[25] The PBE0 and B3LYP peaks are the closest to the experimental data.

The d $\longrightarrow$ d peaks are not correlated with the amount of HF exchange included in the functional, Fig. 4.30.d. The peaks generated by the PBE0, B3LYP, and ωB97X functionals come closest to the experimental data.

Experimental UV-vis of octahedral nickel complexes formed in ILs (ionic liquids) with Cl and $[C_3OHC_1Im]^+$ ligands found that when a higher proportion of Cl ligands are present in solution the d $\longrightarrow$ d peak shifts from 401 nm for a Cl/Ni ratio of 0 to 450 nm for Cl/Ni ratios of 4-6.[2] (When Cl/Ni = 20 only peaks associated with $[NiCl_4]^{2-}$ are observed.) Cl/Ni ratios of 4-6 produce spectra with an additional shoulder at 490nm. The authors concluded that octahedral complexes with more Cl ligands produce d $\longrightarrow$ d transitions at higher wavelengths than octahedral complexes with fewer or zero Cl ligands.

TD-DFT calculations (B3LYP-GD3BJ functional, SMD solvation environment) were carried out on the $[Ni(Eg)_3]^{2+}$, $[NiCl_2(Eg)_2]$, $[NiCl_4(Eg)]^{2-}$ series of complexes, Fig. 4.31.a. ($[NiCl_4]^{2-}$ results are included for comparison). Charge transfer peaks were calculated for all the octahedral complexes, but a peak corresponding to a d $\longrightarrow$ d transition was produced for $[NiCl_4(Eg)]^{2-}$ only.

The HOMO-LUMO region for β MOs has been plotted and the energy gap evaluated, Fig. 4.31.b. The tetrahedral complex $[NiCl_4]^{2-}$ has the smallest HOMO-LUMO gap (and the lowest energy (longest wavelength) UV-vis peak experimentally), which can be rationalised via crystal field theory arguments; the ligands approach the metal "between" the d-orbitals in tetrahedral complexes but directly towards the d-orbitals in octahedral complexes, thus the energy gap is smaller in tetrahedral complexes. This is visible in the calculated MOs - the octahedral complexes have more direct overlap between metal and ligand, resulting in stronger ligand-metal interactions and higher LUMOs and lower HOMOs.

The HOMO-LUMO energy gap in the octahedral complexes decreases as the number of Cl ligands increases. The energy of the LUMO increases slightly but the
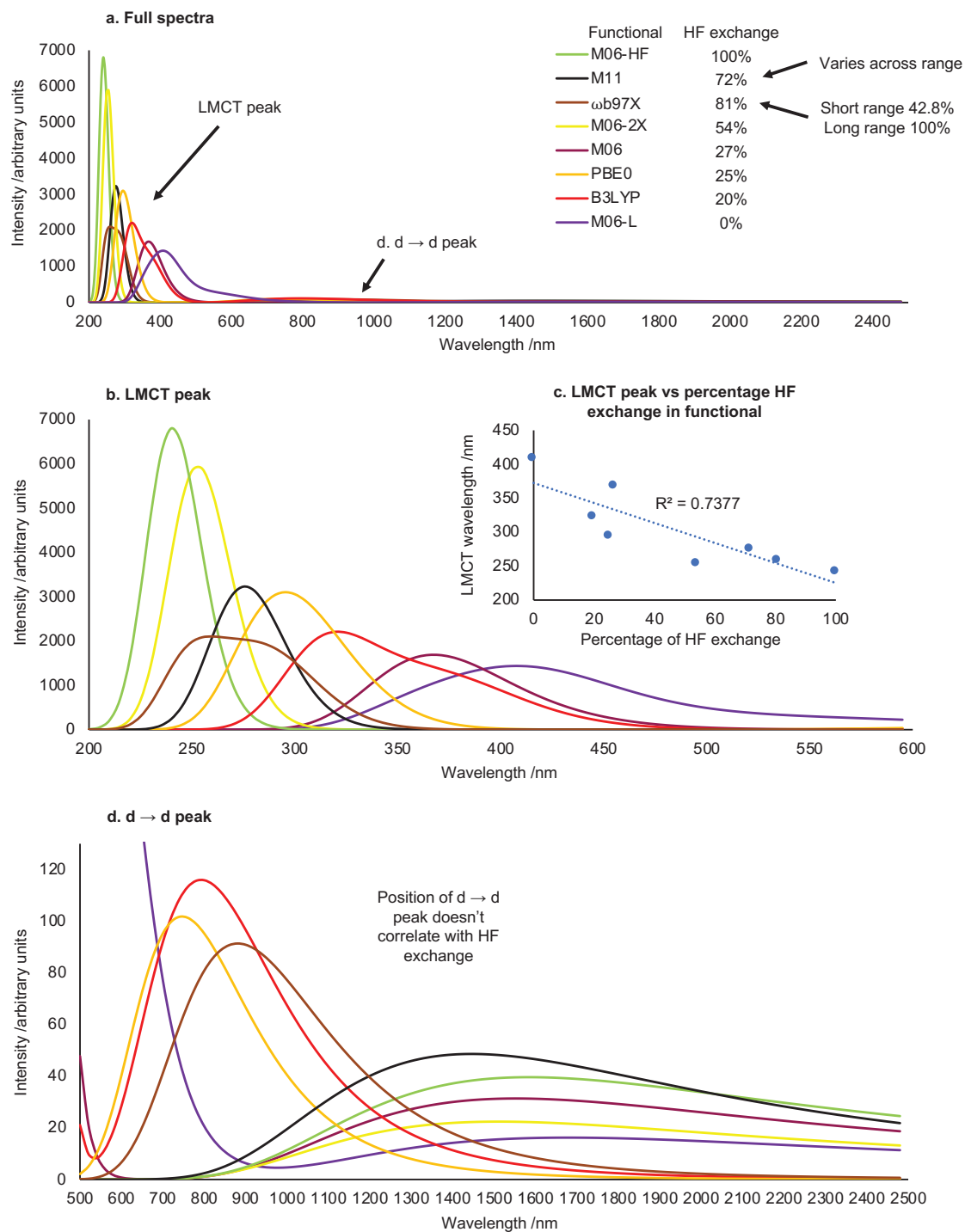
Figure 4.30: Gas phase TD-DFT of $[NiCl_4]^{2-}$. a. Full spectra. b. LMCT peak. c. LMCT peak maximima vs percentage HF exchange in functional. d. d $\longrightarrow$ d peak.
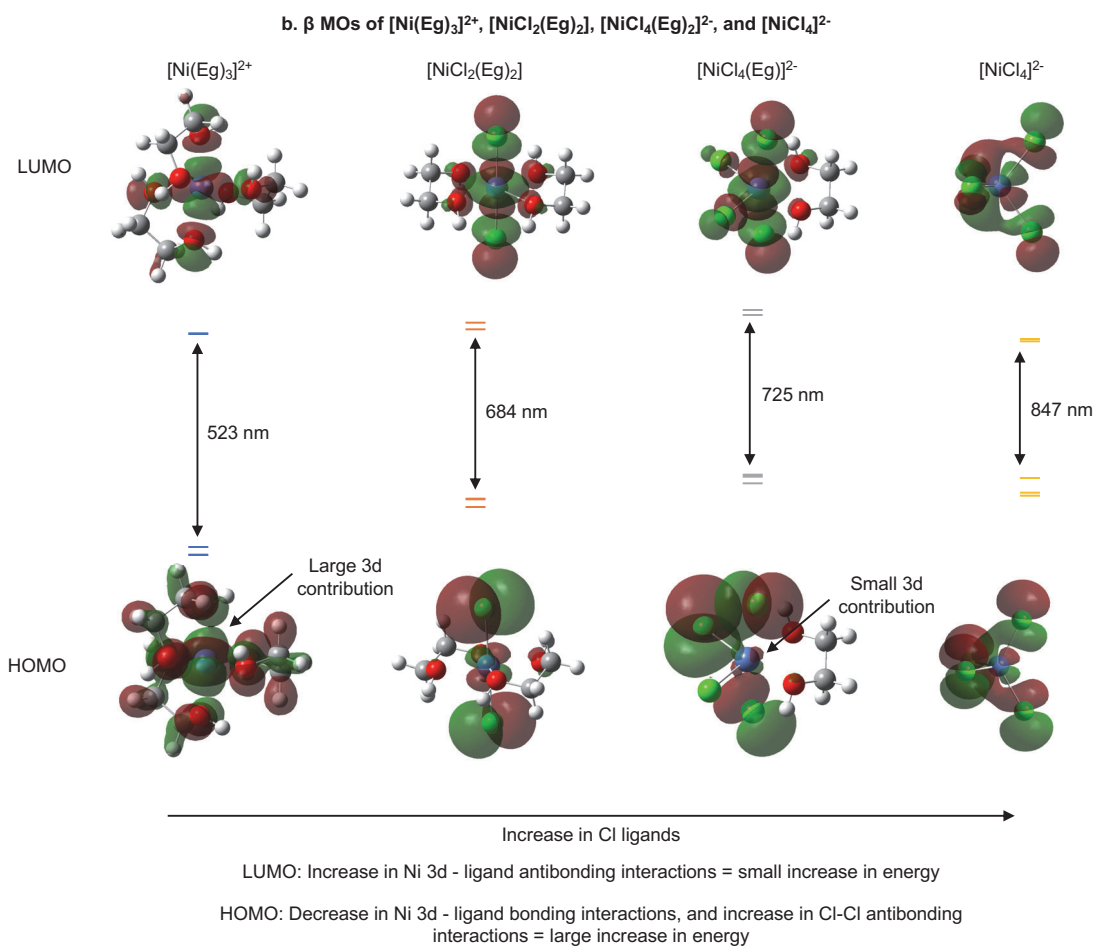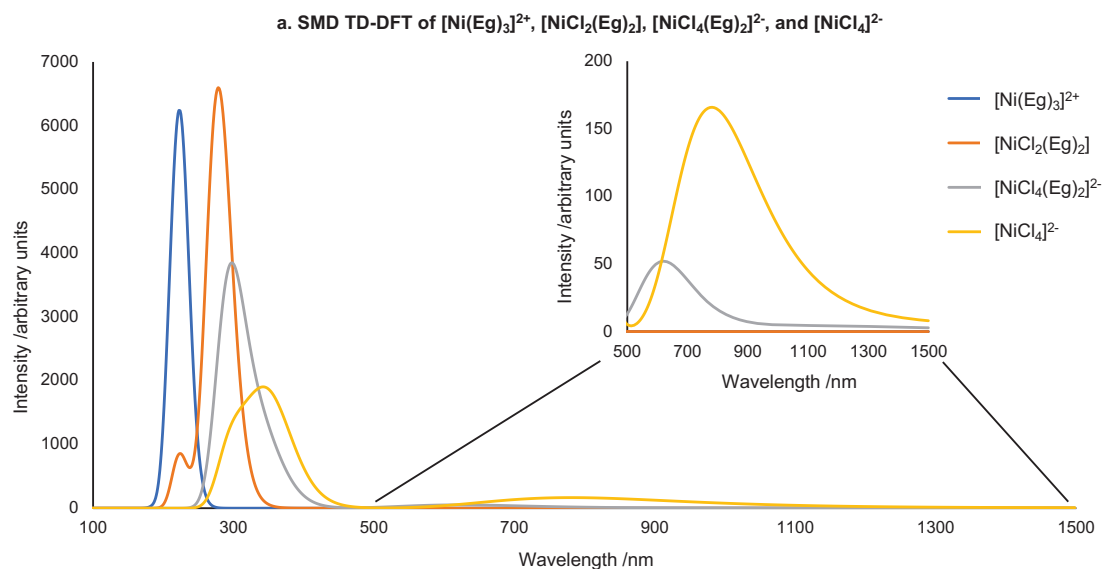
Figure 4.31: a. TD-DFT of $[Ni(Eg)_3]^{2+}$, $[NiCl_2(Eg)_2]$, $[NiCl_4(Eg)]^{2-}$, and $[NiCl_4]^{2-}$ in SMD environment. b. β MOs. Energy levels are plotted to scale.

HOMO energy increases significantly as the number of Cl ligands increases. These trends were rationalised by visualising the MOs, Fig. 4.31.b. The LUMO energy increases with the number of Cl ligands due to increased antibonding interactions between the metal and the ligands. The Cl-Ni antibonding interaction is stronger than the O-Ni antibonding interaction. The Ni 3d character of the HOMO decreases as Cl ligands are added, and the ligand character increases; the $[NiCl_4(Eg)]^{2-}$ is essentially an antibonding Cl ligand orbital with a small Ni 3d contribution. Therefore the ligand-metal bonding interactions in the HOMO are decreased as more Cl ligands are added and the ligand-ligand antibonding interactions are increased, leading to a significant increase in the HOMO energy. The Kohn-Sham MOs investigated here do not provide quantitative agreement with experimental data, but qualitative trends have been reproduced and a model for the physical origins of the trends has been established.

4.6   Conclusion

DFT (UB3LYP-GD3BJ/Aug-cc-pVDZ) calculations have been employed to study the molecular structure, intermolecular interactions, speciation, and electronic structure of HMDESs. Previous experimental work on the ethaline-MCl HMDES found that a different metal containing species was formed for M = Ni ($[Ni(Eg)_3]^{2+}$) than for M = Fe, Co, Cu, Zn ($[MCl_4]^{2-}$). The theoretical work presented here found that both Ni$-$Cl and Ni$-$Eg interactions are significantly stronger for M = Ni than for the the other metals in the series. This effect is increased for the Ni$-$Eg interaction, and $[Ni(Eg)_3]^{2+}$ is the favoured species in terms of electronic energy. The underlying reason for stronger interaction appears to be the small Ni radius.

A more detailed investigation of the ethaline-NiCl$_2 \cdot 6\,H_2O$ HMDES was undertaken to understand the experimentally observed thermochromic behaviour. In the DC model (complexes modeled as discrete entities with charges from -2 to +2) enthalpic contributions to the relative energies of the systems were determined by the charge on the overall complex, with neutral complexes having low enthalpies and highly charged complexes high enthalpies. In order to mitigate this effect an NC model was utilised (complexes modeled within clusters with a neutral overall charge) in which positively charged complexes have the lowest enthalpies due to strong intermolecular H-bonding between the Cl ions in the clusters and the OH groups in the ligands on the complex. Entropic factors favour complexes with fewer water ligands, especially $[NiCl_4]^{2-}$. Overall the NC-$[Ni(Eg)_3]^{2+}$ and NC-$[NiCl_2(Eg)_2]$ systems are the most stable and NC-$[NiCl_4]^{2-}$

is $+15$ kJ mol^{-1}, correlating with the experimental findings than [NiCl$_4$]$^{2-}$ is formed at elevated temperatures.

The electronic structure of [NiCl$_4$]$^{2-}$, [Ni(Eg)$_3$]$^{2+}$ and the octahedral intermediate species [NiCl$_2$(Eg)$_2$] and [NiCl$_4$(Eg)]$^{2-}$ have been investigated. When more Cl ligands are coordinated to the nickel centre the HOMO-LUMO gap is decreased, correlating with experimental findings that the d $\longrightarrow$ d transition found in UV-vis of Ni based HMILs is shifted to higher wavelengths when the proportion of Cl in solution is increased.

Bibliography

[1] J. M. Hartley, C. M. Ip, G. C. H. Forrest, K. Singh, S. J. Gurman, K. S. Ryder, A. P. Abbott and G. Frisch, *Inorganic Chemistry*, 2014, **53**, 6280–6288.

[2] X. Wei, L. Yu, D. Wang, X. Jin and G. Z. Chen, *Green Chemistry*, 2008, **10**, 296.

[3] A. P. Abbott, A. Ballantyne, R. C. Harris, J. A. Juma, K. S. Ryder and G. Forrest, *Electrochimica Acta*, 2015, **176**, 718–726.

[4] S. Wellens, B. Thijs, C. Möller and K. Binnemans, *Physical Chemistry Chemical Physics*, 2013, **15**, 9663–9669.

[5] M. J. Frisch, G. W. Trucks, H. B. Schlegel, G. E. Scuseria, M. A. Robb, J. R. Cheeseman, G. Scalmani, V. Barone, B. Mennucci, G. A. Petersson, H. Nakatsuji, M. Caricato, X. Li, H. P. Hratchian, A. F. Izmaylov, J. Bloino, G. Zheng, J. L. Sonnenberg, M. Hada, M. Ehara, K. Toyota, R. Fukuda, J. Hasegawa, M. Ishida, T. Nakajima, Y. Honda, O. Kitao, H. Nakai, T. Vreven, J. Montgomery, J. A., J. E. Peralta, F. Ogliaro, M. Bearpark, J. J. Heyd, E. Brothers, K. N. Kudin, V. N. Staroverov, R. Kobayashi, J. Normand, K. Raghavachari, A. Rendell, J. C. Burant, S. S. Iyengar, J. Tomasi, M. Cossi, N. Rega, M. J. Millam, M. Klene, J. E. Knox, J. B. Cross, V. Bakken, C. Adamo, J. Jaramillo, R. Gomperts, R. E. Stratmann, O. Yazyev, A. J. Austin, R. Cammi, C. Pomelli, J. W. Ochterski, R. L. Martin, K. Morokuma, V. G. Zakrzewski, G. A. Voth, P. Salvador, J. J. Dannenberg, S. Dapprich, A. D. Daniels, Ö. Farkas, J. B. Foresman, J. V. Ortiz, J. Cioslowski and D. J. Fox, *Gaussian 09, Revision D.01*, 2009.

[6] A. D. Becke, *The Journal of Chemical Physics*, 1993, **98**, 5648.

[7] C. Lee, W. Yang and R. G. Parr, *Physical Review B*, 1988, **37**, 785–789.

[8] S. Grimme, S. Ehrlich and L. Goerigk, *Journal of Computational Chemistry*, 2011, **32**, 1456–1465.

[9] A. D. Becke, *Physical Review A*, 1988, **38**, 3098–3100.

[10] P. J. Stephens, F. J. Devlin, C. F. Chabalowski and M. J. Frisch, *The Journal of Physical Chemistry*, 1994, **98**, 11623–11627.

[11] T. H. Dunning, *The Journal of Chemical Physics*, 1989, **90**, 1007.

[12] D. E. Woon and T. H. Dunning, *The Journal of Chemical Physics*, 1993, **98**, 1358.

[13] R. F. Bader, *Atoms in Molecules: A Quantum Theory*, Oxford University Press, 1994.

[14] T. A. Keith, *AIMAll (Version 17.01.25)*, 2016.

[15] S. Keinan, J. Contreras-García, E. R. Johnson, W. Yang, P. Mori-Sánchez and A. J. Cohen, *Journal of the American Chemical Society*, 2010, **132**, 6498–6506.

[16] A. V. Marenich, C. J. Cramer and D. G. Truhlar, *The Journal of Physical Chemistry B*, 2009, **113**, 6378–96.

[17] P. Winget, D. M. Dolney, D. J. Giesen, C. J. Cramer and D. G. Truhlar, *Minnesota solvent descriptor database*, 1999, http://amsol.chem.umn.edu/solvation/mnsddb.pdf, ac.

[18] A. Jindal and S. Vasudevan, *The Journal of Physical Chemistry B*, 2017, **121**, 5595–5600.

[19] J. Cirera, P. Alemany and S. Alvarez, *Chemistry - A European Journal*, 2004, **10**, 190–207.

[20] M. Gruden-Pavlović, M. Zlatar, C. W. Schläpfer and C. Daul, *Journal of Molecular Structure: THEOCHEM*, 2010, **954**, 80–85.

[21] J. R. Lane, J. Contreras-García, J. P. Piquemal, B. J. Miller and H. G. Kjaergaard, *Journal of Chemical Theory and Computation*, 2013, **9**, 3263–3266.

[22] R. D. Shannon and C. T. Prewitt, *Acta Crystallographica Section B Structural Crystallography and Crystal Chemistry*, 1968, **25**, 925–946.

[23] S. Keinan, J. Contreras-García, E. R. Johnson, W. Yang, P. Mori-Sánchez and A. J. Cohen, *Journal of the American Chemical Society*, 2010, **132**, 6498–6506.

[24] M. Queen, *PhD thesis*, Montana State University, 2014.

[25] D. Jacquemin, E. A. Perpète, G. E. Scuseria, I. Ciofini and C. Adamo, *Journal of Chemical Theory and Computation*, 2008, **4**, 123–135.

Chapter 5

Conclusion

Bismuth(III) based HMILs were recently synthesised for the first time. They are the densest HMILs reported to date, and are thermally stable with mass loss onset above 300 °C. Potential applications include catalysis, metal separation, and liquid batteries. Speciation of Bi HMILs is difficult to ascertain via experimental techniques; for example $[BiCl_4]^-$ and $[Bi_2Cl_8]^{2-}$ are chemically similar and most experimental methods cannot distinguish between the two. Theoretical methods were therefore applied to the following research questions: What is the anionic speciation of Bi HMILs? Does speciation vary with halide or mole fraction of BiX_3? What is the character of the cation-anion interactions? Can the electronic structure of Bi HMILs be accurately modelled via DFT calculations?

These questions were addressed via DFT calculations in the gas phase and utilising the SMD solvation model. Appropriate SMD parameters were selected and calculated to produce an IL-SMD model. TD-DFT was applied to generate UV-vis transitions. A range of monomeric and dimeric candidate anionic species were optimised for X = Cl, Br, and I. Selected anionic species were paired with cations to form neutral ion clusters. Structural, energetic, and electronic analysis was then completed on chosen systems to approach the research questions.

Monomeric anion structures were significantly affected by solvation environment, but not by halide type. The IL-SMD environment stabilised structures with charge anisotropy and non-zero dipole moments, whereas the gas phase stable structures have dipole moments of zero. For example $[BiCl_4]^-$ is tetrahedral in the gas phase and sawhorse in the IL-SMD. Dimeric conformer structures were similar across solvation environments and halide types. In neutral ion clusters the anion conformations were similar to the IL-SMD lone anion structures, e.g. in $[C_2C_1Im][BiCl_4]$ the anion is

sawhorse in all gas phase and IL-SMD conformers. Overall similar ion-cluster conformers were found in the gas phase vs IL-SMD, but with larger distances between ions in the IL-SMD structures. This is expected as each ion interacts with both the cavity charges and the other ion(s) in the IL-SMD but only with the other ions in the gas phase.

The IL-SMD association energies of the ion clusters are small; the relative energies of different anionic speciations are similar whether the anions are modelled inside ion clusters, or as lone ions in the IL-SMD environment. This finding allowed the use of lone anion calculations to predict the anionic speciation of Bi HMILs for four mole fractions of BiX_3, for X = Cl, Br, I. At mole fractions of 0.67 the only anionic species predicted is $[Bi_2X_7]^-$, which is also predicted at mole fractions of 0.5. A second group of species, $[Bi_2X_9]^{3-}$, $[Bi_2X_8]^{2-}$, and $[BiX_4]^-$ are predicted for mole fractions of 0.5, 0.33, and 0.25. Thirdly X^- and $[BiX_5]^{2-}$ are predicted at mole fractions of 0.33 and 0.25. These results are similar to the those reported for Al HMILs, although $[Al_2X_8]^{2-}$, $[Al_2X_9]^{2-}$ and $[AlX_5]^{2-}$ are not known. The exchange of halides between anions was modelled as an associative reaction mechanism and found to be facile.

Experimental XPS and UV-vis spectra of Bi HMILs were reproduced qualitatively and rationalised theoretically. Bi HMILs with Cl halides are colourless, with Br halides yellow, with a mix of I and other halides red, and with only I halides purple. This was found to be due to the decrease in LUMO energy as halide weight increases.

The results of this work support the conclusion that the IL-SMD accurately simulates the environment experienced by bismuth halide anions in HMILs. This implies that the cation-anion interactions between bismuth halide anions and imidazolium cations are non-specific, and predominantly Coulombic, as directional covalent interactions such as strong H-bonding are not well represented by an SMD environment. Further work, both experimental and theoretical, could therefore centre on exploring Bi HMILs with strongly interacting cations, such as protic imidazolium or ammonium cations.

Nickel(II) based HMDESs are currently experiencing a surge of research effort due to their interesting electrodeposition and thermochromic properties. Specifically $NiCl_2 \cdot 6\,H_2O$ dissolved in ethaline, a 1:2 mixture of choline chloride and ethylene glycol, has been found to change colour from yellow to blue as temperatures increase, and to electrodeposit nickel in different and superior morphologies to aqueous solutions. The colour change has been attributed to the predominance of octahedral $[Ni(Eg)_3]^{2+}$ at low temperatures and formation of tetrahedral $[NiCl_4]^{2-}$ at elevated temperatures. For M =

Fe, Co, Cu, and Zn the tetrahedral $[MCl_4]^{2-}$ anion was indicated at low temperatures. Ethaline-MCl_2 was investigated via DFT calculations for M = Fe, Co, Ni, Cu, and Zn to rationalise the anomalous behaviour exhibited by the M = Ni system. The M = Ni system was then investigated, with the following research questions: Which Ni(II) complexes form in solution? What are the driving forces behind the relative stabilities of complexes containing different ligands? How do the nickel complexes interact with other species in solution? Can TD-DFT rationalise the experimental UV-vis spectra reported at high and low temperatures?

The equilibrium $[MCl_4]^{2-} + 3\,Eg \rightleftharpoons [M(Eg)_3]^{2+} + 4\,Cl^-$ was modelled for M = Fe, Co, Ni, Cu, and Zn. Ni(II) was found to interact more strongly with both Cl^- and Eg ligands, due to its smaller ionic radius. The increase in interaction strength was larger for Eg and the $[M(Eg)_3]^{2+}$ side of the equilibrium was favoured for M = Ni but not for the other metals, matching previously reported experimental results.

To investigate the ethaline-$NiCl_2 \cdot 6\,H_2O$ system in more detail a range of complexes with Cl^-, Eg, and H_2O ligands were studied, the charges on the complexes ranged from -2 to +2. In the discrete complexes model the complexes were modelled as individual complexes, and in the neutralised complexes model Cl^- or Ch^+ ions were added around the complex such that the charge on the cluster was zero. Significant intramolecular H-bonding was observed in the discrete complexes model, between Cl ligands and OH containing ligands. This was reduced in favour of intermolecular H-bonding between ligands and coordinating neutralising species in the neutralised complexes model.

The relative stabilities of the complexes in the discrete complexes model were dictated by the overall charge on the complexes, with the more charged complexes being higher in energy. Enthalpic effects were significantly larger than entropic factors in the discrete complexes model. In the neutralised complexes model the enthalpic effects were reversed and the highly charged complexes (modelled within neutral clusters) were the most stable. The entropic and enthalpic effects are of similar significance in the neutralised complexes model. Overall the most stable species were $[M(Eg)_3]^{2+}$ (indicated by experiments at room temperature) and $[MCl_2(Eg)_2]$. $[NiCl_4]^{2-}$ is less stable than $[M(Eg)_3]^{2+}$ but still accessible, matching the experimental finding that it forms at elevated temperatures. These results have reproduced the experimental conclusions about these systems, and rationalised the driving factors behind the observations.

191

Chapter 6

Appendix

6.1 Thermochemical data for species reported in Chapter 3

Conformer	ΔE_{elec}	Δzpe	ΔE	ΔH	$T\Delta S$	ΔG
Sawhorse	0.00	0.00	0.00	0.00	0.00	0.00
Tetrahedral	0.01	-0.27	-0.01	-0.01	-0.71	0.7

Table 6.1: Relative thermochemical parameters for conformers of $[BiBr_4]^-$ in IL-SMD.

Conformer	ΔE_{elec}	Δzpe	ΔE	ΔH	$T\Delta S$	ΔG
Tetrahedral	0.00	0.00	0.00	0.00	0.00	0.00
Sawhorse	-1.65	0.37	-1.63	-1.63	-4.03	2.4

Table 6.2: Relative thermochemical parameters for conformers of $[BiI_4]^-$ in IL-SMD.

Conformer	ΔE_{elec}	Δzpe	ΔE	ΔH	$T\Delta S$	ΔG
sh_small_axial	0.00	0.00	0.00	0.00	0.00	0.00
sh_mixed_axial	4.03	0.28	4.11	4.11	-0.93	5.04
sh_large_axial	9.27	-0.05	9.38	9.38	1.15	8.23

Table 6.3: Relative thermochemical parameters for conformers of $[BiCl_2Br_2]^-$ in IL-SMD.

Conformer	ΔE_{elec}	Δzpe	ΔE	ΔH	$T\Delta S$	ΔG
sh_small_axial	0.00	0.00	0.00	0.00	0.00	0.00
sh_mixed_axial	3.35	0.45	3.49	3.49	-0.97	4.47
sh_large_axial	5.74	0.55	5.98	5.98	0.62	5.37

Table 6.4: Relative thermochemical parameters for conformers of $[BiCl_2I_2]^-$ in IL-SMD.

Conformer	ΔE_{elec}	Δzpe	ΔE	ΔH	$T\Delta S$	ΔG
sh_large_axial	0.00	0.00	0.00	0.00	0.00	0.00
sh_mixed_axial	2.18	-0.04	2.17	2.17	0.43	1.74
sh_small_axial	4.46	-0.19	4.4	4.4	1.1	3.3

Table 6.5: Relative thermochemical parameters for conformers of $[BiBr_2I_2]^-$ in IL-SMD.

Conformer	ΔE_{elec}	Δzpe	ΔE	ΔH	$T\Delta S$	ΔG
sh_sh_a	0.00	0.00	0.00	0.00	0.00	0.00
sh_sh_b	11.36	-0.45	11.4	11.4	6.77	4.62
sbp_sbp	35.12	-0.02	34.99	34.99	-2.04	37.04
sh_sbp	18.03	-0.97	18.01	18.01	14.0	4.01

Table 6.6: Relative thermochemical parameters for conformers of $[Bi_2Cl_7]^-$ in the gas phase.

Conformer	ΔE_{elec}	Δzpe	ΔE	ΔH	$T\Delta S$	ΔG
sh_sh_a	0.00	0.00	0.00	0.00	0.00	0.00
sh_sbp	10.81	-0.37	10.82	10.82	3.88	6.93
sbp_sbp	24.16	-0.17	24.04	24.04	0.15	23.89

Table 6.7: Relative thermochemical parameters for conformers of $[Bi_2Cl_7]^-$ in IL-SMD.

Conformer	ΔE_{elec}	Δzpe	ΔE	ΔH	$T\Delta S$	ΔG
sh_sh_a	0.00	0.00	0.00	0.00	0.00	0.00
sbp_sbp	34.45	-0.12	34.38	34.38	-0.36	34.73
sh_sbp	15.71	-0.59	15.7	15.7	12.72	2.98
sh_sh_b	9.35	-0.29	9.36	9.36	5.75	3.61

Table 6.8: Relative thermochemical parameters for conformers of $[Bi_2Br_7]^-$ in the gas phase.

Conformer	ΔE_{elec}	Δzpe	ΔE	ΔH	$T\Delta S$	ΔG
sh_sh_a	0.00	0.00	0.00	0.00	0.00	0.00
sh_sbp	12.94	0.04	12.98	12.98	0.69	12.29
sh_sh_b	3.55	0.15	3.58	3.58	-1.58	5.16

Table 6.9: Relative thermochemical parameters for conformers of $[Bi_2Br_7]^-$ in IL-SMD.

Conformer	ΔE_{elec}	Δzpe	ΔE	ΔH	$T\Delta S$	ΔG
sh_sh_a	0.00	0.00	0.00	0.00	0.00	0.00
sh_sh_b	6.7	-0.21	6.7	6.7	4.45	2.25

Table 6.10: Relative thermochemical parameters for conformers of $[Bi_2I_7]^-$ in the gas phase.

Conformer	ΔE_{elec}	Δzpe	ΔE	ΔH	$T\Delta S$	ΔG
sh_sh_a	0.00	0.00	0.00	0.00	0.00	0.00
sh_sh_c	36.63	-0.1	36.65	36.65	3.67	32.98
sh_sbp	11.97	0.03	11.98	11.98	-0.22	12.2
sh_sh_b	0.07	0.34	0.1	0.1	-3.62	3.72

Table 6.11: Relative thermochemical parameters for conformers of $[Bi_2I_7]^-$ in IL-SMD.

Conformer	ΔE_{elec}	Δzpe	ΔE	ΔH	$T\Delta S$	ΔG
oct_sbp	0.00	0.00	0.00	0.00	0.00	0.00
sbp_sbp_c	43.68	1.0	43.91	43.91	-3.65	47.56
sbp_sbp_b	4.74	-0.01	4.77	4.77	1.13	3.63
sbp_sbp_a	7.43	0.25	7.48	7.48	-2.33	9.81
sbp_bipy	12.75	-0.01	12.77	12.77	-0.04	12.82

Table 6.12: Relative thermochemical parameters for conformers of $[Bi_2Cl_8]^{2-}$ in IL-SMD.

Conformer	ΔE_{elec}	Δzpe	ΔE	ΔH	$T\Delta S$	ΔG
oct_sbp	0.00	0.00	0.00	0.00	0.00	0.00
sbp_sbp_c	34.86	-0.07	34.88	34.87	2.61	32.27

Table 6.13: Relative thermochemical parameters for conformers of $[Bi_2I_8]^{2-}$ in IL-SMD.

Conformer	ΔE_{elec}	Δzpe	ΔE	ΔH	$T\Delta S$	ΔG
front_eth	0.00	0.00	0.00	0.00	0.00	0.00
front_me	-1.38	0.68	-1.17	-1.17	-1.24	0.07
top_a	-1.58	2.54	0.58	0.58	-4.24	4.82
top_b	0.38	2.93	3.05	3.05	-3.41	6.45
side_me	34.98	0.77	35.49	35.49	0.79	34.7
top_c	3.92	2.7	6.42	6.42	-1.75	8.17
back	63.02	0.35	64.24	64.24	8.3	55.94
side_eth	31.23	0.75	31.93	31.92	-0.94	32.87

Table 6.14: Relative thermochemical parameters for conformers of $[C_2C_1Im]Cl$ in the gas phase.

Conformer	ΔE_{elec}	Δzpe	ΔE	ΔH	$T\Delta S$	ΔG
front	0.00	0.00	0.00	0.00	0.00	0.00
side_me	12.09	1.83	13.4	13.4	-3.56	16.96
back	13.12	0.35	11.41	11.41	-6.34	17.75
side_eth	7.95	0.28	5.78	5.78	-9.65	15.43

Table 6.15: Relative thermochemical parameters for conformers of $[C_2C_1Im]Cl$ in IL-SMD.

Conformer	ΔE_{elec}	Δzpe	ΔE	ΔH	$T\Delta S$	ΔG
a_ax_front_me	0.00	0.00	0.00	0.00	0.00	0.00
b_ax_front_eth	0.02	0.01	0.07	0.07	-0.03	0.1
c_ax_front_me	-2.88	0.68	-2.66	-2.66	-4.32	1.66
d_ax_front_me	-5.25	0.61	-5.2	-5.2	-6.89	1.69
e_eq_front_me	1.43	0.43	1.83	1.84	-2.14	3.98
f_back	1.04	0.27	1.44	1.44	-3.8	5.25
g_back	1.72	0.23	1.98	1.98	-5.28	7.25
h_back	6.09	-0.12	6.03	6.03	-4.06	10.1

Table 6.16: Relative thermochemical parameters for conformers of $[C_2C_1Im][BiCl_4]$ in the gas phase.

Conformer	ΔE_{elec}	Δzpe	ΔE	ΔH	$T\Delta S$	ΔG
a_ax_front_eth	0.00	0.00	0.00	0.00	0.00	0.00
b_back	-7.35	1.04	-6.98	-6.98	-7.33	0.36
c_back	2.93	-0.14	2.82	2.82	1.38	1.44
d_eq_front_me	1.44	0.29	1.63	1.63	-1.19	2.82
d_ax_front	0.26	0.46	0.45	0.45	-2.48	2.94
e_back	1.58	0.04	1.63	1.63	-3.05	4.68
f_back	4.03	0.38	4.49	4.49	-0.27	4.76
g_eq_front_me	1.91	0.6	2.28	2.28	-3.61	5.89
h_ax_front_me	0.63	0.63	0.8	0.8	-5.73	6.53
i_eq_front_eth	2.88	0.59	3.24	3.24	-3.55	6.8
j_ax_front_me	1.77	0.93	2.21	2.21	-4.79	7.0
k_ax_front_eth	0.8	1.24	1.32	1.32	-7.07	8.38
l_eq_front_eth	3.43	1.26	4.11	4.11	-5.53	9.64
m_top	3.38	1.11	3.87	3.87	-6.05	9.92
n_back	4.16	1.04	4.79	4.79	-5.45	10.24
o_top	2.94	1.58	3.75	3.75	-7.43	11.18
p_ax_front	4.52	1.93	5.15	5.15	-8.9	14.05

Table 6.17: Relative thermochemical parameters for conformers of [C_2C_1Im][$BiCl_4$] in IL-SMD.

Conformer	ΔE_{elec}	Δzpe	ΔE	ΔH	$T\Delta S$	ΔG
a_back	0.00	0.00	0.00	0.00	0.00	0.00
b_back	12.07	-1.73	11.48	11.48	10.67	0.81
c_back	10.65	-1.52	10.16	10.16	7.53	2.63
d_ax_front_me	10.33	-1.24	9.85	9.85	6.06	3.79
e_top	11.95	-1.21	11.48	11.48	6.53	4.95
f_top	13.23	-1.07	12.86	12.86	5.72	7.14

Table 6.18: Relative thermochemical parameters for conformers of [C_2C_1Im][$BiBr_4$] in IL-SMD.

Conformer	ΔE_{elec}	Δzpe	ΔE	ΔH	$T\Delta S$	ΔG
a_ax_front_me	0.00	0.00	0.00	0.00	0.00	0.00
b_back	-0.96	0.59	-0.6	-0.6	-1.61	1.01
c_ax_front_eth	0.04	0.46	0.36	0.36	-0.9	1.27
d_top	0.35	-0.26	0.12	0.12	-1.76	1.88
e_top	-2.4	0.16	-2.58	-2.58	-4.86	2.28
f_back	1.53	0.77	1.98	1.98	-3.09	5.07
g_ax_front_eth	8.34	0.93	8.8	8.8	-0.81	9.61

Table 6.19: Relative thermochemical parameters for conformers of [C_2C_1Im][BiI_4] in IL-SMD.

Conformer	ΔE_{elec}	Δzpe	ΔE	ΔH	$T\Delta S$	ΔG
a_ax_front_eth	0.00	0.00	0.00	0.00	0.00	0.00
b_ax_front_me	0.81	0.14	0.93	0.93	-4.56	5.49
c_ax_front_me	15.26	-0.43	15.39	15.39	1.27	14.11
d_top	5.45	0.49	5.71	5.71	-5.84	11.55
e_eq_front_eth	13.29	-0.43	13.5	13.5	0.59	12.91
f_ eq_front_eth	-1.07	0.65	-0.87	-0.87	-6.39	5.52

Table 6.20: Relative thermochemical parameters for conformers of [C_2C_1Im][Bi_2Cl_7] in the gas phase.

Conformer	ΔE_{elec}	Δzpe	ΔE	ΔH	$T\Delta S$	ΔG
a_ax_front	0.00	0.00	0.00	0.00	0.00	0.00
b_top	12.68	2.88	14.33	14.33	-2.09	16.42
c_back	3.21	0.92	3.84	3.84	1.04	2.8
f_bridge_side_eth	14.33	-0.56	14.31	14.31	7.2	7.11

Table 6.21: Relative thermochemical parameters for conformers of $[C_2C_1Im][Bi_2Cl_7]$ in IL-SMD.

Conformer	ΔE_{elec}	Δzpe	ΔE	ΔH	$T\Delta S$	ΔG
a_sbp_sbp_b	0.00	0.00	0.00	0.00	0.00	0.00
b_sbp_sbp_b	10.93	-0.55	11.07	11.07	2.27	8.8
c_sbp_sbp_b	10.5	-0.59	10.54	10.54	1.31	9.23
d_eq_oct_sbp	14.33	-0.82	13.73	13.73	-0.23	13.95
e_sbp_sbp_a	13.66	0.09	13.74	13.74	-2.67	16.41
f_sbp_sbp_a	10.87	0.13	10.5	10.5	-6.3	16.8

Table 6.22: Relative thermochemical parameters for conformers of $[C_2C_1Im]_2[Bi_2Cl_8]$ in the gas phase.

Conformer	ΔE_{elec}	Δzpe	ΔE	ΔH	$T\Delta S$	ΔG
a_sbp_sbp_b	0.00	0.00	0.00	0.00	0.00	0.00
b_oct_sbp	14.04	-1.47	13.53	13.53	7.87	5.66
c_sbp_sbp_b	14.82	0.08	15.75	15.75	8.13	7.62
d_oct_sbp	9.19	0.21	9.46	9.46	-0.04	9.49
e_oct_sbp	12.09	-1.38	11.62	11.62	1.87	9.75
f_oct_sbp	13.29	-0.95	13.11	13.11	2.34	10.77

Table 6.23: Relative thermochemical parameters for conformers of $[C_2C_1Im]_2[Bi_2Cl_8]$ in IL-SMD.

6.2 Thermochemical data for species reported in Chapter 4

Conformer	ΔE_{elec}	Δzpe	ΔE	ΔH	TΔS	ΔG
DC-[Ni(Eg)$_3$]$^{2+}$	0.00	0.00	0.00	0.00	0.00	0.00
DC-[NiCl$_2$(Eg)$_2$]	-1216.33	-3.87	-1219.84	-1222.32	-13.22	-1209.10
DC-[NiCl$_2$(H$_2$O)$_2$(Eg)]	-1237.62	5.90	-1232.09	-1237.04	-36.43	-1200.61
DC-[NiCl$_2$(H$_2$O)$_4$]	-1265.17	20.04	-1249.75	-1257.18	-71.03	-1186.16
DC-[NiCl$_3$(H$_2$O)$_3$]$^-$	-955.66	9.87	-948.44	-953.39	-25.79	-927.60
DC-[NiCl$_3$(H$_2$O)(Eg)]	-912.95	-5.16	-917.31	-919.78	6.56	-926.34
DC-[NiCl(H$_2$O)(Eg)$_2$]$^+$	-760.50	2.24	-758.07	-760.54	-16.46	-744.09
DC-[NiCl(H$_2$O)$_3$(Eg)]$^+$	-781.25	15.08	-769.20	-774.15	-49.16	-724.98
DC-[NiCl(H$_2$O)$_5$]$^+$	-783.16	24.21	-762.87	-770.30	-74.98	-695.32
DC-[NiCl$_4$]$^{2-}$	-211.31	-21.22	-230.08	-227.59	110.48	-338.07
DC-[NiCl$_4$(H$_2$O)$_2$]$^{2-}$	-304.69	-0.04	-304.50	-306.98	22.55	-329.52
DC-[Ni(H$_2$O)$_2$(Eg)$_2$]$^{2+}$	22.09	8.14	29.64	27.17	-25.57	52.74
DC-[Ni(H$_2$O)$_4$(Eg)]$^{2+}$	24.62	19.73	41.69	36.74	-53.42	90.16
DC-[Ni(H$_2$O)$_6$]$^{2+}$	28.02	29.83	54.16	46.74	-79.03	125.76
DC-[Ni(Eg)$_2$]$^{2+}$	270.48	-11.67	257.64	260.12	57.39	202.73
DC-[Ni(H$_2$O)$_4$]$^{2+}$	343.85	9.43	349.30	346.83	4.49	342.33

Table 6.24: Relative thermochemical parameters for DC-*complex* systems in the gas phase.

System	ΔE_{elec}	Δzpe	ΔE	ΔH	TΔS	ΔG
DC-[Ni(Eg)$_3$]$^{2+}$	0.00	0.00	0.00	0.00	0.00	0.00
DC-[NiCl$_4$]$^{2-}$	75.21	-30.51	48.28	50.75	103.82	-53.07
DC-[NiCl$_2$(Eg)$_2$]	-37.65	-5.28	-40.75	-43.23	-8.72	-34.51
DC-[NiCl$_3$(H$_2$O)(Eg)]	-5.63	-8.52	-11.32	-13.80	4.33	-18.13
DC-[NiCl$_2$(H$_2$O)$_2$(Eg)]	-48.70	3.62	-43.47	-48.42	-34.85	-13.57
DC-[NiCl$_4$(Eg)]$^{2-}$	58.21	-22.46	40.81	40.81	47.25	-6.44
DC-[NiCl(H$_2$O)(Eg)$_2$]$^+$	-27.31	4.39	-23.62	-26.10	-22.41	-3.69
DC-[NiCl$_3$(H$_2$O)$_3$]$^-$	-14.96	3.11	-9.90	-14.86	-19.15	4.30
DC-[NiCl$_4$(H$_2$O)$_2$]$^{2-}$	40.72	-10.05	33.34	30.86	18.38	12.49
DC-[NiCl$_2$(H$_2$O)$_4$]	-54.73	14.83	-39.18	-46.61	-60.61	14.00
DC-[NiCl(H$_2$O)$_3$(Eg)]$^+$	-38.43	11.72	-28.86	-33.82	-48.37	14.56
DC-[Ni(H$_2$O)$_2$(Eg)$_2$]$^{2+}$	-7.24	14.18	4.07	1.59	-33.03	34.62
DC-[NiCl(H$_2$O)$_5$]$^+$	-38.23	24.44	-15.40	-22.83	-71.07	48.24
DC-[Ni(H$_2$O)$_4$(Eg)]$^{2+}$	-7.75	23.60	12.60	7.65	-57.30	64.95
DC-[Ni(Eg)$_2$]$^{2+}$	132.44	-9.93	121.11	123.58	54.87	68.71
DC-[Ni(H$_2$O)$_6$]$^{2+}$	-9.42	26.26	14.63	7.19	-75.68	82.88
DC-[Ni(H$_2$O)$_4$]$^{2+}$	116.32	12.19	124.96	122.48	1.56	120.93

Table 6.25: Relative thermochemical parameters for DC-*complex* systems in the Eg SMD.

System	ΔE_{elec}	Δzpe	ΔE	ΔH	$T\Delta S$	ΔG
NC-$[Ni(Eg)_3]^{2+}$	0.00	0.00	0.00	0.00	0.00	0.00
NC-$[NiCl_4]^{2-}$	23.43	-17.77	16.84	19.32	82.09	-62.77
NC-$[NiCl_4(Eg)]^{2-}$	-33.35	-9.40	-30.14	-30.15	26.81	-56.95
NC-$[NiCl_4(H_2O)_2]^{2-}$	-70.62	4.57	-56.61	-59.09	-4.16	-54.93
NC-$[NiCl_3(H_2O)(Eg)]$	-3.60	-2.38	-0.07	-0.07	28.29	-28.36
NC-$[NiCl_3(H_2O)_3]^{-}$	-23.74	10.35	-9.39	-11.87	2.75	-14.62
NC-$[Ni(H_2O)_2(Eg)_2]^{2+}$	-32.33	12.88	-22.55	-25.03	-30.05	5.03
NC-$[NiCl(H_2O)(Eg)_2]^{+}$	47.05	-0.98	47.33	47.33	22.41	24.92
NC-$[Ni(H_2O)_4(Eg)]^{2+}$	-42.43	25.23	-23.55	-28.50	-60.22	31.72
NC-$[NiCl_2(Eg)_2]$	103.57	-10.39	95.93	98.41	65.01	33.40
NC-$[NiCl(H_2O)_3(Eg)]^{+}$	14.35	15.57	26.47	23.99	-12.22	36.21
NC-$[NiCl_2(H_2O)_2(Eg)]$	80.78	1.97	84.55	84.56	41.05	43.50
NC-$[NiCl(H_2O)_5]^{+}$	-9.11	27.01	12.50	7.55	-39.79	47.34
NC-$[Ni(H_2O)_6]^{2+}$	-56.14	36.45	-28.59	-36.02	-88.77	52.74
NC-$[NiCl_2(H_2O)_4]$	53.23	16.11	66.88	64.41	6.46	57.95
NC-$[Ni(Eg)_2]^{2+}$	188.18	-18.85	169.02	171.50	61.93	109.58
NC-$[Ni(H_2O)_4]^{2+}$	134.16	13.60	139.38	136.91	-4.45	141.36

Table 6.26: Relative thermochemical parameters for NC-*complex* systems in the gas phase.

System	ΔE_{elec}	Δzpe	ΔE	ΔH	$T\Delta S$	ΔG
NC-$[Ni(Eg)_3]^{2+}$	0.00	0.00	0.00	0.00	0.00	0.00
NC-$[NiCl_2(Eg)_2]$	63.88	-8.77	56.17	58.65	62.23	-3.59
NC-$[NiCl(H_2O)(Eg)_2]^{+}$	20.08	1.42	20.46	20.46	14.64	5.83
NC-$[NiCl_4]^{2-}$	95.48	-22.04	82.41	84.89	74.61	10.28
NC-$[Ni(H_2O)_2(Eg)_2]^{2+}$	-23.45	12.41	-14.17	-16.65	-28.47	11.82
NC-$[NiCl_2(H_2O)_2(Eg)]$	52.83	0.13	53.46	53.46	36.10	17.36
NC-$[NiCl(H_2O)_3(Eg)]^{+}$	0.50	12.84	10.42	7.94	-12.72	20.66
NC-$[Ni(H_2O)_4(Eg)]^{2+}$	-32.63	23.29	-14.11	-19.06	-53.46	34.39
NC-$[NiCl_3(H_2O)(Eg)]$	59.17	-4.56	59.10	59.10	23.26	35.84
NC-$[NiCl_4(Eg)]^{2-}$	50.46	-11.34	47.47	47.47	4.52	42.95
NC-$[NiCl_2(H_2O)_4]$	46.80	11.34	57.74	55.27	10.35	44.92
NC-$[Ni(Eg)_2]^{2+}$	129.63	-15.07	115.27	117.75	67.53	50.22
NC-$[NiCl(H_2O)_5]^{+}$	1.94	23.59	21.95	17.00	-36.15	53.15
NC-$[NiCl_3(H_2O)_3]^{-}$	46.25	6.53	55.66	53.18	-4.14	57.32
NC-$[Ni(H_2O)_6]^{2+}$	-44.43	32.81	-18.98	-26.41	-84.34	57.93
NC-$[NiCl_4(H_2O)_2]^{2-}$	53.88	0.30	61.16	58.68	-17.62	76.29
NC-$[Ni(H_2O)_4]^{2+}$	81.12	13.05	88.24	85.76	2.71	83.05

Table 6.27: Relative thermochemical parameters for NC-*complex* systems in the Eg SMD.

System	ΔE_{elec}	Δzpe	ΔE	ΔH	$T\Delta S$	ΔG
$\delta\delta\delta$-$[Fe(Eg)_3]^{2+}$	0	0	0	0	0	0
$\delta\delta\lambda$-$[Fe(Eg)_3]^{2+}$	13.91	-2.53	13.26	13.26	7.31	5.95
$\delta\lambda\lambda$-$[Fe(Eg)_3]^{2+}$	9.57	0.12	9.57	9.57	-0.09	9.66
$\lambda\lambda\lambda$-$[Fe(Eg)_3]^{2+}$	2.96	0.28	3.11	3.11	-0.52	3.63
$\delta\delta\delta$-$[Co(Eg)_3]^{2+}$	0	0	0	0	0	0
$\delta\delta\lambda$-$[Co(Eg)_3]^{2+}$	3.83	-0.58	3.79	3.79	1.32	2.47
$\delta\lambda\lambda$-$[Co(Eg)_3]^{2+}$	21.78	-0.36	21.7	21.7	-0.06	21.75
$\lambda\lambda\lambda$-$[Co(Eg)_3]^{2+}$	15.01	1.62	15.71	15.7	-5.1	20.8
$\delta\delta\delta$-$[Ni(Eg)_3]^{2+}$	0	0	0	0	0	0
$\delta\delta\lambda$-$[Ni(Eg)_3]^{2+}$	17.39	-3.74	15.68	15.69	4.78	10.91
$\delta\lambda\lambda$-$[Ni(Eg)_3]^{2+}$	7.69	-1.08	7.21	7.21	1.51	5.69
$\lambda\lambda\lambda$-$[Ni(Eg)_3]^{2+}$	1.8	0.01	1.75	1.75	-1.93	3.68
$\delta\delta\delta$-$[Cu(Eg)_3]^{2+}$	0	0	0	0	0	0
$\delta\delta\lambda$-$[Cu(Eg)_3]^{2+}$	19.54	-5.29	17.48	17.48	9.23	8.24
$\delta\lambda\lambda$-$[Cu(Eg)_3]^{2+}$	0.3	0.09	0.34	0.35	-0.01	0.35
$\lambda\lambda\lambda$-$[Cu(Eg)_3]^{2+}$	8.43	-1.88	7.69	7.69	3.01	4.68
$\delta\delta\delta$-$[Zn(Eg)_3]^{2+}$	0	0	0	0	0	0
$\delta\delta\lambda$-$[Zn(Eg)_3]^{2+}$	2.72	-0.51	2.48	2.48	-1.25	3.73
$\delta\lambda\lambda$-$[Zn(Eg)_3]^{2+}$	14.17	-4.67	12.33	12.33	6.68	5.65
$\lambda\lambda\lambda$-$[Zn(Eg)_3]^{2+}$	7.83	-2.05	6.99	6.99	2.86	4.13

Table 6.28: Relative thermochemical parameters for $[M(Eg)_3]^{2+}$ conformers in the gas phase.

System	ΔE_{elec}	Δzpe	ΔE	ΔH	$T\Delta S$	ΔG
$\delta\delta\delta$-$[Fe(Eg)_3]^{2+}$	0	0	0	0	0	0
$\delta\delta\lambda$-$[Fe(Eg)_3]^{2+}$	1.48	-4.64	-2.95	-2.95	0.49	-3.44
$\delta\lambda\lambda$-$[Fe(Eg)_3]^{2+}$	0.49	-2.25	-0.79	-0.79	0.62	-1.41
$\lambda\lambda\lambda$-$[Fe(Eg)_3]^{2+}$	3.02	-5.03	-2.07	-2.07	-3.2	1.13
$\delta\delta\delta$-$[Co(Eg)_3]^{2+}$	0	0	0	0	0	0
$\delta\delta\lambda$-$[Co(Eg)_3]^{2+}$	9.79	-4.68	7.55	7.55	9.3	-1.75
$\delta\lambda\lambda$-$[Co(Eg)_3]^{2+}$	15.68	-6.21	10.13	10.13	1.71	8.43
$\lambda\lambda\lambda$-$[Co(Eg)_3]^{2+}$	3.01	-2.28	-0.05	-0.05	-0.86	0.81
$\delta\delta\delta$-$[Ni(Eg)_3]^{2+}$	0	0	0	0	0	0
$\delta\delta\lambda$-$[Ni(Eg)_3]^{2+}$	-0.04	-3.95	-5.11	-5.11	-3.96	-1.15
$\delta\lambda\lambda$-$[Ni(Eg)_3]^{2+}$	1.57	-2.25	0.04	0.04	-0.94	0.98
$\lambda\lambda\lambda$-$[Ni(Eg)_3]^{2+}$	6.34	-4.35	3.89	3.89	5.87	-1.98
$\delta\delta\delta$-$[Cu(Eg)_3]^{2+}$	0	0	0	0	0	0
$\delta\delta\lambda$-$[Cu(Eg)_3]^{2+}$	0.75	2.72	6.44	6.44	3.9	2.54
$\delta\lambda\lambda$-$[Cu(Eg)_3]^{2+}$	3.35	1.38	8.3	8.3	-1.19	9.48
$\lambda\lambda\lambda$-$[Cu(Eg)_3]^{2+}$	5.07	1.97	9.56	9.56	-3.68	13.25
$\delta\delta\delta$-$[Zn(Eg)_3]^{2+}$	0	0	0	0	0	0
$\delta\delta\lambda$-$[Zn(Eg)_3]^{2+}$	4.68	-3.51	3.23	3.23	11.37	-8.13
$\delta\lambda\lambda$-$[Zn(Eg)_3]^{2+}$	-2.05	-0.23	-4.52	-4.52	-7.37	2.85
$\lambda\lambda\lambda$-$[Zn(Eg)_3]^{2+}$	1.34	-3.38	-0.03	-0.03	4.16	-4.19

Table 6.29: Relative thermochemical parameters for $[M(Eg)_3]^{2+}$ conformers in the Eg SMD.

6.3 Licence agreements for reuse of figures

Physical chemistry chemical physics

Order detail ID: 71919932

ISSN: 1463-9084
Publication Type: e-Journal
Volume:
Issue:
Start page:
Publisher: ROYAL SOCIETY OF CHEMISTRY
Author/Editor: Royal Society of Chemistry (Great Britain)

Permission Status: ✓ Granted

Permission type: Republish or display content
Type of use: Thesis/Dissertation
Order License Id: 4605441166880

⊟ Hide details

Requestor type	Academic institution
Format	Print, Electronic
Portion	chart/graph/table/figure
Number of charts/graphs/tables/figures	1
The requesting person/organization	Imperial College London
Title or numeric reference of the portion(s)	Figure 14
Title of the article or chapter the portion is from	Competitive pi interactions and hydrogen bonding within imidazolium ionic liquids
Editor of portion(s)	N/A
Author of portion(s)	Richard P. Matthews, Tom Welton and Patricia A. Hunt
Volume of serial or monograph	N/A
Page range of portion	3249
Publication date of portion	23rd December 2013
Rights for	Main product
Duration of use	Life of current edition
Creation of copies for the disabled	yes
With minor editing privileges	yes
For distribution to	Worldwide
In the following language(s)	Original language of publication
With incidental promotional use	no
Lifetime unit quantity of new product	Up to 499
Title	Halometallate ionic liquids and deep eutectic solvents via density functional theory
Institution name	Imperial College London
Expected presentation date	Aug 2019

PERMISSION/LICENSE IS GRANTED FOR YOUR ORDER AT NO CHARGE

PERMISSION/LICENSE IS GRANTED FOR YOUR ORDER AT NO CHARGE

License Number	4641010577742
License date	Aug 02, 2019
Licensed Content Publisher	Elsevier
Licensed Content Publication	Journal of Natural Gas Chemistry
Licensed Content Title	Ab Initio Calculation of Room Temperature Ionic Liquid 1-Ethyl-3-Methyl-Imidazolium Chlorocuprate (I)
Licensed Content Author	Renqing Lü,Hejin Tangbo,Zuogang Cao
Licensed Content Date	Mar 1, 2007
Licensed Content Volume	16
Licensed Content Issue	1
Licensed Content Pages	8
Type of Use	reuse in a thesis/dissertation
Portion	figures/tables/illustrations
Number of figures/tables/illustrations	1
Format	both print and electronic
Are you the author of this Elsevier article?	No
Will you be translating?	No
Original figure numbers	Figure 2
Title of your thesis/dissertation	Halometallate ionic liquids and deep eutectic solvents via density functional theory
Publisher of new work	Imperial College London
Expected completion date	Aug 2019
Estimated size (number of pages)	1
Requestor Location	Rebecca Rowe 5 John Strachey House Clem Attlee Court

Fulham, London SW6 7SQ United Kingdom Attn: |
| Publisher Tax ID | GB 494 6272 12 |
| Total | 0.00 USD |

Physical chemistry chemical physics

Order detail ID: 71970114
Order License Id: 4641011425439

ISSN: 1463-9084
Publication Type: e-Journal
Volume:
Issue:
Start page:
Publisher: ROYAL SOCIETY OF CHEMISTRY
Author/Editor: Royal Society of Chemistry (Great Britain)

Permission Status: ✅ Granted

Permission type: Republish or display content
Type of use: Thesis/Dissertation

⊟ Hide details

Requestor type	Academic institution
Format	Print, Electronic
Portion	chart/graph/table/figure
Number of charts/graphs/tables/figures	2
The requesting person/organization	Rebecca Rowe
Title or numeric reference of the portion(s)	Figure 2.a.
Title of the article or chapter the portion is from	The acidity/basicity of metal-containing ionic liquids: insights from surface analysis and the Fukui function
Editor of portion(s)	N/A
Author of portion(s)	Wu, Weihong Lu, Yunxiang Ding, Hairong Peng, Changjun Liu, Honglai
Volume of serial or monograph	17
Issue, if republishing an article from a serial	2
Page range of portion	1342
Publication date of portion	2015
Rights for	Main product
Duration of use	Life of current edition
Creation of copies for the disabled	no
With minor editing privileges	yes
For distribution to	Worldwide
In the following language(s)	Original language of publication
With incidental promotional use	no
Lifetime unit quantity of new product	Up to 499
Title	Halometallate ionic liquids and deep eutectic solvents via density functional theory
Institution name	Imperial College London
Expected presentation date	Aug 2019